Multiplexed Biosensors Based on Multimode Nanoslits

Marcos Valero Recio Ramirez

Thesis submitted to the University of Ottawa in partial fulfillment of the requirements for the degree of Doctor of Philosophy in Electrical Engineering

School of Electrical Engineering and Computer Science
Faculty of Engineering
University of Ottawa

Abstract

Surface plasmon-based biosensors are widely recognized for their exceptional sensitivity, ease of integration, and versatility across various fields, including biomedical diagnostics, environmental monitoring, and chemical analysis. While these sensors have demonstrated significant potential for real-time, label-free detection, they still face key challenges—one of the most critical being multiplexing. The ability to simultaneously detect multiple biomarkers is particularly important in medical diagnostics, where comprehensive assessments can lead to earlier and more precise disease detection. However, current surface plasmon technologies face limitations in achieving effective multiplexing, underscoring the need for innovative configurations.

This thesis presents the design, modeling, fabrication, and experimental validation of a novel surface plasmon resonance (SPR) interferometric biosensor capable of supporting multiplexed detection. The proposed device operates by exciting and interfering counter-propagating surface plasmon waves in a nanoslit structure using optimized grating couplers, achieving high-visibility interference patterns. Full-wave electromagnetic simulations demonstrate a maximum bulk sensitivity of $S_b = -3.87\,\mathrm{W/(m{\cdot}RIU)}$, a surface sensitivity of $S_s = 0.002\,\mathrm{W/(m{\cdot}nm)}$, and a resolution down to $R_b = 6.3 \times 10^{-6}\,\mathrm{RIU}$ and $R_s = 10\,\mathrm{pm}$, depending on the nanoslit geometry. The optimal grating coupler design reached a total coupling efficiency of 54.7%, ensuring effective SPR excitation with Gaussian beam illumination.

To enable multiplexing, a shadowing structure was developed and integrated to allow simultaneous excitation of multiple sensing units with a single expanded Gaussian beam. Simulations confirmed that the device maintains independent sensing responses in each channel with minimal crosstalk. A complete fabrication process, including gold deposition, electron beam lithography, focused ion beam milling, and CYTOP-based microfluidic integration, was implemented. The final device successfully detected refractive index changes in water-glycerol mixtures, experimentally validating the interferometric sensing principle and confirming agreement with theoretical predictions.

These findings demonstrate that the interferometric SPR platform not only functions as a highly sensitive refractive index sensor, but also offers scalable multiplexing capabilities. This work lays the groundwork for future

advancements in three key directions: miniaturizing the optical system for portable diagnostics, functionalizing the sensor for selective biomarker detection, and integrating spatial light modulators for real-time, multi-channel interrogation. Together, these developments promise to enhance the applicability of SPR biosensing in real-world biomedical and clinical diagnostics.

Dedication

I dedicate this thesis to the Mexican society and the people of Mexico. Thanks to the public support from institutions like CONACYT, individuals like me have had the opportunity to pursue academic and professional goals abroad. Education and technological innovation are the keys to a nation's development, and I hope to always give back to my country for the opportunities it has given me.

Acknowledgments

First and foremost, I want to express my deepest gratitude to Dr. Israel De León for inviting me to this project, considering me for the first dual-degree program between the University of Ottawa and Tecnológico de Monterrey, and for never abandoning the project despite the changes. To Dr. Mallar Ray, for taking on my project midway and supporting me in every way possible, always highlighting his exceptional human qualities. I feel fortunate to have had him as my advisor. And to Dr. Pierre Berini, the head of this project, for his unwavering support in all aspects, always believing in me, motivating me to be better, and ensuring I had everything I needed. Without his guidance, this thesis would not be possible.

Furthermore, my colleagues were also an essential part of this journey. In Canada, I want to thank Luis for helping with the optical setup to test my microchips; Ewa, who taught me to design and create the microchip layouts; Howard and Deepthi for training me in the Nanofab laboratory; and Hyung and Spyros for their constant support in the clean room.

In Mexico, I extend my gratitude to Martín at Tecnológico de Monterrey, always a great support, and to Kevin and Irving for their help in the labs.

To all my colleagues, for their closeness and support. And to my students who inspired me to keep learning and growing.

Finally, and most importantly, I want to thank my mom, María Eugenia, and my sister, Mariana. Your unconditional support and love have been my pillars through this process. Everything I am is because of you. I love you both and will always strive to be the person you deserve as a son and brother.

I acknowledge the use of AI-assisted tools for organizing, refining, and correcting this thesis, particularly in the state-of-the-art section. However,the intellectual and creative contributions, including the conceptualization, experimental work, and design, are entirely my own.

Publications

Papers submitted and accepted in refereed journals:

- Valero, M., De Leon, I., Ray, M., & Berini, P. (2024). Multiplexed biosensors based on interference of surface plasmons in multimode nanoslits. *Applied Optics, 64*(1), 50-63.
- Valero, M., Mayoral-Astorga, L. A., Northfield, H., Choi, H. W., De Leon, I., Ray, M., & Berini, P. (2025). Selective modal excitation in a multimode nanoslit by interference of surface plasmon waves. *Nanoscale Advances*.
- Valero, M., Northfield, H., Choi, H., Killaire, G., & Berini, P. (Submitted 2025). Fabrication of a Surface Plasmon Resonance Biosensor Based on the Selective Excitation of Multimodal Electrical Field Distributions in a Gold Nanoslit. *Submitted to Journal of Physics: Photonics*.

Contents

List of Figures

List of Tables

1

Introduction

A sensor is defined as a device capable of converting one type of signal into another. Since ancient times, humans have developed their own natural sensors, such as the photoreceptor cells in the eye or the tactile receptors in the skin, which allow us to perceive our surroundings.

In addition to these natural sensors, humans have created artificial sensors to expand their capabilities. A primitive example is Galileo Galilei's thermometer, invented around 1592. This device used the principles of thermodynamics to measure temperature changes by observing the contraction and expansion of air in a sealed container, which moved a column of water.

Since then, sensor technology has evolved tremendously. In the past century, the development of electromagnetism by James Maxwell and other engineers revolutionized technological applications, leading to the rise of optical technology and the development of optical sensors. These advances have enabled the creation of increasingly compact and sensitive sensors, capable of detecting minute changes in the environment for various applications, including medicine.

In the medical field, optical sensors can measure biomarkers, enabling disease diagnosis and monitoring. These types of sensors are known as optical biosensors, which have been explored in multiple configurations. This is a broad field with numerous developments, where the main goal is to find devices with better performance, higher sensitivity, an optimal cost-benefit ratio, a compact design, and ease of operation.

In this context, surface plasmon-based sensors play a crucial role. These sensors use electromagnetic waves that propagate along the surface of metals to detect, with unparalleled sensitivity and specificity, changes in the refractive index of a substance caused by modifications in its chemical composition.

To further enhance their performance, these sensors can be integrated into interferometric configurations, which allow the detection of extremely small variations of some analyte. An interferometer is an optical device that measures changes in the phase of light waves through interference, making it an ideal tool to amplify the detection of subtle changes in the sensor's

environment.

There is growing interest in multiplexed devices, where multiple sensors are integrated on a single platform allowing the simultaneous analysis of multiple samples or the detection of multiple biomarkers within a single sample. This approach is promising, as it enables the identification of various diseases by a single sensor, providing a more comprehensive picture of a patient's health.

For all these reasons, in this thesis, we explore the development of an interferometric biosensor based on surface plasmons, designed to achieve high sensitivity and multiplexed detection of biomarkers.

A schematic of the proposed configuration is shown in Figure 1.1a. The device consists of a metallic film deposited on a transparent substrate, with two grating couplers fabricated symmetrically on either side of a central nanoslit. These gratings are used to launch counter-propagating surface plasmon polaritons (SPPs) along the metal-dielectric interface, which are excited with a pair of Gaussian beams. The metallic surface is coated with a dielectric polymer layer, such as CYTOP, which provides optical matching with aqueous analytes and serves as a structural support for microfluidic integration. A microfluidic channel is then etched into the CYTOP layer, aligned with one of the SPP propagation paths, allowing the sensing fluid to interact directly with the gold surface while the other arm serves as a reference.

The interference of the SPPs at the nanoslit results in the excitation of distinct resonant modes whose nature depends on the phase difference between the incoming waves. This behavior is illustrated in Figure 1.1b. When the SPPs arrive in phase, the field distribution within the slit exhibits even symmetry, corresponding to excitation of a dipolar resonance. Conversely, a phase difference of $\Delta\phi = \pi$ leads to an odd-symmetric near-field distribution, exciting a quadrupolar resonance. These modes result in characteristically different radiation patterns into the substrate, which can be monitored to infer refractive index changes in the sensing region.

This configuration forms the basis for a multiplexed biosensor design, in which multiple unit cells can be arrayed laterally and interrogated simultaneously.

The details of the proposed interferometric biosensor, including its geometry, electromagnetic modeling, and performance evaluation, will be presented throughout this thesis, which is organized as follows:

In Chapter 2, we present a state-of-the-art review where we explore in detail the fundamentals of surface plasmons, their application in biosensors,

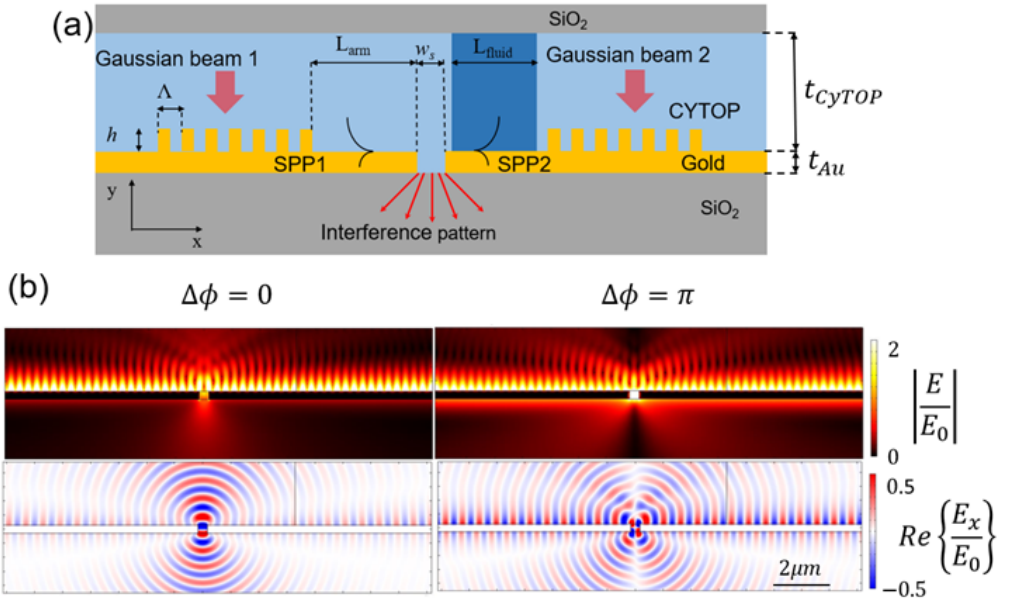

Figure 1.1: Schematic of the proposed interferometric biosensor. (a) Top view showing the gold film with two grating couplers symmetrically placed on either side of a central nanoslit. The surface is coated with a CYTOP layer into which a microfluidic channel is etched above the sensing arm. (b) Simulated electric field distributions inside the nanoslit showing dipolar mode excitation for $\Delta\phi = 0$ (left) and quadrupolar mode excitation for $\Delta\phi = \pi$ (right).

and the main components of these devices. We also analyze a wide range of previous studies in this field to understand the current technological landscape, identify its advances and limitations, and position our work within the latest research.

In Chapter 3, we introduce the design and electromagnetic modeling of a new type of multiplexed biosensor based on the interference of surface plasmons in multimode nanoslits. This chapter establishes the theoretical foundations and the steps required to optimize and design this structure, considering the physical properties that determine its performance and sensitivity.

In Chapter 4, we experimentally demonstrate that our configuration can be used as an interferometer, allowing us to detect extremely small changes in

the phase of a surface plasmon wave. Additionally, we show how optimizing each component of the device directly impacts its performance, opening the possibility of improving its sensitivity and precision metrics when it is used in a biosensing application.

In Chapter 5, we detail the fabrication process of these devices, utilizing state-of-the-art microfabrication and nanofabrication techniques. Furthermore, we explain how these sensors should be handled and operated and compare the experimental results with the theoretical calculations provided in Chapter 3. We find a strong correlation between the two, validating our methodology. As proof of concept, we demonstrate the detection of changes in the refractive index of a glycerol-water mixture, paving the way for future applications and optimizations in biosensor design.

Finally, in Chapter 6, we present the conclusions of this work and discuss the future of this project. Given its high potential, this sensor can continue to evolve and generate new scientific and technological advancements.

The development of this sensor still has a long way to go, but it represents a significant advance in our ability to understand reality and improve biomedical detection tools.

Thesis Contributions

This thesis makes several key contributions to the development of multiplexed interferometric surface plasmon biosensors:

First, a comprehensive finite element method (FEM) simulation framework was proposed, starting with a rigorous mode analysis to replicate known theoretical resonances and proceeding to full field scattering simulations. This approach enabled the modeling of the sensor as a coupled system, including grating couplers, nanoslit, and microfluidic channel, allowing precise optimization of each component's geometry and electromagnetic performance.

Second, a new optical strategy was introduced to simplify the experimental setup and improve system robustness. Instead of relying on two precisely aligned Gaussian beams, a single wide Gaussian beam was used in combination with a custom-designed shadowing element. This element was engineered to block direct illumination of the nanoslit, thereby preserving interferometric behavior and enabling a common-path interferometer configuration. This strategy also allowed for the illumination of multiple sensing units in parallel, enabling optical multiplexing.

Third, a complete cleanroom fabrication process was developed and im-

plemented. This process includes metal deposition, electron-beam lithography, focused ion beam (FIB) milling, polymer deposition and etching, wafer bonding, and chip dicing. Using this methodology, fully functional sensor chips were successfully fabricated. In parallel, a custom mechanical jig holder was developed to support experimental testing. This jig was specifically designed to hold the chips securely in place and to enable perpendicular optical interrogation using two microscope objectives—one above and one below the device. Additionally, the jig allowed the precise interfacing of three microfluidic channels simultaneously, using a gasket-based sealing mechanism to prevent fluid leakage and ensure stable measurements.

Fourth, a complex dual-beam optical setup was designed and experimentally implemented to enable precise excitation and detection of the interferometric signal. This system includes multiple optical components that allow the splitting of a coherent, TM-polarized Gaussian beam into two parallel beams, which are then focused onto the chip surface with approximately 10 µm beam diameters and a separation of about 100 µm. The setup provides fine control over the intensity and position of each beam, allowing them to selectively excite the grating couplers and generate interference at the nanoslit. A second microscope objective was used to collect the transmitted signal, which was then recorded with a CCD camera. This configuration enabled the acquisition of real-time data and the generation of sensograms for subsequent signal analysis.

Fifth, interferometric behavior was experimentally demonstrated using a pre-functionalized version of the sensor based on a gold–air interface. In this configuration, the excitation and interference of surface plasmons was clearly observed, validating the optical design. Devices were fabricated with varying geometrical parameters—including different grating periods, nanoslit widths, and arm lengths—to investigate how these features affect performance. The experimental results were in strong agreement with full-wave electromagnetic simulations, confirming the predictive accuracy of the design model and validating the principle of tunability through geometry.

Finally, the sensor was operated as a functional refractometric platform by performing bulk sensing experiments using water–glycerol mixtures to induce controlled changes in the surrounding refractive index. The sensor exhibited a clear and repeatable response to these changes, establishing its functionality as a label-free SPR-based refractive index sensor. This demonstration confirms that the platform is ready for future surface functionalization to enable the detection of specific biochemical targets.

Together, these contributions establish a robust theoretical, experimental, and fabrication foundation for the advancement of multiplexed SPR interferometric biosensing technologies.

2

State of the art

2.1 Introduction to Surface Plasmon Resonance

Surface Plasmon Resonance (SPR) refers to the coherent oscillation of free electrons at the interface between a metal and a dielectric, which is typically excited by incident light at a specific angle and wavelength [1,2]. SPR is a fundamental phenomenon that arises when the momentum of incident photons (assisted by a coupling mechanism) aligns with the momentum of surface plasmons. This alignment is achieved when the wavevector (or momentum) of the light in the dielectric matches the surface plasmon wavevector at the interface. Since photons typically have a lower momentum than surface plasmons, this matching condition is made possible through specific experimental setups, such as prism coupling or grating configurations, which alter the incident light's wavevector to achieve SPR [3,4]. SPR phenomena is broadly categorized into two types: localized surface plasmon resonance (LSPR) and propagating surface plasmon polariton (PSPP) [5]. LSPR rely on the localized oscillations of free electrons around metallic nanostructures, such as nanoparticles, resulting in highly confined electromagnetic fields in a small spatial region. In contrast, PSPP is based on surface plasmon waves propagating along a planar metal-dielectric interface. These waves, similar to ripples in water, decay as they propagate and confine their energy near the interface. Both mechanisms are illustrated in Figure 2.1, where (a) depicts LSPR on nanoparticles, and (b) shows PSPP along a flat gold-dielectric interface.

The ability of materials to support SPR depends significantly on their dielectric properties. For metals like gold or silver, the permittivity is negative in the visible to near-infrared range, which allows them to support surface plasmons [6-8]. This negative permittivity creates a phase-matching condition by reducing the wavevector of the plasmon to a level comparable with the incident light. As a result, the electromagnetic field becomes highly localized at the metal-dielectric interface, leading to a strong enhancement of

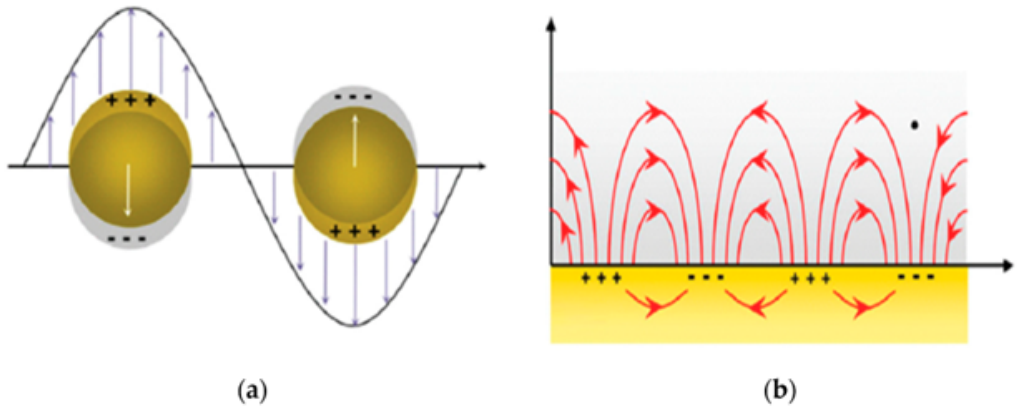

Figure 2.1: Schematic representation of SPR mechanisms. (a) LSPR is illustrated on metallic nanoparticles (yellow spheres), where oscillating electron densities create localized fields in the surrounding dielectric medium. (b) PSPP travel along a flat gold-dielectric interface, represented by the gold (yellow) layer beneath a dielectric (gray) medium. The oscillating fields and charges are depicted as sinusoidal distributions, indicating the interaction at the interface. Adapted from [5].

the electric field intensity, often orders of magnitude higher than the incident field. This field enhancement is central to applications of SPR, such as in biosensing, where it amplifies the interaction of light with nearby molecules, making them detectable at extremely low concentrations [9,10].

2.1.1 Historical Background

The history of plasmonic phenomena can be traced back to intriguing artifacts like the Lycurgus Cup, an ancient Roman chalice that exhibits a remarkable color change depending on the direction of illumination, as shown in Figure 2.2 [11]. This unique property is caused by embedded metal nanoparticles—gold and silver—that create a dichroic effect. When the cup is lit from the front, it appears green; when backlit, it shifts to a deep red. This color change results from the interaction of light with the metal nanoparticles, which generates SPR, selectively scattering and absorbing certain wavelengths. The cup stands as one of the earliest examples of plasmonic effects in human craftsmanship and highlights how metal nanoparticles can induce

vibrant, wavelength-specific colors.

Figure 2.2: The Lycurgus Cup, an ancient Roman artifact, exhibits a dichroic effect due to embedded gold and silver nanoparticles. When illuminated from the front, the cup appears green, while backlighting reveals a deep red color. This remarkable example of plasmonic phenomena is displayed in the British Museum. Figure taken from [11].

Scientific investigation into SPR began with observations made in the early 20th century by researchers like Wood and Lord Rayleigh [12,13]. Wood first observed anomalous diffraction patterns, also known as Wood's anomalies, in metallic gratings in 1902, which were later explained by Rayleigh in terms of surface waves, laying the foundation for the understanding of SPR. However, it wasn't until the 1960s and 1970s that SPR began to be applied in a more practical sense, particularly with the development of experimental configurations that could reliably excite surface plasmons. The two most significant configurations that emerged were the Kretschmann and Otto configurations [14,15], which utilized prism coupling to excite surface plasmons at metal-dielectric interfaces. In both cases, light is reflected through a prism, and at the correct angle, a dip in the reflected light signal is observed, corresponding to the excitation of surface plasmons at the metal interface. The key difference between the two lies in the positioning of the metal layer. In the Kretschmann configuration, the metal layer is directly coated onto the base of the prism, enabling surface plasmon excitation at the metal-dielectric interface when light passes through the prism and interacts with the metal. In contrast, the Otto configuration introduces a thin dielectric spacer layer between the prism and the metal, creating a small air gap. Surface plasmons

are excited at the metal-air interface when the evanescent wave penetrates through the dielectric spacer. These configurations can be seen in Figure 2.3 [16], where the geometries and mechanisms of each setup are illustrated.

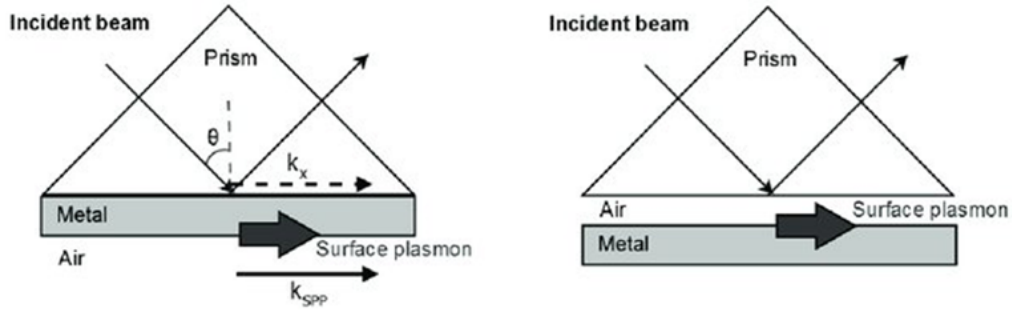

Figure 2.3: Schematic representation of (a) the Kretschmann configuration and (b) the Otto configuration for exciting surface plasmons using prism coupling. In the Kretschmann configuration, the metal layer is directly coated onto the prism base, enabling surface plasmon excitation at the metal-dielectric interface. In the Otto configuration, a thin air gap separates the prism from the metal, allowing surface plasmons to be excited at the metal-air interface via the evanescent wave. Image adapted from [16].

Over the decades, SPR has evolved from a theoretical curiosity to a practical tool used in various scientific fields. By the 1990s, SPR had become a cornerstone in biosensing technologies due to its ability to detect real-time changes in the refractive index at the metal-dielectric interface with high sensitivity [17-20]. Today, SPR is not only used for sensing but also for investigating fundamental plasmonic phenomena, enabling advances in nanotechnology, photonics, and materials science [21-26].

2.1.2 Single-Interface Plasmonic Waveguides

Plasmonic waveguides are structures designed to confine and guide electromagnetic waves at metal-dielectric boundaries by leveraging surface plasmon polaritons [27-29]. In this work, we focus on the single-interface plasmonic waveguide, which leverages the simplicity of using only one metal-dielectric boundary. This straightforward design eases fabrication and integration while still providing strong field confinement.

To examine the propagation properties of SPPs in single-interface plasmonic waveguides, we start from Maxwell's curl equations, assuming there are no external charge ($\rho = 0$) or current ($\mathbf{J} = 0$) densities. This allows us to write [1]:

$$\nabla \times \nabla \times \mathbf{E} = -\mu_0 \frac{\partial^2 \mathbf{D}}{\partial t^2}, \tag{2.1}$$

where μ_0 is the permeability of free space and $\mathbf{D}$ is the electric displacement field. The electric displacement is related to the electric field by $\mathbf{D} = \epsilon \mathbf{E}$, with $\epsilon = \epsilon_r \epsilon_0$, where ϵ_0 is the permittivity of free space and ϵ_r is the relative permittivity of the medium. Similarly, the magnetic flux density is given by $\mathbf{B} = \mu \mathbf{H} = \mu_r \mu_0 \mathbf{H}$, where μ_r is the relative permeability.

The refractive index n of a material is defined as:

$$n = \sqrt{\epsilon_r \mu_r}, \tag{2.2}$$

and for most non-magnetic materials at optical frequencies, $\mu_r \approx 1$, leading to:

$$n \approx \sqrt{\epsilon_r}. \tag{2.3}$$

Therefore, the permittivity of the material plays a central role in determining how light and SPP waves propagate through it—higher permittivity generally implies a higher refractive index and slower light propagation.

Continuing with the derivation, using the vector identity $\nabla \times \nabla \times \mathbf{E} = \nabla(\nabla \cdot \mathbf{E}) - \nabla^2 \mathbf{E}$, and that $\nabla \cdot \mathbf{D} = 0$, we get:

$$\nabla \left(-\frac{1}{\epsilon} \mathbf{E} \cdot \nabla \epsilon \right) - \nabla^2 \mathbf{E} = -\mu_0 \epsilon_0 \epsilon \frac{\partial^2 \mathbf{E}}{\partial t^2}. \tag{2.4}$$

Assuming that variations of the dielectric function $\epsilon(\mathbf{r})$ are negligible on the order of one optical wavelength, this simplifies to:

$$\nabla^2 \mathbf{E} - \frac{\epsilon}{c^2} \frac{\partial^2 \mathbf{E}}{\partial t^2} = 0, \tag{2.5}$$

where $c = 1/\sqrt{\mu_0 \epsilon_0}$ is the speed of light in vacuum.

We now assume harmonic time dependence $\mathbf{E}(\mathbf{r}, t) = \mathbf{E}(\mathbf{r}) e^{-i\omega t}$, which transforms the wave equation into the Helmholtz equation:

$$\nabla^2 \mathbf{E} + k_0^2 \epsilon \mathbf{E} = 0, \tag{2.6}$$

where $k_0 = \omega/c$ is the free-space wavenumber.

For one-dimensional propagation along the x-direction, with no variation along y, and dielectric constant $\epsilon = \epsilon(z)$, we use the ansatz $\mathbf{E}(x, z) = \mathbf{E}(z)e^{i\beta x}$, where β is the propagation constant. Substituting this into the Helmholtz equation yields:

$$\frac{d^2\mathbf{E}(z)}{dz^2} + \left(k_0^2\epsilon - \beta^2\right)\mathbf{E} = 0. \tag{2.7}$$

We now restrict ourselves to transverse magnetic (TM) modes, for which only the components E_x, E_z, and H_y are nonzero. The wave equation for the magnetic field becomes:

$$\frac{d^2H_y}{dz^2} + \left(k_0^2\epsilon - \beta^2\right)H_y = 0. \tag{2.8}$$

We analyze a single interface at $z = 0$ between a dielectric ($z > 0$) with permittivity ϵ_2, and a metal ($z < 0$) with complex permittivity $\epsilon_1(\omega)$, as illustrated in Figure 2.4.

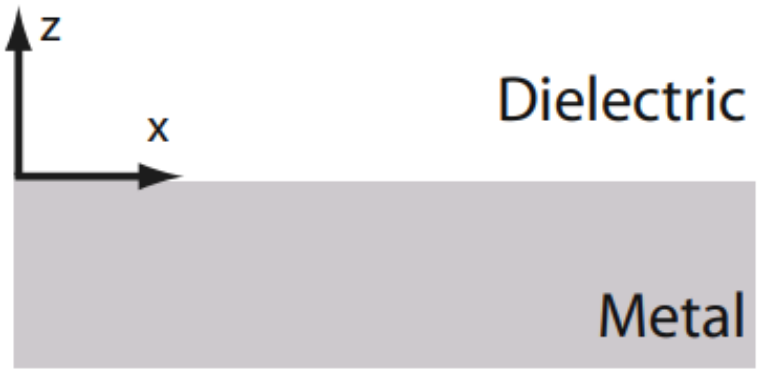

Figure 2.4: Schematic of a metal-dielectric interface, showing the propagation direction of the SPP along the x-axis and the exponential decay in the z-direction [1].

The magnetic and electric field components for transverse magnetic (TM) modes are:

$$H_y(z) = \begin{cases} A_2 e^{i\beta x}e^{-k_2 z}, & z > 0 \\ A_1 e^{i\beta x}e^{k_1 z}, & z < 0 \end{cases}$$

$$E_x(z) = \begin{cases} iA_2 \frac{1}{\omega\epsilon_0\epsilon_2} k_2 e^{i\beta x} e^{-k_2 z}, & z > 0 \\ -iA_1 \frac{1}{\omega\epsilon_0\epsilon_1} k_1 e^{i\beta x} e^{k_1 z}, & z < 0 \end{cases}$$

$$E_z(z) = \begin{cases} -A_2 \frac{\beta}{\omega\epsilon_0\epsilon_2} e^{i\beta x} e^{-k_2 z}, & z > 0 \\ -A_1 \frac{\beta}{\omega\epsilon_0\epsilon_1} e^{i\beta x} e^{k_1 z}, & z < 0 \end{cases}$$

where the decay constants are:

$$k_1^2 = \beta^2 - k_0^2\epsilon_1, \quad k_2^2 = \beta^2 - k_0^2\epsilon_2. \tag{2.9}$$

The boundary conditions at $z = 0$ require the continuity of H_y and ϵE_z, which lead to:

$$\frac{k_2}{\epsilon_2} = -\frac{k_1}{\epsilon_1}. \tag{2.10}$$

Solving this system yields the well-known dispersion relation for surface plasmon polaritons:

$$\beta = k_0 \sqrt{\frac{\epsilon_1\epsilon_2}{\epsilon_1 + \epsilon_2}}. \tag{2.11}$$

We now briefly analyze the possibility of TE-polarized surface modes at a single metal-dielectric interface. For transverse electric (TE) modes, only the components E_y, H_x, and H_z are nonzero. The wave equation for the electric field becomes:

$$\frac{d^2 E_y}{dz^2} + \left(k_0^2\epsilon(z) - \beta^2\right) E_y = 0. \tag{2.12}$$

The corresponding field components in each region are:

$$E_y(z) = \begin{cases} A_2 e^{i\beta x} e^{-k_2 z}, & z > 0 \\ A_1 e^{i\beta x} e^{k_1 z}, & z < 0 \end{cases}$$

$$H_x(z) = \begin{cases} -iA_2 \frac{k_2}{\omega\mu_0} e^{i\beta x} e^{-k_2 z}, & z > 0 \\ iA_1 \frac{k_1}{\omega\mu_0} e^{i\beta x} e^{k_1 z}, & z < 0 \end{cases}$$

$$H_z(z) = \begin{cases} A_2 \frac{\beta}{\omega\mu_0} e^{i\beta x} e^{-k_2 z}, & z > 0 \\ A_1 \frac{\beta}{\omega\mu_0} e^{i\beta x} e^{k_1 z}, & z < 0 \end{cases}$$

Continuity of E_y and H_x at the interface $z = 0$ requires:

$$A_1(k_1 + k_2) = 0. \tag{2.13}$$

Since confinement requires $\mathrm{Re}[k_1] > 0$ and $\mathrm{Re}[k_2] > 0$, the only way to satisfy this condition is with $A_1 = A_2 = 0$. Therefore, no nontrivial solutions exist for TE-polarized surface waves.

Having established the TM mode as the only configuration capable of supporting SPPs, we can now analyze the propagation constant β, which characterizes the propagation properties of SPPs at a single metal-dielectric interface.

The propagation constant β is complex, with its real and imaginary parts providing distinct information about the SPP behavior. The real part of β is related to the phase velocity of the SPP and the effective wavelength λ_{eff} of the plasmonic wave, where:

$$\lambda_{\text{eff}} = \frac{2\pi}{\mathrm{Re}(\beta)}. \tag{2.14}$$

This effective wavelength describes the spatial periodicity of the wave along the interface and is typically shorter than the free-space wavelength, indicating the highly confined nature of the SPP. This effective wavelength is especially important because it scales the geometry of components in plasmonic devices. In SPR-based devices, especially in biosensors, the effective wavelength plays a crucial role in determining the ideal geometric dimensions of the components for maximizing device performance.

The imaginary part of β, on the other hand, corresponds to the decay constant of the wave, representing the attenuation of the SPP as it propagates along the interface. This attenuation arises because part of the SPP's energy is absorbed by the metal, leading to a gradual decrease in amplitude. The propagation distance L_{SPP}, over which the power decays to $1/e$ (or approximately 37%) of its initial value, is given by:

$$L_{\text{SPP}} = \frac{1}{\mathrm{Im}(\beta)}. \tag{2.15}$$

This distance quantifies how far the SPP can travel before its intensity significantly diminishes, a critical parameter in applications requiring efficient plasmonic waveguiding over defined lengths.

To illustrate how effective wavelength and propagation distance influence plasmonic devices, consider the air-gold and water-gold interfaces at a free-space wavelength of 850 nm. For the air-gold interface (with $n_{\text{air}} = 1$ [30] and $\epsilon_{\text{gold}} = -27.1 + 1.9i$ [7]), we find an effective wavelength:

$$\lambda_{\text{eff}} = 834.3 \text{ nm}. \tag{2.16}$$

This effective wavelength, being shorter than the free-space wavelength, defines the spatial periodicity of the SPP along the interface and sets the ideal feature sizes for components in SPR-based devices. The propagation distance:

$$L_{\text{SPP}} = 99.4\,\mu\text{m}, \tag{2.17}$$

indicates how far the SPP can travel while retaining sufficient intensity, providing an optimal interaction length for applications like sensing.

For the water-gold interface, with $n_{H_2O} = 1.33$ [31], the effective wavelength decreases further due to the increased refractive index:

$$\lambda_{\text{eff}} = 617.9 \text{ nm}. \tag{2.18}$$

This scaling down affects the geometrical requirements for device components and supports even more confined fields. However, the propagation distance in this case is shorter:

$$L_{\text{SPP}} = 40.4\,\mu\text{m}. \tag{2.19}$$

indicating higher absorption losses and a more limited effective range for interaction. By adjusting the dielectric medium, we can tailor λ_{eff} and L_{SPP} to fine-tune component geometries and optimize the figures of merit for devices, especially in high-sensitivity applications like biosensing.

2.1.3 Coupling Methods for SPR

Each of these coupling methods enhances SPR's adaptability, making it possible to tailor SPR systems for specific needs across biomedical, environmental, and industrial applications.

SPR technology employs coupling methods to excite surface plasmons by achieving momentum matching between incident light and surface plasmons at the metal-dielectric interface. These methods are designed to enhance

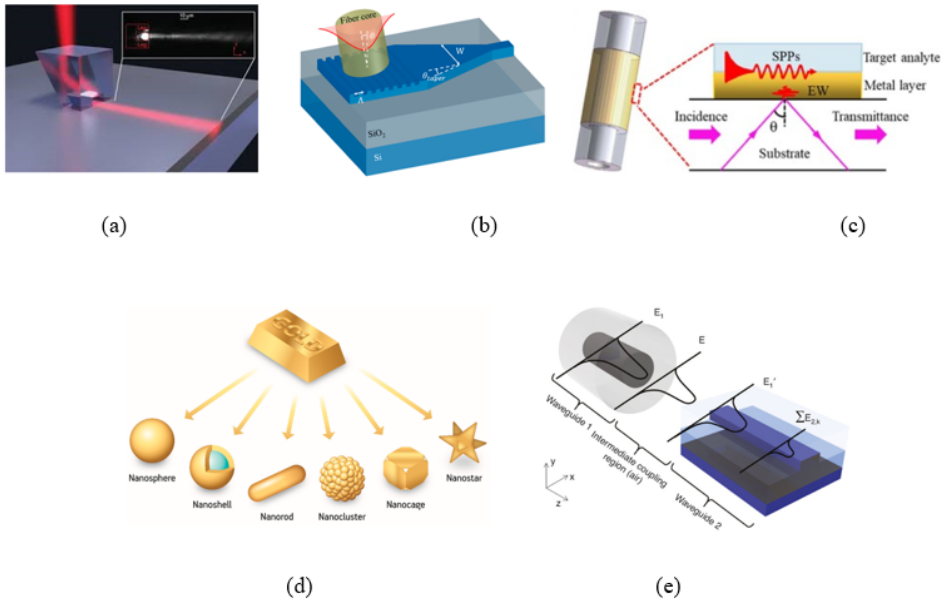

Figure 2.5: Overview of coupling methods for surface plasmon resonance. (a) Prism coupling, illustrating a 3D out-of-plane coupler adapted from [33]; (b) Grating couplers for compact and scalable designs, based on Cheng et al. [36]; (c) Fiber optic SPR using a D-shaped gold-coated fiber, adapted from Hiba Kh. Abbas and Zainab F. Mahdi [40]; (d) Localized surface plasmon resonance (LSPR) showing various gold nanoparticle shapes, highlighting the role of sharp tips in field confinement, adapted from [45]; (e) End-fire coupling using a focused Gaussian beam for precise excitation, adapted from [48].

coupling efficiency, which refers to the effective transfer of light energy into surface plasmon waves, as well as to facilitate ease of integration and ensure experimental compatibility. The main coupling methods include:

Prism Coupling (Kretschmann and Otto Configurations)

This method uses a prism to match the momentum of photons with surface plasmons via total internal reflection, as described by the Fresnel equations for multilayer optics [14–16,32]. Figure 2.5(a) illustrates this coupling method, introducing a concept of a 3D out-of-plane coupler [33]. This mi-

croscale prism leverages frustrated total internal reflection in the Otto configuration to excite surface electromagnetic waves or near-surface waveguide modes.

Grating Couplers

These couplers use diffraction gratings to excite surface plasmons and can be fabricated lithographically, allowing for precise tuning to meet specific requirements. This tunability enables their seamless integration into SPR devices and multiplexed configurations [34–36]. Grating couplers are ideal for portable diagnostics and industrial use, though their reliance on lithography increases fabrication complexity and cost. In this work, we prioritize grating couplers for their compatibility with scalable and affordable designs, as discussed in Section 3. The grating coupler is illustrated in Figure 2.5(b), adapted from Cheng et al.'s study, which provides a comprehensive description of various types of grating couplers.

Fiber Optic SPR

This coupling method involves coating optical fibers with a thin metal layer, typically gold, to support surface plasmon resonance by generating supermodes through the interaction of guided light and the metal layer [37–39]. Compact and portable, fiber optic SPR is well-suited for *in situ* diagnostics and remote applications. However, its shorter light-medium interaction lengths compared to prism setups limit sensitivity, and maintaining optical stability in varying environments remains a challenge. Figure 2.5(c), adapted from the work of Hiba Kh. Abbas and Zainab F. Mahdi, illustrates this method, where a D-shaped fiber coated with a gold nano-layer serves as the basis for a highly sensitive SPR optical fiber sensor [40].

Localized Surface Plasmon Resonance (LSPR)

LSPR leverages nanostructures such as nanorods, nanospheres, and other shapes to generate localized plasmonic fields, providing high sensitivity for detecting small refractive index changes [41–43]. The shape of these nanoparticles plays a critical role in their performance; sharp, pointed geometries, known as tips, enhance the confinement of field distributions due to their antenna-like behavior, intensifying the local electromagnetic fields [44]. This

makes LSPR particularly effective in applications requiring nanoscale sensitivity. Figure 2.5(d) illustrates various types of gold nanoparticles, showcasing the diversity in shapes that enable unique plasmonic properties and optimized field enhancements [45].

End-Fire Coupling

This coupling technique involves directing a focused Gaussian beam transversally to the waveguide, ensuring excitation occurs at one side of the sensing layer [27,46,47]. This approach allows for high precision and control over the excitation process, making it particularly valuable in experimental and research setups where fine-tuned alignment is necessary to optimize sensitivity and performance. However, a disadvantage is that it requires extremely precise alignment, which can be challenging to maintain and may limit its practicality for large-scale or field-based applications. This method is illustrated in Figure 2.5(e) [48].

2.1.4 Emerging Trends and Future Directions of SPR

The field of Surface Plasmon Resonance (SPR) continues to evolve rapidly, propelled by its inherent versatility and its integration with cutting-edge nanophotonic technologies. Among the most prominent emerging trends is the incorporation of nanostructures such as metasurfaces, nanorods, and plasmonic antennas, which enable refined control over light–matter interactions [49–53]. These innovations are expanding the frontiers of SPR, enhancing its performance in applications ranging from biosensing and energy harvesting to quantum optics, all within increasingly compact and efficient platforms. Simultaneously, the fusion of SPR with advanced imaging techniques—such as super-resolution microscopy and nanoscale surface imaging—has allowed researchers to probe molecular interactions with unprecedented detail [54–59]. These developments are proving particularly transformative in healthcare, enabling early disease detection, and in environmental monitoring, where real-time, high-resolution analysis is critical.

Furthermore, SPR is being integrated into hybrid analytical platforms, combining with techniques such as Raman spectroscopy and fluorescence microscopy to create multimodal systems that offer both chemical specificity and dynamic, real-time monitoring capabilities [60–64]. This holistic approach is broadening SPR's impact in chemical and biological sciences. On

the frontier of quantum and topological photonics, the merging of SPR with quantum nanophotonics and topological concepts is opening new possibilities for secure communications, robust photonic circuitry, and applications in quantum computing and encryption technologies [65–70].

Equally important is the ongoing miniaturization of SPR systems. Advances in fabrication techniques are driving the development of compact and portable SPR-based devices, which are particularly suited for point-of-care diagnostics and remote sensing applications [71–75]. This trend is crucial for scaling SPR technologies beyond the laboratory into widespread, real-world use. Finally, SPR is also being explored for its potential in sustainable energy applications, including roles in next-generation solar cells and thermophotovoltaic systems, where its unique optical properties contribute to improved energy conversion efficiencies [76–79].

Together, these advancements illustrate the transformative trajectory of SPR, as it transitions from a fundamental sensing platform to a cornerstone of modern nanophotonics. Looking ahead, the future of SPR is expected to be marked by deeper integration with quantum technologies, heightened sensitivity, and expanded functionality in emerging areas such as topological photonics, solidifying its role in addressing critical challenges in healthcare, energy, and advanced manufacturing [80].

2.1.5 Challenges and Disadvantages of SPR Technology

Despite the transformative potential of SPR technology, several core challenges and disadvantages continue to limit its broad adoption and integration across real-world systems.

First, the efficient excitation of surface plasmons requires precise optical coupling—often through angular alignment in prism configurations or via nanostructured gratings. This sensitivity to optical alignment makes SPR setups highly vulnerable to mechanical instabilities. In practice, most systems must be mounted on vibration-isolated optical tables to maintain measurement reliability, which constrains portability and usability in field-deployable applications.

Second, SPR devices typically rely on nanostructures with subwavelength features—often below 500 nm, such as grating couplers or nanoslits. These features demand high-resolution fabrication techniques, including electron-

beam lithography (EBL) or focused ion beam (FIB) milling. These methods are not only expensive and time-consuming but also difficult to scale for mass production. Additionally, SPR systems frequently use costly materials such as gold and specialized polymers, which contribute further to fabrication overhead.

Another limitation is plasmon propagation loss due to ohmic damping in metals like gold. This restricts the range over which plasmons can travel and limits sensing volume. Moreover, surface roughness or fabrication imperfections introduce scattering losses, degrading device performance.

Finally, integration with other photonic or electronic systems remains a non-trivial challenge, particularly due to the geometry and material stack required by SPR structures. Creating compact, robust, and reproducible SPR platforms requires tight control over optical interfaces and alignment, which is difficult to maintain outside controlled environments.

While these limitations are significant, they are not insurmountable. Many can be addressed through advanced engineering solutions, such as new low-loss materials, scalable nanofabrication methods, or compact optical architectures using components like spatial light modulators (SLMs). The field continues to evolve in this direction, pushing SPR technology toward more integrated and accessible platforms.

2.2 Biosensing Methods and the Role of Surface Plasmon Resonance (SPR)

A biosensor is defined as an analytical device that detects biological molecules and converts a biological response into a measurable signal [81–84]. Typically, it integrates a biological recognition element, such as an enzyme, antibody, or nucleic acid, with a transducer that translates the interaction into a quantifiable output.

There are various types of transducers used in biosensors, each tailored to different detection mechanisms. These include electrochemical, piezoelectric, and thermal biosensors, each leveraging distinct physical principles for signal transduction.

Electrochemical Biosensors

These biosensors measure electrical changes such as impedance or current resulting from biochemical interactions [85,86]. Figure 2.6a) illustrates the

basic principle of an electrochemical biosensor, adapted from [86]. In this system, an analyte interacts with a biorecognition element (e.g., enzyme, antibody, or DNA probe) immobilized on the electrode surface. This interaction triggers an electrochemical reaction involving electron transfer and oxygen consumption, leading to a measurable electrical signal. The transducer converts this response into an output displayed on an electronic interface, enabling real-time monitoring of biochemical processes.

Piezoelectric Biosensors

These sensors rely on mass changes that affect the resonance frequency of a crystal, enabling precise mass detection at the molecular level [87,88]. As shown in Figure 2.6b), adapted from [87], a typical 10 MHz piezoelectric (PZ) crystal with gold electrodes is mounted on a holder (left). The middle diagram represents the schematic structure of this system, while the rightmost image presents an alternative design where the gold electrodes are arranged to provide contact pads on the same side. This modified configuration facilitates use in liquid environments, enhancing the sensor's applicability in biosensing applications.

Thermal Biosensors

These biosensors detect heat variations arising from biochemical reactions, offering a highly specific means of measuring metabolic activity [89,90]. Figure 2.6c), adapted from [90], depicts a thermal biosensor based on an enzyme thermistor. In this setup, a sample is introduced via a sample valve and flows through an enzyme column, where an exothermic biochemical reaction occurs. The resulting temperature change is detected by a thermistor and analyzed through a Wheatstone bridge circuit, ensuring precise measurement. Heat exchangers are also incorporated into the system to regulate temperature fluctuations and enhance measurement stability.

Optical Biosensors

This technology plays a crucial role in molecular detection by leveraging light as the primary interrogation method, providing high spatial and temporal resolution to detect small changes in a sample and track biological interactions in real time [91–95]. This capability is particularly valuable for studying fast molecular dynamics or subtle variations in biological systems.

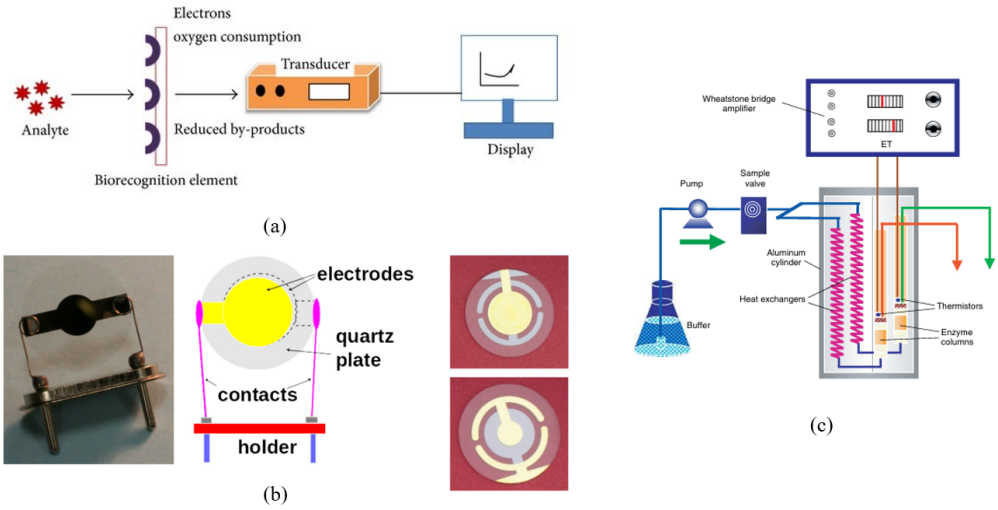

Figure 2.6: (a) Electrochemical biosensor, adapted from [86], showing the basic principle where an analyte interacts with a biorecognition element, leading to an electrochemical response measured by a transducer. (b) Piezoelectric biosensor, adapted from [87], depicting a 10 MHz quartz crystal resonator with gold electrodes (left), its schematic representation (middle), and an alternative electrode arrangement for liquid-phase applications (right). (c) Thermal biosensor, adapted from [90], illustrating an enzyme thermistor setup, including a sample valve, enzyme column, heat exchangers, thermistor, and Wheatstone bridge circuit for precise temperature-based biochemical detection.

A key advantage of optical biosensors is their flexibility, as light can be manipulated in various ways to optimize detection. By adjusting wavelength, intensity, polarization, and phase, researchers can fine-tune sensitivity and select optimal conditions for detecting specific biomolecular interactions. The broad spectral range—from ultraviolet to infrared—further enhances adaptability, enabling precise measurements across different applications.

Additionally, optical biosensors are non-invasive and non-destructive, allowing for repeated or long-term measurements without altering the sample, which is crucial for biomedical diagnostics and live-cell analysis. Their contact-free nature also minimizes contamination risks and ensures sample integrity.

Beyond conventional sensing, optical biosensors can be integrated into

quantum sensors, which represent the next frontier in precision measurements [96–100]. Quantum-enhanced biosensors exploit quantum entanglement and superposition to surpass classical detection limits, offering unprecedented sensitivity in detecting minute biological changes. This quantum advantage has the potential to revolutionize biomedical diagnostics, ultra-sensitive disease detection, and single-molecule analysis, paving the way for the next generation of biosensing technologies.

Optical biosensors can be further classified based on their underlying principles. Some of the most widely used types include: Fluorescence-based biosensors, which utilize fluorophores for signal enhancement [101–103], Raman biosensors, which rely on vibrational spectroscopy for molecular identification [104–107] and Surface Plasmon Resonance (SPR) biosensors, which exploit plasmonic phenomena to detect biomolecular interactions with high specificity [108–115].

SPR biosensors have emerged as one of the most powerful label-free biosensing techniques, leveraging surface plasmon waves to monitor molecular binding events in real-time. The concept of SPR was first explored in the early 20th century, but its application in biosensing became practical and revolutionary in the 1980s. Researchers such as Liedberg, Nylander, and Lundström [17] pioneered the development of the first SPR-based biosensors for real-time monitoring of biomolecular interactions, laying the foundation for extensive research and the commercialization of SPR instrumentation for life sciences and diagnostics.

SPR biosensors offer numerous advantages that have contributed to their widespread adoption in research and diagnostics. One of their key benefits is label-free detection, which eliminates the need for fluorescent or radioactive labels, simplifying experiments and avoiding potential interference. Additionally, SPR enables real-time monitoring of binding events, providing valuable kinetic data essential for understanding biomolecular interactions. Another significant advantage is reusability, allowing sensors to be used multiple times, which not only reduces material costs but also promotes sustainable research practices. The compact and portable design of modern SPR instruments makes them well-suited for point-of-care diagnostics and field applications. Furthermore, SPR systems are designed for user-friendly operation, requiring minimal specialized training and making them accessible to both academic and industrial users.

2.2.1 Configurations and Sensing Mechanisms of SPR Biosensors

The exceptional sensitivity of SPR biosensors arises from their ability to detect minute changes in the refractive index at the metal-dielectric interface. These changes influence the properties of surface plasmon waves, affecting their phase, amplitude, and the optimal resonance wavelength.

When the refractive index of the surrounding dielectric medium, often water, changes, it alters the phase velocity of the surface plasmons, resulting in a measurable phase shift. This phase sensitivity is crucial in interferometric SPR setups, which are designed to detect extremely small refractive index variations, making them highly effective for monitoring biomolecular interactions at very low concentrations. Notable interferometric configurations include Mach-Zehnder interferometers (MZIs) [116-120], which split a coherent light beam into two arms—one interacting with the sample and the other serving as a reference—measuring the phase difference induced by refractive index changes.

In Figure Figure 2.7, we illustrate two significant MZI configurations. Figure 2.7(a) presents the innovative approach by Gao et al. [117], who proposed a plasmonic Mach-Zehnder interferometer using a dual-layer metallic film, where the reference arm was formed by the second layer of a thick metal film. Figure 2.7(b) (right) showcases the fabricated long-range surface plasmon MZI developed by Fan and Berini [121]. Their design enabled bulk sensing by utilizing long-range surface plasmon modes, which can propagate over longer distances but require thinner metal waveguides to support such modes efficiently. Additionally, this design integrates a lithographically fabricated microfluidic channel, allowing precise control of the analyte flow within the sensing region. This is an example of the notable interferometric SPR configuration involving long-range surface plasmon polariton (LRSPP) interferometers [121-124]. These designs utilize LRSPPs propagating along thin metal strips embedded in a dielectric environment, enabling extended propagation lengths and enhanced sensitivity. This approach is particularly effective for detecting extremely low concentrations of analytes and monitoring real-time biomolecular interactions, making it a valuable tool for high-sensitivity biosensing applications.

These examples highlight the versatility and optimization strategies for SPR interferometers, demonstrating how structural modifications and coupling techniques enhance sensitivity and detection capabilities.

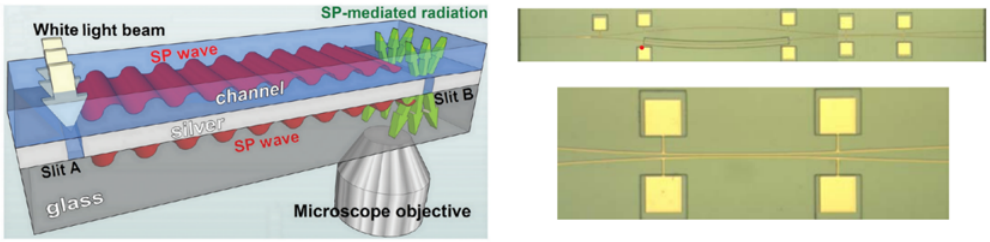

Figure 2.7: Examples of plasmonic Mach-Zehnder interferometers (MZIs) for SPR-based sensing. (a) Configuration proposed by Gao et al. [117], where the reference arm is formed by a second metallic layer in a thick metal film, enabling interferometric sensing using white light illumination. (b) LRSP MZI developed by Fan and Berini [118], which utilizes thin metal waveguides to support long-range plasmon modes. The top image shows the complete Mach-Zehnder device, while the bottom image provides a close-up view of the junction.

For SPR systems using broadband light, refractive index changes result in a shift of the optimal resonance wavelength. Wavelength interrogation methods are widely used in systems where tracking these shifts provides high-resolution data on molecular interactions [125-130]. Well-recognized examples include systems that utilize spectrometers to monitor resonance shifts across a wide spectrum.

SPR biosensors operate in two main detection modes. The first, bulk sensing, measures refractive index changes across the entire sample volume, typically resulting from variations in chemical composition [131–133]. This method captures overall shifts in the medium, making it useful for detecting broad environmental or compositional changes. The second mode, textbf-surface sensing, focuses on refractive index changes localized at or near the sensor surface. It is particularly effective for studying molecular interactions, as the confined plasmonic field enhances sensitivity to surface-bound analytes, enabling real-time monitoring of binding events and kinetic analysis [134–137].

2.2.2 Sensograms in SPR Biosensing

A sensogram is the graphical output generated during an SPR experiment, providing a real-time representation of biomolecular interactions at the sensor surface [138]. The x-axis shows time, while the y-axis indicates the response units (RUs), corresponding to changes in the refractive index near the sensor interface. This visualization allows researchers to observe and analyze binding events as they occur, offering a dynamic understanding of molecular interactions.

Bulk sensing produces simpler sensograms because it measures changes in the refractive index of the medium as concentrations of the solution vary. The resulting sensogram typically consists of bulk steps corresponding to overall refractive index changes across the sample volume.

In contrast, surface sensing is more sophisticated and is used to detect the binding of biomarkers to a previously functionalized surface. This complexity allows for detailed kinetic analysis, making it crucial for applications in biomedical research and drug development. As depicted in Figure 2.8, surface sensing sensograms are essential for capturing the dynamics of biomolecular interactions at the sensor surface, such as antigen-antibody binding events used in diagnostic assays.

The sensogram in Figure 2.8 visually represents how molecules interact with a sensor surface over time. It begins with a stable period where only a liquid (buffer) flows over the sensor, ensuring there is no unwanted background signal. Once this baseline is set, the next phase starts when the target molecules (analyte) are introduced. These molecules attach to the surface, causing an increase in the signal, which shows how much binding is occurring. This step is crucial in detecting interactions such as drug binding or antibody recognition.

If enough molecules attach, the signal reaches a steady level, meaning the rate at which they are binding and detaching is balanced. When the flow of analyte stops, the molecules slowly begin to detach, and the signal starts to decrease, showing how stable the interaction was. Finally, a special solution is used to clean the surface, bringing the signal back to its starting point so that the sensor can be reused. This process helps researchers measure how strongly and quickly molecules bind and detach, which is essential for fields like medicine and biotechnology. Below the sensogram, Figure 2.8 illustrates the molecular events.

This graphical representation is a valuable tool for analyzing biomolecu-

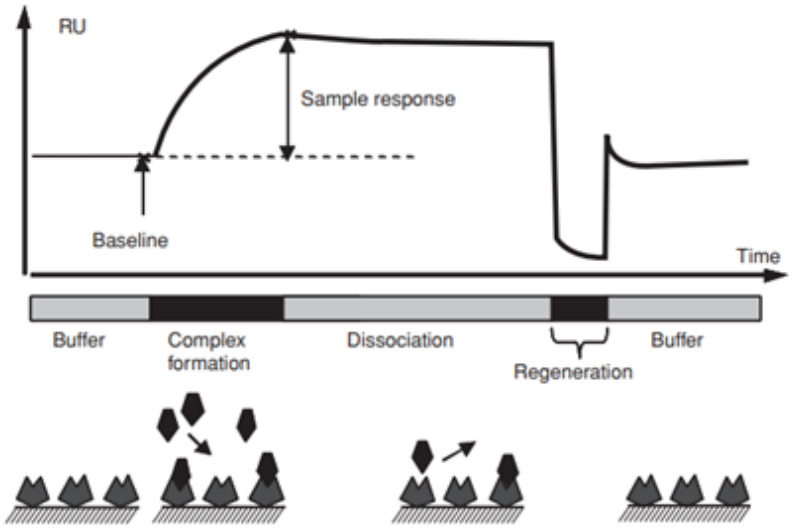

Figure 2.8: A typical SPR sensogram showing the different phases of molecular interaction. Initially, a buffer solution flows over the sensor to establish a stable baseline. When the analyte is introduced, it binds to the sensor surface, causing the signal to rise. If equilibrium is reached, the signal stabilizes. Once the analyte flow stops, the bound molecules gradually detach, leading to a decrease in signal. Finally, a regeneration solution resets the sensor surface to its original state, allowing for repeated measurements. The molecular events below the graph illustrate these key steps in real-time detection [138].

lar interactions and serves as a motivation for continuing with this sensing project. It can also serve as a practical guide for functionalizing the sensor, ensuring its effective use in detecting and analyzing molecular interactions.

2.2.3 Applications of SPR Biosensing

The versatility of SPR biosensors has led to their application across multiple fields. In pharmaceutical research and drug discovery, SPR biosensors have become indispensable tools in the pharmaceutical industry, particularly for drug discovery and development [139–142], as they are widely used for screening drug candidates and providing real-time data on binding affinities and kinetics. In the field of clinical diagnostics and biomarker detection, their ability to perform label-free, real-time detection has made them pivotal, es-

pecially for the detection of disease biomarkers [143–146]. SPR technology is also highly effective for environmental monitoring, given its capacity to detect even trace amounts of contaminants and pollutants in diverse environmental settings [147–149]. Furthermore, in the food industry, SPR biosensors contribute to food safety and quality control by enabling rapid and reliable monitoring of foodborne pathogens and contaminants, thereby ensuring product integrity and consumer protection [150–152].

2.2.4 Multiplexed SPR Biosensing

One of the most significant advancements in SPR biosensors is multiplexed sensing. Multiplexing enables the simultaneous measurement of multiple samples, drastically improving diagnostic times for numerous patients [153-157]. Additionally, it allows for the detection of several biomarkers within a single sample, enhancing the depth and accuracy of diagnostic information. Microarray-Based SPR Sensors represent a major leap forward in this regard. These sensors feature arrays of functionalized spots on a single sensor chip, each designed to capture a specific analyte. This approach has proven particularly beneficial in areas such as cancer diagnostics, where multiple biomarkers can be analyzed in a single assay to support early detection and personalized treatment. Another impactful multiplexing approach is seen in Multi-Channel SPR Sensors, which use separate flow channels in a single sensor setup. Each channel is functionalized to capture different target molecules, enabling parallel monitoring. Furthermore, advanced techniques like wavelength and angle division multiplexing have broadened SPR's analytical power. These methods use variations in the optical properties of light to distinguish between signals from different analytes, facilitating efficient and simultaneous detection.

Figure 2.9, adapted from [156], illustrates a multiplexed SPR biosensing scheme proposed by Dostálek et al., where a special prism coupler is designed for sequential excitation of surface plasmon waves (SPW). Unlike conventional prism-based coupling, this system features a prism with a special cut at the top, allowing light to reflect back onto the sensing surface instead of exiting the system. This configuration enables the excitation of multiple sensing areas within the same prism coupler, with each area functionalized to detect a different biomarker. Figure 2.9a) shows the special prism coupler used for sequential excitation of SPW and wavelength division multiplexing of sensing channels. Figure 2.9b) presents the resulting spectrum of trans-

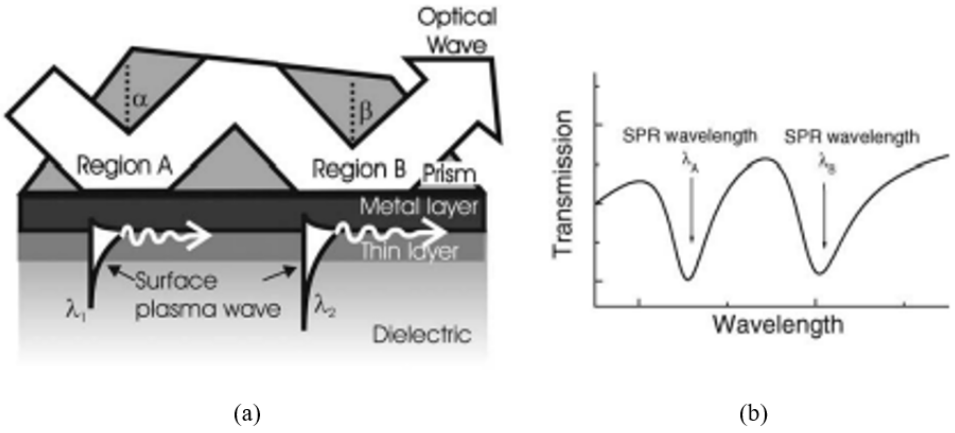

Figure 2.9: Multiplexed SPR biosensing scheme adapted from [156]. (a) Special prism coupler for sequential excitation of surface plasmon waves (SPW) and wavelength division multiplexing of sensing channels. (b) Resulting spectrum of transmitted light, showing distinct wavelengths corresponding to different sensing areas, enabling the simultaneous detection of multiple biomarkers.

mitted light, demonstrating how distinct wavelengths correspond to different sensing areas, allowing for the simultaneous detection of multiple biomarkers.

Figure 2.9a) shows the special prism coupler used for sequential excitation of SPW and wavelength division multiplexing of sensing channels. Figure 2.9b) presents the resulting spectrum of transmitted light, demonstrating how distinct wavelengths correspond to different sensing areas, allowing for the simultaneous detection of multiple biomarkers.

2.2.5 Challenges and Disadvantages of SPR-Based Biosensing

While SPR biosensors offer powerful advantages, such as label-free detection and high sensitivity in real time, their implementation in biological sensing environments introduces a distinct set of challenges and disadvantages.

A major concern is signal instability and baseline drift. Biological measurements are often affected by temperature changes, fluidic pressure fluctuations, or mechanical vibrations, all of which can introduce noise into the SPR signal. These systems typically require optical tables and environmen-

tal isolation to ensure reproducible results—conditions not always feasible in clinical or field settings.

Another fundamental issue is non-specific adsorption. Biological fluids contain a variety of molecules (e.g., proteins, lipids, salts) that can adhere to the exposed gold surface, even when not part of the target analyte. This fouling can lead to false positives, signal suppression, or reduced selectivity.

Surface functionalization also remains a persistent challenge. Achieving reproducible, stable, and selective chemical coatings that bind only the target biomarker is difficult, especially when dealing with diverse sample matrices or when long-term stability is required.

SPR biosensors are also difficult to miniaturize. They often require external illumination using lasers or LEDs, polarization control, and high-resolution imaging with CCD or CMOS cameras. Combined with precise optical alignment, these requirements make current systems bulky and challenging to integrate into compact, portable devices.

From a fluidic standpoint, delivering analytes to SPR sensing regions requires well-aligned and reliable microfluidic interfacing. In multiplexed devices, where several sensing elements are located on a single chip, maintaining consistent flow rates and avoiding cross-contamination becomes increasingly complex.

Additionally, close spacing between devices introduces the risk of modal cross-talk, where plasmonic fields from neighboring sensors interact, distorting the signal and complicating interpretation.

Although these challenges are substantial, they are common across biosensing platforms and can be addressed through careful engineering. Advances in adaptive optics, microfluidic control, surface passivation, and new interrogation schemes—including the potential use of spatial light modulators (SLMs)—may help overcome many of these barriers and bring SPR biosensors closer to practical, real-world applications.

2.3 Grating Couplers

Grating couplers are periodic structures that enable efficient coupling of incident light into surface plasmon waves (SPWs) at a metal-dielectric interface [158–163]. Unlike traditional prism-based excitation methods, such as the Kretschmann or Otto configurations, grating couplers provide a compact and integrated approach for achieving SPR excitation directly on the metal surface. By eliminating the need for bulky optical components, grating cou-

plers facilitate SPR applications in miniaturized and on-chip systems, where space and integration flexibility are critical.

The fundamental operation of grating couplers is based on overcoming the natural momentum mismatch between free-space photons and surface plasmons. Photons in free space generally have lower momentum than surface plasmons, making direct excitation difficult. Grating couplers resolve this by adding in-plane momentum to the incident photons through the periodic structure on the metal surface. This additional momentum enables phase matching with the SPWs, a necessary condition for efficient coupling. The design of the grating's structural parameters can be carefully optimized to achieve this phase-matching condition, enabling effective coupling of light into plasmon modes at specific wavelengths and angles.

Several key parameters influence the performance and efficiency of grating couplers, including:

Grating Period

The grating period, or the spacing between adjacent grooves, is one of the most critical factors in coupling efficiency. This parameter defines the in-plane momentum introduced by the grating structure. For any given incident wavelength, there is an optimal period that enables efficient coupling by aligning the momentum of the incident photons with that of the surface plasmons. When the period is correctly matched to the operating wavelength, it creates the necessary conditions for phase matching. If the period is too small or too large, the in-plane momentum may misalign with the SPWs, leading to lower coupling efficiency.

Grating Depth

The depth of each groove in the grating impacts how much of the incident light interacts with the structured surface. Deeper gratings generally enhance the interaction between light and the metal, potentially increasing coupling efficiency by strengthening the generated plasmonic field. However, excessive depth can also introduce losses through scattering, so it must be optimized carefully.

Duty Cycle

The duty cycle, defined as the ratio of ridge width to the period, controls the balance of metal and dielectric material across the grating. This parameter influences the resonance characteristics of the coupler, impacting factors like reflection and transmission efficiency. Adjusting the duty cycle allows for tuning of the plasmonic response, minimizing reflection losses and optimizing light coupling into plasmon modes.

Number of Periods

The number of periods in the grating determines how much of the Gaussian beam interacts with the grating. To achieve optimal coupling efficiency, it is crucial to select the number of periods so that the grating size matches the size of the incident beam. If the grating has too few periods, it will be too small, causing some sections of the incident beam to be reflected rather than efficiently coupled. Conversely, if the grating is too large, the surface plasmons may decouple and scatter at the edges of the grating. Therefore, optimizing the grating size to fit the incident beam is essential to balance coupling efficiency and minimize losses.

Material Selection

The choice of material for the grating is a fundamental factor in SPR coupling performance, as it dictates the plasmonic characteristics of the device. Gold and silver are the most commonly used metals due to their strong plasmonic properties and minimal optical losses at visible and near-infrared wavelengths. However, these materials are costly, and their use may be limited by fabrication constraints or device budgets, especially in large-scale or disposable applications. Alternative materials, such as copper, aluminum, or plasmonic alloys, are being explored to reduce costs, though they often require trade-offs in terms of coupling efficiency or signal quality [164,165]. Conductive polymers and emerging materials like graphene also offer promising plasmonic properties with potential for cost-effective implementation [166,167]. However, their compatibility with high-sensitivity SPR applications is still under investigation. Material selection must balance factors such as plasmonic efficiency, durability, cost, and wavelength compatibility to meet the specific demands of SPR devices in various applications.

Through careful tuning of these parameters, grating couplers can achieve high coupling efficiency at specific wavelengths and angles. These parameters can be observed in Figure 2.10, adapted from [160], where Yoon et al. illustrate the main components of a grating coupler, providing a detailed visualization of its structure and working principle.

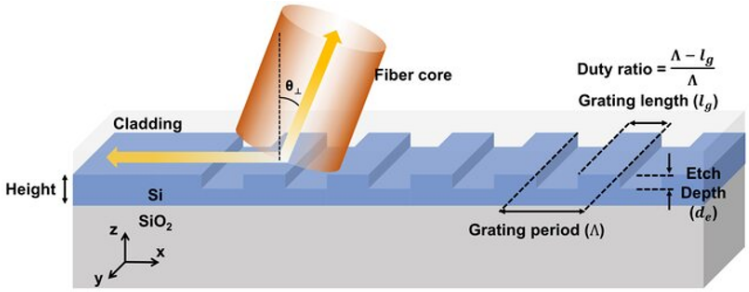

Figure 2.10: Illustration of the main components of a grating coupler, adapted from [160]. The figure, presented by Yoon et al., showcases the key structural elements of a grating coupler, highlighting how carefully tuned parameters such as grating period, etching depth, and incident angle influence coupling efficiency at specific wavelengths.

Grating couplers are commonly used in plasmonic sensors because they provide an efficient way to excite surface plasmons at specific wavelengths. For instance, they are essential in integrated photonic circuits for efficient light coupling [168,169]. They are also employed in optical communication systems, where they facilitate high-speed data transfer by coupling light into and out of waveguides with minimal losses [170,171]. Additionally, grating couplers enhance light-matter interactions in advanced research areas like quantum optics and spectroscopy, enabling precise control and manipulation of optical fields [172–176].

2.3.1 Design and Optimization of Grating Couplers

To understand the derivation of the grating equation and its role in SPR, it's essential to grasp how grating couplers enable light coupling into surface plasmon waves (SPWs) by addressing the inherent momentum mismatch between photons and surface plasmons. Unlike prism-based coupling, where a high refractive index medium provides additional momentum to the photons,

grating couplers use a periodic structure etched onto the surface of a metal. This periodic pattern adds in-plane momentum, facilitating the phase matching necessary for SPWs to be excited without additional refractive materials.

The grating equation provides a quantitative condition for this phase matching, describing how the grating period Λ, the wavelength λ_0, and the angle of incidence θ interrelate to enable coupling. This equation can be derived by setting the total momentum in the plane of the surface (the sum of the photon's in-plane momentum and the momentum contribution from the grating) equal to the surface plasmon wavevector.

The in-plane component of the incident photon's wavevector $k_{\parallel}$ is given by [161]:

$$k_{\parallel} = k_0 \sin\theta, \tag{2.20}$$

where k_0 is the wavevector of the incident light in free space, defined as:

$$k_0 = \frac{2\pi}{\lambda_0}. \tag{2.21}$$

For surface plasmons to be excited, this in-plane momentum $k_{\parallel}$ must match the surface plasmon wavevector k_{SP}, which is the characteristic wavevector of SPWs on a metal-dielectric interface.

To provide the additional momentum required for matching, the grating introduces a periodic structure with period Λ, contributing discrete momentum values in multiples of $2\pi/\Lambda$. This contribution allows the total in-plane momentum to be modified as follows:

$$k_{\mathrm{SP}} = k_0 \sin\theta \pm \frac{2\pi}{\Lambda} \cdot m, \tag{2.22}$$

where m is an integer representing the grating diffraction order ($m = 0, \pm1, \pm2, \ldots$). This is the general form of the grating equation, and it expresses the condition for phase matching between the incident photons and the SPWs.

To simplify, consider broadside excitation, where $\theta = 0$ and the lowest-order diffraction ($m = 1$) for efficient coupling. Under these conditions, the equation reduces to:

$$\Lambda = \frac{\lambda_0}{n_{\mathrm{eff},a}}, \tag{2.23}$$

where $n_{\text{eff},a}$ is the averaged effective refractive index over the grating coupler, as approximated by Eqs. 2.25 and 2.27. This result shows that the period Λ is directly related to the resonance wavelength λ_0, with shorter wavelengths requiring smaller grating periods to maintain coupling. This relationship is crucial because tuning Λ allows the grating coupler to optimize coupling efficiency at specific wavelengths, which is valuable in applications demanding precise control over SPR excitation.

As an example, let us determine the optimal pitch for the air-gold and water-gold interfaces, taking the values calculated with λ_{eff} as approximated in Equation (5).

For the air-gold interface at $\lambda_0 = 850$ nm:

$$n_{\text{eff,air}} = \frac{\lambda_0}{\lambda_{\text{eff,air}}} = \frac{850 \text{ nm}}{834.3 \text{ nm}} \approx 1.019, \tag{2.24}$$

and therefore, the optimal grating pitch for air-gold is:

$$\Lambda_{\text{air}} \approx \lambda_{\text{eff,air}} = 834.3 \text{ nm}. \tag{2.25}$$

For the water-gold interface at the same resonance wavelength:

$$n_{\text{eff,water}} = \frac{\lambda_0}{\lambda_{\text{eff,water}}} = \frac{850 \text{ nm}}{617.9 \text{ nm}} \approx 1.375, \tag{2.26}$$

leading to an optimal grating pitch for water-gold of:

$$\Lambda_{\text{water}} \approx \lambda_{\text{eff,water}} = 617.9 \text{ nm}. \tag{2.27}$$

This example demonstrates how grating coupler design depends directly on the effective wavelength of the plasmon mode, with shorter effective wavelengths requiring smaller grating pitches. By tailoring Λ to match λ_{eff} for different media, we can achieve maximum coupling efficiency, optimizing SPR for various interfaces.

This initial calculation provides a first approximation of the optimal pitch for coupling, but in designing grating structures, it serves only as a preliminary value. Realizing effective coupling requires iterative adjustments to parameters such as duty cycle, depth, pitch, and the number of grating periods, often influenced by the size and profile of the incident exciting light. This multi-iteration approach typically uses finite element methods (FEM) to simulate and refine these variables, as we will explore in Charpter 3.

The iterative design process is essential because the approximation $\Lambda \approx \lambda_{\text{eff}}$ assumes a weak coupling condition. This assumption applies to shallow gratings with small depth, where the coupling efficiency remains relatively low. However, to achieve strong coupling and higher efficiency, deeper gratings are needed, which necessitates detailed adjustments through iterative optimization.

Another effective strategy to improve coupling efficiency involves adjusting the angle of incidence. By optimizing the angle, we can favor coupling to one side of the interface, which is useful in applications where a directional plasmon flow is desired. Beam alignment is also critical, as even slight misalignment of the incident light on the grating structure can significantly reduce coupling efficiency. Ensuring precise alignment is essential to maintain the grating's resonance condition and achieve optimal SPR excitation.

Through refined designs, efficiencies in coupling have reached upwards of 69% in optimized SPR systems [177,179], demonstrating the potential for high-performance grating couplers when careful parameter tuning and advanced simulation techniques are applied.

2.3.2 Evolution and Advancements in Grating Coupler Designs for SPR

Grating couplers have significantly evolved, playing a pivotal role in the advancement of SPR technology. Early efforts focused on transitioning from prism-based phase-matching methods to more compact grating-based designs. Pockrand et al. demonstrated the feasibility of using gratings instead of bulky prisms, paving the way for miniaturized and portable SPR devices [180].

As the field matured, innovations like subwavelength gratings (SWGs) emerged to improve light confinement and enhance SPR excitation. Unlike traditional diffraction gratings, SWGs have a period Λ smaller than the incident wavelength in the medium, suppressing higher-order diffraction and behaving as an effective refractive index structure. This property allows precise control over the optical wavevector, enabling tunable coupling conditions for SPR devices [181].

Recently, Wang et al. demonstrated the feasibility of SWGs for broadband coupling in silicon-on-insulator (SOI) photonic platforms [182,183]. Their results show that SWGs can be fabricated lithographically using a

single-etch process, and their effective index can be tailored by adjusting the grating duty cycle. These properties make SWGs highly suitable for integrated SPR sensors and multiplexed configurations, where precise and tunable plasmonic excitation is required.

Further advancements in the field include tunable and reconfigurable grating couplers, which provide real-time control over resonance conditions [184]. Additionally, grating couplers have found applications in quantum plasmonics, where their ability to manipulate surface waves at the nanoscale is essential for quantum information processing and entanglement control [185-187]. Hyperbolic metasurfaces, which are periodic structures designed to exhibit extreme anisotropy, have also been explored in this context [188,189].

These advancements demonstrate how grating coupler technology has become increasingly sophisticated, contributing to high-performance, adaptable SPR-based systems for diverse applications ranging from biosensing to quantum technology.

2.4 Nanoslits and Extraordinary Optical Transmission

Light passing through subwavelength apertures always behaves in an interesting and often counterintuitive manner. Classical wave optics predicts that as the aperture size decreases, the transmitted power should also decrease according to Bethe's small-hole diffraction theory [190-194]. However, when these apertures are structured in metallic films, additional physical effects come into play, leading to enhanced transmission beyond what classical diffraction models predict.

Interestingly, nature provides its own examples of nanoscale structures manipulating light. Peacock feathers, butterfly wings, and beetle shells serve as natural examples where periodic nanostructures selectively reflect or transmit specific wavelengths, producing vibrant, angle-dependent colors [195]. In these cases, the nanostructures—akin to arrays of tiny nanoscale apertures—form periodic patterns that selectively interact with certain wavelengths of light, creating striking iridescence.

Figure 2.11 illustrates this phenomenon, showing optical and scanning electron microscope (SEM) images of butterfly wing scales. These biological structures exploit structural coloration mechanisms similar to those leveraged in engineered nanoslit arrays for selective wavelength manipulation. Such biological instances of color production have inspired the development

of photonic devices that utilize structural color and enhanced optical transmission through periodic nanostructures.

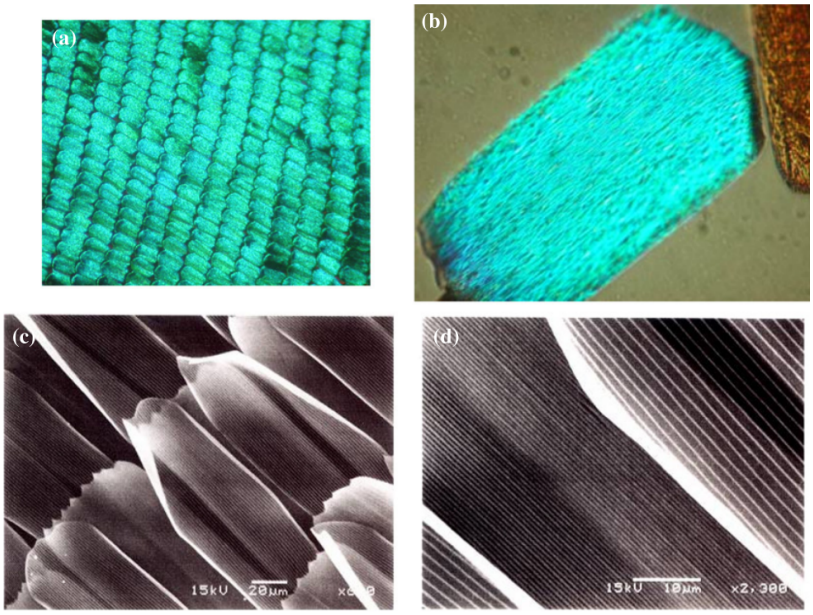

Figure 2.11: Optical and SEM images of butterfly wing scales illustrating structural coloration. (a, b) *Morpho rhetenor* under epi- and transmitted illumination. (c, d) *Morpho didius* scales showing periodic nanostructures responsible for iridescence. Adapted from [196].

The situation becomes even more intriguing when the apertures are not in dielectric materials like those found in biological structures, but rather in metals. As discussed in Section 2.1, metallic nanoslits support surface plasmons—electromagnetic waves that propagate along metal-dielectric interfaces. When the nanoslit dimensions approach the operational wavelength regime, these surface plasmons significantly enhance the transmission of light through the aperture.

According to Bethe's aperture theory, light transmission through subwavelength apertures should scale poorly, diminishing sharply as the aperture size decreases below the wavelength of incident light. For circular apertures, this classical relationship is described by Bethe's expression, where transmission T scales with the fourth power of the ratio of the aperture diameter d to the wavelength λ, specifically [193]:

$$T \propto \left(\frac{d}{\lambda}\right)^4 \tag{2.28}$$

However, the advent of nanoscale apertures in metallic films has fundamentally reshaped the classical perspective described by Bethe's theory. While Bethe predicted that light transmission through subwavelength apertures should be extremely low—scaling with the fourth power of the aperture size relative to the wavelength—experiments have shown that metallic nanoslits can exhibit remarkably enhanced transmission. This phenomenon, known as extraordinary optical transmission (EOT), is largely attributed to the excitation of surface plasmon polaritons (SPPs) at the metal-dielectric interface, which mediate efficient coupling and funneling of light through the aperture [197,198].

EOT is not adequately captured by simple theoretical models; instead, it has been extensively studied through experimental observations and numerical simulations, which have revealed that transmission efficiency is highly dependent on a combination of slit geometry, material permittivity, and wavelength. Specifically, high transmission occurs when the geometry and material properties support strong confinement and resonant excitation of SPPs near the aperture [199–201].

These studies show that even small variations in slit width, film thickness, or the dielectric environment can significantly alter the transmission behavior. The electromagnetic fields in and around the slit are strongly enhanced under the right conditions, leading to efficient energy transfer across the aperture. As a result, precise control of the nanoslit dimensions and surrounding materials becomes essential to optimize performance, especially for applications in plasmonic biosensing and photonic devices [202–206].

At the same time, computational methods such as finite-difference time-domain (FDTD) and finite element methods (FEM) have been extensively used to analyze field distributions in EOT structures. These simulations reveal hotspots of field enhancement at the nanoslit edges, where plasmonic interactions are strongest, and demonstrate how waveguiding effects confine light within the slit. The local field intensity $|E(x, y)|^2$ is particularly amplified in these regions, highlighting pathways of concentrated energy flow and areas where interactions with nearby materials are intensified [207-209]. This behavior is particularly advantageous in sensing applications, where nanoslit-based EOT structures can detect minute changes in refractive in-

dex or chemical composition by tracking shifts in the plasmonic resonance condition. Such visualizations not only validate theoretical predictions but also illustrate how nanoslit design can be tailored to specific applications by adjusting parameters such as slit width, metal type, and dielectric environment.

2.5 Microfluidic Channels

In our proposed device (as introduced in Charpter 1), the analyte is delivered in aqueous solution through integrated microfluidic channels. Microfluidic channels are compact fluidic systems, precisely designed to handle and manipulate minute volumes of liquids, often on the scale of nanoliters to microliters [210-215]. These channels, integral to lab-on-a-chip devices, leverage the principles of laminar flow—a regime where fluid moves in smooth, predictable layers due to the dominance of viscous forces over inertial forces at such small scales. Unlike turbulent flow at larger scales, laminar flow in microfluidics allows for precise control over fluid movement, making microfluidic channels essential for applications in biosensing, chemistry, and cellular studies. Figure 2.12, adapted from Whitesides [210], presents two examples demonstrating the potential of microfluidic devices.

Figure 2.12a) showcases a microfluidic chemostat, used to study the growth of microbial populations. This system incorporates a high density of pneumatic valves, allowing for controlled fluid manipulation within a highly integrated network. The precise flow control in such a device is crucial for continuous culturing and real-time monitoring of microbial behavior.

Figure 2.12b) highlights a low-cost, easy-to-operate microfluidic device designed for sandwich immunoassays, widely used in medical diagnostics and biological research. This system includes manually operated valves, represented by screws (circled in the image), which enable fluid flow regulation without requiring complex external control mechanisms. The green-dyed water marks the microfluidic channels, illustrating how liquid moves through the system. Such affordable, portable microfluidic platforms could be particularly valuable in resource-limited settings, expanding the accessibility of advanced diagnostic tools.

In SPR systems, microfluidic channels play a critical role in biosensing applications, where the precise delivery of analytes—molecules or biomolecules suspended in fluid—onto a plasmonic sensor surface is essential for monitoring molecular interactions in real time [216-219]. SPR-based biosensors de-

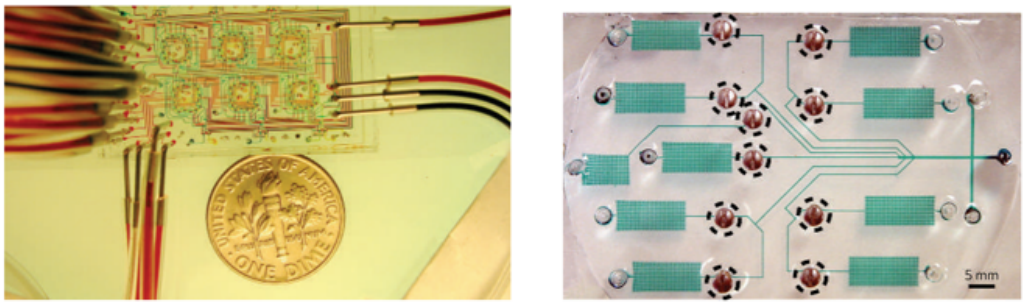

(a) (b)

Figure 2.12: Examples of microfluidic devices, adapted from Whitesides [210]. (a) Microfluidic chemostat, used to study microbial growth with an integrated network of pneumatic valves for precise fluid control. (b) Low-cost microfluidic device performing sandwich immunoassays, featuring manual screw valves (circled) for flow regulation, demonstrating affordable and portable microfluidic solutions for medical diagnostics.

tect changes in the refractive index on the sensor surface, which corresponds to the binding events occurring between analytes and the sensor's functionalized surface. Microfluidic channels facilitate a controlled environment where analytes can interact steadily and consistently with the sensor, making real-time monitoring possible. This controlled delivery also enables the efficient and repeatable collection of data, a necessary feature for ensuring the reliability of SPR measurements. The history of microfluidic technology in biosensing began with the emergence of microfabrication techniques in the 1980s, primarily from research in MEMS (Microelectromechanical Systems) and materials science [220-222]. Early on, researchers discovered that they could create micro-scale channels using silicon and glass substrates, but the field transformed in the 1990s with George Whitesides' work in soft lithography at Harvard University. Whitesides and his team introduced polydimethylsiloxane (PDMS), a flexible, transparent, and biocompatible material, as a practical substrate for microfluidic devices [223]. This material could be easily molded to create intricate designs, enabling scalable and cost-effective production of microfluidic channels. The introduction of PDMS in microfluidics led to the creation of lab-on-a-chip devices, small portable platforms capable of performing complex laboratory processes on a chip, often with microfluidic channels at their core. Pioneers like Andreas Manz and Albert van den

Berg further propelled microfluidics by applying these channels in chemical analysis and biosensing. Manz envisioned microfluidic systems as a means to reduce sample and reagent consumption in chemical processes, leading to the first lab-on-a-chip applications that performed complex analyses on a single, compact platform [224,225]. Van den Berg's innovations in electrochemical detection within microfluidic systems expanded the possibilities for miniaturized analysis. By incorporating electrodes into microfluidic channels, van den Berg enabled sensitive detection of ions and molecules at extremely low concentrations, laying the groundwork for today's high-sensitivity biosensors [226-228]. The structured and controlled environment provided by microfluidic channels enables SPR sensors to reach their full potential in biosensing applications. By ensuring that biomolecules are delivered in a consistent, reproducible manner, microfluidic channels enhance the accuracy and efficiency of SPR measurements, making these devices indispensable tools in diagnostics, research, and environmental monitoring. These channels, a direct result of the foundational work of pioneers in microfluidics, continue to drive forward the capabilities of SPR biosensors, underlining the importance of microfluidic innovation in the future of biosensing technologies

2.5.1 Recent Advancements in Microfluidics

Microfluidics have significantly transformed the field of biosensing and diagnostics, enhancing the precision, efficiency, and versatility of fluidic control in various applications. One key trend is the miniaturization of devices, which has led to the development of microfluidic channels embedded directly into lab-on-a-chip platforms [228-232]. This integrated design reduces the overall system footprint and ensures that analytes are efficiently handled in a compact environment, yielding faster response times and requiring smaller sample volumes—an essential feature for point-of-care diagnostics.

Materials like polydimethylsiloxane (PDMS), glass, and novel polymers are central to these advancements, each offering specific benefits. PDMS, for instance, is favored for its flexibility, transparency, and compatibility with biological samples [233-236]. Its pliability allows the formation of intricate channel designs and the integration of microvalves directly into the microfluidic structure. Hybrid systems combining PDMS microchannels with glass substrates have proven especially effective, enhancing device stability and reducing signal interference, which is critical in applications like the detection of biomarkers for early disease diagnosis [237,238].

The development of new metrics for assessing microfluidic printability has also emerged as a key area of advancement. Torres-Alvarez et al. introduced the concept of the Lowest Printable Characteristic Length (LPCL) for SLA 3D printing of embedded negative microstructures [239]. This geometrical metric helps predict the printability of microfluidic channels based on their design, addressing common challenges like channel clogging or collapse due to resin dragging. Their study showed that the LPCL for successful printing varies with the orientation of the channels and the type of resin used, providing guidelines for optimizing 3D printing settings to achieve accurate and functional microfluidic designs. This advancement is particularly relevant for the direct fabrication of monolithic microfluidic devices where precision and reliability are crucial.

Control over fluid flow within these microfluidic systems has also advanced significantly. Microvalves, which allow precise control over the release of samples into designated areas, have improved measurement precision and efficiency [240,241]. Kim et al. demonstrated the integration of pneumatic microvalves into lab-on-a-chip systems, using compressed air to manage sample flow effectively [242]. This advancement is particularly useful for controlling the sequential delivery of reagents and analytes, optimizing reagent use, and ensuring accurate timing for chemical or biological reactions. Similarly, miniaturized peristaltic pumps have been developed to provide continuous and clog-resistant fluid flow. Ferretti et al. showcased peristaltic pumps that maintained steady flow rates, crucial for the analysis of viscous biological samples like blood plasma, thereby preserving the assay's accuracy and integrity [243]. As illustrated in Figure 2.13a), this peristaltic pump consists of a series of rollers compressing a flexible tube, creating a constant and controlled flow rate. The system ensures precise fluid handling in microfluidic applications, particularly for biological and biochemical analyses.

Moreover, advancements in mixing techniques within microfluidic channels have enhanced the efficiency of various assays. Given that laminar flow predominates in microfluidic systems, achieving thorough mixing of reagents can be challenging. To overcome this, researchers have introduced innovative channel geometries that generate controlled microvortices and improve mixing efficiency [244-247]. One such approach is the use of capillary pumps, as shown in Figure 2.13b), adapted from Safavieh et al. [245]. These serpentine and leading-edge capillary pumps are designed for passive fluid transport in microfluidic networks. The pump consists of precisely etched microstructures that guide fluid through capillary action, ensuring self-sustained and efficient

liquid transport without external power sources.

Additionally, serpentine microchannels, depicted in Figure 2.13c), have been optimized for particle focusing and separation, as demonstrated by Ebrahimi et al. [244]. These zigzag-shaped microchannels leverage inertial forces to manipulate particle trajectories, enhancing cell sorting and biochemical assays. The ability to focus and separate particles with high precision makes this design ideal for lab-on-a-chip applications.

Lastly, spiral microchannels with enhanced fluid mixing capabilities are illustrated in Figure 2.13d), adapted from Altay [246]. This design leverages Dean vortices, where centrifugal forces induce secondary flows, effectively improving fluid mixing. The zero Dean velocity line, shown in the figure, highlights the point where the flow transitions between primary and secondary circulations, optimizing reagent distribution for improved assay performance.

Multiplexing, as discussed in Section 2.2.4, has been a transformative advancement in SPR biosensing, enabling the simultaneous measurement of multiple samples or biomarkers, thereby significantly improving diagnostic efficiency. A key enabling technology for multiplexing is microfluidics [248,249], which allows for precise control over fluid transport at the microscale, ensuring the efficient delivery and management of multiple analytes within a single device.

Microfluidic systems achieve multiplexing by integrating multiple independent channels within a compact platform, where each channel can be functionalized with specific biorecognition elements to target different biomarkers simultaneously. This configuration eliminates the need for separate testing procedures, reducing sample volume requirements and shortening analysis times [250-253].

2.6 Numerical Simulations and Finite Element Method

The Finite Element Method (FEM) is a numerical technique that approximates solutions to complex physical problems by discretizing them into smaller, manageable subdomains called finite elements. It is especially effective in applications involving structural mechanics, heat transfer, and electromagnetics [254–257], due to its ability to handle complex geometries, heterogeneous materials, and arbitrary boundary conditions.

FEM has proven highly effective in the analysis and optimization of photonic and plasmonic structures, particularly in Surface Plasmon Resonance

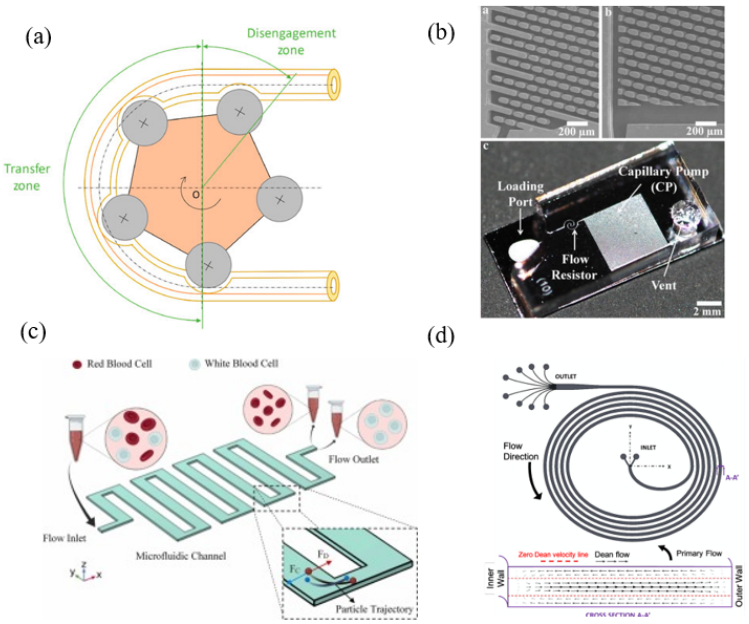

Figure 2.13: Recent examples of microfluidic technology. (a) Peristaltic pump, adapted from Ferretti et al. [243], illustrating a constant-flow mechanism for handling biological samples. (b) Capillary pump, adapted from Safavieh et al. [245], showing a passive microfluidic pumping system for autonomous fluid transport. (c) Serpentine microchannel, adapted from Ebrahimi et al. [244], demonstrating enhanced particle focusing and separation techniques. (d) Spiral microchannel, adapted from Altay [246], utilizing Dean vortices to improve fluid mixing efficiency in microfluidic assays.

(SPR) systems. By discretizing Maxwell's equations over complex domains, FEM enables accurate modeling of field enhancements at metal-dielectric interfaces, which are critical for SPR sensor performance [265,266].

One key advancement in SPR modeling using FEM was introduced by Yan and Qiu in 2007 [267], who developed an anisotropic FEM approach tailored for curved plasmonic geometries. Their method uses curved elements that conform more accurately to material interfaces, significantly improving modeling accuracy in systems with circular symmetry.

This improvement is demonstrated in Figure 2.14, which compares conventional FEM meshing with the anisotropic approach. Figure 2.14a) shows

the difference in mesh quality near a material interface (red line), while Figure 2.14b) compares the H-field distribution calculated with the anisotropic FEM (red dots) to the analytical solution (black line), highlighting their close agreement. The inset further visualizes the H-field intensity and vector field distribution, showcasing the accuracy of this method for modeling plasmonic wave propagation.

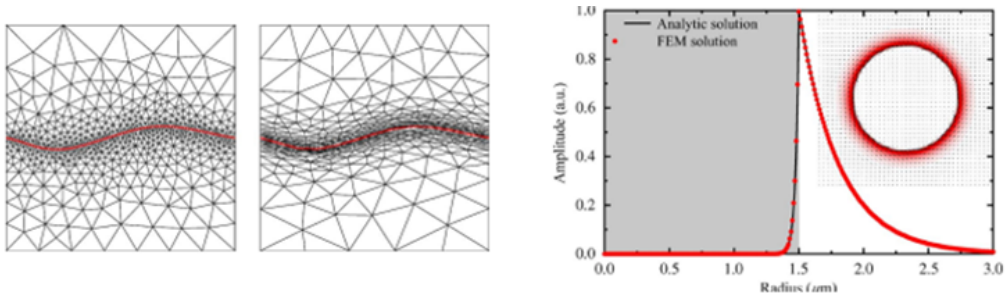

Figure 2.14: Anisotropic finite element modeling of Surface Plasmon Polaritons (SPPs), adapted from Yan and Qiu [267]. (a) Schematic finite-element meshes of a domain with a material interface, indicated by the red line. Left: conventional FEM mesh. Right: anisotropic FEM mesh, which adapts more precisely to the material interface. (b) Comparison of the H-field computed using anisotropic FEM (15,482 unknowns) with the analytical solution. The inset shows the H-field intensity (colormap) and the H-field distribution (quiver plot), demonstrating the accuracy of the method.

Building on these advancements, Smajic et al. in 2009 conducted a comprehensive comparison of numerical methods for plasmonic structures, evaluating FEM alongside other computational techniques. Their work highlighted FEM's strengths in flexibility and accuracy, particularly in handling complex material interfaces and nanoscale geometries [268]. This comparison established FEM as a powerful tool for analyzing and optimizing plasmonic devices, confirming its ability to capture intricate electromagnetic interactions with high precision. From this foundation, the field has expanded significantly, with researchers developing new plasmonic devices that can be optimized and simulated using FEM [269-271]. The rapid growth in computational power and the increasing efficiency of numerical solvers have enabled the modeling of more complex structures, allowing for enhanced sensor de-

signs, improved light confinement, and novel integrated photonic systems.

As FEM continues to evolve, it remains a cornerstone in the development of next-generation plasmonic and nanophotonic devices. Today, several specialized software packages make FEM accessible for a wide range of engineering applications, including electromagnetics and microfluidics. Popular tools like COMSOL Multiphysics and Ansys HFSS are widely used for simulating electromagnetic fields and designing complex microfluidic devices. COMSOL is particularly favored for its user-friendly interface and multiphysics capabilities, allowing the simultaneous simulation of fluid dynamics, heat transfer, and electromagnetics. Lumerical (now part of Ansys) is another essential tool, especially in nanophotonics and plasmonics, where it provides advanced features for modeling light-matter interactions at the nanoscale.

In the Annex 1 of this thesis, we provide a comprehensive step-by-step guide for using the Wave Optics Module and the Electromagnetic Waves, Frequency Domain (ewfd) interface in COMSOL 5.4 to perform 2D FEM simulations of new SPR-based designs and technologies [272]. This guide covers essential aspects such as geometry setup, material definitions, boundary conditions, mesh generation, solver settings, and post-processing of simulation results. By following this structured approach, researchers can efficiently model and optimize SPR sensors and plasmonic devices, gaining valuable insights into their electromagnetic behavior, resonance conditions, and field distributions.

2.7 Fabrication Strategies for SPR Devices

2.7.1 From Simulation to Fabrication: Layout Designing

The layout design process serves as the critical bridge between numerical simulations and the physical realization of nanophotonic devices. It translates the optimized geometries obtained from FEM simulations into precise design files for nanofabrication, using software platforms such as DW2000 [273] and KLayout [274]. These tools enable the definition of high-resolution photomasks or e-beam lithography (EBL) patterns necessary for fabrication techniques like photolithography, EBL, and focused ion beam (FIB) etching. The specific fabrication processes used in this work are described in Charpter 5.

Layout design begins by defining individual nanostructures, such as nanoslits,

grating elements, microfluidic channels, and alignment marks—based on parameters optimized through simulation. These elementary structures are then spatially arranged to build more complex components. For example, a grating coupler is formed by repeating a basic grating unit multiple times to create an array that effectively couples light into the device. Once these components are defined, they are combined to form a complete device layout. Multiple instances of these devices, potentially with varied parameters for testing, are then replicated across a wafer (typically 2-inch or 4-inch in diameter).

In practice, each component of a photonic or plasmonic device often requires a distinct fabrication step. Therefore, the layout design includes a separate mask for each process layer, with each mask corresponding to a specific fabrication step. These masks must be carefully aligned during fabrication to ensure proper overlap and registration between layers. To achieve this, alignment marks are incorporated into the layout. These consist of complementary patterns used to visually or optically align one layer to another with high precision during lithography. Additionally, labeling is integrated directly into the layout to uniquely identify devices, variations, or chips. These labels—often large text or numbers—assist in cataloging and tracking devices throughout fabrication, testing, and analysis.

In addition to academic references, such as Rizvi's comprehensive overview on photomask fabrication [275] and Chrostowski's work on photonic circuit design [276], users are encouraged to consult official software documentation available on manufacturer websites. These resources, along with video tutorials and open-source tools, enable broader access to layout design, even without high-performance computing resources or expensive software.

2.7.2 Fabrication Methods and Cleanrooms

Fabrication methods for creating micro- and nanostructures essential to SPR (Surface Plasmon Resonance) devices are typically categorized as either top-down or bottom-up approaches [277]. In our work, we employed top-down fabrication, which involves sculpting features from bulk materials using techniques such as lithography and etching. This method is well-suited for devices requiring precise geometries, such as nanoslit interferometers and grating couplers.

Clean rooms are essential for enabling these high-precision fabrication processes [278,279]. These environments maintain ultra-low levels of airborne

contaminants using advanced HEPA and ULPA filtration, controlled airflow, and strict gowning protocols. Clean room spaces are typically divided into white areas for general processing and yellow rooms for UV-sensitive photolithography steps. Personnel wear specialized suits to avoid introducing particles during fabrication.

Since their introduction, clean rooms have undergone significant technological advances, allowing for more complex, precise, and cost-effective device manufacturing [280–282]. These improvements have supported the shift from early SPR implementations to modern nanoscale plasmonic architectures [283]. Current clean room standards now support sub-10 nm fabrication with innovations such as robotic handling, adaptive environmental controls, and real-time monitoring systems [284–288].

2.7.3 Fabrication Techniques

The development of SPR devices relies on a variety of advanced fabrication techniques, each offering unique advantages in terms of precision, material compatibility, and scalability. These methods are crucial for creating the micro- and nanoscale structures that underpin SPR functionality, such as nanoslits, grating couplers, microfluidic channels, and photonic waveguides. While this work focuses on specific techniques optimized for SPR applications, numerous other fabrication approaches exist, each selected based on the unique requirements of different devices and research objectives [288]. These fabrication methods include:

Photolithography

(Figure 2.15a) is the most widely used technique for patterning microstructures, serving as a cornerstone of microfabrication since the mid-20th century [289,291]. Its widespread adoption is due to its cost-effectiveness and ability to expose entire wafers simultaneously, allowing for the mass production of microchips. This method utilizes ultraviolet (UV) light, selectively blocked by a photomask, to define the desired pattern on a light-sensitive resist layer. In this work, a hard mask was used, designed in the layout process. The choice between bright-field and dark-field photomasks depends on the application; here, a bright-field mask was employed for microfluidic channels, ensuring that aluminum trenches remained open in the designated regions.

Despite its efficiency, photolithography faces challenges below the 1-micron scale due to light scattering, which compromises pattern fidelity. While Extreme Ultraviolet (EUV) lithography offers higher resolution, it is prohibitively expensive. For sub-micron structures, alternative techniques like Electron Beam Lithography (EBL) or Focused Ion Beam (FIB) milling are preferred.

Electron Beam Lithography (EBL)

(Figure 2.15b) employs a highly focused electron beam to expose a sensitive resist layer, commonly PMMA (polymethyl methacrylate), which undergoes structural modification upon exposure [292–294]. When developed, the exposed areas dissolve, forming precise nanoscale openings, which can later be filled with metal to create intricate sub-micron to hundreds-of-micron structures.

Although EBL offers unmatched precision, it is time-intensive due to its serial exposure process—each pattern must be written device by device, making it impractical for large-scale manufacturing. Furthermore, beam scattering and resist limitations make it difficult to achieve feature sizes below 100 nm, though it remains an ideal tool for prototyping and research.

Focused Ion Beam (FIB) Milling

(Figure 2.15c) utilizes a gallium ion beam to directly mill materials at the nanoscale, providing an effective means for fabricating intricate SPR components, such as nanoslits and grating couplers [295–297]. Unlike EBL, which requires a resist, FIB enables direct material removal, offering a high degree of control over surface modifications.

However, FIB has certain trade-offs: surface roughness introduced by ion bombardment can scatter surface plasmons, affecting SPR sensor performance. Additionally, FIB is not automated for batch processing, requiring manual adjustments, making it a labor-intensive process. Nevertheless, it remains a powerful tool for fabricating SPR structures with sub-100 nm resolution.

Electron Beam (E-Beam) Evaporation

(Figure 2.16a) utilizes a focused electron beam to heat and evaporate the metal source within a vacuum chamber [298,299]. The metal, typically held

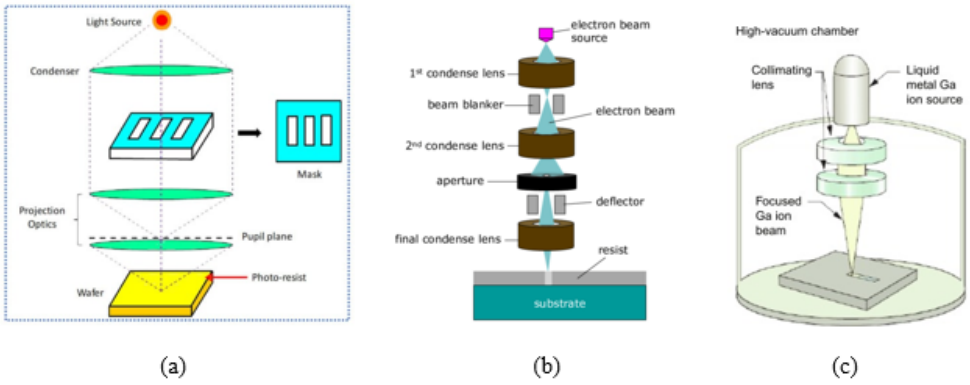

Figure 2.15: Schematic representations of fabrication techniques used in SPR device development. (a) Photolithography, illustrating how UV light passes through a photomask to define microstructures on a photoresist layer [290]. (b) Electron Beam Lithography (EBL), showing an electron beam scanning a resist-coated substrate for high-resolution patterning [294]. (c) Focused Ion Beam (FIB) milling, demonstrating direct material removal using a gallium ion beam in a high-vacuum chamber for nanoscale fabrication [296].

in a graphite or tungsten crucible, is vaporized and condenses onto the substrate, forming a thin, uniform metal layer with high purity and precise thickness control. In this work, e-beam evaporation was used to deposit thick metal layers exceeding 100 nm. However, the surface roughness achieved with this technique was high, as will be discussed in Chapters 4 and 5 of this work. Due to its roughness, this technique was also used for mask plasma etching of the microfluidic channels, where the roughness of the aluminum mask was not a limiting factor.

Thermal Evaporation

(Figure 2.16b) relies on resistive heating to gradually heat a crucible, often made of materials like alumina or quartz, until the metal evaporates and deposits onto the target surface [300]. This method is simpler than e-beam evaporation but has limitations due to the smaller crucible size, which can lead to overheating and potential cracking. As a result, thermal evaporation is more suitable for depositing thinner layers. In this work, it was used to fabricate grating couplers with a thickness of approximately 50 nm, where

high precision and minimal surface roughness were required.

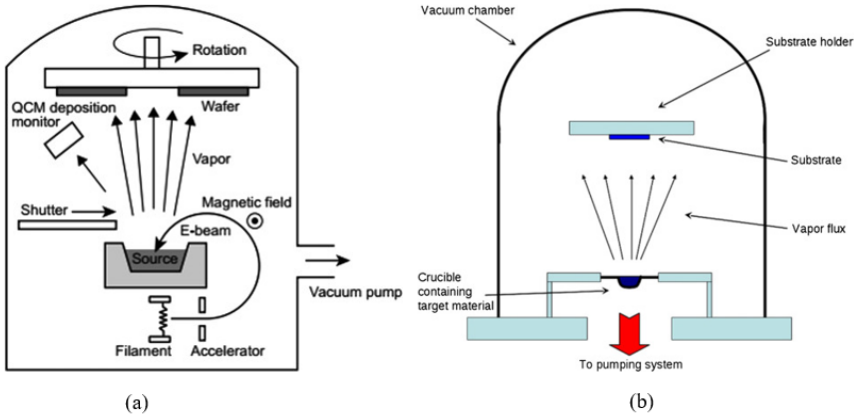

Figure 2.16: Schematic representations of metal deposition techniques used in SPR device fabrication. (a) Electron beam (e-beam) evaporation, where a focused electron beam heats a metal target in a vacuum chamber, causing metal vapor deposition onto a rotating wafer substrate [299]. (b) Thermal evaporation, where resistive heating gradually evaporates a metal source, allowing for thin-film deposition on a substrate placed within a vacuum chamber [300].

Spin Coating

is a widely used technique for depositing thin, uniform films onto a substrate by applying a liquid material and spinning it at high speeds [301,302]. The centrifugal force spreads the liquid evenly, allowing precise control over the film thickness by adjusting parameters such as spin speed and solution viscosity. In this work, spin coating was essential for the deposition of CYTOP to create the microfluidic channels. Additionally, it played a key role in the deposition of SPR (spin photoresist) and LOAR (lift-off resist) layers used in photolithography, where uniformity was crucial.

Plasma Etching

is a key process used to create precise patterns in polymers by selectively removing material through a controlled plasma reaction [303–305]. This tech-

nique relies on a reactive gas, typically oxygen, to break down and burn the polymer in the exposed areas while a lithographically defined metal mask protects the unetched regions. Careful optimization is required to prevent over-etching, which can lead to excessive material removal or complete consumption of the metal mask. In this work, plasma etching was used to fabricate the microfluidic channels of the biosensor, ensuring well-defined structures with controlled depth. After etching, the metal mask was removed using an acid-based solution, such as ITO etchant, leaving behind the final patterned polymer structures.

Wafer Bonding

is a technique used to merge two wafers, often to create a sealed structure with integrated microfluidic channels [306,307]. The process involves applying pressure to the wafers while a polymer layer between them softens under controlled heating. As the material melts, it enables bonding between the wafers. Once cooled, the polymer solidifies, ensuring a strong and stable connection. If the temperature ramping is done properly (see Chapter 5), typically very slowly, the microfluidic channels etched in the bottom wafer will be securely sealed without deformation. This method is crucial for maintaining precise alignment and preventing leaks, making it ideal for SPR and other optical applications requiring microfluidic integration.

Dicing

is the final stage in SPR device fabrication, where the wafer is cut into individual chips [308]. Typically, wafers are diced into rectangular chips, so dicing is performed along both horizontal and vertical directions to separate each chip. In this work, the wafer was diced only in horizontal rows, with each row containing four individual chips. This approach allows for efficient dicing in a single direction, but a special holder is required to shift between sensors within the same row.

The dicing process can be automated with precision machinery or done manually. When performed manually, alignment marks must be traced on the wafer's surface to guide the process. The blade must be carefully aligned with each mark to ensure clean cuts and avoid damaging the devices. Proper alignment and controlled cutting speed are crucial to maintaining the integrity of the fabricated sensors.

To fabricate the SPR sensors proposed in this thesis, the described fabrication techniques were employed. The complete workflow, along with a detailed explanation of each process and its limitations, is presented in Chapter 5.

2.7.4 Inspection Tools in SPR Fabrication

Inspection tools are fundamental in SPR fabrication, ensuring that nanoscale structures meet the precise specifications required for high performance and reliability [309–311]. These tools play a crucial role not only at the end of the fabrication process but also at intermediate stages, enabling real-time adjustments and ensuring that deviations can be corrected before progressing further. The inspection tools used in this thesis were the following:

Optical Microscopy

Optical Microscopy captures images using visible light, providing a straightforward method for inspecting larger structures. It was used for quick inspections, alignment verification, and detecting visible defects throughout the fabrication process. In photolithography, it was particularly useful for confirming mask alignments, ensuring reproducibility, and preventing errors before more advanced imaging techniques were required.

Stylus Profilometry

Stylus Profilometry involves a physical needle that moves across the surface, measuring depth and thickness variations. In this work, it was used to monitor CYTOP deposition for microfluidic channel fabrication. After each etching trial, the achieved thickness was measured to confirm process consistency. While profilometry is highly effective for micrometer-scale patterns, it lacks the resolution for nanoscale measurements, where Atomic Force Microscopy was used instead.

Atomic Force Microscopy (AFM)

Atomic Force Microscopy (AFM) operates by scanning a surface with a sharp probe that moves in response to atomic forces, generating a high-resolution topographical map. This method was used to assess surface roughness in our SPR devices, ensuring smooth metallic layers essential for plasmonic

resonance. In this work, AFM was particularly useful for inspecting grating couplers and evaluating metal depositions using witness samples during the metallization process, ensuring precise thickness and uniformity.

Scanning Electron Microscopy (SEM)

Scanning Electron Microscopy (SEM) uses a focused electron beam to scan the surface, producing detailed images of nanoscale structures. This technique was applied after each microfabrication stage to verify that feature dimensions matched design specifications. While SEM provides excellent resolution, interpreting measurements can be challenging since the placement of measurement markers within the image depends on the user's judgment.

These inspection techniques collectively ensure that every step of SPR device fabrication is executed with precision. By catching and correcting errors early, they minimize costly re-fabrications and help maintain high-quality standards. Furthermore, the documentation generated from these inspections supports the credibility of research findings, ensuring that published data accurately reflects the fabricated device's design and performance.

2.7.5 Materials Used in SPR Fabrication

Materials are the foundation of technological advancement, shaping industries and driving human progress [312–315]. Their properties determine how they interact with their surroundings, making material selection critical in any engineering application. In the case of SPR technology, as discussed in Section 2.1, a metallic layer and a dielectric material are required to support surface plasmon resonance.

These materials are characterized primarily by their permittivity constant (or refractive index), which defines their optical behavior, as well as other chemical and physical properties that influence stability, adhesion, and fabrication compatibility. Proper material selection ensures efficient plasmon excitation, minimal losses, and high sensitivity, making it a crucial factor in SPR sensor design. The materials used in this thesis are:

Metallic Materials

Plasmonic metals are essential in SPR technology because they have free electrons that can oscillate collectively to generate surface plasmons. Their

permittivity constant is negative, a key requirement for supporting SPR. The dielectric function of these metals is typically obtained from experimental tables or estimated using the Drude model, which describes the free-electron response in metals [7,316].

Among plasmonic materials, gold and silver are the most widely used due to their excellent plasmonic properties. Silver provides stronger plasmonic resonance but oxidizes easily, making it less stable over time. Gold, in contrast, does not rust, making it particularly suitable for aqueous applications where analytes flow in water-based environments, ensuring long-term stability in biosensing applications. In this thesis, gold was used to fabricate the single-interface SPR waveguide, the grating couplers, and the nanoslit, which are key components of the proposed SPR sensor design.

Substrates and Coatings

The substrate refers to the raw wafer used as the base for fabrication, typically silicon or glass. In this work, glass was chosen as the main substrate because of its optical transparency, allowing the radiated signal to propagate out of the sensor for detection. The refractive index of glass is assumed to be 1.5 for modeling and calculations.

To ensure structural integrity and seal the microfluidic channels, a second glass wafer was bonded to the sensor using a wafer bonder, providing mechanical stability and preventing leakage. The microfluidic channels themselves were fabricated using Cytop, a fluoropolymer that is optically transparent and has a refractive index of 1.333, matching that of water. This optical matching minimizes reflections and scattering at the fluid interface, ensuring efficient interaction between the analyte and the plasmonic surface.

Adhesion and Lithography Layers

A titanium or HMDS adhesion layer ensures proper bonding of gold to the substrate, preventing delamination. LOR and SPR resists are used in lithography to define nanoscale features, with aluminum masks serving as durable etching stencils. Oxygen plasma etching ensures high precision by removing organic residues and structuring polymer layers.

Cleaning and Lift-Off

To maintain optical purity, acetone, IPA, and DI water are used to clean surfaces before fabrication. Acetone also facilitates lift-off processes, ensuring precise pattern formation after metal deposition.

The choice of materials directly impacts the optical performance, stability, and efficiency of SPR sensors. Advances in material science continue to refine these selections, expanding the capabilities of SPR technology in biosensing, photonics, and environmental monitoring.

2.7.6 Testing of Fabricated Chips

Once the individual microchips are fabricated, they must be tested in the laboratory to validate their functionality. In this thesis, the SPR devices are designed for biosensing applications, requiring two primary types of testing: fluidic testing and optical testing.

For fluidic testing, the microfluidic channels must be properly connected and sealed. In this case, the device features three microfluidic inlets, which must be aligned with high precision to prevent leakage. Ensuring tight seals and precise alignment is crucial, as even minor misalignments can affect fluid flow and sensor performance.

For optical testing, the chip must be illuminated from the top using a microscope objective, while the radiated signal is collected from the bottom with a second microscope objective (for details, see Charpter 5). This setup allows for controlled excitation of surface plasmons and efficient signal capture.

A major challenge in this process is designing a custom jig holder with the necessary tolerances to support both fluidic and optical testing. This holder must include precisely machined inlets for microfluidic connections and a gasket material to seal the chip. In this case, the fluidic interface is end-facet, requiring a robust sealing mechanism.

Once the chip is securely mounted, testing is conducted on an optical table in a controlled illumination environment. A fixed-wavelength laser is used for stable and coherent excitation of surface plasmons, particularly in multiplexed devices where multiple channels require simultaneous excitation.

Optical components, including lenses, mirrors, and beam splitters, guide the laser beam to the SPR sensor, ensuring optimal alignment. Polarizers and wave retarders are used to achieve TM polarization, which is necessary

for efficient plasmon excitation. Microscope objectives focus the beam onto the grating coupler, aligning the beam waist with the coupler's dimensions to maximize coupling efficiency.

Cameras and auxiliary illumination play a key role in data acquisition. Cameras capture real-time plasmonic effects, enabling researchers to analyze reflected or transmitted light and visually inspect device performance. Since the SPR chips are millimeter-sized, precision holders ensure accurate positioning within the optical system.

When incorporating microfluidic channels, the alignment of inlets and outlets becomes even more critical. Gasket materials with micrometric laser-cut holes are used to form tight seals, ensuring robust fluid connections while maintaining optical alignment. Syringe pumps deliver analytes at controlled flow rates, allowing for precise sensing experiments.

Initial testing typically involves bulk sensing using chemical mixes, such as glycerol and water solutions, to characterize the device's response to refractive index changes. Later, biochemical tests with proteins or antibodies validate the device's biosensing capabilities. This stepwise approach ensures that the SPR sensor performs reliably across different experimental conditions, preparing it for real-world applications.

2.8 Conclusions

This state-of-the-art review has provided the theoretical and technological foundations necessary to understand the operation and motivation behind the SPR-based biosensor developed in this thesis. The review covered essential topics such as the physics of surface plasmons, coupling strategies using grating structures, extraordinary optical transmission through nanoslits, the role of microfluidics in biosensing, and the use of numerical simulations and nanofabrication techniques.

While SPR technology has matured significantly, challenges remain, particularly in achieving highly sensitive, compact, and multiplexed biosensors suitable for real-world applications. Current approaches still face limitations in efficiently integrating fluidic delivery, optimizing plasmonic excitation, and ensuring reproducibility across device batches.

This thesis addresses these gaps by proposing a novel SPR interferometric configuration that integrates grating couplers, nanoslit-based EOT structures, and microfluidic delivery channels into a manufacturable layout. Through modeling, design, fabrication, and testing, this work contributes

new insights into how SPR-based interferometry can be scaled and multiplexed, paving the way for advanced biosensing platforms.

3

Multiplexed biosensors based on interference of surface plasmons in multimode nanoslits

3.1 Summary

In this theoretical study supported by numerical simulations, we propose a multiplexed biosensor based on the selective excitation of multimode distributions in a gold nanoslit via the interference of surface plasmon waves. The nanoslit acts as an interferometric combiner, where surface plasmon waves, excited by grating couplers, converge and interfere, generating the transmitted signal. The unitary device consists of two grating couplers deposited on a thick gold layer on top of a glass substrate, with the nanoslit milled between the grating couplers, extending through the substrate. A fluoropolymer layer covers the gold layer, and a microfluidic channel etched into this polymer to transport the analyte in an aqueous solution to the sensing area. The sensor is designed to detect small changes in the refractive index through bulk and surface sensing.

The sensor is interrogated in terms of the power transmitted through the glass substrate. The grating couplers are illuminated with a pair of Gaussian beams, and an optimized optical setup is proposed to achieve this. Numerical simulations were performed to optimize the grating couplers for efficient coupling and to study the transmitted power, which is used to evaluate the sensitivity and resolution of the device for both bulk and surface sensing scenarios.

To achieve multiplexing, the unitary device is linearly arranged. To simplify the optical setup and avoid the need for precise alignment of small Gaussian beams, particularly in multiplexed configurations, a shadowing element is incorporated to prevent direct illumination of the nanoslit. This design allows the entire device to be illuminated with a single large Gaussian beam, which excites all the grating couplers simultaneously.

3.2 Contribution

This work was made possible thanks to the invaluable contributions of Dr. Israel De Leon, who proposed the original concept and theoretical framework

for multimode interferometric biosensors, and Dr. Pierre Berini, who provided essential guidance in addressing key technical challenges. I also extend my gratitude to Dr. Mallar Ray for welcoming me into his research group, supporting my work at Tecnológico de Monterrey, and providing access to the necessary computational resources.

In this work, I developed the full electromagnetic model of the device and carried out all numerical simulations. I also performed the CAD design of the biosensor and proposed a novel simplification for the optical excitation: using a large Gaussian beam in combination with a shadowing element to block direct illumination of the nanoslit. I defined the geometry, materials, and positioning of this shadowing element. Furthermore, I optimized key parameters such as the grating coupler dimensions, nanoslit width, gold layer thickness, and microfluidic channel length. I also proposed using the transmitted power as the main readout metric, avoiding the need to analyze the far-field angular distribution, thereby simplifying the detection scheme. I analyzed the simulation results and wrote the first draft of the manuscript independently.

3.3 Article

The submitted article follows verbatim.

Multiplexed biosensors based on interference of surface plasmons in multimode nanoslits

Marcos Valero,[1,2]Israel De Leon,[1,3] Mallar Ray,[2] and Pierre Berini[1,4,5, *]

[1]School of Electrical Engineering and Computer Science, University of Ottawa, Ottawa, Canada
[2]School of Engineering and Science, Tecnológico de Monterrey, Monterrey, Mexico
[3]ASML Netherlands B.V., Velhoven, The Netherlands
[4]Department of Physics, University of Ottawa, Ottawa, Canada
[5]Nexus for Quantum Technologies Institute, University of Ottawa, Ottawa, Canada

* pberini@uottawa.ca

Abstract: Multiplexed biosensors enable the simultaneous detection of multiple analytes within a single sample – a capability that holds significant importance in various fields, including environmental monitoring, food safety, and medical diagnostics. In medical diagnostics, detecting multiple biomarkers simultaneously is crucial for enhancing the diagnostic accuracy of conditions such as infectious diseases, cancer, and metabolic disorders. Biosensors based on surface plasmon resonance (SPR) are remarkable due to their high sensitivity compared to other technologies. However, current multiplexed SPR-based biosensors are bulky, expensive, and difficult to integrate in lab-on-a-chip configurations. Here we propose a multiplexed biosensor as a periodic array of plasmonic biosensor unit cells, consisting of a plasmonic interferometer located on the top of the substrate, excited by a pair of grating couplers such that the surface plasmons converge to a multimode nanoslit that produces the output signal emerging through the substrate. Microfluidic channels are integrated into the structure, thereby defining the sensing regions of each interferometer. The biosensor unit cells can be monitored individually and simultaneously by imaging their output onto a camera. Absorbing shadow elements are integrated into the structure to minimize crosstalk and background light, thereby enabling excitation of the entire array by a single large monochromatic Gaussian beam. The array can be scaled lithographically, and its interrogation is scaled by increasing the size and power of the Gaussian beam, and the size of the monitoring camera. We demonstrate the concept via electromagnetic simulations and predict resolutions of $R_b = 6.3 \times 10^{-6}$ RIU and $R_s = 10$ pm for bulk and surface sensing.

1. Introduction

There is an increasing demand for reliable and inexpensive multiplexed biosensors that can perform fast and simultaneous detection of multiple analytes in a single biological sample [1-7]. Multiplexing allows the identification of several biomarkers within a single sample related to a medical condition such as cancer, diabetes, rheumatoid arthritis, or heart failure, significantly improving the diagnostic and treatment of those diseases. Multiplexed biosensors are also capable of testing different samples in a single measurement run. In a biosensor, a biological response produced by an analyte is converted into a measurable signal by different transduction mechanisms such as piezoelectric, magnetic, thermoelectric, electrochemical, micromechanical and optical [8-11]. The most common optical biosensing methods involve luminescence or surface plasmon resonance (SPR) [12-14]. SPR biosensors offer several benefits over other sensing approaches, like high sensitivity, real-time detection, label-free protocols, and the potential for integration into lab-on-a-chip (LOC) devices [15,16]. SPR biosensors can also be integrated in multiplexed configurations [17-19].

There are numerous biosensing approaches involving surface plasmons, including those based on SPR in a prism-coupled arrangement [20,21], localized surface plasmon resonances (LSPR) on nanoparticles [22,23], and long-range surface plasmon polaritons (LRSPPs) on waveguides [24-28]. The concept of interference of surface plasmons has also been explored, including in Mach-Zehnder interferometers based

on surface plasmon waveguides [29], or on arrangements of SPR prisms [30]. Surface plasmon biosensors involving extraordinary optical transmission (EOT) have also been investigated [31-34]. Recently, Felix-Rendon *et al*. proposed a plasmonic interferometric biosensor based on EOT, where two surface plasmons incident on a nano-slit excite a combination of dipole and quadrupole resonances depending on the relative phases of the surface plasmons [35]. The light emerging from the slit produces a far-field angular distribution that depends on the relative phase of the incident surface plasmons, thereby enabling a phase-sensitive detection scheme.

Here we evolve this concept into a biosensor unit cell optimized for arraying into a multiplexed biosensor. We optimize grating couplers to excite each unit cell and adjust the sensing arm length and nanoslit geometry to optimize the bulk and surface sensitivities. An absorbing shadow element has been introduced into the unit cell to shield the nanoslit from direct illumination when grating couplers on either side of the slit are illuminated by a single Gaussian beam. We propose an illumination and imaging scheme that require trivial alignment and enable simultaneous interrogation of a periodic array of biosensor unit cells. Finally, we demonstrate the operation of the multiplexed concept. We constrain our designs to ensure manufacturability using standard semiconductor wafer processing tools.

This article is organized into the following sections: Section II describes the proposed biosensor unit cell and its main components as well as the principle of operation and the methodology for modelling the structure and optimizing its main performance parameters. Section III reports the results of our modelling of the biosensor unit cell and of a small periodic arrangement of unit cells. Section IV gives concluding remarks.

2. Biosensor concept and methodology

2.1 Interferometric nanoslit biosensor unit cell and principle of operation

A transversal cross-sectional sketch of the proposed interferometric biosensor unit cell is illustrated in Fig. 1. The structure consists of a $t_{Au} = 300$ nm thick gold layer deposited on a fused silica substrate, featuring a nanoslit of width w_s milled therein. The gold film is thick enough to support uncoupled single-interface surface plasmon polariton (SPP) modes. The film is covered by the fluoropolymer CYTOP, into which a fluidic channel flowing along z is etched. Two grating couplers located on the top gold surface at distances, $L_{arm} = 40$ µm from either side of the nanoslit. The grating couplers are used to couple monochromatic light into the SPP mode of the gold-CYTOP surface, exciting two counter-propagating SPP waves in the regions between the gratings toward the nanoslit, as sketched in Fig. 1.

The regions between the nanoslit and the gratings define the two arms of the interferometer. Part of the CYTOP is removed from the right arm to form a microfluidic channel, leaving the gold surface exposed to the sensing fluid over a distance $L_{fluid} = 38$ µm (corresponding to the width of the channel). Changes in the refractive index of the fluid or the growth of a biochemical adlayer on the surface produce phase shifts in the SPP that propagates through the sensing (right) channel relative to the reference (left) channel. These SPPs are incident on the nanoslit, which supports dipolar and quadrupolar resonant modes [35]. The relative phase of the SPPs determines the extent to which these resonant modes are excited – for instance when they are in phase, the dipolar mode is exclusively excited, whereas when they are out of phase by π, only the quadrupolar mode is excited. Intermediate phase differences result in the excitation of both resonant modes as a weighted sum. The power output from the nanoslit on the substrate side as well as the radiation pattern produced depend strongly on the relative phase of the SPPs leading to a high-sensitivity transducer. Initially, we consider excitation of the unit cell by a pair of Gaussian beams, as sketched in Fig. 1, but later we introduce an absorbing shadowing element to enable interrogation using a single large diameter Gaussian beam which is presented in Subsection III-E. This unit cell is then replicated periodically in the *x*-*z* plane to form a multiplexed biosensor, as discussed in Subsection III-F.

CYTOP (M grade) is selected as the material forming the top layer of the biosensor because it is highly transparent, and its refractive index is similar to that of aqueous solutions typically used for biosensing. The latter ensures that deleterious SPP reflections from the fluidic channel interfaces are minimized. It is also relatively easy to deposit films of this material via spin-coating and thermal curing, to etch microfluidic channels, and it does not dissolve in solvents typically used in biosensor cleaning, functionalization, and operation [36]. The free-space operating wavelength selected is $\lambda_0 = 850$ nm because SPPs are well-supported on gold at this wavelength, and inexpensive lasers, optoelectronics and imaging optics are readily available, including high-quality silicon imaging sensors needed to detect multiple outputs in a multiplexed configuration.

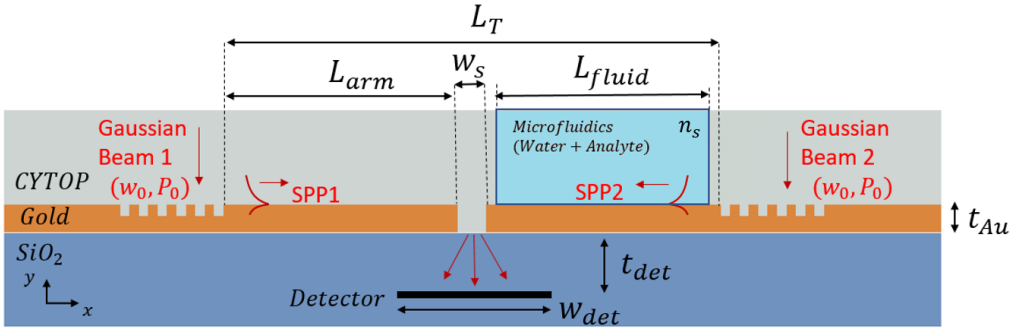

Figure. 1. Surface plasmon biosensor based on a nanoslit interferometer. Transversal sketch of the device, which consists of two grating couplers on a gold film of thickness t_{Au}, deposited on a fused silica wafer (substrate). The grating couplers are each located L_{arm} away from the nanoslit of width w_s, and are covered by a layer of CYTOP. A microfluidic channel of width L_{fluid} transports the sensing fluid and is etched on the right arm of the interferometer.

2.2 Modelling methodology

The electromagnetic modeling of the proposed sensor was carried out in two dimensions using the finite element method (COMSOL 5.6, Electromagnetic Waves Frequency Domain module), whereby Maxwell's equations are solved as a scattering problem [37]. To minimize unwanted reflections in the simulation domain from the terminating boundary conditions we coated the latter by perfectly matched layers (PMLs) of thickness of 0.5 µm. These PMLs were defined to absorb radiation at our wavelength of operation, $\lambda_0 = 850$ nm. For the light diffracted into the SPPs traveling along the gold-CYTOP interface in the $\pm x$ directions to the left and right boundaries of the simulation domain, the PMLs were defined for operation at the guided wavelength of these SPPs ($\lambda_{eff} = \lambda_0/n_{eff} = \lambda_0/1.37 = 620$ nm) in order to properly absorb them. Initially we consider excitation of the sensor by two 2D Gaussian beams (*cf.* Fig. 1), but subsequently consider illumination by a single large diameter beam (Subsections III-E, III-F).

In the simulation settings, electromagnetic ports were manually introduced for each beam to accurately model the excitation of the grating couplers. A transverse magnetic (TM) 2D Gaussian beam propagating in the vertical direction (along the y axis, Fig. 1) has the expression [37-39]:

$$E_x(x,y) = E_0\sqrt{\frac{w_0}{w(y)}}e^{\left(-\frac{x^2}{w^2(y)}\right)}e^{-j\left(\frac{kx^2}{2R(y)}+ky-\frac{\psi(y)}{2}\right)} \quad (1)$$

with the wavenumber $k = 2\pi n/\lambda_0$ where n is the refractive index of the medium in which the beam propagates, and w_0 is its waist radius. Also:

$$w(y) = w_0\sqrt{1 + \left(\frac{\lambda_0 y}{\pi w_0^2}\right)^2} \tag{2}$$

$$R(y) = y(1 + \left(\frac{\pi w_0^2}{\lambda_0 y}\right)^2 \tag{3}$$

$$\psi(y) = \tan^{-1}(\frac{\lambda_0 y}{\pi w_0^2}) \tag{4}$$

where $w(y)$ corresponds to the beam radius, $R(y)$ to the radius of curvature of the wavefront, and $\psi(y)$ to the Gouy phase of the Gaussian beam. The incident power of the 2D Gaussian beam is denoted by P_0 and the electric field strength at the origin, $|E_0|$, is related to P_0 using:

$$\frac{|E_0|^2}{\mathrm{Z}} = \sqrt{\frac{8}{\pi}}\frac{P_0}{w_0} \tag{5}$$

where Z corresponds to the wave impedance of the medium through which this Gaussian beam propagates, in this case, CYTOP. The wave impedance in CYTOP is dependent to the wave impedance in vacuum Z_0, with the relation $\mathrm{Z} = \mathrm{Z}_0/n_{CYTOP} \approx 376.7\Omega/1.345 = 280$,. Note that power is in units of W/m for a 2D Gaussian beam, because the beam and the structure are implied invariant along the z-direction (out of the page). In some cases, we set $P_0 = 1\ \mathrm{W/m}$ to calculate efficiencies, and in other cases we set $E_0 = 1\ \mathrm{V/m}$ to determine field enhancements, always ensuring that Eq. (5) is respected.

After defining the electromagnetic input, the geometry of the system is defined, and the value of the refractive index associated with each region is specified. The refractive index of the materials adopted are listed in Table 1 of Appendix 1. The refractive index of CYTOP, n_{CYTOP}, is taken from data supplied by the manufacturer. The refractive index of the substrate, n_{sub}, is taken as that of fused silica. The refractive index of the sensing fluid, n_s, is set initially to that of CYTOP, but then is perturbed to calculate the bulk sensitivity. These materials are highly transparent at the wavelength of operation, so the imaginary part of their refractive index is set to zero. The rest of the materials used in the design are gold, aluminum, and silicon, which have the experimentally determined refractive indices listed in Table 1 [40-43] (aluminum and silicon are used for the shadow elements, as discussed in Subsection III-E). Once the electromagnetic input port and the geometry of the biosensor are defined, the scattered electric fields are calculated, which includes the electromagnetic field distribution of the SPPs, as well as the near and far fields emerging from the nanoslit. The far fields are taken as the output of the biosensor. To calculate the power carried by these far fields, a detector of width w_{det} is placed beyond the nanoslit within the substrate on which the Poynting vector $\vec{S}$ is determined. The real part of its normal component $Re\{\|\vec{S}\|\}$ is numerically integrated to compute the output power of the biosensor, P_{out}, taken as a measurand.

3. Results

3.1 Grating couplers

The grating couplers are fundamental to the operation of a biosensor unit cell as these components are used to couple the incoming radiation into SPPs. To investigate their design, we assumed a 2D Gaussian beam as described in Subsection II-B of waist radius $w_0 = 5$ μm, located within the CYTOP layer, and originated

from an electromagnetic port 10 μm above the grating, designed as a horizontal arrangement of slits in the gold layer, as sketched in Fig. 2a. The main parameters of the grating couplers to be optimized are the pitch (Λ), depth (h), duty cycle (dc), and the number of periods (n_g), as defined in Fig. 2a. The aim of the optimization is to maximize the efficiency, (η), of the grating in coupling the incident beam to SPPs propagating along the gold-CYTOP interface.

As a first approximation to the grating period, Λ, the momentum conservation condition is used [45-47]:

$$\Lambda = \frac{m\lambda_0}{n_{eff,a} - n_1 \sin\theta} \tag{6}$$

where m is the order of the grating, $n_{eff,a}$ is the average effective index of the SPP propagating along the grating on the gold-CYTOP interface, θ is the angle of incidence of the exciting beam, and n_1 is the refractive index of the medium bounding the structure (*i.e.*, CYTOP). For this grating, the lowest diffraction order, $m = 1$, is taken and the angle of incidence is set to the normal to the grating, $\theta = 0$, such that the grating pitch can be approximated by:

$$\Lambda = \frac{\lambda_0}{n_{eff,a}} \tag{7}$$

The real part of the effective index of the SPP propagating along the gold-CYTOP interface is $n_{eff} = 1.37$, which we take as $n_{eff,a}$, yielding an initial value for the pitch as $\Lambda = 614$ nm. Eq. (7) holds for weak gratings (small h) which are not efficient as grating couplers at normal incidence. To maximize the coupling efficiency, the depth of trenches must be increased, so the weak perturbation condition (Eq. (7)) is no longer valid. We thus proceed numerically to model and optimize the grating iteratively, using $\Lambda = 614$ nm, $h = 25$ nm, and $n_g = 10$ as initial guesses, while the duty cycle remains fixed at, $dc = 0.5$. We proceed by sweeping the geometrical parameters of the grating one at a time holding the others fixed until the maximum coupling efficiency is reached.

To determine the coupling efficiency of the grating into the SPPs, it is necessary to place a detector at a location away from the grating, $L_{det} = 40$ μm as shown in Fig. 2a, to determine the power P_f carried by the SPP by integrating the real part of the normal component of the Poynting vector $\mathrm{Re}\{\|\vec{S}\|\}$ along the detector height. The power of the SPP emerging directly from the grating, P_i, is then obtained after compensating for its propagation loss to the detector location:

$$P_i = P_f e^{-2\alpha L_{det}} \tag{8}$$

where $\alpha = 21.6\ \mathrm{mm}^{-1}$ is the attenuation constant of the SPP propagating in the air-gold interface (imaginary part of its wavenumber), and it is calculated using the dispersion relation and the relative permittivity of both materials. Finally, the coupling efficiency, η, can be obtained by comparing the power carried by the SPP, P_i, to the power carried by the incident Gaussian beam ($P_0 = 1\ \mathrm{W/m}$):

$$\eta = \frac{P_i}{P_0} \tag{9}$$

This method of calculating the coupling efficiency is necessary because if the detector is placed too close to the grating, the transmitted power, P_f, may include radiated power in other diffraction orders.

The efficiency η was maximized by optimizing the geometrical parameters of the grating coupler. The optimal parameters obtained are: $\Lambda = 590$ nm, $h = 35$ nm, and $n_g = 16$, for $dc = 0.5$. The maximum

coupling efficiency achieved is $\eta = 27.36$ % into each SPP propagating away from the grating in both lateral directions, so the total coupling efficiency into SPPs is $\eta_T = 54.72$ %.

The enhanced electric field distribution $|E/E_0|$ of the total fields (incident and scattered) interacting with the grating coupler of optimized parameters ($\Lambda = 590$ nm, $h = 35$ nm, $n_g = 16$, $dc = 0.5$), is shown in Fig. 2b. The excitation of SPPs in both directions along the gold-CYTOP interface is clearly observable on this plot, along with a field enhancement factor of 10.8, the color bar on Fig. 2b is set from 0 to 6 so the incident Gaussian beam and the SSP wave are observable. The optimization curves for the grating pitch, Λ, and depth, h, are shown in Figs. 2c and 2d, respectively. Fig. 2e plots the coupling efficiency *vs*. the number of periods, n_g, as the beam radius of the exciting Gaussian beam, w_0 is changed, to determine the optimal values of both, which are $w_0 = 5$ µm and $n_g = 16$ periods. The efficiency of the grating is noted to drop as the beam radius increases, which implies that the power of the incident beam will need to be increased when interrogating a periodic array of unit cells with a single beam (Subsections III-E, III-F).

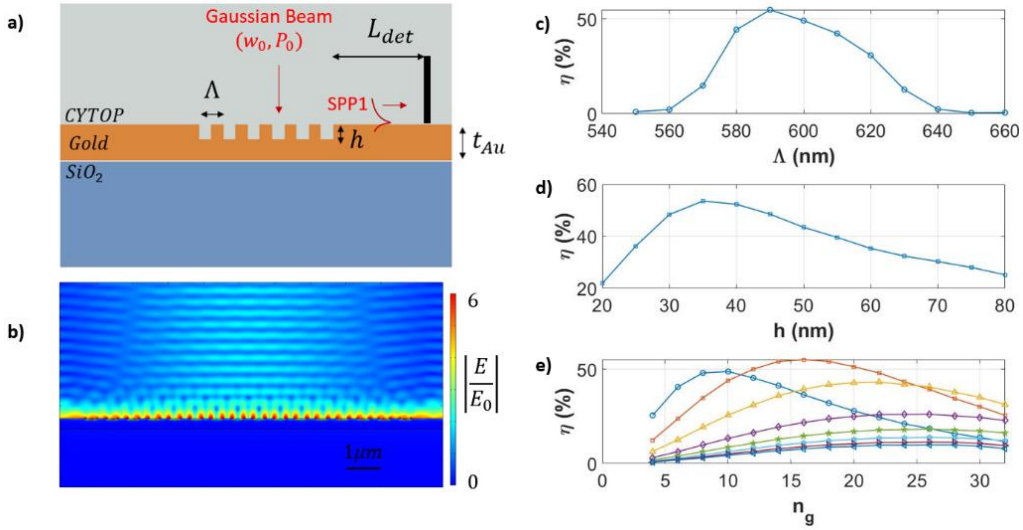

Figure. 2. a) Transversal sketch of a grating coupler and its main parameters, pitch Λ and depth h into the gold film. b) Electric field enhancement $|E/E_0|$ under Gaussian beam illumination ($w_0 = 5$ µm) of the optimal grating design, revealing strong coupling into two SPPs propagating laterally away from the grating. The maximum field enhancement is $|E/E_0| = 10.8$, and occurs at the corners of the grating coupler elements. c) Grating coupling efficiency *vs*. grating period for $w_0 = 5$ µm and $n_g = 16$. The maximum efficiency occurs at $\Lambda = 590$ nm. d) Grating coupling efficiency *vs*. grating depth for $w_0 = 5$ µm and $n_g = 16$. The maximum efficiency occurs at $h = 35$ nm. e) Grating coupling efficiency *vs*. number of periods for different Gaussian beam waist radii ($w_0 = 2$, 5, 10, 20, 30, 40, 50 and 60 µm), $\Lambda = 590$ nm and $h = 35$ nm. The maximum efficiency occurs for $w_0 = 5$ µm and $n_g = 16$. The coupling efficiencies plotted in Parts (c)–(e) are into both SPPs emerging laterally from the grating.

3.2 Biosensor operation – Unit cell

To illustrate the sensing mechanism of the proposed biosensor unit cell (Figs. 1, 3a), we refer to the results in Fig. 3b, which show the near-field distributions in the vicinity of the nanoslit obtained when two identical 2D Gaussian beams (TM polarized, $w_0 = 5$ µm, $P_0 = 1$ W/m) illuminate each optimized grating ($\Lambda = 590$ nm, $h = 35$ nm, $n_g = 16$, $dc = 0.5$). Recall that $t_{Au} = 300$ nm, $L_{arm} = 40$ µm and $w_s = 340$ nm. This excitation scheme generates counter-propagating SPPs having relative phase difference, $\Delta\phi = 0$, traveling along both arms of the sensor (SPP1, SPP2). If the sensing fluid has the same refractive

index as the CYTOP cladding ($n_s = n_{CYTOP}$), the near field distribution at the nanoslit location has even symmetry about the slit width. The symmetric near-field distribution thus preferentially excites the dipolar resonant mode of the nanoslit, resulting in a dipole-like far-field emission through the slit, as observed on the top and bottom left panels of Fig. 3b. Now consider a change in the fluid within the sensing arm ($n_s \neq n_{CYTOP}$) which will change the phase of the SPP propagating through, producing a relative phase difference in both SPPs (SPP1, SPP2) incident on the nanoslit. For the case where the relative phase difference, $\Delta\phi = \pi$, the near-field distribution at the nano-slit has odd symmetry and preferentially excites the quadrupolar mode of the nanoslit, resulting in a quadrupole-like far-field emission through the slit, as observed on the top and bottom right panels of Fig. 3b.

The transmission efficiency of the unit cell is obtained as the ratio of the total power transmitted through the nanoslit, P_{out}, to the total incident power. The latter is given by $P_{\text{in}} = 2P_0$, as two identical Gaussian sources are used. The former is monitored in our simulation by a $w_{det} = 100$ μm wide power detector placed at a distance $t_{det} = 4$ μm from the nanoslit into the substrate (Fig. 3a). Fig. 3c plots the norm of the real part of the Poynting vector $\text{Re}\{\|\vec{S}\|\}$ of the fields radiated by the nanoslit over the detector width. Note that, as mentioned earlier, for $\Delta\phi = 0$, a single peak (dipole-like) spatial distribution is obtained, for which $P_{\text{out}} = 0.0239\ \text{W/m}$ is calculated by integrating the distribution over the detector width, leading to an efficiency of $\eta_{\text{device}} = 1.19\ \%$ in this case. For $\Delta\phi = \pi$, the distribution features two symmetric peaks (quadrupole-like), yielding an integrated value of $P_{\text{out}} = 0.044\ \text{W/m}$, and an efficiency of $\eta_{\text{device}} = 2.22\ \%$ Although low, these efficiencies are sufficient for straightforward imaging and detection using low power (mW) incident beams.

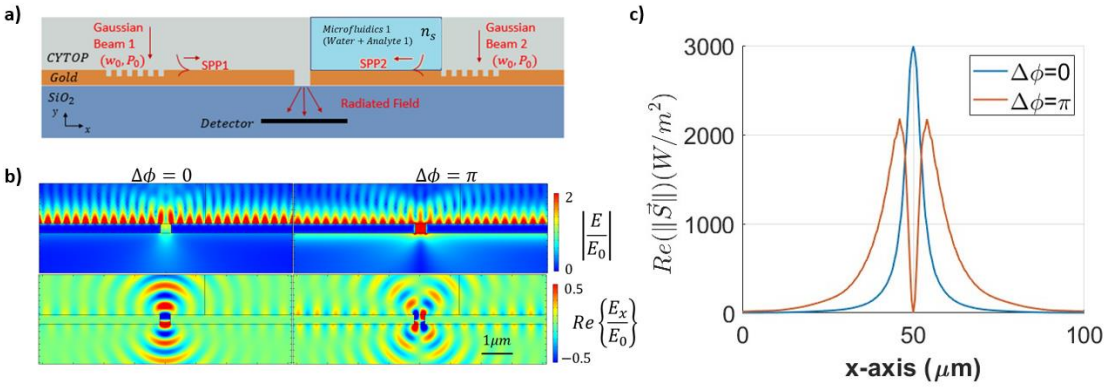

Figure 3. a) Transversal sketch of the biosensor unit cell (*cf.* Fig. 1). b) Electric field enhancement ($|E/E_0|$) top panels, and E_x/E_0 bottom panels), resulting from the illumination of the biosensor by a pair of Gaussian beams each with $E_0 = 1\ \text{V/m}$. If both SPPs arrive at the nanoslit with the same phase, the dipolar mode is excited therein (left panels), and when the phase difference between them is $\Delta\phi = \pi$, the quadrupolar mode is generated (right panels). At the nanoslit, the maximum field enhancement observed is $|E/E_0| = 3.5$. c) Intensity distribution, taken as the norm of the real part of the Poynting vector $Re\{\|\vec{S}\|\}$ of the fields radiated by the dipolar and quadrupolar modes in the nanoslit, on the detector located $t_{det} = 4$ μm below. In this case, each Gaussian beam carries a power of $P_0 = 1\ \text{W/m}$.

3.3 Power transmission responses – Unit cell

There are two sensing mechanisms capable of changing the relative phase between the two SPPs (SPP1, SPP2) incident on the nanoslit. The first consists of changes in the refractive index of the sensing solution

in the sensing arm (bulk sensing), and the second consists of biomaterial accumulating on the gold surface within the sensing arm (surface sensing). We consider both in this section for the unit cell design described in the previous section, using the transmitted power as the measurand.

In the bulk sensing mechanism, changes in the refractive index of the sensing solution are monitored. Such changes may be caused by changes in the constitution (*e.g.*, concentration, composition) or temperature of the solution. In our sensing configuration, such changes result in a refractive index change, Δn, between the sensing channel and the reference channel ($\Delta n = n_s - n_{CYTOP}$), which in turn induces a phase difference, $\Delta\phi$, between the SPPs propagating in both arms of the interferometer. For $\Delta n = 0$ the induced phase difference in the SPPs is $\Delta\phi = 0$, and the dipolar mode of the nanoslit is excited. Alternatively, for $\Delta n = 10^{-2}$ a phase difference of $\Delta\phi = \pi$ is numerically obtained, leading to the excitation of the quadrupolar mode of the nanoslit. For other values of $\Delta\phi$, the SPPs excite a linear combination of the dipolar and quadrupolar modes in the nanoslit. The far field radiation pattern evolves from a single to a double lobe pattern as the difference in the refractive index increases, as shown in Fig. 4a, and if this radiated field is spatially integrated, the radiated power is obtained.

The radiated power computed on the detector follows a sinusoidal characteristic, similar to that of Mach Zehner interferometers [48-51]. Fig. 4b plots the power computed on the detector as the index of the sensing fluid increases from $\Delta n = 0$ to 2×10^{-2}, such that the phase difference between the SPPs varies from $\Delta\phi = 0$ to 2π. For a biosensor nanoslit width of $w_s = 340$ nm (Fig. 4b, red dots), the operational range of the biosensor is the largest, according with [35], the quadrupolar mode is supported and the power transmission follows the fitted relation (Fig. 4b, red dashed):

$$P_{out}(\Delta n) \cong 0.034 + 0.01\sin(\pi(100\Delta n - 0.5)) \quad \text{W/m} \tag{10}$$

where the visibility is $V = 30\%$.

If the nanoslit width is reduced to $w_s = 200$ nm, (this value was proposed in [35] for a high sensitive operation of the biosensor), then it no longer supports the quadrupolar mode, and when the phase difference between surface plasmons is $\Delta\phi = \pi$, the transmitted power is $P_{out} = 0$. For the case of dipolar mode excitation ($\Delta\phi = 0$) the transmitted power becomes $P_{out} = 0.025$ W/m. In this case (Fig. 4b, blue dots), the transmitted power as a function of the refractive index change is described by the fitted equation (Fig. 4b, blue dashed)):

$$P_{out}(\Delta n) \cong 0.012 + 0.012\sin(\pi(100\Delta n + 0.5)) \quad \text{W/m} \tag{11}$$

Note that using a narrower slit which does not support the quadrupolar mode results in a visibility of $V = 100\%$.

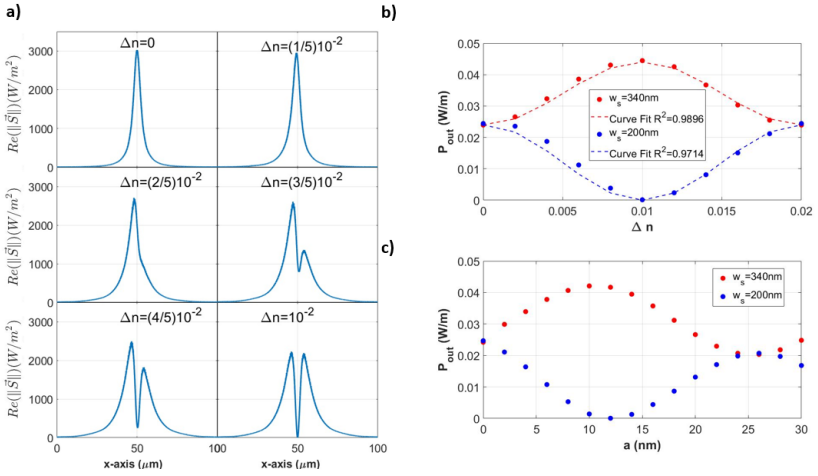

Figure 4. a) Far field intensity patterns on the detector located $t_{det} = 4$ μm below the nanoslit, showing the transition from the dipolar to the quadrupolar mode as the difference in refractive index is increased from $\Delta n = 0$ to 10^{-2} (bulk sensing), for a biosensor nanoslit width of $w_s = 340$ nm. Power output computed on the detector placed below the nanoslit, for two cases of nanoslit width, $w_s = 340$ nm and $w_s = 200$ nm, for b) bulk sensing as the refractive index difference increases from $\Delta n = 0$ to 2×10^{-2}, and c) surface sensing as a biochemical adlayer grows from $a = 0$ to 30 nm.

For surface sensing, the accumulation of biomaterial on the gold surface in contact with the sensing channel forms an adlayer, which we model as a thin dielectric layer of refractive index $n_a = 1.5$ (typical of biomaterial) [52], and thickness a. The adlayer is assumed to be comprised of recognition biochemistry affixed to the gold surface, binding selectively with the target analyte (biochemical) in the sensing solution. As the analyte binds, the adlayer grows thicker. Fig. 4c shows the surface sensing performance, characterized by the transmitted power as a function of adlayer thickness for both cases of nanoslit widths, $w_s = 340$ nm and $w_s = 200$ nm. For an adlayer of thickness $a = 0$, the phase difference between the SPPs is $\Delta\phi = 0$, resulting in the excitation of the dipolar mode. As the adlayer thickness increases, $\Delta\phi$ increases proportionally. A phase difference of $\Delta\phi = \pi$ is induced for an adlayer thickness $a = 12$ nm, leading to the excitation of the quadrupolar mode in the $w_s = 340$ nm wide nanoslit, and reaching a maximum in transmitted power of $P_{out} = 0.042$ W/m. Conversely, the transmitted power in the case of the $w_s = 200$ nm wide nanoslit is $P_{out} = 0$ for this adlayer thickness, because the quadrupolar mode is not supported. The transmitted power follows a sinusoidal pattern as the adlayer thickness increases, completing a period at $a = 26$ nm. Note that the curves of Fig. 4c resemble damped sinusoids, *i.e.*, their amplitudes decrease slightly as the adlayer thickness increases. This is caused by increased attenuation of the sensing SPP due to increased localization and penetration into the gold layer as the adlayer grows.

We can use Eqs. (10) and (11), along with the curves in Fig. 4, to work backward and obtain sensing information from the measured output power, such as the bulk refractive index of the sensing solution, or the thickness of the surface adlayer forming at the gold/solution surface.

3.4 Bulk and surface sensitivities – Unit cell

The bulk sensitivity of a unit cell, S_b, is the variation in the output power calculated at the detector when the index of refraction of the sensing fluid changes. The bulk sensitivity is taken as the derivative of the

output power with respect to the index of refraction of the sensing fluid, $S_b = dP_{out}/dn_s$. As noted in the previous section, the detected power, $P_{out}(\Delta n)$, oscillates periodically as the refractive index of the sensing fluid increases. Using Eq. (10), the bulk sensitivity is obtained as:

$$S_b \cong \pi \cos\left(\pi\left(100\Delta n - \frac{1}{2}\right)\right) \quad \mathrm{W/(m \cdot RIU)} \tag{12}$$

for the case of the biosensor with the nanoslit width $w_s = 340$ nm. Using Eq. (11) we find:

$$S_b \cong 1.2 * \pi \cos\left(\pi\left(100\Delta n + \frac{1}{2}\right)\right) \quad \mathrm{W/(m \cdot RIU)} \tag{13}$$

for the nanoslit of width $w_s = 200$ nm.

For the nanoslit of width $w_s = 340$ nm, the bulk sensitivity oscillates between positive and negative values, maximizing in magnitude to $|S_{b,max}| \cong \pi$ W/(m · RIU) for $\Delta n = 0.005, 0.015, \ldots$ and minimizing to $|S_{b,min}| = 0$ for $\Delta n = 0, 0.01, 0.02, \ldots$ as the sinusoidal power response (Eqs. (10) and (11)) transitions through exclusive dipolar or quadrupolar mode excitation. According to the analytical formula for S_b, when $w_s = 200$ nm (Eq. (13)), the magnitude of the maximum possible sensitivity increases by 20%, in this case to $|S_{b,max}| \cong 1.2\pi$ W/(m · RIU). The sign of the sensitivities for $w_s = 340$ nm and 200 nm are always opposite.

The design of our device allows easy tuning of sensitivity which is of general interest for developing a biosensor [53-55]. This can be achieved here by increasing the length of the sensing channel, L_{fluid}, which also increases power loss, but is a sensible strategy as long as the fields radiated by the nanoslit carry sufficient power to be easily detected. Alternatively, the nanoslit width w_s, can be altered in combination with the detector width, w_{det}. The method used to compute the relationship between the bulk sensitivity (S_b) and the detector width (w_{det}) is the following: Initially, the dependence was examined by analyzing the entire range of angular components of the far field radiated patterns as the refractive index difference Δn increased from 0 to 10^{-2} (following Fig. 4b), in seven incremental steps to adequately represent the bulk sensing sinusoid. Recall that the maximum sensitivity corresponds to the maximum slope of the sinusoidal curve describing the dependence of the integrated radiated power, P_{out}, on the refractive index Δn, which occurs at $\Delta n = (10^{-2})/2$. Thus, the two proximate bulk steps, $\Delta n = (3/7) \times 10^{-2}$ and $\Delta n = (4/7) \times 10^{-2}$, are identified and used to compute the slope yielding the maximum bulk sensitivity, $S_{b,max}$. Finally, the detector width, w_{det}, is reduced in steps of 2 μm to examine the sensor performance in terms of this design parameter.

For the nanoslit width of $w_s = 340$ nm, the quadrupolar mode is supported in addition to the dipolar mode, and the radiation pattern changes from dipolar (Fig. 3c, $\Delta\phi = 0$) to quadrupolar in nature (Fig. 3c, $\Delta\phi = \pi$), depending on the relative weight of these modes excited in the nanoslit. The maximum bulk sensitivity remains constant at $|S_{b,\max}| \cong \pi$ W/(m · RIU) with detector width as long as the latter is large enough to capture all angular components of the radiated light, which occurs for $w_{det} \cong 50$ μm, as observed from Fig. 5a. As the detector width decreases, the captured power also decreases but becomes dependent on the radiation distribution over the sensor. For instance, $|S_{b,max}| = 0$ when the detector width is reduced to $w_{det} = 13$ μm, because integrated over this width the change of the vectorial components of the Poynting vector $S_b = dP_{out}/dn_s$ cancel each other. From here, the bulk sensitivity becomes negative as the detector width decreases, reaching a value of $S_{b,max} \approx -1.31$ W/(m · RIU) for $w_{det} \approx 6$ μm, to eventually reach $|S_{b,max}| = 0$ as the detector vanishes ($w_{det} \to 0$).

Altering the nanoslit width changes the resonances supported therein, as discussed in Subsection III-C. For a nanoslit width of $w_s = 200$ nm only the dipolar mode is supported, and the radiated fields always have a transversal distribution consisting of one centered peak (*cf.* Fig. 3c, $\Delta\phi = 0$), which is captured by the detector located $t_{det} = 4$ μm below the slit. If the detector is reduced in width, a smaller fraction of the intensity distribution is captured, and the sensitivity is reduced monotonically until $S_{b,max} = 0$ for $w_{det} = 0$. Conversely, the maximum sensitivity is achieved when the detector width is large enough to capture all of the radiated light, which occurs for $w_{det} > 50$ μm as observed in Fig. 5a, beyond which the bulk sensitivity remains constant at its maximum value of $S_{b,max} = -3.87\ \mathrm{W/(m \cdot RIU)}$.

Given the similarity of the power response curves for surface sensing (Fig. 4b) to those for bulk sensing (Fig. 4a), we expect a similar behavior in the surface sensitivity relative to the detector width. Recall that the power response with adlayer growth (Fig. 4b), follows a damped sinusoid. If all the radiated field components emerging from the nanoslit are captured by selecting a wide detector width, $w_{det} = 50$ μm, the maximum surface sensitivity, $S_{s,max}$, obtained near $a = 5$ nm is $S_{s,max} \approx 0.002\ \mathrm{W/(m \cdot nm)}$ for $w_s = 340$ nm, and $S_{s,max} \approx -0.0026\ \mathrm{W/(m \cdot nm)}$ for $w_s = 200$ nm. We thus observe from Fig. 5 that the best bulk and surface sensitivities are obtained using a detector width that is large enough to capture all of the light emitted by the nanoslit, when only dipolar resonance ($w_s = 200$ nm) is supported. For the present geometry, the required minimum detector width is $w_{det} = 50$ μm when placed $t_{det} = 4$ μm below the nanoslit but would need to be widened if placed further below.

An important parameter of a biosensor is the resolution R, which represents the minimum detectable change in measurand. The resolution can be calculated with the following expression [56]:

$$R_b = \frac{m\sigma}{S_b}, \tag{14}$$

for bulk sensing, and,

$$R_s = \frac{m\sigma}{S_s}, \tag{15}$$

for surface sensing, where $m = 1,2,3$ ... accounts for different multiplicative factors of the standard deviation, σ, of the baseline noise in the system. In a recent work [57], Krupin *et al.* found that the standard deviation of the noise in power-interrogated surface plasmon waveguide biosensors, was ~1000× smaller than the average sensing signal. In our device, the largest change in signal is $\Delta P_{out} = 0.024\ \mathrm{W/m}$ (Fig. 4b)) for the $w_s = 200$ nm nanoslit, and $\Delta P_{out} = 0.02\ \mathrm{W/m}$ for the $w_s = 340$ nm nanoslit, so taking a standard deviation that is ~1000× smaller (as in [57]) yields $\sigma = 2.4 \times 10^{-5}\ \mathrm{W/m}$ and $\sigma = 2 \times 10^{-5}\ \mathrm{W/m}$, respectively. Using these values, the expected resolutions are $R_b = 6.3 \times 10^{-6}$ RIU and $R_s = 10$ pm, in both cases.

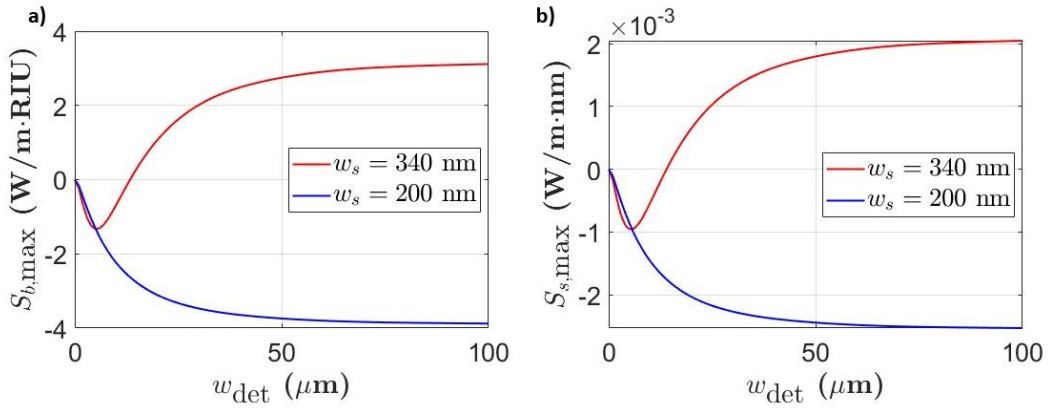

Figure 5. Maximum a) bulk and b) surface sensitivities, $S_{b,max}$ and $S_{s,max}$, *vs*. the width of the detector, w_{det}, used to capture the radiated power from the nanoslit. The detector is located $t_{det} = 4$ μm below the nanoslit. Nanoslits of width $w_s = 340$ nm and $w_s = 200$ nm are considered. Altering the nanoslit width changes the resonances supported therein, as discussed in Subsection III-C. For a nanoslit width of $w_s = 200$ nm only the dipolar mode is supported, and the radiated fields always have a transversal distribution consisting of one centered peak (*cf.* Fig. 3c, $\Delta\phi = 0$), which is captured by the detector located $t_{det} = 4$ μm below the slit. If the detector is reduced in width, a smaller fraction of the intensity distribution is captured, and the sensitivity is reduced monotonically until $S_{b,max} = 0$ for $w_{det} = 0$. Conversely, the maximum sensitivity is achieved when the detector width is large enough to capture all of the radiated light, which occurs for $w_{det} > 50$ μm as observed in Fig. 5a, beyond which the bulk sensitivity remains constant at its maximum value of $S_{b,max} = -3.87\ \mathrm{W/(m \cdot RIU)}$.

3.5 Interrogation using a single Gaussian beam

In order to interrogate the biosensor unit cell it is essential to excite both the grating couplers simultaneously. Optical interrogation using a dual beam system is possible with beam splitters and mirrors, a microscope objective with the right numerical aperture and focal length, and by tilting precisely one of the mirrors as shown in the proposed optical set-up given in Appendix 2 [58]. Although this optical arrangement is suitable, it has some disadvantages, such as complexity and the need to align several optical components, making it difficult to implement in a lab-on-chip configuration. A simpler interrogation scheme would be to excite both gratings simultaneously using a single large beam, say of waist radius $w_0 = 80$ μm, to overlap with both. However, if the device is illuminated with a large beam, the nanoslit would be illuminated directly by the central part of the beam, and the light transmitted would be significant even though the nanoslit is subwavelength in width, because the beam excites the dipolar resonant SPP mode therein directly. This transmitted light would interfere with the biosensing signal and spoil the sensitivity of the scheme. One solution to this problem consists of introducing a shadowing element over the nanoslit preventing it from being directly illuminated by the beam while allowing excitation of both grating couplers. A simplified optical set-up for interrogating a biosensor incorporating a shadowing element using a large Gaussian beam is proposed in Appendix 3.

The shadowing element must be designed to minimize the lensing effect [59], caused by the incident Gaussian beam diffracting at its edges and producing a bright spot (Poisson spot) behind that would illuminate the nanoslit (resulting in a counterproductive solution). This effect can be minimized by tuning the width of the shadowing element, w_{sh}, and placing it close enough to the nanoslit, such that the Poisson spot created by diffracted light is weak and located (virtually) far into the substrate. It was determined

through modelling that choosing an aluminum film of thickness $t_{Al} = 100$ nm and width $w_{sh} = 55$ µm as the shadowing element and positioning the element at a distance $t_{sh} = 10$ µm above the nanoslit, yields good performance in this regard.

Another challenge is that the light diffracted by the edges of the shadowing element is reflected by the gold layer (of thickness $t_{Au} = 300$ nm). If the shadowing element is made only of a reflective material, such as aluminum, then light becomes trapped between the two metal films, leading to inadvertent excitation of the resonant modes in the nanoslit and transmitted background light that obscures the biosensing signal. The proposed solution is to add an absorbing layer, for instance silicon, under the aluminum layer, which strongly absorbs light at the operating wavelength, greatly diminishing the light trapping effect caused by the shadowing element above the biosensor. The width of the silicon layer was set to match that of the aluminum layer, and through modelling, it was determined that a thickness of $t_{Si} = 400$ nm was suitable. The transversal cut of the configuration is shown in Fig. 6a.

Fig. 6b shows the performance of the proposed configuration including the bilayer shadowing element, illuminated by a large Gaussian beam, for a phase difference between the SPPs of $\Delta\phi = 0$ and $\Delta\phi = \pi$, achieved by changing the refractive index of the solution in the microfluidic channel, for $\Delta n = 0$ and $\Delta n = 10^{-2}$ respectively. The shadowing element recovers the biosensing signal, and it allows the sensor to be interrogated with a large beam, making the device simpler to test and integrate into lab-on-a chip devices. Both layers of the shadowing element have a different thickness, as noted above, the aluminum layer is $t_{Al} = 100$ nm thick, whereas the silicon layer is $t_{Si} = 300$ nm thick. These values were optimized numerically to maximize the visibility ($V = 85.2$ %) of the radiated quadrupolar mode. Fig. 6c shows the distribution of the intensity on the detector when the dipolar or quadrupolar modes are excited. This graph (after scaling) is very similar to that given in Fig. 3c, thus demonstrating the efficacy of the shadowing element.

To further illustrate the design considerations and performance of the shadowing element, Appendix 4 presents how different widths affect the electric field distribution. The simulations presented here highlight the progression from significant lensing effects at narrow widths to the mitigation of these issues as the width increases. They also show the impact of multiple reflections between the aluminum and gold layers and how the addition of the absorbing Si layer helps to minimize these reflections. This analysis underscores the importance of optimizing not only the width and thickness of the layers but also the distance of the shadowing element from the nanoslit to effectively suppress unwanted light while preserving the sensor's high sensitivity and functionality.

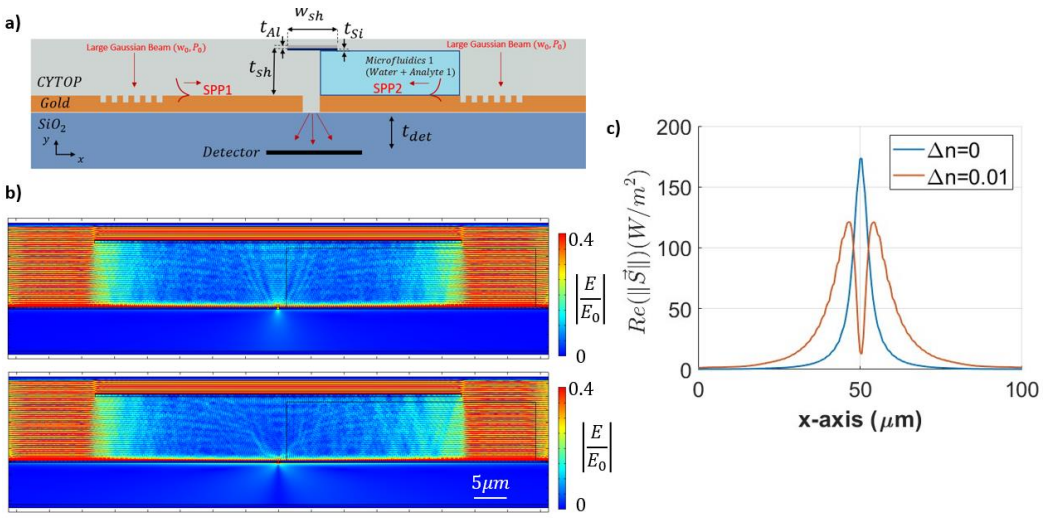

Figure 6. Implementation of a shadowing element to prevent direct illumination of the nanoslit by a large Gaussian beam ($w_0 = 80$ µm) used to simultaneously excite both gratings. a) The shadowing element is comprised of a bilayer of aluminum of thickness $t_{Al} = 100$ nm on a silicon layer of thickness $t_{Si} = 300$ nm, located $t_{sh} = 10$ µm above the nanoslit. The width of the bilayer is $w_{sh} = 56$ µm. b) Distribution of the enhanced total electric field $|E/E_0|$ for $\Delta\phi = 0$ (top, excitation of the dipolar mode only) and for and for $\Delta\phi = \pi$ (bottom, excitation of the quadrupolar mode only). The maximum field enhancement in this configuration occurs in the corner of the grating couplers and is $|E/E_0| = 2.4$. c) Intensity distribution, taken as the norm of the real part of the Poynting vector $Re\{\|\vec{S}\|\}$ of the fields radiated by the dipolar and quadrupolar modes in the nanoslit, on the detector located $t_{det} = 4$ µm below.

3.6 Multiplexed configuration

Recall from Fig. 2b that a grating excited at normal incidence will couple to two SPPs propagating in the $\pm x$ directions with the same efficiency. Thus, a single grating can be used to excite two nanoslits, one located on either side of the grating. This motivates a multiplexing arrangement where biosensor unit cells are arrayed periodically in 1D along the lateral direction. The fluidic channels are directed along the longitudinal axis ($\pm z$) and can be designed to terminate at in-plane inlets and outlets along the front and back facets of the chip [60]. Furthermore, if each unit cell incorporates a shadowing element, as shown in Fig. 6a, then the entire array can be excited by a single large-diameter Gaussian beam. Fig. 7a shows the cross-sectional view of such an arrangement. The concept can also be scaled along the longitudinal axis ($\pm z$), because of the circular cross-section of a Gaussian beam, so the total number of available channels scales with the beam waist radius, w_0.

To demonstrate this multiplexing concept, two channels were modeled, using $w_s = 340$ nm as the nanoslit width, illuminated by a single Gaussian beam of waist radius $w_0 = 200$ µm. In this arrangement, the performance of each channel follows the performance of a unit cell as investigated in the previous sub-sections, and each channel can operate independently. Fig 7b gives the computed electric field enhancement of the multiplexed sensing configuration for an incident Gaussian Beam of strength $E_0 = 1$ V/m, with all the considerations described above. Fig. 7c gives the computed intensity distribution, taken as the norm of the real part of the Poynting vector $\mathrm{Re}\{\|\vec{S}\|\}$ of the fields radiated by the nanoslits, on detectors located $t_{det} = 4$ µm below. In these computations, the refractive index in the left sensing channel was set to

produce $\Delta n = 0$ relative to its reference channel to illustrate excitation of the dipolar resonance, and the right channel to $\Delta n = 0.01$ to illustrate excitation of the quadrupole mode.

The interrogation of an array can be carried out using the set-up described in Appendix 3, where the Gaussian beam diameter is expanded to cover the full size of the array. The sensing signals emerging from each slit through the substrate, is imaged at the focal plane set by $t_{det} \approx 4$ μm with a lens system having a large enough field of view to collect the fields radiated from each slit. If the focal plane is placed at a larger distance, the fields radiated by the channels will mix, creating a complex distribution that cannot be easily analyzed. The image plane should also be magnified sufficiently to ensure adequate resolution on the detection camera. A specific optical design for the detection system would depend on the size of the array to be interrogated.

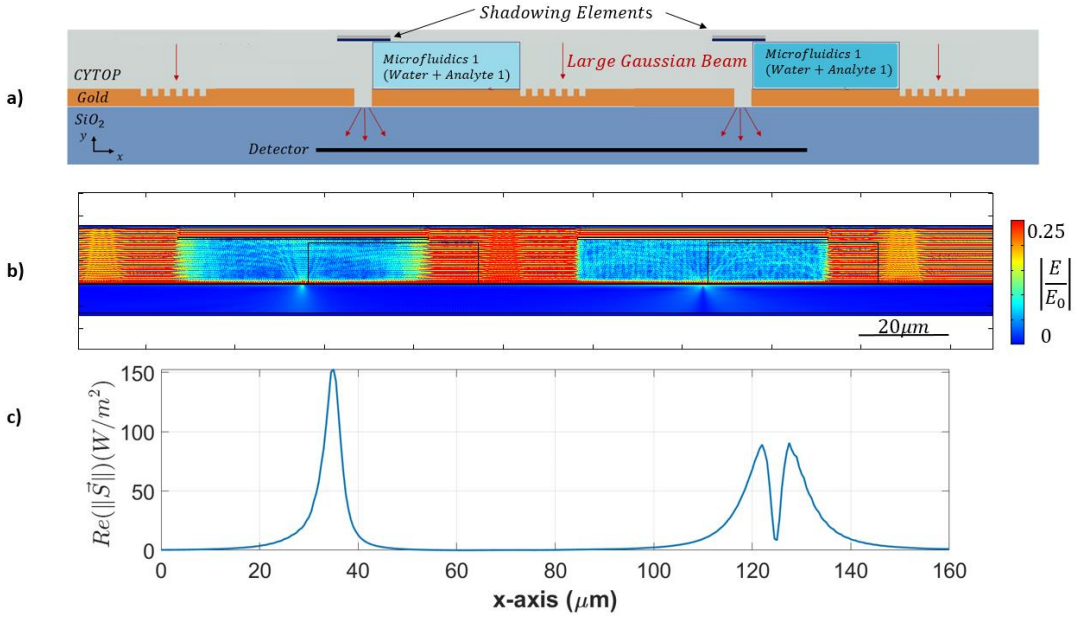

Figure 7. a) Model of multiplexed interferometric biosensors as a lateral periodic array of two unit cells (Fig. 6a). The system is illuminated by a Gaussian beam of waist radius $w_0 =$ 200 μm,which is large enough to excite both biosensors. b) Enhanced electric field distribution $|E/E_0|$ of the total fields over the cross-section of the system. The maximum field enhancement is $|E/E_0| = 2.4$ at the corners of the gratings. c) Intensity distribution, taken as the norm of the real part of the Poynting vector $\mathrm{Re}\{\|\vec{S}\|\}$ of the fields radiated by the nanoslits, on detectors located $t_{det} = 4$ μm below the nanoslits. In b) and c) the left sensing channel was set to $\Delta n = 0$ relative to its reference channel to illustrate excitation of the dipolar resonance, and the right channel to $\Delta n = 0.01$ to illustrate excitation of the quadrupole mode.

3.7 Proposed Fabrication Flow

Although our primary focus is the proposal of a multiplexed interferometric biosensor and its modelling, we suggest a fabrication methodology justified on the basis of previous work [59-61]. The fabrication process begins with substrate preparation, where, *e.g.*, a 100 mm diameter glass wafer, 500 μm thick, is

used as the transparent base. This substrate is essential for observing the radiation pattern emitted by the slit modes and serves as the foundation for subsequent layers. Next, a gold layer, 300 nm thick, is deposited onto the wafer using electron beam deposition. This gold layer functions as a plasmonic waveguide, enabling the propagation of surface plasmons.

Grating ridges are then patterned onto the gold layer using e-beam lithography [59]. These ridges are critical for coupling light into surface plasmon modes. Following this, a focused ion beam (FIB) [31] is used to mill a nanoslit between the grating couplers with high precision. The nanoslit penetrates through the gold layer to the substrate and allows the interference of surface plasmons, giving the sensor tunability and control over mode selection.

Subsequently, a CYTOP layer, approximately 10 μm thick, is applied using spin coating. CYTOP is chosen for its optical transparency and a refractive index close to that of water, which helps minimize reflections and supports efficient fluidic integration. The material encapsulates the sensor while providing structural stability and compatibility with microfluidic features. Plasma etching, using an aluminum mask, is then used to define the microfluidic channels in the CYTOP layer [61]. This step carefully carves out the channel that will direct the fluid flow over the sensing areas, enabling both bulk and surface refractive index measurements.

Sealing the microfluidic channels would involve aligned wafer bonding. A second glass wafer, coated with a 5 μm thick CYTOP layer, is used as the cover. The shadowing elements would be defined on this lid using photolithography and lift-off of two material evaporations, the first to deposit an aluminum layer and the second to deposit a Si layer. These shadowing elements and are then precisely aligned to the substrate using a wafer aligner-bonder [60,61]. The bonding process also seals the microfluidic channels, maintaining controlled and stable fluid flow over the sensing regions. Finally, the wafer is diced into individual chips. These chips are then ready for integration into experimental setups.

A 3D model is given in Fig. 8 to illustrate the proposed biosensor design, showcasing how the microfluidic channels are accessed in-plane via the front and back edges of the chip. In this sketch, two channels are illustrated, each capable of flowing a different solution, but the system can be further arrayed by lateral concatenation to increase the multiplexing density.

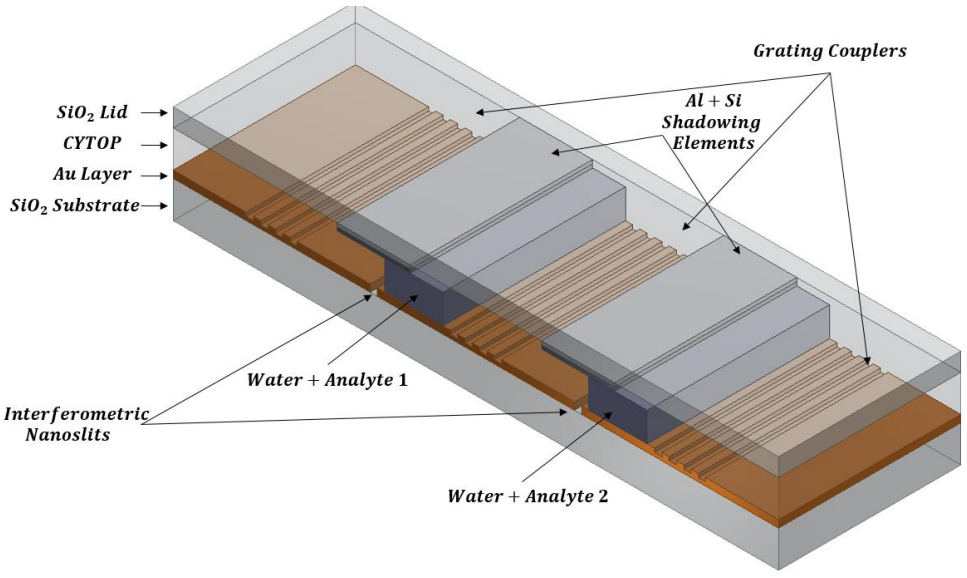

Figure 8. 3D model of the proposed interferometric biosensor, showcasing the key components. The biosensor features a gold layer on a glass substrate with grating couplers and precisely milled interferometric nanoslits. Microfluidic channels, integrated within a CYTOP layer, allow for lateral fluid access from the sides of the chip. Shadowing elements made of aluminum and silicon, placed above the nanoslits, prevent direct illumination, ensuring accurate sensing. The model illustrates how two separate channels can hold different biomarkers, enabling efficient multiplexed measurements.

4. Concluding remarks

We explored theoretically a biosensor unit cell based on the interference of SPPs in a nanoslit that can support two resonance modes – dipolar and quadrupolar. The biosensor consists of a gold film bearing a pair of gratings and a nanoslit and operates by illuminating the gratings to excite reference and sensing SPPs. As the phase difference between the SPPs varies, their interference at the nanoslit excites the dipolar and quadrupolar modes with varying weights, changing the transmitted light radiation pattern from single-lobed, corresponding to exclusive excitation of the dipolar resonance, to double-lobed, corresponding to the exclusive excitation of the quadrupolar resonance. The transmitted power varies periodically with the phase difference between the SPPs, with extreme values observed when dipolar and quadrupolar modes are excited. The maximum transmitted power efficiency of a biosensor unit cell was calculated to be in the range of 1 to 2 %. Two methods to alter the phase difference between the reference and sensing SPPs were investigated. First, bulk sensing by changing the refractive index of the sensing arm, and second, surface sensing by growing a dielectric layer on the gold surface in the sensing channel to model the growth of a biological adlayer. The bulk sensitivity peaks at $S_{b,max} \approx \pm\pi\ \mathrm{W/(m \cdot RIU)}$. A similar behavior was observed in surface sensing, where the maximum sensitivity of $S_{s,max} \approx \pm 0.002\ \mathrm{W/(m \cdot nm)}$ was achieved. In the case of surface sensing, the output power not only oscillates but also decays slightly as the thickness of the adlayer increases due to the increasing confinement of the SPP with increasing adlayer thickness. Two slit widths were studied ($w_s = 340$ nm and $w_s = 200$ nm), and it was demonstrated that the biosensor with $w_s = 200$ nm is about 18% more sensitive. The expected resolutions are $R_b = 6.3 \times 10^{-6}$ RIU (bulk) and $R_s = 10$ pm (surface).. To excite the reference and sensing SPPs, we used grating couplers, optimizing the geometric parameters to maximize coupling efficiency. For a $w_0 = 5$ µm incident Gaussian beam, the maximum total coupling efficiency (into two SPPs propagating laterally) is $\eta_T \approx 55$ %. A simplified optical testing setup using a large Gaussian beam to simultaneously excite both gratings was proposed, along with the introduction of an absorbing shadowing element comprising of silicon and aluminum layers, positioned above the nanoslit to prevent direct illumination of the nanoslit. The integration of shadowing elements and the increased size of the illuminating Gaussian beam allow for the interrogation of multiple biosensors simultaneously, enabling multiplexed configurations constructed as periodic arrangements of biosensor unit cells. We modelled the operation of a multiplexed configuration excited by a large Gaussian beam of waist radius, $w_0 = 200$ µm. The concept is extendible to large 2D arrays formed by the periodic arrangement of many unit cells, and further increasing the diameter and power of the interrogating Gaussian beam. We also proposed a fabrication methodology exploiting conventional cleanroom fabrication tools and processes to enable experimental verification of the concept.

Appendix 1: Optical parameters used in the modeling

Table 1. Index of refraction of the different materials used in the biosensor at $\lambda_0 = 850$ nm.

Material	Refractive index	Element in the device	Reference
CYTOP	$n_{CYTOP} = 1.345$	Microfluidic channels	[40]
Silica	$n_{sub} = 1.5$	Substrate	----

Sensing solution	n_s	Biosensing target	----
Gold (Au)	$n_{Au} = 0.1640 - 5.3194i$	Surface Plasmon waveguide, grating couplers and nanoslit	[41]
Aluminum (Al)	$n_{Al} = 2.5884 - 8.1687i$	Shadowing element	[42]
Silicon (Si)	$n_{Si} = 3.6410 - 0.0036i$	Shadowing element	[43]

Appendix 2: Proposed dual-beam interrogation set-up

A dual-beam optical set-up to interrogate the biosensor is proposed in the sketch shown in Fig. 9. As the illumination source, a coherent TM-polarized Gaussian beam operating at a free-space wavelength of $\lambda_0 = 850$ nm emerges from a fiber connectorized laser source. Its polarization is controlled with a linear polarizer, while its diameter is modified with the beam collimator and the beam expander. The interferometric biosensor is illuminated with two Gaussian beams of waist radius $w_0 = 5$ µm, separated by a distance $L_T = 80$ µm from each other. To produce this pair of relatively small Gaussian beams, it is necessary to use a microscope objective to obtain the desired spot diameters, and a dual beam system for splitting the input Gaussian beam, creating the beams that will excite the reference and sensing arms. The pair of beams is captured with the microscope objective and the distance between them is set by tilting one of the mirrors by a very small angle with respect to the optical axis as indicated. To image the output signal of the sensor, a $M = 40\times$ microscope objective and a CMOS camera beam profiler are proposed. The radiated fields can then be digitally integrated to obtain the output power P_{out}.

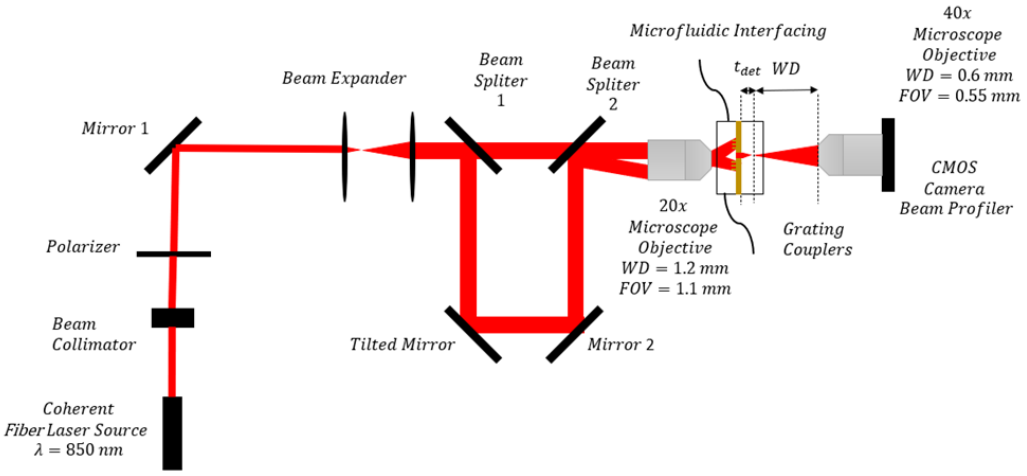

Figure 9. Sketch of a proposed dual-beam interrogation set-up.

Appendix 3: Proposed single-beam interrogation set-up

A single-beam optical set-up to interrogate a biosensor (or an array of biosensors) incorporating shadowing elements is proposed in the sketch shown in Fig. 10. The set-up produces a large diameter Gaussian beam that illuminates all of the grating couplers simultaneously. The set-up is a simplified version of that sketched in Appendix 2 in that all components between the beam expander and the device under test are eliminated.

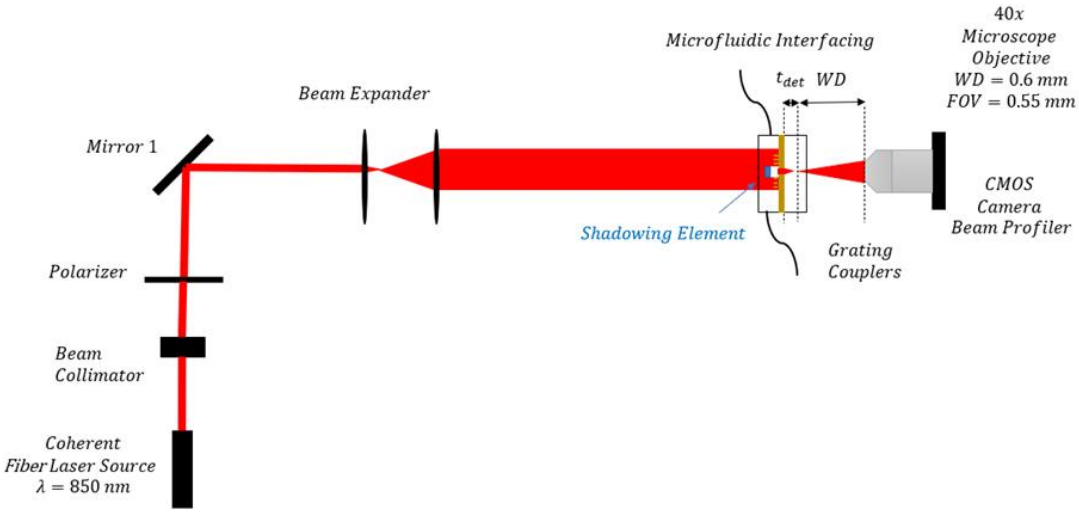

Figure 10. Sketch of a proposed single-beam interrogation set-up.

Appendix 4: Effect of Shadowing Element Width on Sensor Performance

Fig. 11 presents computations illustrating the behavior of the normalized electric field ($|E/E_0|$) near the nanoslit when different widths of the shadowing element, made of aluminum and silicon, are employed. The shadowing element, consisting of an aluminum layer with a thickness $t_{Al} = 100$ nm and a silicon layer with a thickness $t_{Si} = 400$ nm, is positioned at a distance of $t_{sh} = 10$ µm above the nanoslit. The widths w_{sh} of the shadowing element vary from 5 to 75 µm.

For smaller widths, specifically between 5 to 15 µm, a pronounced lensing effect is observed. This effect, caused by light diffraction at the edges of the shadowing element, focuses light behind the element near the slit and compromises the intended shadowing function. As the width increases from 25 to 45 µm, the lensing effect diminishes, but a new challenge arises in the form of multiple reflections. These reflections occur due to the waveguide-like behavior formed between the aluminum layer and the underlying gold surface, caused by diffracted light reflecting thereon. This issue is mitigated by the Si layer, which absorbs the reflected light. Therefore, the shadowing element must be wide enough to significantly reduce the intensity of the light as it reflects multiple times, minimizing the power that reaches the slit.

At a width of 55 µm, both the lensing effect and multiple reflections are effectively reduced. However, if the width increases further to 65 and 75 µm, the shadowing element begins to interfere with the operation of the grating couplers, capturing diffraction orders. These diffraction orders, increase the light trapped between the aluminum and gold layers.

In summary, the simulations demonstrate that a carefully optimized width of 55 µm for the shadowing element is ideal. This width minimizes both the lensing and waveguide (trapped light) effects while avoiding the capture of grating diffraction orders.

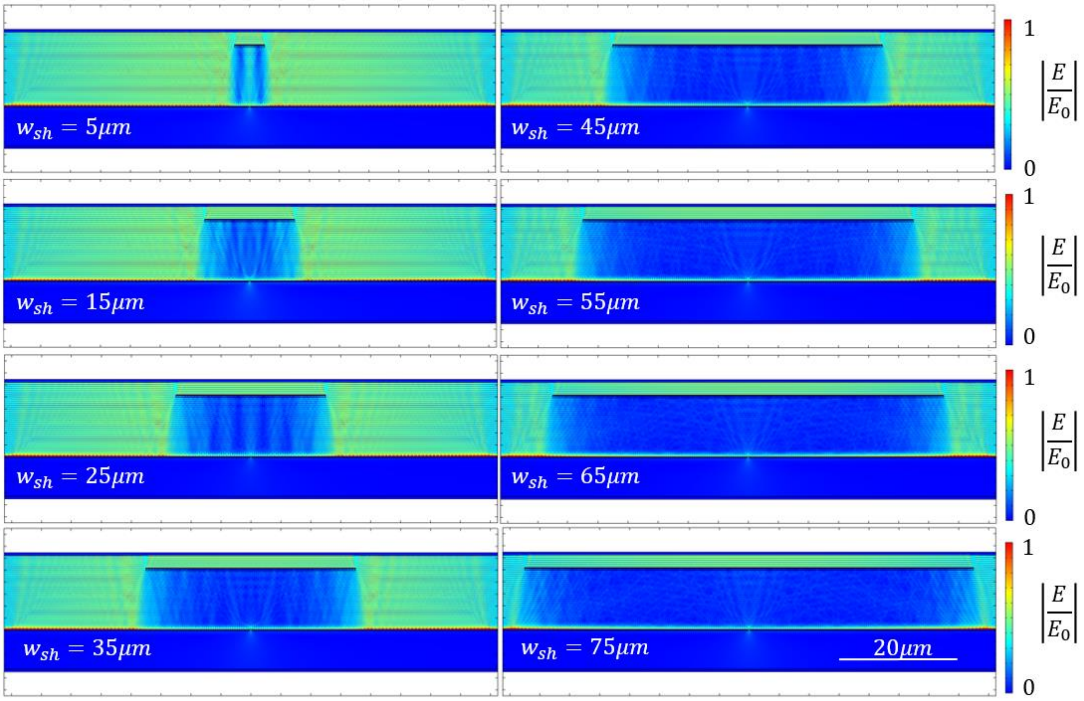

Figure 11. Simulation of the electric field ($|E/E_0|$) near the nanoslit for various widths (w_{sh}) of the shadowing element made of aluminum ($t_{Al} = 100$ nm) and silicon ($t_{Si} = 400$ nm), placed $t_{sh} = 10$ µm above the nanoslit. The lensing effect is prominent at smaller widths but diminishes as the width increases, while multiple reflections are absorbed by the silicon layer. At 55 µm, these effects are minimized, but widths greater than 55 µm begin to capture diffraction components from the grating couplers.

Funding. Natural Sciences and Engineering Research Council of Canada, grant number 210396, CONACyT National System of Researchers (SNI 1047863), Federico Baur Endowed Chair in Nanotechnology (ILST002-23ID69001), Graduate Seed Program of Tecnológico de Monterrey, CONACYT (CVU 900707).

Disclosures. The authors declare no conflicts of interest.

Data availability. No data were generated or analyzed in the presented research.

References

[1] N. S. Balasaheb, *et al.* "Biomarker detection technologies and future directions," Analyst 141(3), 740-755 (2016).
[2] K. Kayoung *et al.* "Clinically accurate diagnosis of Alzheimer's disease via multiplexed sensing of core biomarkers in human plasma," Nature Communications 11(1) 119, (2020).
[3] A. L. Washburn *et al.*, "Quantitative, label-free detection of five protein biomarkers using multiplexed arrays of silicon photonic microring resonators," Analytical Chemistry 82(1), 69-72 (2010).

[4] B. Bottazzi *et al.*, "Multiplexed label-free optical biosensor for medical diagnostics," Journal of Biomedical Optics 19(1), 017006 (2014).
[5] G. Breglio *et al*., "Fiber optic sensor arrays: a new method to improve multiplexing capability with a low complexity approach," Sensors and Actuators B: Chemical 100, 147-150 (2004).
[6] G. Zheng *et al*., "Multiplexed electrical detection of cancer markers with nanowire sensor arrays," Nature Biotechnology 23(10), 1294-1301 (2005).
[7] M. J. Linman, A. Abdennour, and Q. Cheng, "Interface design and multiplexed analysis with surface plasmon resonance (SPR) spectroscopy and SPR imaging," Analyst 135(11), 2759-2767 (2010).
[8] G. Rizzi *et al*., "On-chip magnetic bead-based DNA melting curve analysis using a magnetoresistive sensor," Journal of Magnetism and Magnetic Materials 380 215-220 (2015).
[9] D. Arpita *et al*., "Integrated label-free silicon nanowire sensor arrays for (bio) chemical analysis," Analyst 138(11), 3221-3229 (2013).
[10] A. Alodhayb *et al*., "Towards detecting the human immunodeficiency virus using microcantilever sensors," Applied Physics Letters 102, 173106 (2013).
[11] T. Kumeria *et al*., "Label-free reflectometric interference microchip biosensor based on nanoporous alumina for detection of circulating tumour cells," Biosensors and Bioelectronics 35,167-173 (2012).
[12] G. L. Glish and R. W. Vachet, "The basics of mass spectrometry in the twenty-first century," Nature Reviews Drug Discovery 2, 140-150 (2003).
[13] M. J. P. Leiner, "Luminescence chemical sensors for biomedical applications: scope and limitations," Analytica Chimica Acta 255(2), 209-222 (1991).
[14] E. Benito-Peña *et al*. "Fluorescence based fiber optic and planar waveguide biosensors. A review," Analytica Chimica Acta 943, 17-40 (2016).
[15] B. Špačková *et al*., "Optical biosensors based on plasmonic nanostructures: a review," Proceedings of the IEEE 104(12), 2380-2408 (2016).
[16] M. A. Otte *et al*., "Identification of the optimal spectral region for plasmonic and nanoplasmonic sensing," ACS Nano 4(1), 349-357(2010).
[17] J. A. Ruemmele *et al*., "A localized surface plasmon resonance imaging instrument for multiplexed biosensing," Analytical Chemistry 85(9), 4560-4566 (2013).
[18] C. Rosman *et al*., "Multiplexed plasmon sensor for rapid label-free analyte detection," Nano Letters 13(7), 3243-3247 (2013).
[19] J. Chen *et al*., "Multiplexed holograms by surface plasmon propagation and polarized scattering," Nano Letters 17(8), 5051-5055 (2017).
[20] E. Kretschmann, "Die bestimmung optischer konstanten von metallen durch anregung von oberflächenplasmaschwingungen," Zeitschrift fur Physik 241(4), 313-324 (1971).
[21] P. S. Pandey, S. K. Raghuwanshi, and S. Kumar, "Recent advances in two-dimensional materials-based Kretschmann configuration for SPR sensors: A review," IEEE Sensors Journal 22(2), 1069-1080 (2021).
[22] K. M. Mayer and J. H. Hafner, “Localized surface plasmon resonance sensors,” Chem. Rev. 111(6), 3828–3857 (2011).
[23] E. Hutter, and J. H. Fendler, "Exploitation of localized surface plasmon resonance," Advanced Materials 16(19), 1685-1706 (2004).
[24] J.-Y. Jing, Q. Wang, W.-M. Zhao, and B.-T. Wang, “Long-range surface plasmon resonance and its sensing applications: A review,” Opt. Lasers Eng. 112, 103–118 (2019).
[25] P. Berini, "Long-range surface plasmon polaritons," Advances in Optics and Photonics 1(3), 484-588 (2009).
[26] A. Boltasseva *et al*., "Integrated optical components utilizing long-range surface plasmon polaritons," Journal of Lightwave Technology 23(1), 413 (2005).
[27] H. Fan and P. Berini, “Bulk sensing using a long-range surface-plasmon triple-output Mach–Zehnder interferometer,” J. Opt. Soc. Am. B 33(6), 1068–1074 (2016).
[28] W. R. Wong and P. Berini, “Integrated multichannel young’s interferometer sensor based on long-range surface plasmon waveguides,” Opt. Express 27(18), 25470–25484 (2019).

[29] Y. Gao, Q. Gan, Z. Xin, X. Cheng, and F. J. Bartoli, “Plasmonic Mach–Zehnder Interferometer for Ultrasensitive On-Chip Biosensing,” ACS Nano 5(12), 9836–9844 (2011).
[30] A. V. Kabashin and P. I. Nikitin, “Surface plasmon resonance interferometer for bio- and chemical-sensors,” Optics Communications 150, 5–8 (1998).
[31] T. W. Ebbesen, H. J. Lezec, H. F. Ghaemi, T. Thio, and P. A. Wolff, “Extraordinary optical transmission through sub-wavelength hole arrays,” Nature 391, 667–669 (1998).
[32] S. G. Rodrigo, F. de León-Pérez, and L. Martín-Moreno, “Extraordinary optical transmission: Fundamentals and applications,” Proc. IEEE 104(12), 2288–2306 (2016).
[33] R. Gordon, D. Sinton, K. L. Kavanagh, and A. G. Brolo, “A new generation of sensors based on extraordinary optical transmission,” Acc. Chem. Res. 41(8), 1049–1057 (2008).
[34] M. Couture *et al*., "EOT or Kretschmann configuration? Comparative study of the plasmonic modes in gold nanohole arrays," Analyst 137(18), 4162-4170 (2012).
[35] U. Felix-Rendon, P. Berini, and I. De Leon. "Ultrasensitive nanoplasmonic biosensor based on interferometric excitation of multipolar plasmonic modes," Optics Express 29(11), 17365-17374 (2021).
[36] C. Chiu et al., "Fabrication of surface plasmon waveguides and devices in Cytop with integrated microfluidic channels," Journal of Vacuum Science & Technology B 28(4), 729-735 (2010).
[37] Wave Optics Module User's Guide, COMSOL Multiphysics® v. 5.4. COMSOL AB, Stockholm, Sweden. (2018).
[38] T.-C. Poon, and P. P. Banerjee, *Contemporary optical image processing with MATLAB* (Elsevier, 2001).
[39] B. E. A. Saleh, and M. C. Teich, *Fundamentals of photonics*, 3rd Ed. (John Wiley & Sons, 2019).
[40] Asahi Glass Company, Technical Information Cytop, distributed by Bellex International Corporation, http://www.bellexinternational.com/.
[41] P. B. Johnson and R. W. Christy, "Optical constants of transition metals: Ti, V, Cr, Mn, Fe, Co, Ni, and Pd," Physical Review B 9(12) 5056 (1974).
[42] A. D. Rakić, "Algorithm for the determination of intrinsic optical constants of metal films: application to aluminum," Applied Optics 34(22), 4755-4767 (1995).
[43] M. A. Green, "Self-consistent optical parameters of intrinsic silicon at 300 K including temperature coefficients," Solar Energy Materials and Solar Cells 92(11), 1305-1310 (2008).
[44] I. Medina, and A. Villaseñor, "A comparative analysis between Drude and Johnson & Christy for nanometric optical demultiplexer," Journal of Physics: Conference Series 2475, 012010 (2023).
[45] P. Berini, "Bulk and surface sensitivities of surface plasmon waveguides," New Journal of Physics 10, 105010 (2008).
[46] A. Khan *et al*., "Mach-Zehnder refractometric sensor using long-range surface plasmon waveguides," Applied Physics Letters 103, 111108 (2013).
[47] F. Hui, and P. Berini. "Bulk sensing using a long-range surface-plasmon dual-output Mach–Zehnder interferometer," Journal of Lightwave Technology 34(11), 2631-2638 (2016).
[48] B. Sepúlveda *et al*., "Optical biosensor microsystems based on the integration of highly sensitive Mach–Zehnder interferometer devices," Journal of Optics A: Pure and Applied Optics 8(7), S561 (2006).
[49] C. Chen, and P. Berini. "Grating couplers for broadside input and output coupling of long-range surface plasmons," Optics Express 18(8), 8006-8018 (2010).
[50] W. L. Barnes *et al*., "Physical origin of photonic energy gaps in the propagation of surface plasmons on gratings," Physical Review B 54(9), 6227 (1996).
[51] C. Chen, and J. Albert, "Photo-induced signal taps for power monitors in planar lightwave circuits," Proc. SPIE 5970, 59700I (2005).
[52] Q. Duan *et al*., "Surface plasmonic sensors: Sensing mechanism and recent applications," Sensors 21(16), 5262 (2021).
[53] J. Youssef *et al*., "Highly sensitive plasmonic biosensors with precise phase singularity coupling on the metastructures," Biosensors 12(10), 866 (2022).

[54] K.-L. Lee *et al*., "Enhancing surface sensing sensitivity of metallic nanostructures using blue-shifted surface plasmon mode and Fano resonance," Scientific Reports 8(1), 9762 (2018).
[55] M. Hong *et al*., "Observing the Modification of Quantum Statistics of Plasmonic Systems," in Quantum Information and Measurement VI, paper Tu2C.3 (2021).
[56] P. Wang *et al*., "Optical microfibre based photonic components and their applications in label-free biosensing," Biosensors 5(3), 471-499 (2015).
[57] O. Krupin *et al*., "Biosensing using straight long-range surface plasmon waveguides," Optics Express 21(1), 698-709 (2013).
[58] E. Hecht, *Optics*, 4th Ed. (Pearson Education, 2001).
[59] S. Mousavi, A. Olivieri, and P. Berini, "Fabrication of a high-speed plasmonic reflection/transmission modulator," AIP Advances 11, 025023 (2021).
[60] M. Asif *et al.*, "Wafer-bonded surface plasmon waveguide sensors with in-plane microfluidic interfaces," Journal of Micromechanics and Microengineering 30(9), 095004 (2020).
[61] D. Sekhar, E. Lisicka-Skrzek, and P. Berini, "Wafer-bonded deep fluidics in BCB with in-plane coupling for lab-on-a-chip applications," Micro and Nano Engineering 21, 100227 (2023).

4

Selective modal excitation in a multimode nanoslit by interference of surface plasmon waves

4.1 Summary

In this paper, we experimentally demonstrate a novel device based on the interference of surface plasmon polariton (SPP) waves in a gold nanoslit. The nanoslit acts as an interferometric combiner, where two surface plasmon waves traveling along a gold-air interface converge, generating different electrical field mode distributions around the slit. These mode distributions depend on the phase difference between the interfering SPP waves.

The SPP waves are excited using grating couplers, which are illuminated by a pair of Gaussian beams, the phase difference between SPP waves is controlled by altering the optical path length of one of the incident Gaussian beams.

We independently studied components of the device, such as the grating pitch, the number of grating grooves, the nanoslit width, and the arm lengths of the interferometer. The analysis focused on the optical transmittance of the device by comparing the incident power of a single Gaussian beam with the radiated signal transmitted through the glass substrate. This approach allowed us to assess how each geometric parameter affects the device's performance. Furthermore, the theoretical predictions were compared with experimental results, showing strong agreement and validating the model.

This work also demonstrates the excitation of dipolar, quadrupolar, and hexapolar modes within the nanoslit. Specifically, dipolar modes are observed for a nanoslit width of 200 nm, quadrupolar modes for 600 nm, and hexapolar modes for 1000 nm. These modes were visualized using a high-numerical-aperture microscope. The sinusoidal modulation of the transmitted light intensity, as the phase difference between the SPP waves is varied, further confirms the interferometric nature of the system. This behavior is analogous to the operation of Mach-Zehnder interferometers and highlights the capability of the system to finely tune plasmonic interference.

4.2 Contribution

The successful experimental demonstration of this novel interferometer was made possible through the use of advanced micro- and nanofabrication techniques, and the support of several collaborators whose contributions were deeply appreciated.

I conducted the full electromagnetic modeling of the device using finite element simulations to optimize its performance at an air–gold interface, where surface plasmons propagate. Based on the simulation results, I designed the geometry of key components — including the grating couplers, nanoslit, and interferometer arm lengths — to maximize coupling efficiency and interference contrast. I also created the CAD models of the chip for fabrication purposes and conceptual presentation.

The fabrication process was primarily carried out by me, including metal deposition, electron-beam lithography, and associated processing steps. The focused ion beam (FIB) milling of the nanoslit was performed by Hyung Woo Choi. All other fabrication steps were executed independently.

After receiving initial training from Luis-Angel Mayoral-Astorga, I designed and built a complete optical testbed from scratch at Tecnológico de Monterrey to characterize the fabricated devices. I performed all experimental measurements, collected the data, and compared the results to the theoretical predictions from my simulations, finding strong agreement. I analyzed and interpreted the data and independently wrote the first draft of the manuscript.

I would also like to acknowledge Howard Northfield, who provided me with training and continuous support in the cleanroom throughout the fabrication process, particularly during the electron-beam lithography phase. My sincere thanks also go to my advisors — Dr. Israel De Leon, Dr. Mallar Ray, and Dr. Pierre Berini — for their continued support and insightful feedback throughout this project.

4.3 Article

The submitted article follows verbatim.

Selective modal excitation in a multimode nanoslit by interference of surface plasmon waves

Marcos Valero,[1,2] Luis-Angel Mayoral-Astorga[2], Howard Northfield[2], Hyung Choi[2], Israel De Leon,[2,3] Mallar Ray,[1] and Pierre Berini[2,4,5,*]

[1]School of Engineering and Sciences, Tecnológico de Monterrey, Monterrey, Nuevo León 64849, Mexico
[2]School of Electrical Engineering and Computer Science, University of Ottawa, Ottawa, Ontario K1N 6N5, Canada
[3]ASML Netherlands B.V., De Run 6501, 5504 DR Veldhoven, The Netherlands
[4]Department of Physics, University of Ottawa, Ottawa, Ontario K1N 6N5, Canada
[5]Nexus for Quantum Technologies Institute, University of Ottawa, Ottawa, Ontario K1N 6N5, Canada

* pberini@uottawa.ca

Abstract: Interference of surface plasmons has been widely utilized in optical metrology for applications such as high-precision sensing. In this paper, we introduce a surface plasmon interferometer with the potential to be arranged in arrays for parallel multiplexing applications. The interferometer features two grating couplers that excite surface plasmon polariton (SPP) waves traveling along a gold-air interface before converging at a gold nanoslit where they interfere. A key innovation lies in the ability to tune the interference pattern by altering the geometrical properties of the gold nanoslit such that one, two or more resonance modes are supported in the nanoslit. Our experimental results validate the approach of our design and modelling process, demonstrating the potential to fine-tune geometrical parameters such as grating coupler pitch, depth, duty cycle, and nanoslit dimensions to alter the transmitted radiation pattern and the transmittance. We demonstrate the ability of a grating coupler to induce focusing of SPP waves to an arbitrary location on chip by illuminating with a converging Gaussian beam. Additionally, we observed far-field interference patterns linked to the multimodal operation of the nanoslit.

1. Introduction

Surface plasmon polariton (SPP) waves are electromagnetic waves that travel along the interface between a metal and a dielectric [1-4]. These waves arise from the coupling of the electromagnetic field with the collective oscillations of the metal's conduction electrons, resulting in a highly confined wave that propagates with enhanced fields and high sensitivity to changes in the local refractive index of the dielectric [5-7]. Similar to light waves, coherent SPP waves can interfere to produce an interference pattern [8,9]. A common configuration for harnessing the interference of SPP waves is the Mach-Zehnder interferometer [10-19]. This configuration splits the SPP wave into two paths, typically a reference arm and a sensing arm, before recombining them to generate interference. The Mach-Zehnder interferometer is widely used because it allows for precise control of the optical phase difference between the two arms, enabling sensitive phase-based detection of changes in the refractive index, which is crucial for applications such as biosensing and environmental monitoring.

Several Mach-Zehnder SPP interferometers have been proposed; however, individual interferometers are generally challenging to arrange closely together in compact configurations. This limitation is particularly troublesome for multiplexing applications, as in biosensors where the detection of multiple biomarkers simultaneously is desirable [20-24]. To address this, we propose an interferometer structure that allows for perpendicular interrogation by utilizing two gold grating couplers, a gold propagation surface acting as interferometer arms, and a nanoslit acting as a combiner. This simple yet effective configuration enables the system to be arranged both vertically and horizontally, making it possible to array multiple interferometers close together for multiplexing capabilities.

A key component of our device is the grating coupler, which is used to efficiently excite SPP waves on the metal-dielectric interface. Grating couplers are structures with periodic variations that match the momentum of incident light to that of the SPP waves, allowing the light to couple into the plasmonic mode [25-32]. This method is widely recognized as one of the most effective ways to excite SPPs due to its ability to achieve high coupling efficiency and its compatibility with various optical setups. Numerous devices in the literature utilize grating couplers for SPP excitation. The design mechanism of the grating couplers in our proposed configuration is similar to those established methods.

The second key element of our device is the gold nanoslit, which serves as the interferometric combiner for SPP waves. Gold nanoslits have been primarily used to filter spectral components of light and support extraordinary optical transmission [33-36]. The gold nanoslit in our case consists of a narrow gap milled into the gold film, capable of supporting one, two or more resonance modes depending on its width. This allows the radiation pattern to be altered and optimized depending on the detection technique used. As predicted in a previous work, optimizing the interference pattern through such adjustments, makes it possible to enhance the sensitivity and operational range of a biosensing device [37, 38].

In this paper we report theoretical and experimental results on interferometer and the elements comprising its structure. Section 2 provides conceptual details on the nanoslit interferometer and its main components. Section 3 describes the optical test set up used to characterize the fabricated test structures and the interferometer. Section 4 reports experiments used to optimize different geometrical parameters of the device, such as grating coupler properties (pitch, depth, duty cycle, and number of periods), nanoslit size, and the length of each arm of the interferometer. Section 5 demonstrates the multimodal operation of the nanoslit and the interference of two SPP waves incident on such a slit, while illustrating the effects of varying the slit size and the phase difference between the interfering SPP waves. Section 6 gives concluding remarks.

2. Proposed Device, Modelling and Fabrication

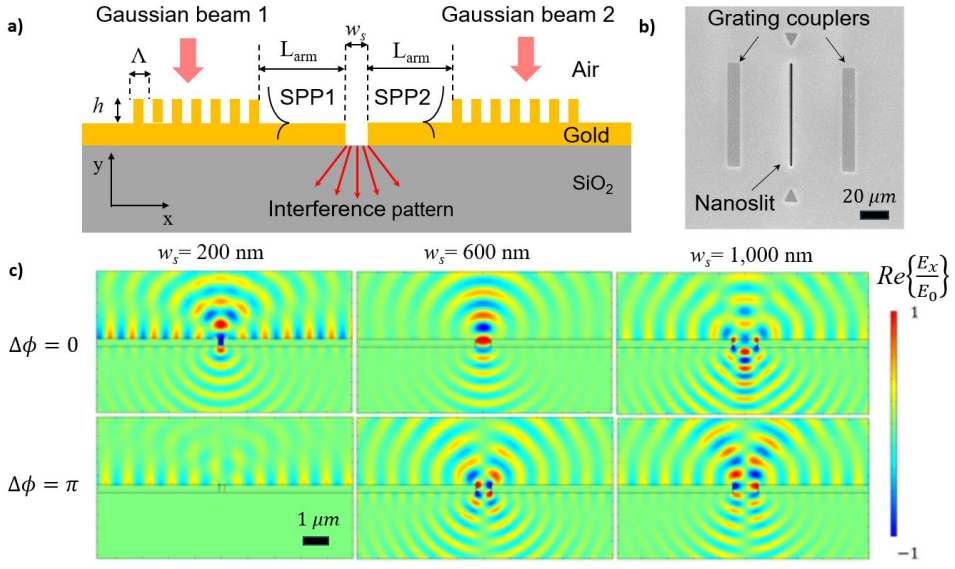

Figure 1. Nanoslit interferometer. (a) Schematic of the transversal section of the device showing its main components: two grating couplers deposited on top of a thick gold layer and equally distanced from a nanoslit milled into the gold layer, two grating couplers on a thick gold layer on a glass substrate equally

distanced from a nanoslit milled into the thick gold layer. The grating couplers are excited by a pair of Gaussian beams, generating two SPP waves propagating in opposite directions along the air-gold interface. These plasmons interfere at the nanoslit, which is designed and optimized to support one or more resonance modes, selectively excited depending on the relative phase difference between the interfering SPP waves. b) SEM image of a typical fabricated device. The two grating couplers and the central nanoslit are indicated with arrows for clarity c) Normalized electric field distributions ($\mathrm{Re}\{E_x/E_0\}$) near the nanoslit for three slit widths ($w_s = 200$ nm, 600 nm and 1,000 nm) and two phase differences between the SPP waves ($\Delta\phi = 0$ in the top row and $\Delta\phi = \pi$ in the bottom row). For $\Delta\phi = 0$, resonant modes with an odd number of lobes along the width are excited in the nanoslit, *e.g.*, dipole and hexapole. In contrast, for $\Delta\phi = \pi$, modes with an even number of lobes along the width emerge, such as the quadrupolar modes. At $w_s = 200$ nm, no mode is observed for $\Delta\phi = \pi$.

A schematic of the transversal cut of the proposed nanoslit interferometer is shown in Fig. 1a. The interferometer is designed to operate with surface plasmon polaritons (SPPs) propagating along a single interface, specifically the gold-air interface. This single-interface SPP is characterized by strong localization of the electromagnetic field at the metal-dielectric boundary. The designed interferometer consists of two grating couplers fabricated on top of a gold layer deposited on a fused silica substrate, with a nanoslit milled in the gold layer. In order to support only a single-interface SPP propagating along its top surface [39], and to support resonance modes in the nanoslit, the optimal thickness of the Au layer was theoretically estimated to be, $t_{Au} = 300$ nm. Experimentally, the thickness of the Au layer in our fabricated device was $t_{Au} = 311$ nm. The grating couplers are separated from each other by a distance of $2L_{arm} + w_s$, where L_{arm} is the length of each interferometer arm and w_s is the nanoslit width. Each grating coupler excites SPP waves propagating in opposite directions along the arms. The SPP waves interfere at the nanoslit and the mode(s) excited therein produce a radiated field pattern on the substrate side, which can be detected and related to the phase difference $\Delta\phi$ between the SPP waves propagating along the arms. A top view of a typical fabricated interferometer device consisting of a central nanoslit flanked by two grating couplers is shown in the SEM micrograph in Fig. 1b. This device features grating couplers with 12 periods, a pitch, $\Lambda = 786$ nm, a duty cycle of $dc = 0.68$, and grating ridges of height of $h = 54$ nm. The arm length of the interferometer is $L_{arm} = 40$ μm, and the nanoslit width, $w_s = 610$ nm.

The electromagnetic modeling of the proposed interferometer was conducted using a two-dimensional (2D) finite element method (COMSOL 5.6, Electromagnetic Waves Frequency Domain module), following a similar approach to that detailed in our previous work [37, 38]. The calculations were specifically performed at an operating wavelength of $\lambda_0 = 850$ nm. This wavelength was chosen because there are commercially available laser sources at 850 nm that offer high coherence, which is essential for interferometric applications. Additionally, light at this wavelength can be detected using Si CCD cameras, making it practical for experimental validation and measurement. The interferometer is perpendicularly excited by a pair of transverse magnetic (TM) polarized Gaussian beams of waist radius $w_0 = 5$ μm, which illuminate the grating couplers on the device. The Gaussian beams were modeled as electromagnetic ports. The relative permittivity of the materials (gold, fused silica) were taken from established experimental tables: the relative permittivity of air, $\varepsilon_d = 1$ [40], fused silica, $\varepsilon_{sub} = 2.25$ [41], and that of gold at our operating wavelength was taken as $\varepsilon_{Au} = -28.2691 + 1.7456i$ [42]. Using these values, the effective index of refraction, n_{eff}, of the SPP waves propagating along the gold-air interface is calculated as [1]:

$$n_{eff} = \sqrt{\frac{\varepsilon_{Au}\varepsilon_d}{\varepsilon_{Au}+\varepsilon_d}} = 1.0181 + 0.0011\mathrm{i} \quad (1)$$

and the effective wavelength λ_{eff} of the SPP waves as:

$$\lambda_{eff} = \frac{\lambda_0}{\mathrm{Re}\{n_{eff}\}} = 835 \text{ nm} \quad (2)$$

The components of the interferometer were designed based on these values. For the grating coupler the pitch for maximum coupling efficiency was initially estimated as, $\Lambda = \lambda_{eff}$ [15]. Subsequently, the optimized pitch was obtained via iterative modelling until the maximum coupling efficiency was achieved (see Section 4.2). The arm length, L_{arm}, was selected considering that the propagating SPP waves excited by the grating couplers have a finite propagation length, due to attenuation along the gold surface captured by the imaginary part of the effective index $\mathrm{Im}\{n_{eff}\}$ (see Section 4.3). Finally, the optimization of the nanoslit width, w_s, was also related to λ_{eff} (see Section 4.4). Optimization of the components were performed by calculating the transmittance T of the device. To achieve this, the scattered fields emerging from the nanoslit were captured, and the Poynting vector integrated to obtain the output power of the device, which was then normalized to the incident power of the Gaussian beams.

The normalized electric field distribution ($\mathrm{Re}\{E_x/E_0\}$) near a nanoslit of varying width, $w_s = 200, 600$ and $1{,}000$ nm, is illustrated in Fig. 1c. The top and bottom rows of the figure correspond to phase differences between the two SPP waves of $\Delta\phi = 0$ and $\Delta\phi = \pi$, respectively. Each column represents a different slit width: $w_s = 200$ nm (left), $w_s = 600$ nm (center), and $w_s = 1{,}000$ nm (right).

For $\Delta\phi = 0$ (top row) and for slit widths of $w_s = 200$ and 600 nm, a dipolar mode, characterized by two distinct lobes in the electric field distribution, is observed, while for $w_s = 1{,}000$ nm, a hexapolar mode, exhibiting six lobes, is excited. This suggests a clear trend where modes having an odd number of lobes along the nanoslit width (*e.g.*, dipolar, hexapolar, and potentially higher order modes) are excited. In these cases, each resonant mode exhibits a symmetric electric field distribution about the slit's vertical bisector and thus are excited by interference of the incoming SPP waves with $\Delta\phi = 0$.

In contrast, for $\Delta\phi = \pi$ (bottom row), modes with an even number of lobes along the nanoslit width are excited. For $w_s = 200$ nm, no mode is excited, leading to the absence of radiation through the nanoslit, whereas for $w_s = 600$ nm, and $w_s = 1{,}000$ nm, a quadrupolar mode characterized by four lobes, is excited, suggesting a similar trend, with potentially higher order modes, *e.g.*, octopolar emerging for larger slit widths. In these cases, each resonant mode exhibits an antisymmetric electric field distribution about the slit's vertical bisector and thus are excited by interference of the incoming SPP waves with $\Delta\phi = \pi$. This phase difference ($\Delta\phi = \pi$) was achieved in the simulations by adjusting the length of one of the arms (L_{arm}), by $\lambda_{eff}/2$.

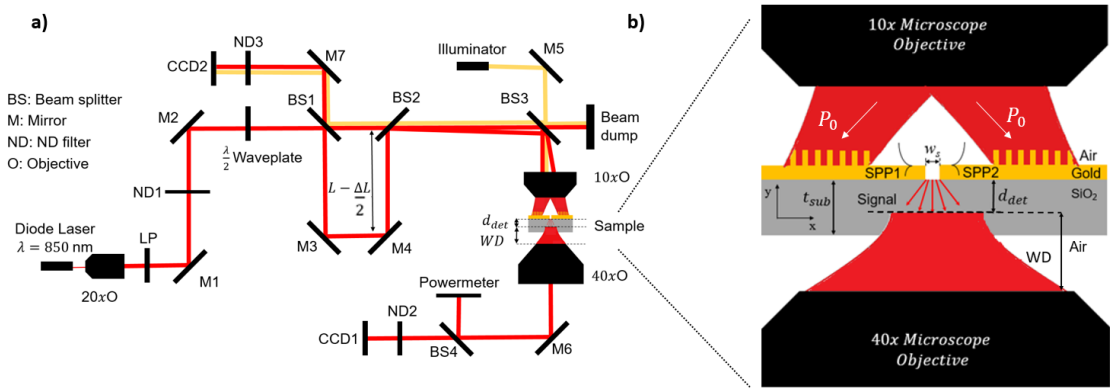

Figure 2. (a) Optical set-up implemented to test the nanoslit interferometer. A TM polarized Gaussian beam ($\lambda_0 = 850$ nm) is expanded and divided using BS 1. The emerging beams are redirected to a 10x microscope objective, and size-reduced to match the grating couplers. The beam waist and separation can be controlled with the beam expander and mirrors 2, 3, and 4. The illuminator and BS allows collecting the reflected image by CCD camera 2. In transmission, the interferometer's radiated far-field is observed (distance of detection is 4 μm) from the nanoslit using a 40x microscope objective which images the radiated pattern on CCD Camera 1. The power associated with the transmitted light can be simultaneously measured using BS 4 and a power meter. (b) Schematic of the excitation and detection setup for the two grating couplers on the plasmonic interferometer device. Two Gaussian beams (w $\approx$ 5 μm) are focused onto the grating couplers using a 10x microscope objective to excite SPP1 and SPP2 traveling in opposite directions. These SPPs interfere at the nanoslit radiating a signal through the substrate and air. The transmitted signal is collected with a 40x microscope objective placed near the slit's focal point to record the interference patterns.

To validate the optimization of the interferometer and its components and to observe interference patterns corresponding to the multimodal excitation of the nanoslit, we fabricated structures and characterized them experimentally. To achieve precise fabrication, we employed nanofabrication techniques. The gold layer deposition was performed using physical vapor deposition (PVD) for thicker Au films and a thermal evaporator for Au gratings. Grating couplers were patterned through e-beam lithography (EBL), followed by gold deposition and lift-off processes. Nanoslits were trenched into the gold film using focused ion beam (FIB) milling. An example of a fabricated device is shown in Fig. 1b.

3. Optical Test Set-up

After fabrication an optical setup is used to illuminate the plasmonic interferometer with two Gaussian beams of radius $w \approx 5$ μm aligned to the grating couplers. Additionally, the setup must be capable of capturing and detecting the output signal from the interferometer slit. The optical setup used is illustrated in Fig. 2a. To generate a coherent Gaussian beam of wavelength $\lambda_0 = 850$ nm, a single mode fiber coupled laser diode (QPhotonics, QFLD-850-100S-PM, 100 mW) was used. The fiber tip is placed in a $x - y - z$ positioner to align the beam to the optical axis of the set-up and is positioned at the focal plane of a microscope objective used as a beam expander (Newport N-20x, NA = 0.4). The z-position of the microscope objective can be changed with a positioner to control the size of the Gaussian beam, which is perfectly collimated only when the fiber tip is exactly at the focal plane of the microscope objective. In this case, the radius of the Gaussian beam at the output of the microscope objective is $w \approx 1$ mm. The beam is then TM polarized with respect to the grating couplers using a linear polarizer (Thorlabs LPVIS050-MP2) and a $\lambda/2$ waveplate (Thorlabs Achromatic 690-1200 nm). The power of the beam is controlled with a neutral density (ND) filters (Thorlabs NDUV04A) and the $\lambda/2$ waveplate controls the polarization axis of the beam allowing positioning the sample in an arbitrary angle with respect to the optical axis. The beam is then divided into two equal beams to excite both grating couplers simultaneously. This is achieved using beam splitter (BS 1) (Thorlabs 50:50 Non-Polarizing 700-1100 nm). The pair of emerging beams travel along different optical paths, with one of them redirected to BS 2, using Mirrors 3 and 4 mounted on a positioner (Thorlabs Nanomax 300 stage) to precisely control its optical path length. The parameter ΔL represents the change in optical path length applied to one of the beams to produce a phase difference between them. For instance, to achieve a phase difference of $\Delta\phi = \pi$, ΔL must be equal to $\lambda_0/2$. Since both mirrors are mounted on the same stage, the stage only needs to move by $\Delta L/2$, as the configuration doubles the change in optical path length. Although this setup is reminiscent of a Mach-Zehnder Interferometer, the two beams do not overlap at BS 2. Instead, they are directed to a 10x microscope objective (Nikon Plan NA=0.25) which reduces their radius to $w_0 \approx 5$ μm. The size of these beams can be controlled with the beam expander, while the separation between them is adjusted by tilting mirror 3. The two Gaussian beams need to be sized to fill the aperture of the microscope objective to achieve the small beam size required in the focal plane where the gratings are located. This can be done by changing the z position of the beam

expander. However, because the beam is not perfectly collimated, the two beams that travel different optical paths will have a slightly different size after focusing. This difference in size can be reduced by decreasing the optical path length of the beams.

Fig. 2b provides a close-up sketch of the device under test, illustrating excitation of the two grating couplers. This excitation generates SPP waves propagating in opposite directions, which then converge on the gold nanoslit of width w_s. The modes excited in the nanoslit radiate through the substrate of thickness of $t_{sub} = 500$ µm and then trough air, before reaching a 40x microscope objective (Nikon Plan, NA = 0.65). The focal plane of the microscope objective is positioned close to the gold-substrate interface ($d_{det} \approx 0$), to avoid unwanted interference of the detected signal caused by reflections at the substrate-air interface. The magnified radiated intensity is then attenuated with a ND Filter (Thorlabs NDUV05A) and captured with CCD Camera 1 (Thorlabs DCC1645C). Before reaching the camera, the signal is redirected with mirror 6 and split by BS 4. The second beam is directed to a power meter, which is used to determine T. This is defined as the ratio between the power ($P_0 = 51.15$ µm) of the incident Gaussian beam on the grating coupler and the power measured by the power meter (P_m), i.e.

$$T = (1/T_r) * (P_m/P_0), \tag{3}$$

T_r accounts for the transmission losses in the receiver components (as shown in Fig. 3a), which include the 40× microscope objective, mirror 6 and BS 4. The power P_0 was measured immediately after the 10x microscope objective, representing the power incident on the sample with a single Gaussian beam. To determine T_r, the incident power P_0 was compared with the measured power P_m without the sample in place, yielding $T_r = 0.25$. This indicates that only about 25% of the signal radiated from the device reaches the power meter after passing through the microscope objective, reflecting off the mirror, and being split by the 50:50 BS.

The sample must also be illuminated with visible light to locate each device under test and precisely position both Gaussian beams at the center of each grating coupler. This is achieved by introducing broadband light from a fiber illuminator (Thorlabs OSL2IR) via BS 3. The unwanted beams emerging from BS 3 are captured by the beam dump. The illumination beam incident on the microscope objective is focused on and reflected by the sample. The reflected light then travels back through the microscope objective, the two BS and a ND filter (Thorlabs NDUV03A) to CCD Camera 2 (Thorlabs DCC1645C). The imaged devices, including the incident Gaussian beams, are displayed on a screen connected to the camera. Additional mirrors (mirror 1, 2, 6 and 7) are placed at different locations in the set-up to redirect the light beams as required. The 850 nm laser source can be replaced with a broadband illuminator (NKT Photonics, Super K Extreme) to find the transmission spectra of the devices, as discussed in Section 3.1. For this purpose, the power meter is replaced with an optical spectrometer (Newport OSM2-400VIS/NIR). All images obtained from CCD1 and CCD2 are presented as captured with no false colouring applied.

4. Break-Out Elements

Modifying the properties of the grating couplers, arm length and slit width influences $\boldsymbol{T}$ of the device and enables the tuning of the interference pattern observed on the substrate side of the nanoslit [37, 38]. Consequently, it is essential to experimentally investigate how variations in the parameters of these individual elements (break-out elements) affect the system. Since the interference of SPPs is not required for analysing these elements, we illuminated one grating coupler only, which excites a single SPP. This approach allows us to isolate and study the contributions of each element independently.

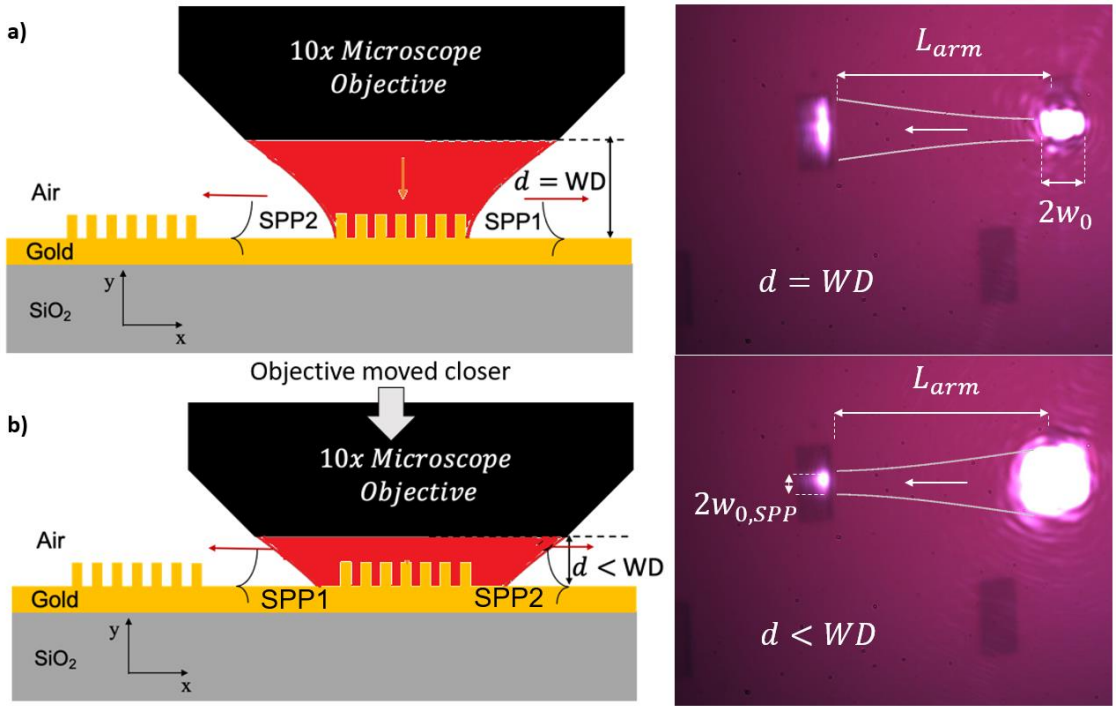

Figure 3. Observation of a SPP wave excited with an optimized grating coupler, traveling certain distance, and outcoupled by the second grating. a) Left panel - microscope objective placed at a separation from the grating equal to its working distance (d = WD) such that the Gaussian beam waist w_0 is located at the grating coupler. Right panel - SPP waves excited by the grating diverge in the plane of propagation, as observed from the spot uncoupled by the second grating which is wider than the incident spot ($2w_{0,SPP} > 2w_0$). b) Left panel - microscope objective placed a few micrometers closer to the sample (d < WD) such that the Gaussian beam is converging at the location of the grating coupler. Right panel – the convergence of the Gaussian beam induces focusing of the SPP wave in the plane of propagation, as observed from the spot uncoupled by the second grating which is narrower than the incident spot ($2w_{0,SPP} < 2w_0$).

4.1 Grating Couplers – Focusing of SPPs

We initially investigated the ability of a grating coupler to excite focused SPPs by exciting a grating coupler with a converging Gaussian beam of wavelength $\lambda_0 = 850$ nm and radius $w \approx 5$ µm. For these experiments, a pair of grating couplers with optimized parameters (height $h = 54$ nm, pitch $\Lambda = 786$ nm, duty cycle $dc = 0.68$ and 12 periods), were defined and separated by a distance of $L_{arm} = 40$ µm, as sketched in Fig. 1a. One of the gratings was used to in-couple SPP waves at the air-gold interface, and the second one to out-couple them. By changing the distance d of the sample from the 10x microscope objective (*cf.* Fig. 2a), the size of the Gaussian beam exciting the grating coupler can be modified; this is illustrated in Fig. 3. When the objective is placed at its working distance from the sample ($d = WD$), the Gaussian beam illuminates the grating having its waist at the grating plane ($2w_0$ in diameter). In this case, the SPP wave diverges along the air-gold interface in the plane of propagation, and once it reaches the second grating, it is out-coupled with a larger width than the incident beam ($2w_{0,SPP} > 2w_0$), as shown in Fig. 3a. Alternatively, if the sample is placed closer to the objective ($d < WD$), as shown in Fig. 3b, the Gaussian beam impinges onto

the grating while it is still converging, resulting in a SPP wave that focuses as it propagates along the air-gold interface. In this case, the second grating out-couples the SPP wave with a smaller width than the exciting beam ($2w_{0,SPP} < 2w_0$). In this manner the SPP beam waist $w_{0,SPP}$ (SPP focus) can be placed on the out-coupling grating, as shown in Fig. 3b, or on any other feature on the chip. This method of tuning the SPP beam diameter is useful for controlling the size of the plasmonic waves that excite the resonant modes of the nanoslit and improves the visibility on the detection camera in the interferometric experiments discussed in Section 5. These experiments provide a qualitative demonstration of the (out-)coupling and existence of SPP waves by observing the reflection in CCD Camera 2 (*cf*. Fig. 2a). Henceforth, experiments are conducted to observe and measure the fields radiated from the nanoslit on the substrate side of the device with the transmission recorded by CCD Camera 1 and the optical power meter or spectrometer (*cf*. Fig. 2a).

4.2 Grating Couplers – Spectral Response, Pitch and Number of Periods

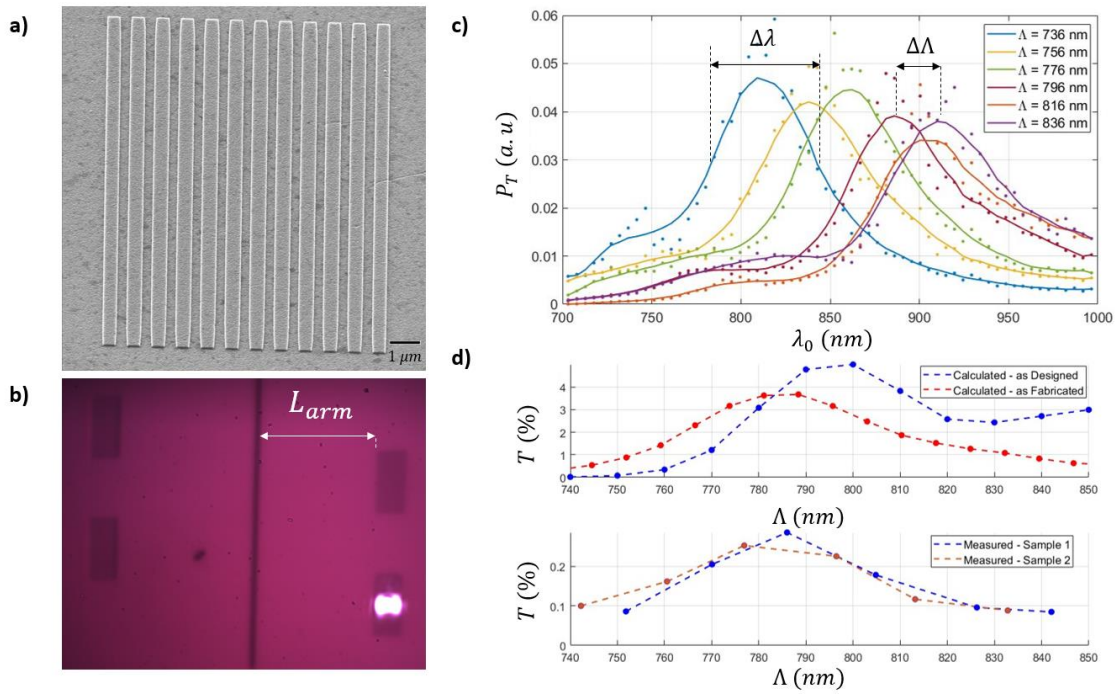

Figure 4. Grating spectral response and pitch variation. (a) SEM image of a grating coupler ($\Lambda = 796$ nm and $dc = 0.68$). (b) Reflected image showing a device under test, captured in situ using CCD Camera 2. This set of grating couplers is arranged along the length of the nanoslit of width $w_s = 610$ nm. The grating pitches vary from $\Lambda = 736$ nm to $\Lambda = 836$ nm, and the duty cycle is set to $dc = 0.68$. The bottom right grating is excited with a Gaussian beam of radius $w \approx 5$ μm centered on the grating. (c) Wavelength response of the transmitted power P_T of the gratings and nanoslit combination, excited with broadband light and measured using a spectrometer. Note that P_T is presented in arbitrary units, as it was not possible to accurately determine the power of the input beam during the measurements. When the pitch of the grating increases, the wavelength of maximum transmittance increases proportionally. (d) T, of gratings excited with a laser centered at $\lambda_0 = 850$ nm, for gratings of various pitch, Λ . The top panel shows the calculated results of the designed (blue curve) and as-fabricated (red curve) gratings. The bottom panel shows the experimental results for two samples each bearing several gratings, demonstrating a similar trend with pitch compared to the calculations.

The design process to optimize the grating couplers is similar to that applied in previous work [37, 38]. The parameters to optimize are the ridge height h, pitch Λ, duty cycle dc, and number of ridges (Fig. 1a). The height of the ridges is defined by thermal evaporation after e-beam lithography exposure. The ridge height achieved for all devices is $h = 54$ nm which is close to the value of $h = 60$ nm ideally needed for maximum coupling efficiency. During the designing process, the duty cycle was fixed to $dc = 0.5$, and the duty cycle achieved in all devices after fabrication is $dc = 0.68$, as can be observed in Fig. 4a, where a grating coupler of pitch $\Lambda = 796$ nm is shown - the ridges are slightly wider than the trenches.

This section explores the effects on the transmitted light on devices composed of one grating separated from a nanoslit by $L_{arm} = 40$ μm, when the grating pitch Λ and number of ridges are varied. The gratings were designed for a normally-incident TM polarized Gaussian beam of wavelength $\lambda_0 = 850$ nm and beam waist radius of $w_0 = 5$ μm. The maximum coupling efficiency of the designed grating occurs for a pitch of $\Lambda = 800$ nm, composed of 12 periods. Under these conditions, the size of the grating coupler is very close to the diameter of the incident Gaussian beam. The designs were comprised of a range of pitches from $\Lambda = 736$ nm to $\Lambda = 836$ nm in steps of $\Delta\Lambda = 10$ nm. Fig. 4b shows the device used for the pitch experiments. It comprises of a linear arrangement of grating couplers on a gold film of thickness $t_{Au} = 311$ nm, positioned a distance of $L_{arm} = 40$ μm from a nanoslit of width $w_s = 610$ nm milled into the gold film.

The grating couplers were initially excited with a Gaussian beam, as previously described, generated from a broadband source. To obtain the spectrum of the transmitted power P_T for each grating coupler and nanoslit combination, the output signal radiated by the nanoslit was measured using a spectrometer. This is illustrated in Fig. 4c. Although the grating pitch varies in increments of $\Delta\Lambda = 10$ nm, we present the results every $\Delta\Lambda = 20$ nm to maintain clarity and prevent graph saturation. Due to the high power of the incident broadband source, the spectrometer became saturated, requiring the use of ND filters to accurately capture the source spectrum. P_T was calculated by comparing the source spectrum with the measured spectrum radiated by the nanoslit for different grating pitches, which did not require attenuation. Since the accurate power measurements for the incident broadband source were not obtained, P_T is presented in arbitrary units. Despite this, as shown in Fig. 4c, the spectra exhibit a full width at half maximum (FWHM) of approximately, $\Delta\lambda \approx 100$ nm for all grating pitches, and the peak transmittance shifts linearly with increasing grating pitch, as expected.

Replacing the broadband illuminator with at laser source at $\lambda_0 = 850$ nm, the incident power of the Gaussian beam ($P_0 = 224$ μW) can be compared to the transmitted power to obtain T for each pitch Λ, The top panel of Fig. 4d shows the calculated T for the designed and fabricated cases, calculated using:

$$T = \frac{1}{P_0}\int_0^{100\mu m} Re\{S\}\, dx\,, \tag{4}$$

where, $P_0 = 1\ W/m$ is the 2D power of the Gaussian beam exciting the grating coupler. S represents the Poynting vector that characterizes the intensity distribution at a distance $d_{det} = 4$ μm below the gold-substrate interface. The calculated maximum T of the fabricated device decreases by 49% with respect to the design because the grating ridges are thinner than expected ($h = 54$ nm, instead of the desired $h = 60$ nm), and the duty cycle is larger than expected ($dc = 0.68$ instead of $dc = 0.5$). The maximum T occurs at a pitch of $\Lambda = 800$ nm $\approx \lambda_{eff} = 835$ nm (Eq. 2) for the designed case, and $\Lambda = 786$ nm for the fabricated case.

The bottom panel of Fig. 4d shows the experimental T obtained using Eq. (3) for two samples bearing devices. The maximum T of the tested devices occurs for $\Lambda = 786$ nm, which is very close to theoretical expectations (1.75%). However, the experimental T is ~10% of the calculated values

because of non-idealities in the experimental case, which include: (i) roughness of the gold layer ($R_q = 5.24$ nm) and grating ridges ($R_q = 5.58$ nm) characterized by the root mean square value R_q of the height variations on the surfaces, (ii) reflections occurring at the glass-air interface along the bottom of the substrate (unaccounted for theoretically), which cause additional losses; (iii) deviations in the grating coupler thickness due to fabrication limitations, which reduce coupling efficiency; (iv) variations in the pitch and duty cycle of the gratings caused by defocusing effects during E-beam lithography, leading to non-ideal grating structures; and (v) 2D calculations using a 1D Gaussian beam, which approximates the 3D nature of the system and overestimates slightly the power coupled by the gratings. These factors collectively explain the differences in transmittance observed across all measurements, such that the experimental T is ~10% of the calculated values for all tested structures. Despite the reduced experimental T relative to design, the output from the device is readily detected using a standard CCD camera, power meter, and spectrometer.

Aligning the center of the Gaussian beam to the center of the grating coupler is essential if meaningful comparisons are to be made with the computations. With centered alignment, the power of the excited SPP waves is equal in both directions of propagation (left and right), whereas if the beam is aligned off-center close to the edge of a grating coupler, one SPP wave is preferentially excited along one direction. For this set of grating coupler experiments, it is particularly important to achieve centered alignment because it was observed that the wavelength of maximum transmission of the grating varies with the position of the Gaussian beam relative to the grating. Centered alignment was achieved by visualizing the reflected beam with CCD Camera 1 and optimizing the alignment. Fig. 4b illustrates a case where the Gaussian beam is placed at the center of the grating coupler, whereas Fig. 5b shows a case where the beam is aligned near the left edge of the grating.

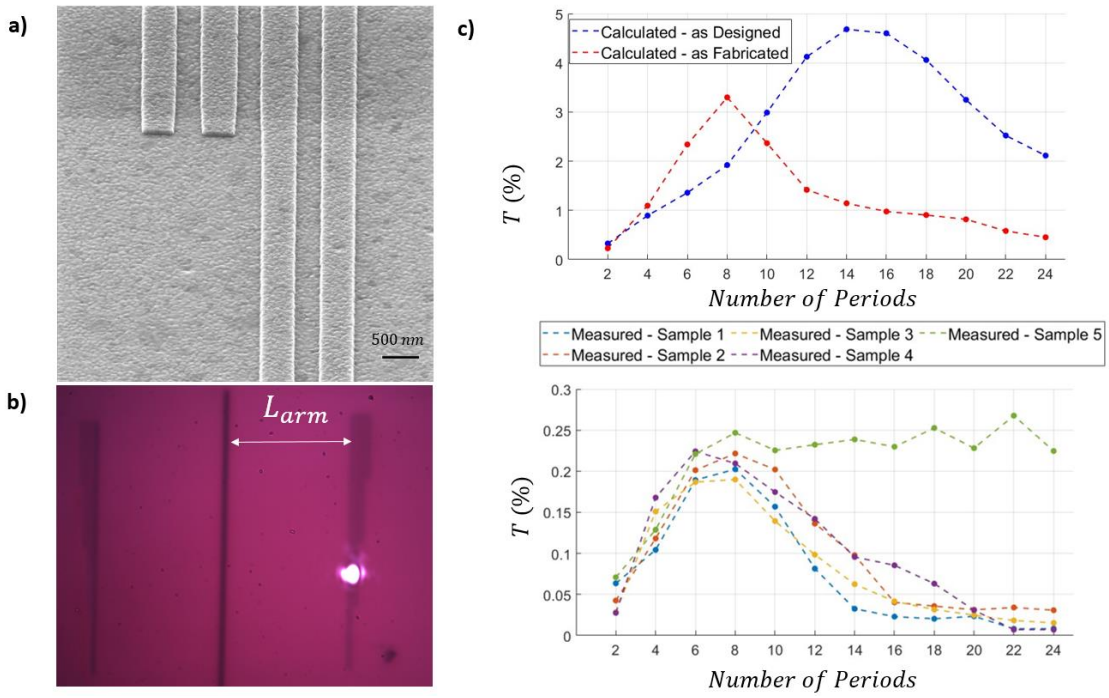

Figure 5. The effect of variation in grating period. (a) SEM image of a section of the sample showing an increase in the number of periods from 2 to 4. (b) Reflected image showing a device under test. This set of grating couplers is arranged along the length of a nanoslit of width $w_s = 610$ nm. The grating periods vary from 2 to 24. A grating coupler is excited with a Gaussian beam of radius $w_0 \approx 5$ µm, aligned at the edge of the grating. (c) The top panel shows the calculated T as a function of the number of grating periods, for designed (blue curve) and fabricated (red curve) gratings, yielding an optimal number of periods of 14 and 8 respectively. The bottom panel presents measured results obtained on 5 samples, demonstrating very similar trends to the calculated case. Sample 5 was tested by aligning the center of the Gaussian beam along the edge of a grating, rather than along its center, thereby maximizing the coupling efficiency of SPPs propagating in the direction of the nanoslit. With this alignment along the edge, T remains constant as the number of periods increases beyond 8.

In addition to the grating pitch Λ variation, another important design parameter of the grating couplers is the number of periods n_g. Fig. 5a shows a SEM image of a section of the experiment where the number of ridges in a grating increase from 2 to 4. Five identical samples were fabricated, each of them consisting of a series of 3 gratings that increase in number of ridges in steps of two. In Fig. 5b, a section of a sample is shown where a Gaussian beam of waist radius $w_0 \approx 5\ \mu m$ excites the left edge of a grating coupler. With this alignment, the SPP wave is preferentially excited to the left (towards the nanoslit). All the samples were tested with the beam centered on the grating except for one case - Sample 5. Fig. 5c shows T as the number of ridges increases. The top panel shows calculations for the designed (blue curve) and fabricated (red curve) cases. In the designed case, the number of periods that maximizes the T is $n_g = 14$. However, for the fabricated case, the maximum T decreases by $\approx 42.86\%$ and the optimal number of periods is $n_g = 8$. This finding is experimentally corroborated, as can be observed in the bottom panel of Fig. 5c. Samples 1 to 4 exhibit the same behavior, confirming the calculated prediction. Sample 5 was excited with the Gaussian beam aligned to the left edge of the grating couplers (nearest the nanoslit). In this case, the maximum T remains constant after the optimal number of ridges is reached.

To achieve maximum coupling of SPPs propagating along one direction from a grating under normal incidence, it is necessary to illuminate the edge. With this approach, the grating coupler will always perform optimally once the optimal number of periods is reached. Conversely, if it is necessary to excite SPPs in both directions of propagation, the best strategy is to illuminate the grating with a beam centered on the grating. In this scenario, it is crucial to use the optimal number of periods such that the grating coupler matches the size of the incident Gaussian beam. This minimizes the outcoupling effect that a large grating induces and maximizes the efficiency of the grating coupler.

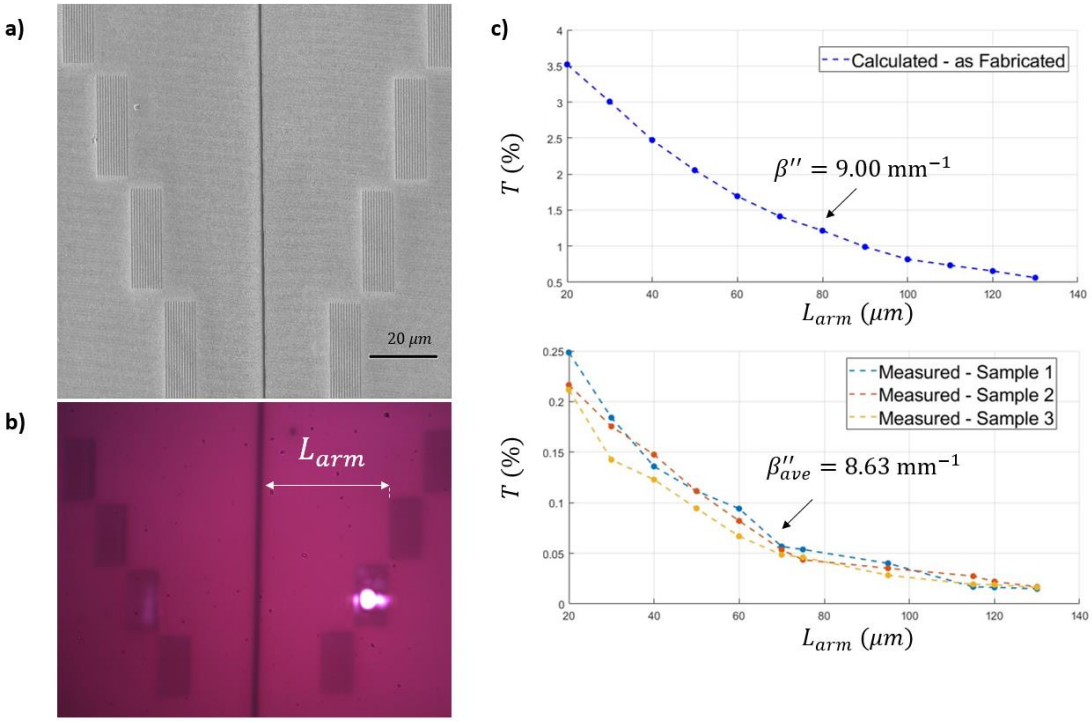

Figure 6. Cut-back measurements. The distance between the grating and the nanoslit of width w_s = 610 nm (arm length) varies from L_{arm} = 20 to 130 μm. (a) SEM image of one of the samples comprised of a linear arrangement of grating couplers along the vertical direction, each grating having a different distance from the nanoslit. (b) Reflected image showing a device under test. A grating coupler is excited with a Gaussian beam of radius $w_0 \approx$ 5 μm, aligned near the left edge of the grating. (c), T, for different arm lengths, L_{arm}. The top panel shows the calculated T as function of L_{arm} for the simulated case. The attenuation constant can be obtained from an exponential fit of the transmittance curve and is $\beta'' = 9.00\ \mathrm{mm}^{-1}$, which varies by 6% from the analytical calculation. The bottom panel shows a set of experiments on three samples demonstrating a very similar trend to the calculated cases. The average decay constant obtained experimentally is $\beta''_{ave} = 8.63\ \mathrm{mm}^{-1}$, which differs by 1.64% from the analytical calculation.

4.3 Cut Back Measurements

The length of the interferometer arm (L_{arm}) is the distance that the SPP waves must travel to reach the nanoslit. This distance must not significantly exceed the SPP propagation length L_p. Considering a power decay of $1/e$ from the excitation location of the SPP wave at the edge of the grating, L_p can be calculated as [1]:

$$L_p = \frac{1}{2\mathrm{Im}(\beta)}, \tag{5}$$

where,

$$\beta = \beta' + i\beta'' = \frac{2\pi}{\lambda_0} n_{eff}, \tag{6}$$

is the propagation constant of the SPP wave. β is a complex number, and its real part β' is the phase constant, whereas the imaginary part $\beta'' = 8.49\ \text{mm}^{-1}$ is the attenuation constant. For an SPP wave traveling along a gold-air interface at $\lambda_0 = 850$ nm, the propagation length is $L_p = 61.5$ µm, using Eqs. (1)-(6). At this distance, the power carried by the wave is 36.8% of its initial value.

In our experiments the arm length was varied from $L_{arm} = 20$ to 130 µm. Fig. 6a shows a SEM image of a portion of a sample under test, which comprises of a linear arrangement of grating couplers along the vertical direction, each grating having a different distance from the nanoslit. In this experiment, a Gaussian beam of radius of $w_0 \approx 5$ µm excites a SPP wave via an optimized grating coupler ($h = 54$ µm, $\Lambda = 786$ nm, $dc = 0.68$, and $n_g = 12$ periods), as shown in Fig. 6b. After propagating over L_{arm}, the SPP wave excites the gold nanoslit of width $w_s = 610$ nm, exciting resonant modes therein, resulting in radiated fields detected on the substrate side. Calculated T (using Eq. (4)), for different arm lengths is shown in the top panel of Fig. 6c. The power carried by the SPP wave decays exponentially when the arm length is increased. At a fixed wavelength of operation, $\lambda_0 = 850$ nm, the attenuation constant β'' depends only on the relative permittivity of the materials used and is estimated to be $9.00\ \text{mm}^{-1}$from an exponential fit. This value is 6% larger than that calculated using Eqs. (1)-(6). Measured T of devices of different arm length L_{arm} on three samples is shown in the bottom panel of Fig. 6c. They exhibit the same exponential trend consistent with the computations. The average attenuation coefficient obtained experimentally is $\beta''_{ave} = 8.63\ \text{mm}^{-1}$ and this value is 1.64% smaller than the value estimated using Eqs. (1)-(6). The experimental attenuation coefficient (Fig. 6c, bottom panel) is closer to the analytical result than the one determined by simulating the entire system (Fig. 6c, top panel) possibly due to limitations in discretizing the system.

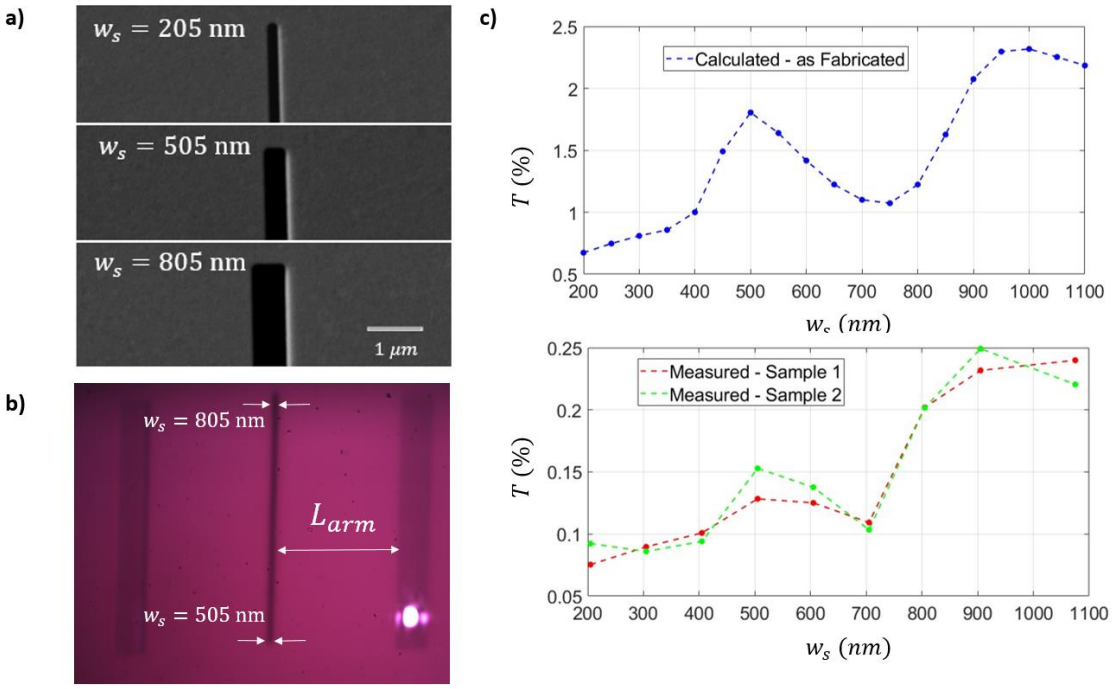

Figure 7. The effect of varying the width of the nanoslit. a) SEM image of nanoslits of different widths $w_s = 205, 505$ and 805 nm milled via FIB in a gold layer of thickness $t_{Au} = 311$ nm on a fused silica substrate. b) Reflected image showing a device under test. The nanoslit is excited by a single SPP wave launched from a grating. The width of the nanoslit achieved after fabrication decreases linearly along the length of the slit from $w_s = 1075$ to 205 nm (top to bottom), and the grating couplers are uniform over the entire length of the slit. The left grating coupler is excited with a Gaussian beam of radius $w_0 \approx 5$ μm, aligned near the left edge of the grating. c) T for different slit widths w_s is computed (top panel) and measured on two samples (bottom panel).

4.4 Nanoslit Width

Previous studies have shown that the resonance modes in a nanoslit are highly sensitive to variations in the slit width w_s [37, 38]. The slit width affects both T and the radiation pattern and consequently has implications on the performance of the device. Nanoslits of different widths were fabricated in a gold film deposited on a fused silica substrate via FIB milling. Fig. 7a shows a SEM image of three nanoslits of different widths ($w_s = 205, 505\ and\ 805$ nm). The fabricated test samples feature a 3-segment nanoslit that exhibits a variable width along its length. Each of the 3 segments is 80 μm long. The nanoslit width varies linearly from at $w_s = 205$ nm to $w_s = 505$ nm in segment 1, from $w_s = 505$ nm to $w_s = 805$ nm in segment 2, and from $w_s = 805$ nm to $w_s = 1{,}075$ nm in segment 3. This segmentation was necessary due to the limitations of the focused ion beam (FIB) milling process. Optimized grating couplers were fabricated alongside the nanoslit ($h = 54$ nm, $\Lambda = 786$ nm, $dc = 0.68$, and $n_g = 12$ periods), at a distance of $L_{arm} = 40$ μm from the nanoslit, and excited with a TM polarized Gaussian beam of wavelength $\lambda_0 = 850$ nm and radius $w_0 \approx 5$ μm to excite a single SPP wave, that then propagates to the nanoslit exciting resonant modes therein. Depending on the width of the slit, the modes exhibit different spatial field distributions, which are described below, producing characteristic radiation patterns. Fig. 7b shows an image captured with CCD Camera 2, showing the implementation of this experiment. The Gaussian beam was positioned vertically along a grating to access a nanoslit region of different width.

Top panel of Fig. 7c shows the calculated T (using Eq. (4)), as a function of the slit width w_s for the calculated device. Interestingly, note that T peaks when the slit width increases from $w_s \approx 200$ nm to $w_s \approx 500$ nm. Recall that only the dipolar resonance is supported by the nanoslit over this range of widths (Fig. 1c, left panel). Beyond $w_s \approx 500$ nm, the quadrupolar mode (Fig. 1c, center panel) is also supported, and the transmission decreases, reaching a minimum when the slit width is approximately $w_s \approx 750$ nm. This behavior is somewhat counterintuitive because normally, as an optical aperture increases in size, the transmitted power increases as well – but this occurs for direct illumination of an aperture, which is not the case here. Rather the aperture (nanoslit) in our case is excited by a propagating SPP which excites resonant modes therein with different weights depending on field overlaps. Thus, beyond $w_s \approx 500$ nm a linear combination of resonant modes is excited which interfere in the nanoslit, altering the radiation pattern and power radiated therefrom. If the slit width is increased beyond $w_s \approx 750$ nm, the T increases again, and a hexapolar mode is excited (Fig. 1c, right panel). This phenomenon is corroborated experimentally, as shown in the bottom panel of Fig. 7c. The experimental results demonstrate that T decreases similarly, mirroring the behavior observed in the calculated case. This consistency between experimental and theoretical results provides robust evidence of the first experimental demonstration of multimode excitation in a nanoslit.

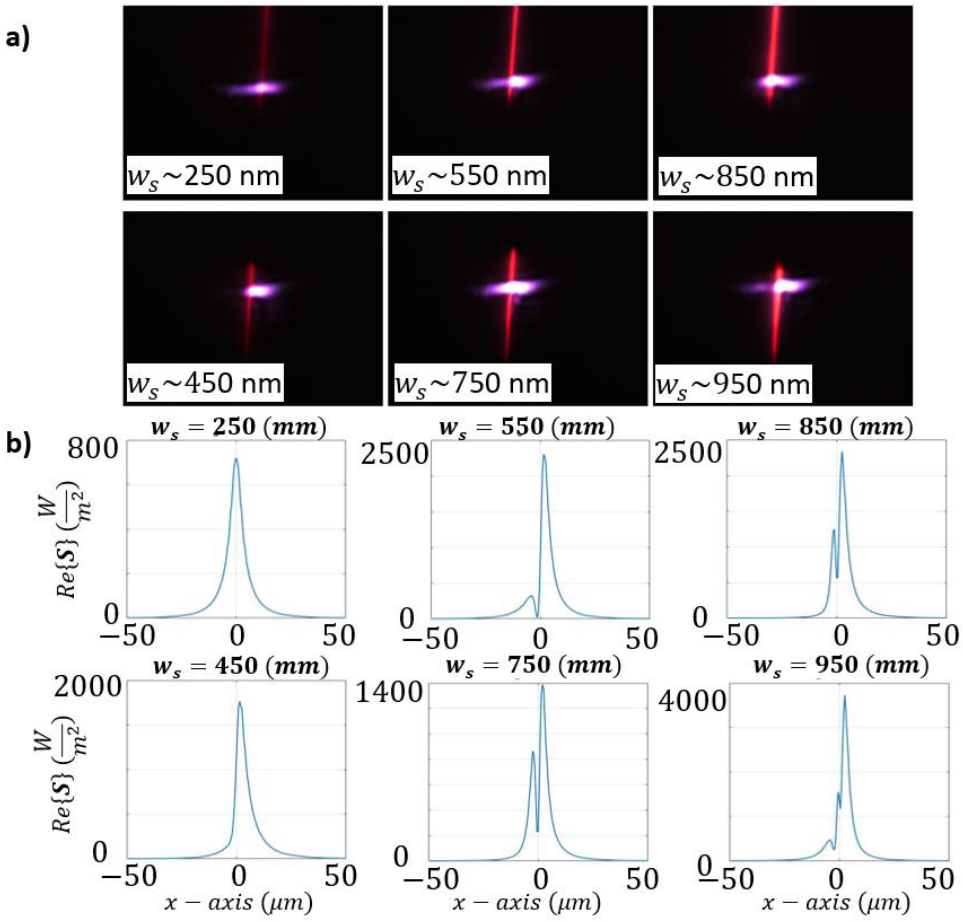

Figure 8. Experimental and theoretical demonstration of multimode excitation in nanoslits in a gold film, for widths ranging from w_s~250 to 950 nm. (a) Experimental visualization of the intensity distribution radiated by nanoslits in the gold film of different widths w_s. The intensity is imaged with a 40x (NA = 0.6) objective whose focal plane is positioned very close to the gold-substrate interface. (b) Calculated distribution of the magnitude of the Poynting vector, 4 μm below nanoslits of different width w_s. As the nanoslit width increases, an increasing number of resonant modes become supported therein. For w_s~250 and 450 nm, the nanoslit supports only the dipolar mode, resulting in a single-lobed radiation pattern. For $w_s \approx 550, 750$ and 850 nm, the dipolar and quadrupolar modes are supported, resulting in a two-lobed radiation pattern. For $w_s \approx 950$ nm, a third lobe appears in the radiated signal, suggesting that a hexapolar mode is supported by nanoslits of this width. The experimental images in (a) match qualitatively with the calculated distributions in (b).

We investigate the multimode operation of the nanoslits in the gold film by imaging the intensity radiated by the nanoslits through the substrate with the receiver microscope objective and CCD Camera 1 (*cf*. Fig. 2a). The focal plane of this objective was positioned very close to the gold-substrate interface to magnify the nanoslit. The imaging process is visual, allowing for a few micrometers of tolerance in the receiver position where the slit appears well-defined. Once the nanoslit is imaged in the substrate side, the grating coupler on the top side is excited by the Gaussian beam to launch an SPP toward the nanoslit (*cf*. Fig. 7b). Images of the radiation emitted by nanoslits of various widths w_s, under SPP excitation, are shown in Fig.

8a, revealing different spatial distributions for different nanoslit widths w_s. The orange/red colour band in the images are due to the nanoslit illuminated by a broadband illuminator to make it clearly visible, whereas the bright localised spots correspond to the out-coupled surface plasmon waves generated by the monochromatic laser (850 nm). For a slit width of $w_s \approx 250$ nm, a symmetrical radiation pattern exhibiting a single lobe is observed, suggesting that only the dipolar resonant mode of the nanoslit is supported (*cf.* Fig. 1c, left panel). As the slit width increases to $w_s \approx 450$ nm, the radiation pattern loses its symmetry, and the intensity maximum shifts away from the center of the nanoslit. For a slit width of $w_s \approx 550$ nm a second lobe becomes observable and persists up to $w_s \approx 750$ and 850 nm, consistent with the emergence of the quadrupolar mode in the nanoslit. One lobe is less intense than the other because the nanoslit is excited by a single SPP wave (launched from the right grating and propagating towards the left – *cf.* Fig. 7b). Perfect symmetry in the two radiated lobes is only achieved when the nanoslit is excited by two identical counterpropagating SPP waves that are out of phase, thereby exciting the quadrupolar mode only (*cf.* Fig. 1c, right panel), as demonstrated in the interference experiments discussed in the next section. For a slit width of $w_s \approx 950$ nm the radiation pattern becomes more complex, suggesting the emergence of a third resonant mode. For the slit width $w_s \approx 950$ nm, the radiated signal suggests a three-lobe distribution which we associate with the hexapole predicted in Section 2. Fig. 8b plots the calculated distribution of the magnitude of the Poynting vector, at a distance of $d_{det} = 4$ μm below the gold-substrate interface. The Poynting vector was calculated by exciting a single grating coupler in the simulation with a Gaussian beam of power $P_0 = 1$ W/m (2D simulation), which was coupled to SPP waves and radiated by the nanoslit. The transition in the number of lobes observed experimentally matches qualitatively the calculations, corroborating our observation of multimode excitation of nanoslits.

5. Interference of SPP Waves on Multimode Nanoslits

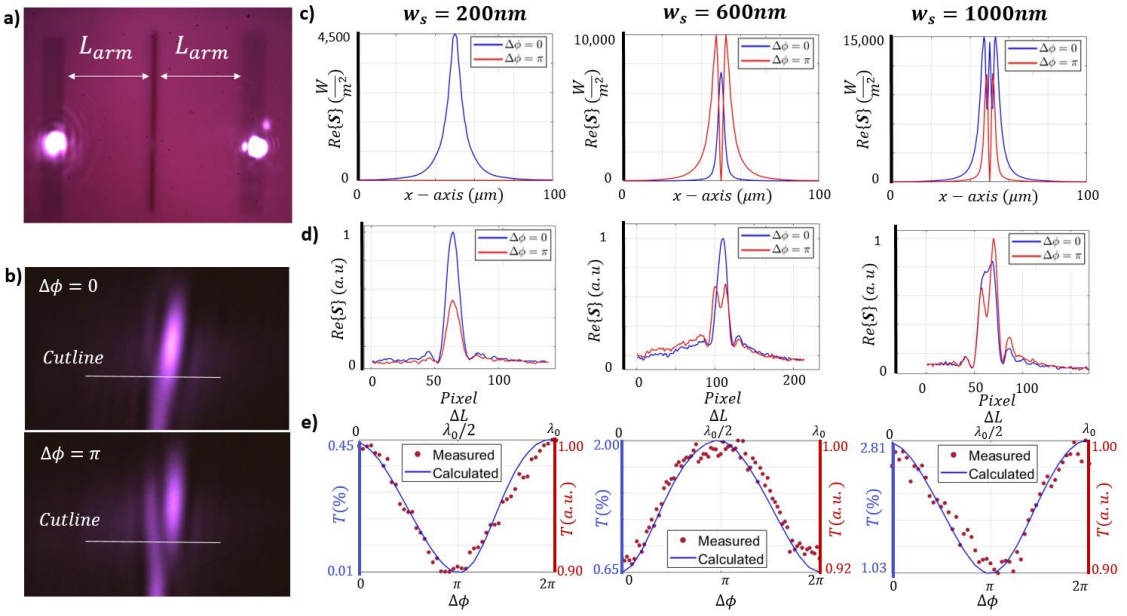

Figure 9. Experimental and theoretical demonstration of selective modal excitation in a multimode nanoslit by the interference of SPP waves. (a) Simultaneous excitation of a pair of grating couplers by Gaussian beams, producing a pair of SPP waves traveling in opposite directions and interfering on the gold nanoslit. (b) The intensity distribution radiated by a nanoslit of width w_s~600 nm through the substrate, imaged at a distance of $d_{det} \approx 4$ μm. For $w_s \approx 600$ nm, the dipolar and quadrupolar modes of the nanoslit are

selectively excited when the phase difference between the interfering SPP waves is $\Delta\phi = 0$ (top panel) and $\Delta\phi = \pi$ (bottom panel). (c) Calculated distribution of the magnitude of the Poynting vector, 4 μm below nanoslits of different width, $w_s = 200,\ 600, \text{and } 1000$ nm. The nanoslits are excited by a pair of SPP waves of phase difference $\Delta\phi = 0$ and π. The nanoslit can support the dipolar, quadrupolar and hexapolar modes depending on the phase difference $\Delta\phi$ between the interfering SPP waves and the nanoslit width w_s. (d) Horizontal cut of the measured intensity distribution radiated below nanoslits of different width, captured by a $40\times$ (NA $= 0.6$) objective and a CCD camera. (e) T obtained by integrating the calculated (blue curve) and measured (red dots) intensity radiated by the nanoslits as a function of the phase difference between the interfering SPP waves over the range $\Delta\phi = 0$ to 2π, yielding the periodic transfer characteristic of the interferometer.

Finally, we investigate the interference of SPP waves on nanoslits and the selective excitation of resonances therein. The number of resonant modes is determined by the nanoslit width w_s, and their selective excitation by the phase difference $\Delta\phi$ between the two SPP waves exciting the nanoslit. For interference of two SPP waves, grating couplers on either side of a nanoslit are excited by a pair of coherent Gaussian beams, with their relative phase adjusted by varying the optical path length, as described in Section 2. Fig. 9a shows an image, where a device under test is illuminated by two beams of radii $w_0 \approx 5$ μm. Both Gaussian beams must have the same size and power to interfere strongly at the nanoslit. However, there is always a small difference in the size of the Gaussian beams because they are focused by the 10x objective illuminated by non-collimated Gaussian beams which travel two different optical paths and are slightly off the optical axis. To match the size of both SPP waves as closely as possible at the nanoslit it is necessary to adjust the z position of the beam expander, shown in Fig. 2a. At the same time, matching the power of the two SPP waves is straightforward: by misaligning one of the beams at its corresponding grating coupler and reducing its power until it matches that of the second beam.

The phase of one of the SPP waves is shifted by adjusting the position of mirrors 3 and 4 in the optical setup shown in Fig. 2a, with a mechanical stage controlled by a piezoelectric actuator. This stage moves in steps of≈ 6 nm, and needs to be shifted $\Delta L = \lambda_0/8 \approx 107$ nm to change the relative phase between both SPP waves by $\Delta\phi = \pi$. Fig. 9b shows the intensity radiated from a nanoslit of width $w_s \approx 600$ nm, through the substrate, associated with the dipolar (top panel) and quadrupolar (bottom panel) resonant modes, when the relative phase difference $\Delta\phi$ between the SPP waves is $\Delta\phi = 0$ and $\Delta\phi = \pi$. The dipolar mode is characterized by a single radiated lobe, whereas the quadrupolar mode exhibits a pair of radiated lobes. Due to the imperfect collimation of the initial beam, the two SPP waves do not overlap precisely, resulting in an interference pattern with unequal sized lobes.

The calculated intensity distributions, defined by the real part of the normalized Poynting vectors $Re\{\boldsymbol{S}\}$, are plotted in Fig. 9c for different nanoslit widths, $w_s \approx 200,\ 600$ and 1000 nm. For $w_s \approx 200$ nm, only the dipolar resonant mode is supported by the nanoslit and the radiated intensity exhibits a centered lobe whose amplitude varies with $\Delta\phi$ to become null for $\Delta\phi = \pi$, as observed from Fig. 9c (left panel). This is corroborated experimentally in Fig. 9d (left panel), although noise, likely due background light, decreases the signal visibility. For $w_s \approx 600$ nm, the dipolar mode is excited for $\Delta\phi = 0$ and the quadrupolar mode is excited for $\Delta\phi = \pi$, and the intensity distribution transitions from a single lobe to a pair of equally sized lobes, as observed from Fig. 9c (center panel). This is also confirmed experimentally in the corresponding plot of Fig. 9d (center panel). For $w_s \approx 1000$ nm, simulations indicate the generation of a third lobe in the radiated field intensity distribution, due the excitation of a hexapolar mode for $\Delta\phi = 0$, as shown in Fig. 9c (right panel). The corresponding experimental result in this case does not agree very well with the computations because the numerical aperture of the objective limits resolution of three lobes. It is important to note that the experimental curves in Fig. 9d are normalized to their maximum value, as these intensity distributions are computed by analyzing a 2D line of the observed modes, where the intensity is related to the intensity of each pixel. This makes it difficult to determine the real values

of the Poynting vector and the actual size of the lobes, which is why the curves are normalized and shown in arbitrary units. However, because the patterns were measured as close as possible to the slit, we expect the lobe sizes to be comparable to those calculated in Fig. 9c.

Integrating the intensity distribution yields the transmittance of the interferometer. These values were calculated as a function of $\Delta\phi$ and are plotted in Fig. 9e, showing the transfer characteristics of the system for each case of nanoslit width w_s. The calculated results (blue curves) agree very well with the experimental values (red dots). In this case, integrating the intensity provides the power at the output, as was done in all the previous experiments. However, for the current scenario, the input power exciting the interferometer, P_0, consists of two Gaussian beams with $P_0 = 1\ W/m$. T is therefore calculated by integrating the intensity distributions of Fig. 9c and comparing it with this total input power. Specifically, T is calculated with E. (4), however, this time $P_0 = 2W/m$, because it accounts for the power two Gaussian beams. This is done for phase differences from $\Delta\phi = 0$ to $\Delta\phi = 2\pi$. These phase differences correspond to changes in the arm length of the interferometer, from $\Delta L = 0$ to $\Delta L = \lambda_{eff}/2$. This is presented in Fig. 9e as the blue curve, with the transmittance scale on the left side of the figure.

On the experimental side, the measurements were performed using the same method explained earlier, where the 2D intensity distributions were captured along a cutline. After integrating for each $\Delta\phi$ (red points), the values of T were normalized to their maximum value and are shown on the right y-axis of Fig. 9e. This was done for all three slit widths. In the experiments visibility is significantly reduced, likely due to dark noise and low coherence of the light source. However, when the theoretical curve is plotted alongside the experimental data, we observe a strong overlap, confirming the periodic behavior of the interferometer as a function of the relative phase difference between the SPP waves $\Delta\phi$.

6 Conclusions

In this study, we present a comprehensive theoretical and experimental analysis of the controlled interference of two counterpropagating SPP waves in a multimode gold nanoslit structure. The SPP waves were generated by exciting grating couplers positioned symmetrically on either side of the nanoslit, each using a Gaussian beam. We demonstrate the ability to precisely modulate the interference pattern by altering the geometrical parameters of the gold nanoslit, enabling the selective excitation of one, two or more resonance modes at the slit. Our theoretical predictions on how the transmitted pattern depends on various geometrical factors—such as grating coupler pitch, height, duty cycle, and nanoslit dimensions—were in good agreement with experimental results. This novel approach for manipulating multimodal resonances in nanoslits offers significant potential for precision applications. The capability to tailor mode excitation opens new possibilities in optical sensing and biosensing, where heightened sensitivity and multiplex detection are essential. Furthermore, the interferometer design developed here could be integrated into photonic circuits, providing scalable solutions for miniaturized optical devices. These advancements hold great promise for applications such as environmental monitoring, medical diagnostics, and next-generation wearable technologies, including smart watches and mobile devices.

Author contributions

We strongly encourage authors to include author contributions and recommend using CRediT for standardised contribution descriptions. Please refer to our general author guidelines for more information about authorship.

Conflicts of interest. There are no conflicts to declare.

Data availability. Data for this article, including codes, simulated data and experimental data are available at: **https://www.scidb.cn/en/s/UjUzue**

Acknowledgements. Funding provided by the Natural Sciences and Engineering Research Council of Canada, grant number 210396, CONAHCYT National System of Researchers (SNI 1047863), Federico Baur Endowed Chair in Nanotechnology (ILST002-23ID69001), Graduate Seed Program of Tecnológico de Monterrey, CONAHCYT (CVU 900707) are gratefully acknowledged.

References:

[1] Maier, Stefan A. Plasmonics: fundamentals and applications. Vol. 1. New York: springer, 2007.
[2] Zhang, Junxi, Lide Zhang, and Wei Xu. "Surface plasmon polaritons: physics and applications." *Journal of Physics D: Applied Physics* 45.11 (2012): 113001.
[3] Pitarke, J. M., et al. "Theory of surface plasmons and surface-plasmon polaritons." *Reports on progress in physics* 70.1 (2006): 1.
[4] Zayats, Anatoly V., Igor I. Smolyaninov, and Alexei A. Maradudin. "Nano-optics of surface plasmon polaritons." *Physics reports* 408.3-4 (2005): 131-314
[5] Novotny, Lukas, and Bert Hecht. *Principles of nano-optics*. Cambridge university press, 2012.
[6] Barnes, William L., Alain Dereux, and Thomas W. Ebbesen. "Surface plasmon subwavelength optics." *nature* 424.6950 (2003): 824-830.
[7] Economou, E. N. "Surface plasmons in thin films." *Physical review* 182.2 (1969): 539.
[8] Zia, Rashid, and Mark L. Brongersma. "Surface plasmon polariton analogue to Young's double-slit experiment." *Nature nanotechnology* 2.7 (2007): 426-429.
[9] Graydon, Oliver. "Plasmonic interferometry." *Nature photonics* 6.3 (2012): 139-139.
[10] Gao, Yongkang, et al. "Plasmonic Mach–Zehnder interferometer for ultrasensitive on-chip biosensing." *ACS nano* 5.12 (2011): 9836-9844.
[11] Thomaschewski, Martin, et al. "Plasmonic lithium niobate Mach–Zehnder modulators." *Nano Letters* 22.16 (2022): 6471-6475.
[12] Haffner, Christian, et al. "All-plasmonic Mach–Zehnder modulator enabling optical high-speed communication at the microscale." *Nature Photonics* 9.8 (2015): 525-528.
[13] Lotfi, Fariba, Nafiseh Sang-Nourpour, and Reza Kheradmand. "High-sensitive plasmonic sensor based on Mach-Zehnder interferometer." *Optics & Laser Technology* 137 (2021): 106809.
[14] El Shamy, Raghi S., Diaa Khalil, and Mohamed A. Swillam. "Mid infrared optical gas sensor using plasmonic Mach-Zehnder interferometer." *Scientific reports* 10.1 (2020): 1293.
[15] Khan, Asad, et al. "Mach-Zehnder refractometric sensor using long-range surface plasmon waveguides." *Applied Physics Letters* 103.11 (2013).
[16] Fan, Hui, Robert Charbonneau, and Pierre Berini. "Long-range surface plasmon triple-output Mach-Zehnder interferometers." *Optics express* 22.4 (2014): 4006-4020.
[17] Charbonneau, Robert, et al. "Demonstration of surface sensing using long-range surface plasmon waveguides on silica." *Sensors and Actuators B: Chemical* 134.2 (2008): 455-461.
[18] Pu, Mingbo, et al. "Directional coupler and nonlinear Mach-Zehnder interferometer based on metal-insulator-metal plasmonic waveguide." *Optics Express* 18.20 (2010): 21030-21037.

[19] Sánchez-Ramírez, Ana, et al. "Comparing dielectric and plasmonic waveguides in a Mach–Zehnder architecture with coherent readout for sensing applications." *Optics & Laser Technology* 168 (2024): 109813.
[20] Gao, Yongkang, et al. "Plasmonic interferometers for label-free multiplexed sensing." *Optics express* 21.5 (2013): 5859-5871.
[21] Nimse, Satish Balasaheb, et al. "Biomarker detection technologies and future directions." *Analyst* 141.3 (2016): 740-755.
[22] Washburn, Adam L., et al. "Quantitative, label-free detection of five protein biomarkers using multiplexed arrays of silicon photonic microring resonators." *Analytical chemistry* 82.1 (2010): 69-72.
[23] Bottazzi, Barbara, et al. "Multiplexed label-free optical biosensor for medical diagnostics." *Journal of biomedical optics* 19.1 (2014): 017006-017006.
[24] Breglio, Giovanni, et al. "Fiber optic sensor arrays: a new method to improve multiplexing capability with a low complexity approach." *Sensors and Actuators B: Chemical* 100.1-2 (2004): 147-150.
[25] Raether, Heinz. "Surface plasmons on smooth surfaces." *Surface plasmons on smooth and rough surfaces and on gratings* (2006): 4-39.
[26] Hibbins, Alastair P., Benjamin R. Evans, and J. Roy Sambles. "Experimental verification of designer surface plasmons." *science* 308.5722 (2005): 670-672.
[27] Deng, Chih-Zong, et al. "Light switching with a metal-Free chiral-sensitive metasurface at telecommunication wavelengths." *ACS Photonics* 7.10 (2020): 2915-2922.
[28] Ding, Fei, Rucha Deshpande, and Sergey I. Bozhevolnyi. "Bifunctional Gap-Plasmon Metasurfaces for Visible Light." *2018 Progress in Electromagnetics Research Symposium (PIERS-Toyama)*. IEEE, 2018.
[29] Mühlenbernd, Holger, et al. "Amplitude-and phase-controlled surface plasmon polariton excitation with metasurfaces." *ACS Photonics* 3.1 (2016): 124-129.
[30] Kraft, Matthias, et al. "Designing plasmonic gratings with transformation optics." *Physical Review X* 5.3 (2015): 031029.
[31] Lequeux, Médéric, et al. "Plasmonic properties of gold nanostructures on gold film." *Plasmonics* 15 (2020): 1653-1660.
[32] Khodami, Maryam, and Pierre Berini. "Grating couplers for (Bloch) long-range surface plasmons on metal stripe waveguides." *JOSA B* 36.7 (2019): 1921-1930.
[33] Genet, Cyriaque, and Thomas W. Ebbesen. "Light in tiny holes." *Nature* 445.7123 (2007): 39-46.
[34] Zhang, Zhijian, et al. "On-fiber plasmonic interferometer for multi-parameter sensing." *Optics express* 23.8 (2015): 10732-10740.
[35] Gao, Yongkang, et al. "Plasmonic interferometric sensor arrays for high-performance label-free biomolecular detection." *Lab on a Chip* 13.24 (2013): 4755-4764.
[36] Wang, Qian, Jing Bu, and X-C. Yuan. "High-resolution 2D plasmonic fan-out realized by subwavelength slit arrays." Optics Express 18.3 (2010): 2662-2667.
[37] Felix-Rendon, Ulises, Pierre Berini, and Israel De Leon. "Ultrasensitive nanoplasmonic biosensor based on interferometric excitation of multipolar plasmonic modes." *Optics Express* 29.11 (2021): 17365-17374.
[38] Valero, Marcos, Israel De Leon, Mallar Ray, and Pierre Berini. "Design of multiplexed biosensors based on the interference of surface plasmons in multimode nanoslits." Submitted for publication, 2024.
[39] Burke, J. J., G. I. Stegeman, and T. Tamir. "Surface-polariton-like waves guided by thin, lossy metal films." *Physical Review B* 33.8 (1986): 5186.
[40] Born, Max, and Emil Wolf. *Principles of optics: electromagnetic theory of propagation, interference and diffraction of light*. Elsevier, 2013.
[41] Malitson, Ian H. "Interspecimen comparison of the refractive index of fused silica." *Josa* 55.10 (1965): 1205-1209.
[42] Johnson, P. B., and R. W. Christy. "Optical constants of transition metals: Ti, v, cr, mn, fe, co, ni, and pd." *Physical review B* 9.12 (1974): 5056.

5

Fabrication of surface plasmon interferometric sensors exploiting multimode nanoslits

5.1 Summary

In this work, we present the fabrication and experimental validation of a novel surface plasmon resonance (SPR) biosensor based on the selective excitation of multimodal electrical field distributions in a gold nanoslit. This device leverages surface plasmon wave (SPW) interference to achieve high sensitivity, and it is arranged linearly for multiplexing capabilities enabling simultaneous detection of 3 analytes at the same time.

The biosensor design includes grating couplers for SPW excitation, a gold nanoslit as the interferometric combiner, and microfluidic channels for analyte delivery. The grating couplers are optimized to couple incident light into SPWs efficiently, and the phase difference between these waves is manipulated either by adjusting the optical path length of one incident Gaussian beam or by varying the refractive index of the analyte. This phase difference modulates the multimodal distributions supported within the nanoslit, which are analyzed through the transmitted light.

The fabrication process involves metal deposition, electron beam lithography, focused ion beam milling, spin coating, hard mask photolithography, oxygen plasma etching, wafer bonding, and dicing. A custom-designed microfluidic jig integrates the chip optically and fluidically, enabling robust operation with three independent channels and providing the potential for future multiplexed detection.

We demonstrated bulk sensing by varying glycerol concentrations in water, providing key figures of merit such as noise level, signal-to-noise ratio, bulk sensitivity, and limit of detection. These results showcase the device's capacity to measure small refractive index changes with high precision, opening possibilities for further surface sensitivity measurements for specific biomarkers in a multiplexed configuration.

5.2 Contribution

This was the most ambitious article among all the works presented in this thesis, particularly due to the complexity of the fabrication process. Unlike the air-based device demonstrated in Chapter 3, this device required a significantly more intricate fabrication protocol involving multiple advanced steps, all carried out in the Nanofab laboratory at the University of Ottawa.

I performed the electromagnetic modeling of the device and created the CAD models, optimizing the geometry of the gratings, nanoslits, and fluidic channels. I also designed a custom microfluidic jig holder, enabling the integration of three microchannels along with dual optical interfacing using microscope objectives on both sides of the chip. Although the jig holder was complex in design, its fabrication was successfully carried out by the mechanical workshop team at uOttawa.

The complete fabrication process was carried out by me, including metal deposition, electron-beam lithography, Cytop spinning and etching, photolithography, wafer bonding, and dicing, along with all intermediate steps. The focused ion beam (FIB) milling of the nanoslits was performed by Hyung Woo Choi, and I gratefully acknowledge his contribution to this final and critical step. Howard Northfield trained me in cleanroom protocols and provided continuous support, particularly in mastering electron-beam lithography.

I also designed and built the optical testbed used for characterization. After receiving initial guidance from Luis-Angel Mayoral-Astorga on optical setups, I was able to replicate and optimize the system independently at Tecnológico de Monterrey. I prepared a series of water–glycerol solutions to systematically vary the refractive index for bulk sensing experiments, performed all measurements, and compared the results with the predictions from my own simulations. I analyzed and presented the data and wrote the first draft of the manuscript independently.

In solving one of the key engineering challenges — sealing the microfluidic interface for three channels without leakage — I received essential support from Graham Killaire and Arnaud Weck, who contributed to the design and fabrication of precise gaskets for the jig holder.

Finally, I would like to express my deep gratitude to my advisors — Dr. Israel De Leon, Dr. Mallar Ray, and Dr. Pierre Berini — for their continuous guidance, insightful feedback, and encouragement throughout the development of this project.

5.3 Article

The submitted article follows verbatim.

Fabrication of Surface Plasmon Interferometric Sensors Exploiting Multimode Nanoslits

Marcos Valero,[1,2] Howard Northfield,[2] Hyung Choi,[2] Luis-Angel Mayoral-Astorga,[2] Graham Killaire,[3] Arnaud Weck,[3,4,6] Israel De Leon,[2,5] Mallar Ray,[1] and Pierre Berini[2,3,6,*]

[1]School of Engineering and Sciences, Tecnológico de Monterrey, Monterrey, Nuevo León 64849, Mexico
[2]School of Electrical Engineering and Computer Science, University of Ottawa, Ottawa, Ontario K1N 6N5, Canada
[3]Department of Physics, University of Ottawa, Ottawa, Ontario K1N 6N5, Canada
[4]Department of Mechanical Engineering, University of Ottawa, Ontario, Canada, K1N 6N5
[5]ASML Netherlands B.V., De Run 6501, 5504 DR Veldhoven, The Netherlands.
[6]Nexus for Quantum Technologies Institute, University of Ottawa, Ottawa, Ontario K1N 6N5, Canada

* pberini@uottawa.ca

Keywords: Surface plasmons, interferometer, sensor, microfluidics, nanofabrication

Abstract: As phase-based sensors, surface plasmon interferometers offer higher sensitivity than resonant or attenuation-based plasmonic sensors. In this paper we realize surface plasmon interferometric sensors based on a multimode nanoslit used as a combiner. The phase difference in the surface plasmon waves, incident on the nanoslit, determines the resonant mode excited therein, and the radiation pattern that emerges therefrom. The device construction integrates on-chip grating couplers, gold sensing and reference surfaces, transparent claddings, sealed microfluidic channels, and a nanoslit in the gold film. The structure can be arrayed with individual microfluidic channels thereby enabling multiplexing. Nanofabrication of the devices using wafer-based processes is discussed in detail. Fabrication involves integration into a full process flow of techniques such as photolithography, electron beam lithography, focused ion beam milling, plasma etching, wafer bonding, and dicing, with several overlay and precision alignment steps. We also describe the design and realization of a test jig useful for mounting a chip under test, providing in-plane sealed microfluidic interfacing to several channels simultaneously, and enabling optical interrogation in the perpendicular direction using microscope objectives. Operation of the devices is demonstrated by refractometric (bulk) sensing experiments. The device concept is of strong interest for multiplexed biosensing applications, and the fabrication flow presented can be scaled to mass-manufacturing.

1. Introduction

Refractometric and biochemical sensors are devices that translate changes in the bulk refractive index of a solution, or that monitor biochemical interactions occurring on a sensing surface, into measurable outputs [1-6]. Among the different types of sensors, optical sensors have gained significant attention due to their high sensitivity and their potential for integration into lab-on-a-chip platforms [7-14]. They also offer label-free detection, real-time monitoring capabilities, and compatibility with multiplexed sensing, making them versatile for a wide range of applications [15-22]. Within optical sensing, surface plasmon resonance (SPR) based sensing stands out as a particularly effective technique. SPR sensors are highly sensitive to changes in the refractive index at the sensor's surface, making them well-suited for refractometric sensing or detecting molecular interactions in real time [23-32]. Compared to other optical sensors, SPR sensors excel due to their label-free nature, the ability to detect low concentrations, and their adaptability to various functionalization strategies for specific molecular detection.

Interferometric surface plasmon sensors, such as those utilizing Mach-Zehnder interferometers [33-40], offer improved sensitivity because they are capable of detecting minute phase changes occurring on the sensing arm relative to the reference arm. Despite this advantage, the challenge of adapting these sensors

to multiplexing remains a critical area of development. Current surface plasmon interferometers are typically designed for single channel detection, as integrating multiple sensing channels within an interferometric setup is technically demanding.

One approach that is promising consists of using grating couplers integrated with a nanoslit in a gold film acting as a multimode combiner, as investigated theoretically [41–43] and demonstrated in air [44]. Such a structure is attractive because it is interrogated perpendicularly and is amenable to arraying, thereby enabling the simultaneous interrogation of several sensors by using imaging techniques. In this paper, we present the first experimental demonstration of this type of interferometric SPR sensor, based on the interference of surface plasmons generated by grating couplers and recombined at a nanoslit, operating as a functional refractometric biosensor. While this geometry had been previously proposed and tested in air, its integration with sealed microfluidic channels and subsequent validation for refractive index sensing in aqueous environments had not been demonstrated before.

To realize this concept, we developed a complete wafer-based fabrication methodology compatible with semiconductor processing equipment. The process can achieve critical features well below our requirement of 200 nm. Fabrication involves eight principal process steps: metal deposition, e-beam lithography, focused ion beam milling, polymer deposition, photolithographic patterning, reactive ion etching, wafer bonding, and dicing – integrated into a reproducible flow after extensive optimization. To demonstrate this, we successfully fabricated three complete 2-inch glass wafers, each containing 22 microchips with three individual sensors per chip, underscoring the reproducibility and consistency of our process across multiple fabrication runs. All devices were visually and functionally consistent, and representative chips from each wafer were tested for refractive index sensing, confirming the functionality and uniform performance of the sensors. In addition, we present a custom-designed test jig and microchip holder, capable of interfacing with three fluidic channels simultaneously using an in-plane (end-facet) coupling approach. The jig enables optical interrogation in transmission through unimpeded top and bottom surfaces using standard microscope objectives, while facilitating microfluidic coupling and multiplexing through edge coupling. Bulk sensing experiments serve as proof-of-concept demonstrations, which along with a novel interferometric geometry, on-chip multiplexing, reproducible wafer-scale fabrication, and practical interfacing, establishes a strong foundation for future developments in real-time, label-free biochemical sensing.

2. Surface Plasmon Interferometric Sensor

The interferometric sensor of interest, illustrated in Fig. 1a, was originally introduced theoretically in previous work [41-43]. Two grating couplers, fabricated at a specific distance from each other on a thick gold film on a fused silica substrate, are designed to excite counter-propagating single-interface SPPs along the top surface from a pair of incident Gaussian beams at the free-space wavelength of $\lambda_0 = 850$ nm. These beams are incident perpendicularly and centered on the middle of each grating. Gold was chosen as the plasmonic material due to its excellent chemical stability and biocompatibility in aqueous environments. The performance of the grating couplers is determined by several parameters: The pitch (Λ), the thickness of ridges (h), the duty cycle (dc), and the number of periods (N_g). These parameters were optimized to maximize the coupling efficiency (η) of the incident beams into surface plasmon polaritons (SPPs). One grating coupler excites SPPs on the reference arm, whereas the other excites SPPs on the sensing arm.

The nanoslit, characterized by its width (w_s), is milled between the grating couplers and extends through the gold film to the silica substrate. It acts as the primary region where the incident SPPs interfere and excite different resonant modes therein depending on the phase difference ($\Delta\phi$) between the SPPs. The sensor leverages the selective excitation of different resonant modes in the nanoslit by the pair of SPPs impinging thereon, generating a radiation pattern in transmission which is characteristic of these resonant modes (and thus $\Delta\phi$).

The surface is coated with a CYTOP layer, a fluoropolymer which has a refractive index that closely matches that of water ($n_{CyTOP} = 1.345$ [45], $n_{H_2O} = 1.333$ [46] at $\lambda_0 = 850$ nm). A microfluidic channel is etched into the CYTOP layer along the sensing arm, allowing the aqueous sensing solution to interact with the gold surface. The use of CYTOP minimizes reflections at the interfaces between the fluidic channel walls and the sensing fluid. The entire device is then bonded to a SiO_2 lid, which serves to seal the microfluidic channel, preventing leakage while allowing fluid flow over the sensing surface.

The effective wavelength, λ_{eff}, of the SPP waves is given by [47]:

$$\lambda_{eff} = \frac{\lambda_0}{Re\{n_{eff}\}}, \tag{1}$$

where n_{eff} is the effective refractive index of the wave, given by:

$$n_{eff} = \sqrt{\frac{\varepsilon_{Au}\varepsilon_d}{\varepsilon_{Au}+\varepsilon_d}}, \tag{2}$$

with ε_{Au} being the permittivity of gold, and ε_d the permittivity of the dielectric (sensing solution or CYTOP cladding). At $\lambda_0 = 850$ nm, $\varepsilon_{Au} = -28.2691 + 1.7456$i [48], $\varepsilon_d = 1.778$ [46] for pure water and $\varepsilon_d = 1.809$ [45] for CYTOP such that $\lambda_{eff} = 617.4$ nm for the gold-water interface and $\lambda_{eff} = 611.5$ nm for the gold-CYTOP interface.

One of the advantages of this sensor structure is its tunability. Key geometrical parameters can be adjusted to optimize sensitivity, range of operation, visibility, and resolution [41-44]. The optimization was performed in previous work [43], at $\lambda_0 = 850$ nm for incident Gaussian beams of diameter $w = 10$ µm. The optimal dimensions for the grating couplers are: $\Lambda = 600$ nm (satisfying the grating equation [49-51]), $h = 35$ nm, $dc = 0.5$, and $N_g = 16$, resulting in a grating length of 9.6 µm which matches the diameter of the Gaussian beam. With these parameters, the grating couplers achieve a coupling efficiency into SPPs of $\eta \approx 52\%$ [43]. The other dimensions were determined as: $t_{Au} = 300$ nm to support single-interface SPP propagation, $L_{arm} = 46$ µm to ensure SPP power attenuation of only ~13.7% after traveling this distance from the grating, $L_{fluid} = 40$ µm to allow a 3 µm separation between the microfluidic channel and the slit on one side and the grating coupler on the other (thereby facilitating fabrication). While longer arm lengths increase sensor sensitivity [41], they also lead to greater attenuation of the SPP. The design balances these factors to maintain sufficient plasmon power at the slit. The slit width was chosen as $w_s = 340$ nm because it supports the dipolar and quadrupolar resonant modes while providing the best balance between sensitivity and range of operation [41].

Using a Finite Element Method (FEM) electromagnetic solver (COMSOL Multiphysics Wave Optics Module), the electric near-field distributions were calculated by exciting the nanoslit with two counter-propagating SPPs, as shown in Fig. 1b (the refractive indices of the fused silica substrate and gold film at $\lambda_0 = 850$ nm are $n_{sub} = 1.5$ [52] and $n_{Au} = \sqrt{\epsilon_{Au}} = 0.14 + 5.31i$ [48]. When $\Delta\phi = 0$, the near-field distribution has even symmetry, preferentially exciting the dipolar mode of the nanoslit, as shown in the top and bottom left panels of Fig. 1b. When $\Delta\phi = \pi$, the near-field distribution exhibits odd symmetry, preferentially exciting the quadrupolar mode, as shown in the top and bottom right panels of Fig. 1b. Given the length of the sensing arm as $L_{fluid} = 40$ µm, the phase difference between the SPPs on the sensing and reference arms is $\Delta\phi \approx \pi$. By monitoring the far-field radiation pattern of these modes, the sensor detects changes in the refractive index along the top gold surface within the fluidic channel, which produce phase changes in the SPPs traveling along the sensing arm. Individual sensors as sketched in Fig. 1a can be concatenated laterally on a single chip to enable multiplexing and monitoring of several sensing fluids simultaneously, as modelled theoretically in previous work [43].

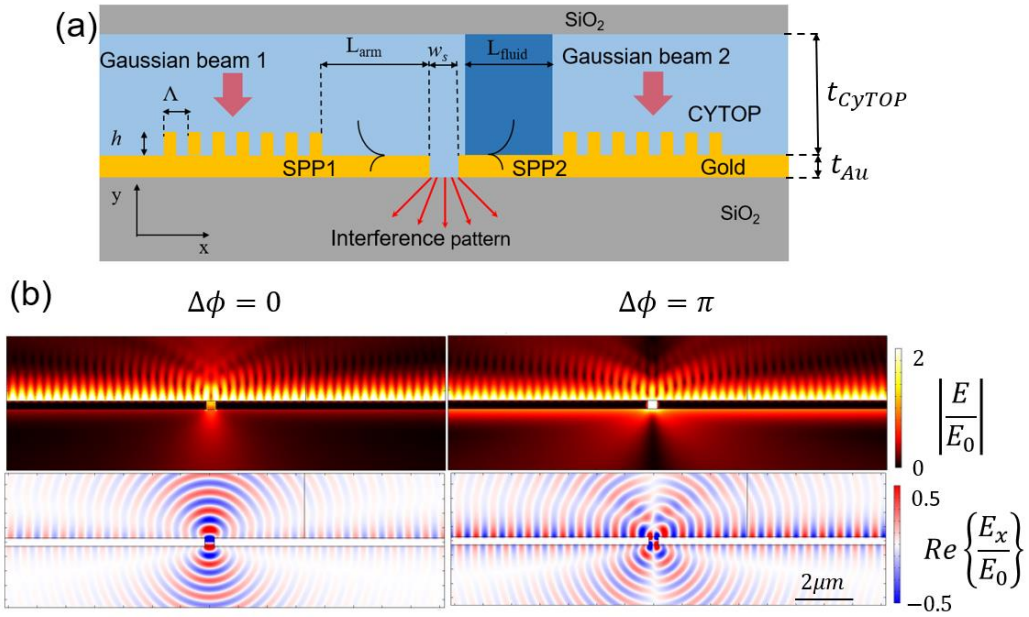

Figure 1. Surface plasmon sensor based on a nanoslit interferometer. (a) Transversal sketch of the device showing the main components, which include two grating couplers deposited on top of a gold film of thickness t_{Au}, supported by a fused silica (SiO_2) substrate. The nanoslit, of width w_s, is positioned between the grating couplers, each separated by a distance L_{arm}. The structure is coated by a CYTOP cladding, which is then etched to define the microfluidic channel of width L_{fluid} in the sensing arm of the interferometer. Finally, the device wafer is bonded to a fused silica wafer to seal the microfluidic channel. (b) Normalized electric field distributions in the nanoslit region, revealing directly the field enhancement ($|E/E_0|$, top panels) and the $Re\{E_x/E_0\}$ component (bottom panels). The distributions result from the illumination of the gratings by a pair of Gaussian beams, each with $E_0 = 1\,V/m$. When both SPPs arrive at the nanoslit with the same phase ($\Delta\phi = 0$), the dipolar mode is excited therein (left panels). Conversely, when the phase difference between the SPPs is $\Delta\phi = \pi$, the quadrupolar mode is generated in the nanoslit (right panels). In the nanoslit, a maximum field enhancement of $|E/E_0| = 3.5$ is observed.

Chip dimensions were set to 8 mm × 5 mm to facilitate handling. Each chip incorporated three independent microfluidic channels, disposed to interface identically with a custom-designed and machined microfluidic jig. Variations on the optimal sensor dimensions given above resulted in distinct designs, as listed in Table 1. Device G1 is designed to adjust the pitch, device H1 varies the arm length, device I1 varies the slit width, device G2 adjusts the duty cycle, device H2 varies the arm length (as device H1) but also introduces an unbalanced interferometer configuration where one arm is shorter by $\lambda_{SPP}/4$, and device I2 changes the number of grating periods.

Table 1. Summary of variations in sensor design.

Device	Λ [nm]	dc	N_g	L_{arm} [µm]	w_s [nm]
G1	570 to 640 (steps of 10)	0.5	16	46	340
H1	600	0.5	16	36 to 106 (steps of 10)	340
I1	600	0.5	16	46	200-1,000 (linearly increased)
J1	600	0.5	16	46	340
G2	600	0.325 to 0.625 (steps of 0.0375)	16	46	340
H2	600	0.5	16	36 to 106 (steps of 10) with one arm shorter by $\lambda_{SPP}/4$	340
I2	600	0.5	8 to 22 (steps of 2)	46	340

3. Fabrication Process

The process flow proposed to fabricate the sensors is shown in Fig. 2, which illustrates the key steps involved. Fabrication occurs on a 50 mm diameter, 500 µm thick fused silica wafer serving as the transparent substrate. A 300 nm thick gold layer, deposited via e-beam evaporation (Fig. 2b), acts as the SPP waveguide and sensing surface. Grating definition (Fig. 2c) uses e-beam lithography, gold evaporation, and lift-off to create grating couplers for SPP excitation. Nanoslit milling (Fig. 2d) employs FIB milling to form a nanoslit down to the substrate. CYTOP deposition (Fig. 2e) adds a ~10 µm thick CYTOP cladding via spin coating. Microfluidic channels are defined via plasma etching (Fig. 2f), and sealing (Fig. 2g) bonds the wafer to a fused silica lid. The wafer pair is then diced into 8 mm × 5 mm chips for integration with the test jig (discussed below). A 50 mm wafer accommodates 22 chips, but larger wafers can be used with compatible tools. Further details are provided in subsequent subsections.

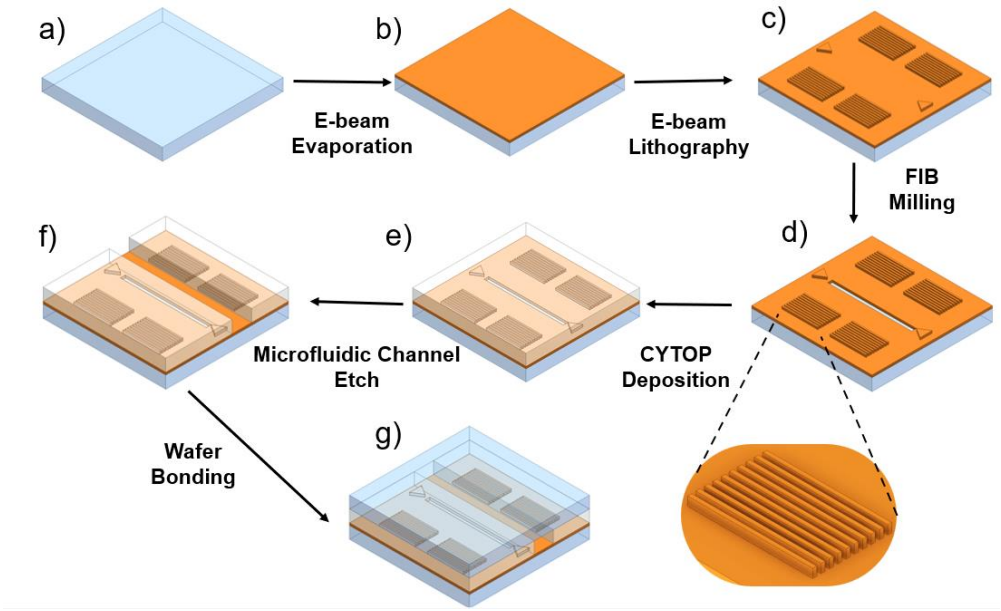

Figure 2. Fabrication flow of the interferometric biosensor. (a) A cleaned fused silica wafer is used as the starting substrate. (b) Thick gold layer deposited via electron beam evaporation. (c) Alignment features and grating ridges patterned using electron beam lithography followed by evaporation on the gold layer and lift-off. (d) Focused ion beam (FIB) milling of the interferometric nanoslit. (e) Deposition of CYTOP cladding layer. (f) Plasma etching of microfluidic channels. (g) Sealing by wafer bonding a fused silica covering lid to the device bearing substrate.

3.1 Gold Layer Deposition

The first step in fabricating the sensors is the deposition of a gold layer of thickness $t_{Au} = 300$ nm on a clean 50 mm diameter 500 µm thick fused silica wafer. Prior to gold film deposition, the wafer was ultrasonically cleaned following the steps in Table S1 of the supplementary materials. We chose electron beam (e-beam) evaporation due to its precision in depositing thicker gold layers with controlled thickness. Before depositing the gold layer, a 4 nm chromium layer is evaporated to promote adhesion of the gold layer to the substrate. Given that a thick (300 nm) gold layer is required, the deposition process was carried out in three steps of ~100 nm each to prevent the evaporator system from overheating, crystal failure and ensure sufficient deposition material. After each deposition step, a witness sample was removed to measure the deposited thickness via atomic force microscopy (AFM). The final thickness of the gold film after three deposition steps was 317 nm. AFM revealed that the gold surface had a root mean square roughness of $Rq = 5$ nm, which is reasonable for a 300 nm thickness, but some spits distributed over the surface were noticeable.

3.2 Grating Couplers

The fabrication of gratings must be accompanied by the fabrication of alignment marks and labels because this is the first lithography process applied in the fabrication flow of Fig. 2 (alignment marks are needed to align subsequent features - nanoslits and microfluidic channels). Fabrication of the gratings and alignment marks begins by thoroughly cleaning the wafer bearing the gold film, as outlined in Table S1 of the supplementary materials. Once cleaned, the wafer is spin-coated with polymethyl methacrylate (PMMA), an electron-sensitive resist. Various preparations of PMMA available from the manufacturer (Kayaku

Advanced Materials) spin on to different thicknesses. For this process, we considered PMMA 950 A2, A4, and A6, ultimately selecting PMMA 950 A4 for its ability to provide a thickness of approximately 125 nm. This specific thickness was critical, as thinner layers could complicate the lift-off process (*e.g.*, by blocking ingress of the lift-off solvent), while thicker layers might reduce resolution during e-beam lithography (EBL). The spin-coating process involved several steps to ensure the formation of a uniform and precise PMMA layer. First, the wafer was placed on the spinner and held securely by vacuum to prevent any movement during the coating process. Using a pipette, PMMA was carefully dispensed onto the wafer, covering approximately one-third of the total area starting from the center. After ensuring an even distribution of PMMA, the spinner was closed, and the spinning was initiated following the steps in Table S2 of the supplementary materials.

The wafer bearing PMMA is placed into the EBL tool, and global and local alignments were carried out following the procedure outlined in Section A of the supplementary materials. Once the alignments are achieved, the next step is to configure the EBL parameters for exposure. To optimize the process, the e-beam exposure is divided into two steps. Large alignment marks and labeling, which require less precision, are exposed with higher dose settings to save time, while the grating couplers, which demand greater accuracy, are exposed with a lower dose. This two-step approach ensures better control and precision, particularly for the grating couplers. The specific parameters for both steps are summarized in Table S3 of the supplementary materials. The write field area (area that the e-beam can pattern without moving the stage) is selected as $100\ \mu m \times 100\ \mu m$. The layout was therefore registered to a $100\ \mu m \times 100\ \mu m$ grid to keep all critical optical features within write fields. The e-beam system aligns write fields at two scales: $20\ \mu m$ for general positioning and $2\ \mu m$ for finer, high-precision features such as written in step 2. The writing time for the first step (alignment marks and labeling) takes ~6 hours to complete, while the second step (grating couplers) requires an overnight exposure due to the smaller, more precise features.

After exposure, we proceed to the development stage, where the exposed areas of the resist are selectively dissolved, unveiling the patterned structures. At the exposure doses adopted, PMMA behaves as a positive resist (exposed regions are soluble in the developer). The sample is developed by placing it in MIBK (Methyl Isobutyl Ketone) for 2 minutes, with constant agitation. Following MIBK development, the sample is rinsed in IPA (Isopropyl Alcohol) for 30 seconds to clean off any remaining solvent. During this process, we spray the sample with IPA to ensure thorough cleaning. After this step, features become visible, appearing as trenches where the PMMA has been removed, as shown in Fig. 3a.

After the features are fully developed, we perform a thermal evaporation of gold, aiming for a thickness of 35 nm. Once the gold is deposited, the lift-off process is initiated by immersing the sample in acetone at room temperature. The acetone dissolves the remaining PMMA, allowing the unwanted gold to lift-off, leaving only the desired patterned gold structures. The lift-off process was carried out for 12 hours to ensure complete removal of the unwanted gold, with periodically applied ultrasonic agitation.

After lift-off, we perform detailed inspections of grating structures and alignment marks using scanning electron microscopy (SEM), AFM, and optical microscopy. These methods allow us to verify the structural integrity and precise alignment of the fabricated gratings, ensuring that the design specifications are met. Fig. 3b shows an optical microscope image of a grating with optimal design characteristics after the lift-off step, this optimal grating coupler was used in most of the devices. The image demonstrates the integrity of the grating structure, confirming its suitability for the intended applications.

In Fig. 3c, we present a SEM image of a section of a grating after the lift-off step, verifying that the grating pitch (Λ) is 600 nm as expected. From several such inspections, we observe that the G1 devices yield grating pitches ranging from 570 to 640 nm, as designed (Table 1). However, the duty cycle is not 0.5, as intended, but approximately 0.4 due to defocusing effects during e-beam exposure. This discrepancy arises from the inherent mechanism of e-beam exposure of a resist, here a 120 nm thick PMMA layer. As the e-beam

penetrates from above, backscattered electrons at the substrate additionally expose the resist. Thus, the G2 gratings present a variable pitch but they differ slightly from those designed (Table 1).

Fig. 3d displays an AFM scan of a grating with the optimal design, revealing a thickness of $h = 33$ nm, which is very close to the target thickness of $h = 35$ nm. The AFM inspection also yields the RMS surface roughness (R_q) of the grating, measured as 5.5 nm, which is close to $R_q = 5$ nm measured after deposition of the thick gold film (sub-section 3.1), suggesting that grating fabrication introduced (at most) minor imperfections. The spits that occurred during deposition of the thick gold film (sub-section 3.1) are observable on this scan.

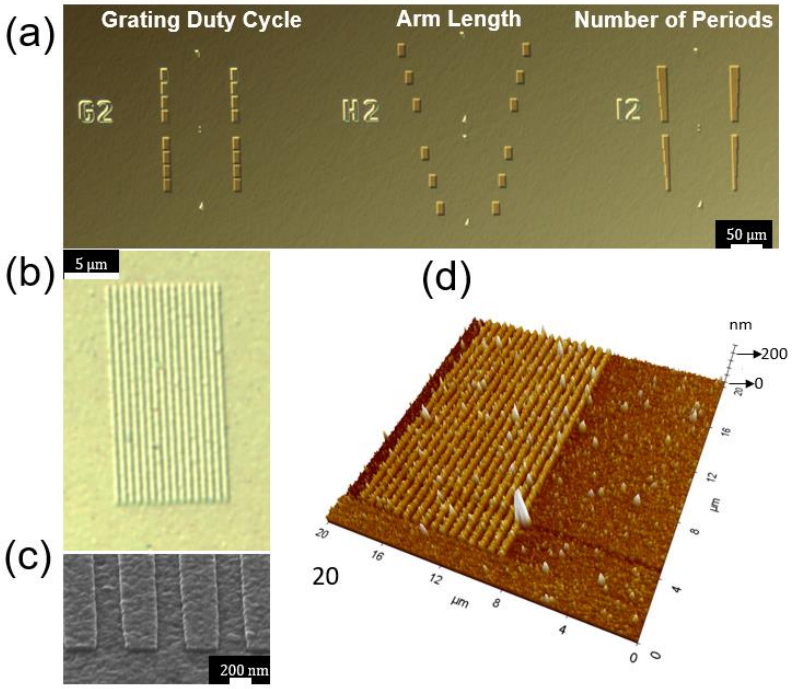

Figure 3. (a) Optical microscope image of a chip after e-beam exposure and development, showing devices G2, H2, and I2, designed to test variations in grating duty cycle, arm length, and number of periods, respectively (*cf*. Table 1). (b) Optical microscope image of the optimized grating structure after lift-off. (c) SEM image of a section of a grating after lift-off, confirming a pitch $\Lambda = 600$ nm as expected, with a duty cycle of $dc \approx 0.4$. (d) AFM image of the grating, showing a thickness of $h = 33$ nm, close to the target of 35 nm, and an RMS surface roughness of $R_q = 5.5$ nm.

3.3 Nanoslit Milling

The nanoslit is the central component of this interferometric sensor because it supports the plasmonic resonant modes and acts as an interferometric combiner. This nanoslit is milled into the 317 nm-thick gold layer using Focused Ion Beam (FIB) milling. The milling process gradually removes material in successive passes, enabling deep and smooth sidewalls. A progressive milling approach ensures that each pass contributes to a clean cut without producing significant gold redeposition. Nanoslit milling was carried out using a Zeiss Orion system equipped with the Fibics Atlas engine, incorporating dual beams of He and Ga ions positioned at 54° to each other. This configuration allows a top view for Ga FIB milling and a tilted

view for imaging with the He beam, facilitating precise control and monitoring of dimensional and positional accuracies. Depending on the areal dose of Ga ions, which is determined by parameters such as beam current, dwell time, spot spacing, and beam travel style, the sputtering of atoms from the Au film to machine nanoslits was successfully achieved. The specific parameters for milling, producing nanoslits that are very close to design, are summarized in Table S4 of the supplementary materials. Prior to FIB milling, the perpendicularity of a nanoslit relative to the gratings was ensured by the rotational alignment of the sample to a precision of 0.1°. The optimal slit width is $w_s = 340$ nm, however, various widths were implemented as discussed in Section 2 on device I1 (Table 1). Each nanoslit was aligned to grating couplers using a pair of arrowhead marks formed during grating fabrication.

Fig. 4a shows an optical microscope image of a chip bearing device G1 (grating pitch varies), H1 (arm length is adjusted, and I1 (slit width is varied), as summarized in Table 1. The slit width is fixed to $w_s = 340$ nm in devices G1 and H1 but varies on device I1 from a narrow slit at the bottom, gradually expanding towards the top. To ensure precision, the structure is divided into two sections: the first section (bottom) has a nanoslit width that varies from 200 to 500 nm, and the second section (top) has a nanoslit width that varies from 600 to 1000 nm. This segmentation is necessary to prevent defocusing during the milling process, as maintaining a consistent focus becomes challenging over longer milling distances. In Fig. 4b, a close-up view obtained with SEM microscopy of device I1 is given, showing that the nanoslit width varies from 200 to 500 nm.

To optimize the milling parameters and ensure a uniform depth profile along the nanoslit, the number of passes were systematically varied, as shown in Fig. 4c. For the milling parameters in Table S4 of the supplementary materials, the number of passes was increased from 5 to 25, corresponding to an areal dose ranging from 135 to 675 μC/μm², in order to evaluate the morphological accuracy of nanoslits. With each successive pass, the nanoslit improved progressively, achieving its cleanest profile at 25 passes. However, it is crucial to control the milling depth carefully, as excessive passes led to penetration into the underlying fused silica substrate. Cross-sectional examination, shown in Fig. 4d, reveals that after 25 passes, the milling extended approximately 185 nm into the substrate. Such over-milling can alter the nanoslit geometry, potentially compromising the interferometric modes and deviating from the intended design. Based on experimental findings, an areal dose of 530 μC/μm² was selected for all nanoslits in this study to ensure optimal morphological accuracy while minimizing substrate damage.

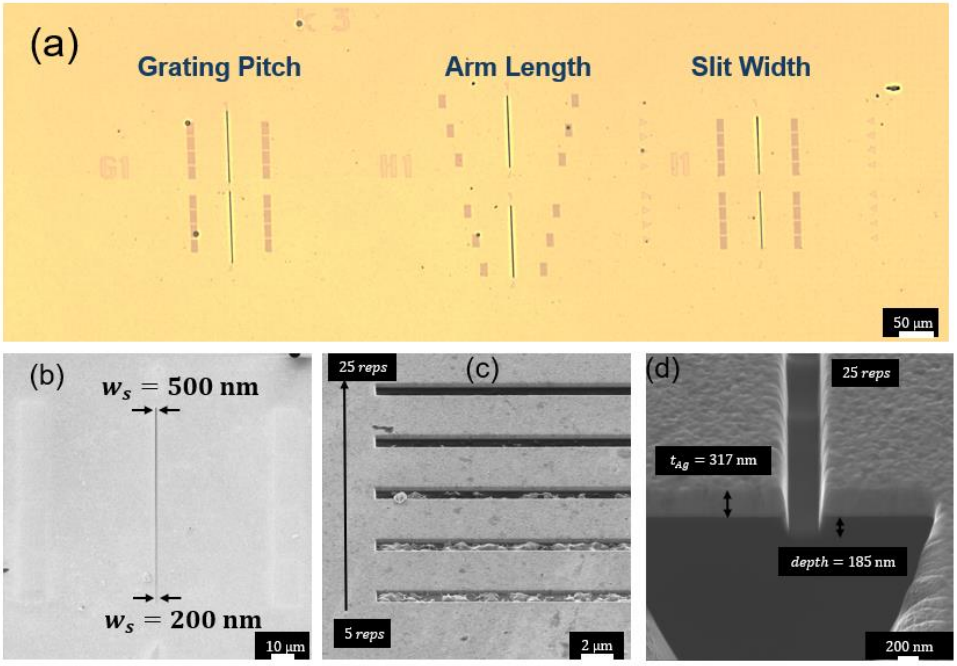

Figure 4. Nanoslit milling. (a) Optical microscope image of a chip bearing three devices labeled G1, H1, and I1 (*cf*. Table 1), after the nanoslits are milled. (b) SEM image of device I1, showing adjustments to the slit width from 200 nm to 500 nm. (c) SEM image displaying the effect of repeat passes in the FIB milling process, demonstrating improvements in nanoslit wall quality as the number of passes increases from 5 to 25, yielding optimal cleanliness at 25 passes. (d) Transversal cut of a nanoslit, revealing clean edges down to a depth of 317 nm, with an additional 185 nm of over-milling into the substrate.

3.4 Cladding Formation

As discussed in Section 2, the fluoropolymer CYTOP was selected as the cladding material for the sensors, into which microfluidic channels are etched, due to its refractive index which closely matches that of water ($n_{CYTOP} = 1.345$). Matching the refractive index minimizes unwanted reflections at the interfaces between biosensing solutions (for which water is the main constituent) and the cladding. CYTOP does not cross-link subject to heating, has a glass transition temperature (Tg) of 107 ºC, and a solvent (CT-Solv) boiling point of 180 ºC [45].

In previous works, CYTOP layer thicknesses of ~10 µm were consistently achieved by repeating a spin-coat and curing process [53,54]. The process begins by cleaning a wafer bearing a thick gold film, gratings, alignment marks, labels and nanoslits (*cf*. Fig. 4a), following the procedure outlined in Table S1 of the supplementary materials, to ensure a clean and particle-free surface. The wafer is then secured in the spin coater using vacuum. Using a pipette, CYTOP A Grade is dispensed to cover approximately one-third of the wafer's central area, and the spin-coating process is initiated following the parameters detailed in Table S5 of the supplementary materials. After the spin cycle completes, vacuum is released, and the wafer is left to rest for five minutes. This spin process results in a CYTOP layer approximately 2.5µm thick. The wafer is then transferred to a hotplate set at 50 °C for 30 min. This soft bake results in partial solvent evaporation and ensures that no solvent bubbles are created. This spin-coat / cure process is repeated four times to build up the desired thickness of 10 µm.

After the fourth layer, the wafer is subject to a hotplate hard curing process where the temperature is ramped from 50 °C to 200 °C at 25°C/hour for a period of 12 hours, then heating is turned off. This slow temperature ramp and prolonged heating permits a slow and thorough solvent evaporation, and since the temperature is taken above Tg a smooth, uniform CYTOP layer results. Once the temperature of the wafer returns naturally to room temperature, it is removed from the hotplate and ready for the next fabrication steps.

We did not observe any adhesion issues between the CYTOP (A Grade) cladding and the underlying gold surface, and we did not observe any defects or non-uniformities in the cladding due to the underlying topography of the substrate (which bears gratings, alignment marks, labels and nanoslits). However we observed the formation of a CYTOP edge bead along the perimeter of the wafer. An edge bead is undesirable because it would interfere with subsequent processing steps, specifically, the hard contact photolithography process used to define the microfluidic channels (Fig. 2f), and the wafer bonding process applied to seal them (Fig. 2g). To remove the edge bead, we shadow-masked the central area of the wafer using a metal disc, exposing only the edge where the bead was present. The wafer was then subjected to oxygen etching for 10 min under controlled conditions: oxygen flow at 10 SCCM (standard cubic centimeters per minute), a pressure of 3 Pa, and a power of 100 W. This process successfully removed the bead, exposing the underlying gold layer at the wafer's edge. The exposed gold layer was then used to measure the final CYTOP thickness using a profilometer, confirming a thickness of $t_{CyTOP} = 10.6\,\mu\text{m}$.

3.5 Microfluidic Channels

As discussed in Section 2, the interferometer arms were set to $46\,\mu\text{m}$ to match the surface plasmon propagation length at the gold–analyte interface, where the power decays to approximately 13.7%. The microfluidic channel was designed to be $40\,\mu\text{m}$ long, leaving $3\,\mu\text{m}$ of clearance on each side between the channel and the grating/nanoslit structures to ensure alignment and bonding during assembly. The channel height was fixed at $10\,\mu\text{m}$, a value reliably achieved by CYTOP spin-coating (see Section 3.4). This thickness ensures mechanical stability and preserves laminar flow while avoiding collapse risks that may occur at greater thicknesses.

The channel width tapers from $200\,\mu\text{m}$ at the inlets to $40\,\mu\text{m}$ in the sensing region and back to $200\,\mu\text{m}$ at the outlets. These channels are curved in layout to bring fluid from inlets spaced $2.4\,\text{mm}$ apart to the center of the chip, where the devices are optically interrogated. The curved design avoids sharp corners, reducing flow resistance and minimizing the risk of bubble formation or recirculation zones.

To realize these designed channels with the required precision in width, curvature, and alignment, we implemented a bi-layer photolithography process on the CYTOP surface, as described in detail in Section B of the supplementary materials. This process enabled the lift-off of an aluminum hard mask used to define the microfluidic channels to be etched in CYTOP. A hard etching mask was selected because of the stringent requirements on channel wall verticality, dimensions, and position relative to the gratings and nanoslits. This mask design includes labelling, dicing marks, designs for the microfluidic channels and alignment marks that register to those defined during the e-beam lithography step to ensure that the microfluidic channels align precisely to grating couplers and nanoslits. A chip bearing developed lithography, featuring devices J1 (Table 1), can be seen in Fig. 5a. After development, the next step was to deposit and lift-off a 45 nm thick aluminum layer to form the etching mask. A chip featuring the aluminum mask is shown in Fig. 5b.

Once the aluminum mask was deposited, the next step was to etch the microfluidic channels into the CYTOP layer using a SAMCO RIE-10NR etcher with parameters tailored for this process. The oxygen flow rate was set to 10 SCCM, with a constant pressure of 3 Pa maintained throughout. Power was the key variable, adjusted to control the etching depth while avoiding damage to the aluminum mask. Starting with high power and gradually reducing it proved to be the most effective strategy, ensuring a controlled and

uniform etch. The etching process began at 100 W for 5 min, removing approximately 2.4 μm of CYTOP. While this high power was efficient for initial etching, prolonged exposure risked degrading the aluminum mask. To balance etching efficiency and mask preservation, the power was reduced to 50 W to complete the etching, verifying periodically using a profilometer the depth achieved. Once the target depth of 10.6 μm (CYTOP thickness) was achieved, etching was stopped. The aluminum mask performed its role effectively, however, it became thin and rough by the end of the process due to prolonged exposure to the etching plasma, as shown in Fig. 5c.

With the microfluidic channels now etched in CYTOP, the next step was to remove the aluminum mask. This was achieved using an ITO etchant (TE-100), a solution that also works to remove aluminum. The wafer was placed in the etchant at 40 °C on a hot plate, covered with a lid, and left for 5 min. Once the aluminum mask was dissolved, the wafer was thoroughly rinsed with deionized water and dried using nitrogen. The microscope image of Fig. 5d shows a chip with etched microfluidic channels and the profilometer measurement presented in Fig. 5e confirms that the etch depth was achieved, and that the gold and CYTOP surfaces are smooth.

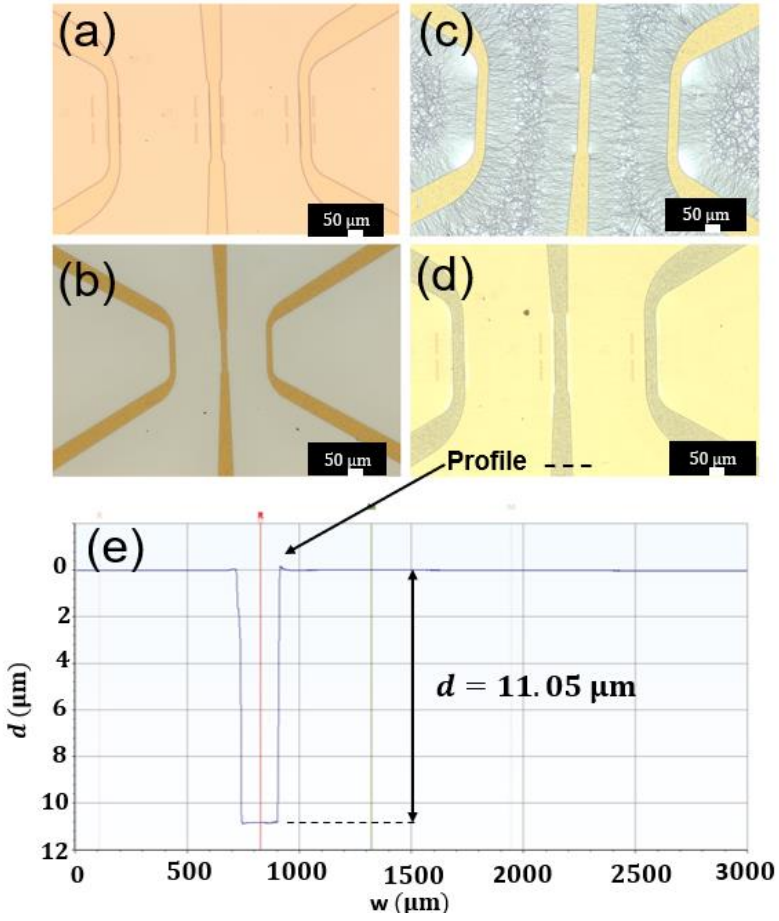

Figure 5. Microfluidic channel etching. (a) Optical microscope image showing the microfluidic channel pattern on a chip featuring devices J1 (cf. Table 1) after development. (b) Optical microscopic image showing the aluminum mask post lift-off (light gray), and the exposed CYTOP (dark orange). (c) Optical microscope image showing the microfluidic channels during the etching process and the aluminum mask

which degrades as the process proceeds. (d) Optical microscopic image of the etched microfluidic channels after removal of the aluminum mask. (e) Profilometry scan of an etched channel showing the CYTOP thickness of $t_{cytop} = 10.6$ μm.

3.6 Wafer Bonding and Dicing

Wafer bonding is the process of joining 2 wafers together under controlled pressure and temperature. Here an AML wafer bonding system was used to bond a fused silica wafer acting as a lid to the device wafer bearing the etched CYTOP layer with microfluidic channels. This step seals the microfluidic channels and provides added mechanical stability. For the lid, we chose a 50 mm diameter 500 μm thick fused silica wafer, identical to the substrate. The transparency of this material allows the incident Gaussian beams to pass through and excite the grating couplers located beneath the CYTOP layer.

To facilitate bonding between the glass lid wafer and the device wafer we apply a layer of CYTOP to the former. This will enable a CYTOP-to-CYTOP polymeric bond at the interface (bonding identical thermoplastics results in a strong and reliable bond). A fused silica wafer (lid) was first thoroughly cleaned following the procedure detailed in Table S1 of the supplementary file. Then AP3000, an adhesion-promoting primer to adhere CYTOP A to a glass surface, was applied to the fused silica wafer. AP3000 was dispensed using a pipette to cover the entire surface of the glass wafer. The wafer was then secured under vacuum in the spinner, and the spin-coating procedure outlined in Table S7 of the supplementary materials was followed. After spinning, the wafer underwent a dehydration bake on a hotplate by heating to 180 °C for 1 min, then cooling to 100 °C and holding for 5 min. The process described in Section 3.4 was then followed to deposit a single layer of CYTOP onto the wafer and to etch the edge bead. A CYTOP thickness of 2.4 μm was measured using a profilometer.

The wafer bonding process begins by first levelling the bonder platens following the manufacturer's procedures to ensure parallelism. The device wafer is positioned at the center of the bottom platen (CYTOP face up). The lid coated with CYTOP is secured to the top platen (CYTOP face down), and manually aligned to ensure overlap with the device wafer and coverage of the microfluidic channels. The bonding chamber is then evacuated to a vacuum level of level of 7.32×10^{-5} torr to ensure that trapped air does not interfere with bonding. Then, the wafers are contacted, and force is gradually applied up to 1 kN. The temperature of both platens is then increased from ambient temperature (23 °C) to 115 °C at a rate of 0.5 °C per minute. The bonding force increases up to about 1.7 kN as the temperature rises to 115 °C due to the thermal expansion of the materials. Once the temperature reaches 115 °C, the system is held steady overnight to allow the bond to form and stabilize. The system is then allowed to cool naturally to ambient temperature over about 8 hours. During cooling, the platen force decreases to eventually stabilize at 0.8 kN by the time the system reaches room temperature.

Once the chamber has cooled to ambient temperature, the chamber is vented, the platen force released, the wafer assembly is removed, and the bond is inspected under microscope. Fig. 6a shows a successfully bonded chip, along with Device G1 (*cf*. Table 1) in expanded view, confirming accurate alignment of the microfluidic channel to the gratings and nanoslit (*cf*. Section 3.4). Most of the devices were bonded cleanly and without issues. However, defects at the bonding interface were apparent on some devices, as shown in Fig. 6b, possibly due to uneven surfaces on the starting wafers. While such defects might seem problematic, experimental testing confirmed that they do not significantly impact the functionality of the device because the bonding interface is far from the grating couplers, sensing surface and nanoslit.

After bonding, the wafer assembly is diced using a precision dicing system (SYJ-800) equipped with a diamond blade of width 350 μm and operating at a rotation speed of 3000 RPM. Fig. 6c shows the wafer assembly mounted to dicing tape and aligned to the saw. The assembly was diced into 6 rows, with each row containing 2 to 4 chips as shown in Fig. 6d. Several wafer assemblies were diced and no bonding failures were observed confirming the strength of all CYTOP bonds (CYTOP-gold on the device wafer,

CYTOP-fused silica on the lid wafer, and CYTOP-CYTOP at the bonding interface). The dicing process also opens the inlets and outlets of the microfluidic channels along the edge facets of the chips needed for in-plane fluidic coupling. It is important for the inlets and outlets to be clear of debris. Thus, after dicing, the chips are cleaned in pure IPA using an ultrasonic cleaner set to a high intensity, which effectively dislodges residual debris from the chips, and then submerged in water [53,54]. A microscope image of the edge facets is shown in Fig. 6e, where it is possible to observe that each individual chip has three fluidic inlets, all of which are clean. The same figure also includes a close-up of the right inlet, further demonstrating that it is free of debris.

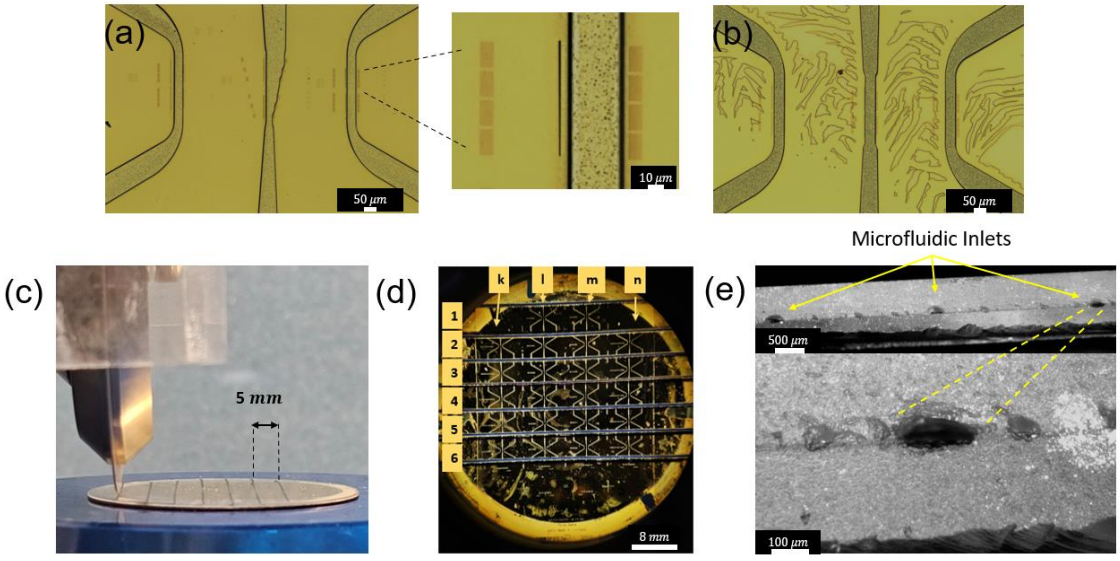

Figure 6. Wafer bonding and dicing. (a) Bonded chip showing the successful attachment of the glass lid to the device wafer, with a close-up view of device G1 (*cf.* Table 1) demonstrating precise alignment of the microfluidic channel to the grating couplers and nanoslit. (b) Bonded chip illustrating bonding defects at the bonding interface. (c) Dicing saw aligned to a wafer assembly on dicing tape (blue). (d) Wafer assembly dicing into rows ready for testing. (e) Microscope image of the edge facets of a diced chip, showing three fluidic inlets that are free of debris. A close-up of the right inlet further demonstrates its cleanliness.

4. Test Jig

Optical and microfluidic interfacing to a chip under test is ensured by a custom-design jig. The jig must secure the chip, enable normal optical interrogation through (water immersion) objectives, and interface the in-plane microfluidic inlets and outlets of the chip to external tubing. All chip designs incorporate three microfluidic channels, each flared to inlets and outlets 200 µm wide, separated by 2.4 mm, and located on the front and back facets of the chip. The jig must also enable a chip to be aligned and interfaced to external fluidic tubing via sealed connections to three microfluidic channels simultaneously.

The jig design is illustrated in Fig. 7a and its construction machined from aluminum is shown in Fig. 7b. The design is in the style of “clamping tweezers”, which provides a secure yet unobtrusive method of holding the chip. The tweezer design, spaced 8 mm apart, allows an unobstructed perpendicular optical path. Edge plates (1 mm thick) provide stability and microfluidic interfacing by pressing against the front

and back facets of the chip. Each plate incorporates three holes spaced 2.4 mm apart to match the configuration of the three microfluidic channels, and they are threaded with microfluidic tubing. Sealing is ensured by a 0.8 mm thick Silicone gasket (Grace Biolabs 664172) placed between the edge plates and the chip. The gasket is pierced with laser-cut holes (aligned with the holes on the edge plate), of diameter 400 µm, selected to be larger than the 200 µm width of the microfluidic inlets and outlets, but smaller than the 1 mm thickness of the chip to ensure that the gasket seals securely around the inlets and outlets. The laser process developed and applied to cut these holes is described in Section C of the supplementary materials. The jig with one side plate threaded with microfluidic tubing and incorporating the gasket is shown aligned to a chip in Fig. 7c.

Fig. 7d gives optical microscope images of a chip mounted in the jig where the microfluidic channels are filled sequentially with water. The images were captured using back illumination to enhance the visibility of the nanoslit, which appears bright under this illumination. The top left panel shows the chip with all microfluidic channels empty, clearly visible due to the refractive index mismatch between the CYTOP cladding and the air in the channels. The remaining panels show the three channels being sequentially filled with water: the center channel on the top right panel, the center and right channels on the bottom left panel, and all three channels filled in the bottom right panel. When filled, the channels disappear because the index of the CYTOP cladding is very close to that of water eliminating reflections from interfaces. These results demonstrate the effectiveness of the jig design and the simultaneous operation of three independent microfluidic channels.

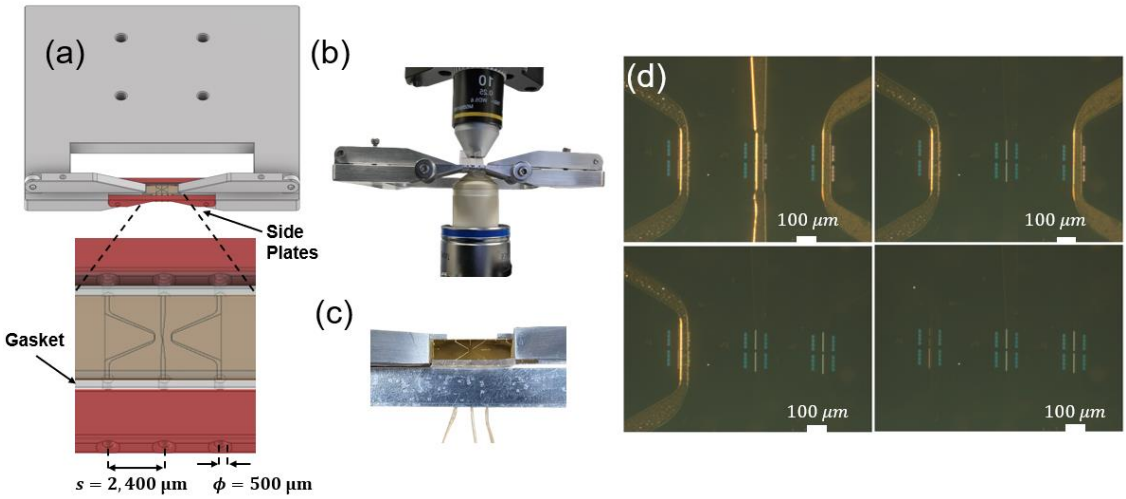

Figure 7. Schematic and demonstration of the test jig. (a) Sketch of the clamping tweezer jig with its mounting plate, showing a chip secured, and providing an unobstructed perpendicular optical path. A close-up view of the edge plates (red) is also shown. (b) Picture of the jig machined in aluminum with water-immersion objectives aligned for optical interrogation. (c) Close-up view of the microfluidic interfacing through a pierced edge plate and a 0.8 mm thick gasket featuring laser-pierced holes (500 µm diameter, spaced 2.4 mm) for leak-free alignment of three microfluidic channels. Three segments of microfluidic tubing threaded through the holes of the edge plate are also visible. (d) Optical microscope image showing the filling sequence of the microfluidic channels: the top left panel shows all fluidic channels empty, visible due to the refractive index mismatch with air. The top right panel demonstrates the central channel filled with water, while the bottom panels display the sequential filling of the remaining channels. Back illumination enhances the visibility of the nanoslit.

5. Interferometric Characterization and Refractometric Sensing

The optical set-up used to characterize the chips illuminates a device under test with two TM-polarized Gaussian beams, each 10 μm in diameter, and separated by ~ 90 μm to align with the grating couplers (*cf.* Fig. 1). The relative phase of the optical beams is adjustable by varying the optical path length of one of the beams. These beams are incident at normal incidence and centered on the grating couplers. This configuration avoids the need for angular alignment, which would be difficult to control for both beams simultaneously, and provides sufficient coupling efficiency for our purposes. The excited SPPs at the reference and sensing arms then interfere at the nanoslit, resulting in a transmitted radiation pattern that is captured on the substrate side using a second microscope objective and a camera. From the imaged radiation pattern recorded over time, a sensorgram is generated. Details of the optical setup are provided in Section D of the supplementary materials.

In this interferometric SPR sensor, the phase difference $\Delta\phi$ between the counter-propagating SPPs determines the modal distribution excited within the nanoslit, and consequently, the far-field radiation pattern. There are two main ways to modify $\Delta\phi$ in this system: (i) Optical path modulation (Section 5.1), which involves adjusting the optical path length (ΔL) of one of the two incident beams exciting the grating couplers using mirrors mounted on a translation stage. (ii) Refractive index modulation (Section 5.2), which involves varying the refractive index in the microfluidic sensing arm, which in turn alters the effective index of the SPP propagating therein, producing a phase shift relative to the reference arm - this approach demonstrates the sensor's capability for bulk refractometric sensing.

We investigated both approaches theoretically and experimentally and observed good agreement in their results. In both cases, $\Delta\phi$ was modulated and the corresponding far-field radiation pattern emerging from the nanoslit was analyzed. In the theoretical case, 2D simulations were used to compute the radiated intensity, along a 1D cutline placed 4 μm below the slit to extract the far-field profile. In the experimental case, the radiated pattern was captured using the optical setup illustrated in Fig. S1 of the supplementary materials. This allowed us to monitor how the modal distribution at the nanoslit output evolved as a function of $\Delta\phi$. An example of this dynamic behavior is provided in Multimedia File 1, which shows a video of the evolution in the nanoslit's far-field radiation pattern as $\Delta\phi$ is varied through optical path modulation. The video clearly shows that the radiated power varies periodically and that the pattern repeats for each 2π cycle in phase difference.

Because the nanoslit is optically long, the resulting radiation pattern extends along the vertical axis, producing light emission along the full length of the slit. This aspect is not captured in our simulations, which were performed in 2D and generated 1D far-field patterns. To compare the simulated and experimental results, we selected a transverse cutline across a portion of the nanoslit where the modal transition from dipolar to quadrupolar was most distinct. This distinct transition only appears in regions where the counter-propagating SPPs are optimally aligned. This experimental cutline is illustrated in Fig. 8 (left panels). The figure presents the far-field radiation patterns for three representative values of $\Delta\phi$, captured using the optical setup. The cutline used for intensity extraction is marked in orange. These experimental profiles are compared to the corresponding theoretical 1D intensity distributions obtained from FEM simulations, and a good agreement is observed. To resolve the structure of the dipolar and quadrupolar radiation patterns, a 63× water-immersion objective (NA = 1.2) was used.

However, this objective has a very short working distance and requires careful handling and immersion alignment, making it less practical for regular use in the optical setup. In contrast, a lower-magnification objective with a larger working distance, a 10× objective (NA = 0.25) in this case, can be used when the goal is not to image the modal distribution, but rather to measure the power carried by the radiated signal. In this configuration, the sensing mechanism is based on tracking changes in the integrated radiated power, rather than resolving the spatial features of the far-field pattern. Because this power variation does not depend on magnification or observation distance, it enables simpler measurements. Thus, we report our

measurements as the normalized integrated radiated power (*NP*). In the case of the theoretical model based on 2D FEM simulations, we placed a virtual cutline a few microns below the nanoslit and computed the 1D far-field intensity distributions for different values of $\Delta\phi$, as shown in the middle panels of Fig. 8. These intensity distributions were numerically integrated then normalized. We followed the same approach in the experimental case: 1D intensity profiles were extracted from the camera images using a cutline across the radiated pattern, as shown in the right panels of Fig. 8, and the resulting curves were integrated numerically then normalized. The exact position of the cutline is indicated in Multimedia File 1 for additional clarity.

To further characterize the sensor's interferometric response, we evaluated its visibility, which quantifies the contrast of the interference pattern, defined as [55,56]:

$$V = \frac{NP_{max} - NP_{min}}{NP_{max} + NP_{min}}, \tag{3}$$

where NP_{max} and NP_{min} are the maximum and minimum values of *NP*, respectively. In our case, the visibility quantifies the contrast between the quadrupolar mode, which produces the highest radiated power, and the dipolar mode, which produces the lowest radiated power. A high visibility indicates a strong modal contrast, which is essential for enhancing the sensor's sensitivity to changes in phase.

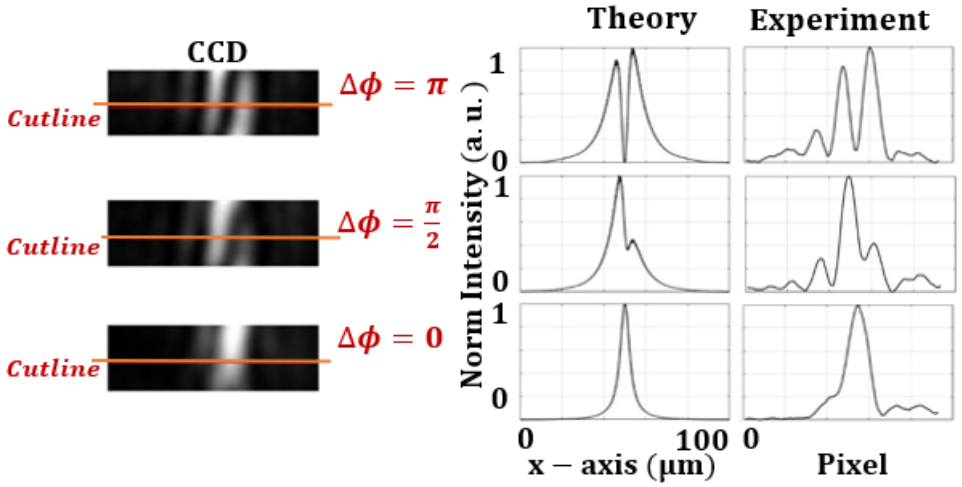

Figure 8. Transition between quadrupolar and dipolar modes: theoretical 1D distributions (middle panels), experimental 1D distributions (right panels), and experimental images (left panels, link to: Multimedia File 1) for $\Delta\phi = 0, \pi/2$, and π.

5.1 Interferometric Response – Optical Path Modulation

The first step in testing the sensor is to demonstrate its interferometric functionality. This can be achieved by adjusting the optical path length (ΔL) of one of the two incident beams exciting the grating couplers, as shown in Fig. S1a of the supplementary materials, thereby inducing a relative phase difference ($\Delta\phi$) between the two SPP waves interfering in the nanoslit. When ΔL is reduced or increased by λ_0 the beam undergoes a phase shift of 2π with respect to its initial value, so $\Delta L = \lambda_0/2$ introduces a phase shift of π [57-59]. The relative phase of the Gaussian beams is conserved by the SPPs excited at the grating couplers. Thus, the radiated pattern transitions from that generated by the quadrupolar mode in the nanoslit to that radiated by the dipolar mode as ΔL changes from 0 to $\lambda_0/2$, corresponding to phase differences of $\Delta\phi = 0$ and $\Delta\phi = \pi$, respectively, as described in Section 2 (for $w_s = 340$ nm).

To conduct this experiment, the microfluidic channel was initially filled with water ($n_{H2O} = 1.333$), which differs slightly from the refractive index of CYTOP ($n_{CYTOP} = 1.345$). Thus, when both grating couplers were illuminated with Gaussian beams of the same relative phase, the refractive index imbalance between the sensing and reference arms introduced a phase difference close to π, resulting in quadrupolar mode excitation and a maximum in *NP*. By adjusting the optical path length of one of the beams using a nanometric stage, the phase difference $\Delta\phi$ could be swept, completing a sensing period in under five seconds. This rapid tuning minimizes the impact of slow drifts from mechanical vibrations or laser fluctuations, which can affect long-term measurements. A real-time recording of this dynamic transition is shown in Multimedia File 1, where the far-field radiation pattern evolves smoothly as $\Delta\phi$ is swept, demonstrating the sensor's interferometric response. The measurements shown in Figs. 8 and 9 were obtained in this manner.

Despite the short acquisition time, some drift remains visible in portions of the sensing curve of Fig. 9. Nonetheless, the experimental *NP* data show a clear sinusoidal trend with $\Delta\phi$, as expected from a Mach–Zehnder-type interferometer [37–39,60–65]. The measurements are plotted as the red dots against the theoretical prediction plotted as the blue curve in Fig. 9, verifying the expected periodic variation over a full sensing period. Vertical error bars are included for each experimental point and represent the standard deviation of the NP signal over a 10-second interval of stable acquisition. This standard deviation reflects the baseline noise level of the system, measured to be $\delta = 6.8 \times 10^{-3}$. The ability to reproduce this interferometric response confirms the phase-sensitive behavior of the device and validates its operation as a plasmonic interferometric sensor.

Using Eq. (3), we determined that the visibility of the interferometric signal is 33% in theory and 18% in practice. This reduction in visibility is attributed to reflections at multiple interfaces in the perpendicular path of the sensor, which trap and redirect light through the nanoslit, and is captured along with the measured signal. Furthermore, slight differences in the size, position, or power of the two Gaussian beams exciting the grating couplers, further contribute to the reduced visibility.

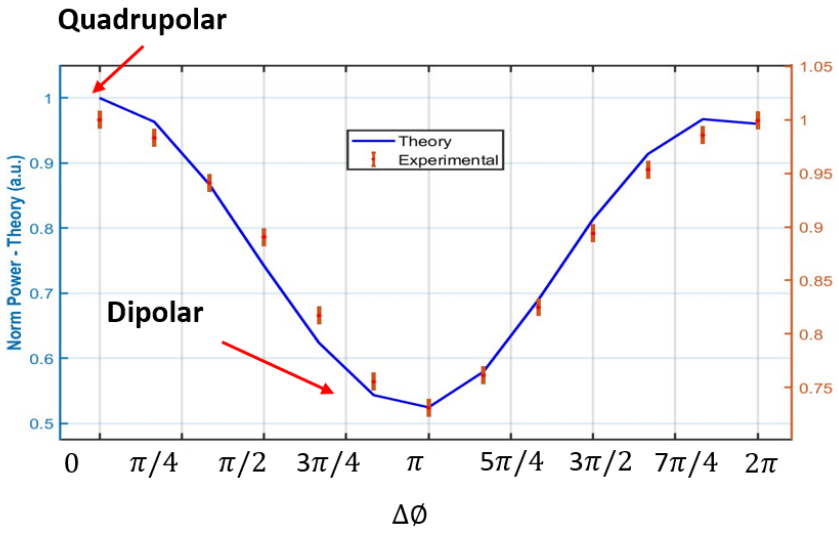

Figure 9. Normalized radiated power as a function of phase difference $\Delta\phi$ controlled experimentally by varying the optical path length ΔL. Theoretical prediction (blue curve) and experimental data (red dots with vertical error bars representing the noise level δ). In this experiment, $\Delta\phi$ was tuned by translating a mirror in fine steps to adjust ΔL between the incident Gaussian beams, producing a full sensing cycle in under 5

seconds. The quadrupolar mode (maximum in normalized power) occurs at $\Delta\phi = \pi$, which corresponds to $\Delta L = 0$. The dipolar mode (minimum in normalized power) occurs at $\Delta\phi = 0$, reached when $\Delta L = \lambda_0/2$. Note the different scales used to plot the experimental and theoretical results.

5.2 Refractometric Response – Bulk Sensing

We now proceed to demonstrate the interferometric behavior of the sensor with $\Delta\phi$ by altering the refractive index of the sensing solution flowing in the microfluidic channel. As previously mentioned, when the microfluidic channel is filled with water ($n_{H_2O} = 1.333$) and both Gaussian beams excite the grating couplers with the same phase, the SPP wave in the sensing arm has a phase difference of $\Delta\phi \approx \pi$ compared to the SPP wave in the reference arm. This phase difference results in the excitation of the quadrupolar mode, characterized by its distinct double-lobe far-field radiation pattern. To transition from this state to that corresponding to the dipolar mode (single lobe in the far-field), the phase difference must change by π, which requires a refractive index increase of $\Delta n \sim 10^{-2}$ from that of water in the sensing arm. Thus, we prepared glycerol-water solutions to slightly increase the refractive index of water over this range. As described in Section E of the supplementary materials, we determined that a glycerol concentration of ~7% (v/v) would produce a refractive index change of $\Delta n \sim 10^{-2}$. Thus, solutions with concentrations ranging from 0% to 10% (v/v) were prepared.

The solutions were then injected into the microfluidic channel of a sensor to observe their effect on *NP*. Fig. 10a plots the experimental data points as the red dots normalized to the maximum value for three glycerol concentrations: 0%, 3% and 7% (v/v). Vertical error bars correspond to the previously defined noise level δ. The measurements are compared on the same plot to the theoretical response (blue curve), computed from FEM simulations of the sensing experiment (as in Fig. 9). The experimental response follows the same sinusoidal trend as theory; however, the experimental visibility calculated with Eq. (3), is 18% whereas the theoretical visibility is 33%. The normalized powers vary sinusoidally with the refractive index change, starting at a maximum when the refractive index is 1.333 (pure water), as described earlier. It decreases to a minimum when the refractive index is approximately 1.345, which corresponds to the refractive index of CYTOP.

To further validate the device's operation, we conducted an additional experiment summarized in Fig. 10b. In this experiment, we measured four distinct bulk steps over a one-minute period. Initially, a 7% glycerol solution was introduced into the sensing channel, followed sequentially by 0%, 3%, and finally 7% again. Integrating the intensity of the 1D profile extracted from each recorded frame, as described at the start of Section 5, generates the sensogram shown in Fig. 10b, demonstrating the sensor's ability to detect refractive index changes in real time. The selected glycerol concentrations (0% and 7%) represent the extreme cases of $\Delta\phi$, transitioning between 0 and π, whereas the 3% concentration serves as an intermediate value.

Although this work does not focus on optimizing detection performance, we performed a basic analysis of figures of merit to estimate the current capabilities of the sensor. This analysis is based on the transition between 3% and 7% glycerol, where the interferometric response is steepest. The signal change (ΔS) between 3% and 7% was measured as $\Delta S = 1.000 - 0.841 = 0.159$. The corresponding refractive index change (Δn) is $\Delta n = 1.3431 - 1.3376 = 5.5 \times 10^{-3}$ RIU. From these values, the signal-to-noise ratio (SNR) is $SNR = \Delta S/\delta = 0.159/6.8 \times 10^{-3} = 23.5$, the bulk sensitivity ($S_b$) is $S_b = \Delta S/\Delta n = 0.159/5.5 \times 10^{-3} = 27.4\ \text{RIU}^{-1}$ and the limit of detection (LOD) for SNR = 1 is $\text{LOD} = \delta/S_b = 6.8 \times 10^{-3}/27.4 = 2.47 \times 10^{-4}$ RIU. Based on the linear relationship between refractive index and glycerol concentration, we estimate that a LOD of 2.47×10^{-4} RIU corresponds to approximately 0.17% v/v glycerol. For a 50 mL sample, this is equivalent to 0.085 mL of glycerol or approximately 1.16×10^{-3} mol, yielding a concentration of ~23.2 mM. The limiting factor in our LOD is not the biosensor architecture but rather the instability of the optical setup, particularly due to mechanical drift and fluctuations - the set-up is mechanically complex as it was constructed to enable dual-beam interrogation with a continuously variable phase difference, rather than optimized for stability.

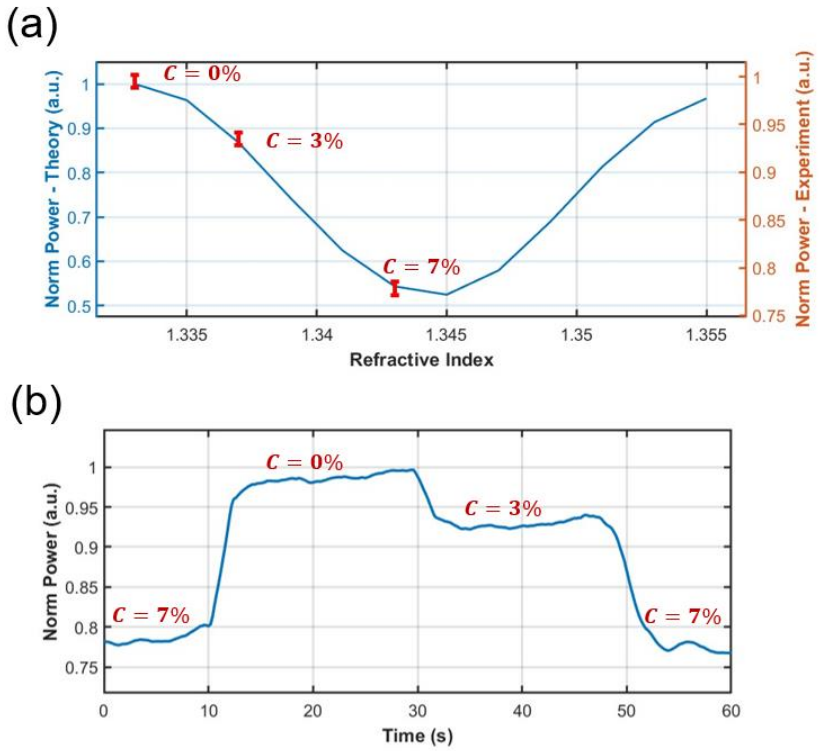

Figure 10. (a) Normalized radiated power *vs*. refractive index increase from that of water (Δn). Theory (blue curve) and experiment (red dots with vertical error bars representing the noise level δ) for $0\%, 3\%,$ and 7% glycerol concentrations. (b) Sensogram showing real-time response to $7\%, 0\%, 3\%,$ and 7% glycerol solutions injected sequentially into the sensor.

6. Conclusion

The fabrication and testing of an interferometric sensor based on the selective excitation of resonant modes in a multimode nanoslit is reported. The fabrication process involved a series of wafer-based fabrication techniques, each optimized to address a specific aspect of fabrication. Electron beam lithography and focused ion beam milling were employed to define and pattern the grating couplers at the nanoscale, and the nanoslits, respectively. CYTOP was used as the optical cladding into which microfluidic channels were etched using reactive ion etching through a hard (aluminum) mask to retain high fidelity of the channel definition and placement. Wafer bonding was used to seal the microfluidic channels, enabling fluid delivery to the sensing region and structural stability. Chips were obtained for testing by dicing wafers using a precision dicing saw. A test jig was developed to hold a chip under test, interface and seal three microfluidic channels simultaneously, while enabling perpendicular optical interrogation and imaging using microscope objectives. The ability of the device to detect phase differences between the surface plasmon waves interfering on a nanoslit was tested using two methods: changing the optical path length of one of the two incident Gaussian beams and injecting various water-glycerol solutions into a microfluidic channel. Additionally, we imaged the transition of the dipolar to quadrupolar modes of the nanoslit as the phase of the sensing SPP was varied relative to the reference SPP. The experimental results exhibit the same trends as expected theoretically. The ability to perform bulk sensing highlights the sensor's potential for detecting

low-concentration analytes with high accuracy, and the ease with which the sensor is arrayed holds promise for multiplexing applications. With improved optical stability and system integration, the platform could reach much lower detection limits, enabling sensing in the micromolar concentration regime and beyond.

Acknowledgements:

Funding provided by the Natural Sciences and Engineering Research Council of Canada (grant number 210396), CONAHCYT National System of Researchers (SNI 1047863), Federico Baur Endowed Chair in Nanotechnology (ILST002-23ID69001), Graduate Seed Program of Tecnológico de Monterrey, and CONAHCYT (CVU 900707) are gratefully acknowledged.

The authors extend special thanks to Deepthi Sekhar for her assistance in the Nanofabrication Laboratory, particularly with the hard mask photolithography process and microfluidic etching of CYTOP. Gratitude is also extended to Ewa Lisicka for her guidance in preparing lithography masks using the DW2000 software, and to Dr. Spyridon Ntais for assistance in the Nanofabrication Laboratory. Further appreciation is expressed to Benoit Raymond and Alexandre Diver from the mechanical workshop at the University of Ottawa for their craftsmanship in fabricating the test jig.

References:

[1] Scheller, F., & Schubert, F. (1991). Biosensors. Elsevier.
[2] Turner, A. P. (2013). Biosensors: sense and sensibility. Chemical Society Reviews, 42(8), 3184-3196.
[3] Justino, C. I., Rocha-Santos, T. A., & Duarte, A. C. (2013). Advances in point-of-care technologies with biosensors based on carbon nanotubes. TrAC Trends in Analytical Chemistry, 45, 24-36.
[4] Karunakaran, C., Rajkumar, R., & Bhargava, K. (2015). Introduction to biosensors. In Biosensors and bioelectronics (pp. 1-68). Elsevier.
[5] Ronkainen, N. J., Halsall, H. B., & Heineman, W. R. (2010). Electrochemical biosensors. Chemical Society Reviews, 39(5), 1747-1763.
[6] Arugula, M. A., Zhang, Y., & Simonian, A. L. (2014). Biosensors as 21st century technology for detecting genetically modified organisms in food and feed. Analytical Chemistry, 86(1), 119-129.
[7] Wolfbeis, O. S. (2015). An overview of nanoparticles commonly used in fluorescent bioimaging. Chemical Society Reviews, 44(14), 4743-4768.
[8] Fan, X., White, I. M., Shopova, S. I., Zhu, H., Suter, J. D., & Sun, Y. (2008). Sensitive optical biosensors for unlabeled targets: A review. analytica chimica acta, 620(1-2), 8-26.
[9] Culshaw, B., & Kersey, A. (2008). Fiber-optic sensing: A historical perspective. Journal of lightwave technology, 26(9), 1064-1078.
[10] Pollet, J., Delport, F., Janssen, K. P. F., Tran, D. T., Wouters, J., Verbiest, T., & Lammertyn, J. (2011). Fast and accurate peanut allergen detection with nanobead enhanced optical fiber SPR biosensor. Talanta, 83(5), 1436-1441.
[11] Schäferling, M. (2012). The art of fluorescence imaging with chemical sensors. Angewandte Chemie International Edition, 51(15), 3532-3554.
[12] Ligler, F. S., & Taitt, C. R. (Eds.). (2011). Optical biosensors: today and tomorrow. Elsevier.
[13] Fan, X., & White, I. M. (2011). Optofluidic microsystems for chemical and biological analysis. Nature photonics, 5(10), 591-597.
[14] Tran Ngoc Huy, D., Iswanto, A. H., Catalan Opulencia, M. J., Al-Saikhan, F., Timoshin, A., Abed, A. M., ... & Van Tuan, P. (2024). Optical and Electrochemical Aptasensors Developed for the Detection of Alpha-Fetoprotein. Critical Reviews in Analytical Chemistry, 54(4), 857-871.
[15] Hu, R., Liu, T., Zhang, X. B., Huan, S. Y., Wu, C., Fu, T., & Tan, W. (2014). Multicolor fluorescent biosensor for multiplexed detection of DNA. Analytical chemistry, 86(10), 5009-5016.

[16] Daems, D., Knez, K., Delport, F., Spasic, D., & Lammertyn, J. (2016). Real-time PCR melting analysis with fiber optic SPR enables multiplex DNA identification of bacteria. Analyst, 141(6), 1906-1911.
[17] Hotate, K., & He, Z. (2006). Synthesis of optical-coherence function and its applications in distributed and multiplexed optical sensing. Journal of Lightwave Technology, 24(7), 2541.
[18] Rodriguez-Lorenzo, L., Fabris, L., & Alvarez-Puebla, R. A. (2012). Multiplex optical sensing with surface-enhanced Raman scattering: a critical review. Analytica chimica acta, 745, 10-23.
[19] Pei, X., Tao, G., Wu, X., Ma, Y., Li, R., & Li, N. (2020). Nanomaterial-based multiplex optical sensors. Analyst, 145(12), 4111-4123.
[20] Werley, C. A., Boccardo, S., Rigamonti, A., Hansson, E. M., & Cohen, A. E. (2020). Multiplexed Optical Sensors in Arrayed Islands of Cells for multimodal recordings of cellular physiology. Nature communications, 11(1), 3881.
[21] Kersey, A. D., & Dandridge, A. (1988). Distributed and multiplexed fibre-optic sensor systems. Journal of the institution of Electronic and Radio Engineers, 58(5S), S99-S111.
[22] Belsley, K. L., Carroll, J. B., Hess, L. A., Huber, D. R., & Schmadel, D. (1986, January). Optically multiplexed interferometric fiber optic sensor system. In Fiber Optic and Laser Sensors III (Vol. 566, pp. 257-264). SPIE.
[23] Singh, P. (2016). SPR biosensors: historical perspectives and current challenges. Sensors and actuators B: Chemical, 229, 110-130.
[24] Olaru, A., Bala, C., Jaffrezic-Renault, N., & Aboul-Enein, H. Y. (2015). Surface plasmon resonance (SPR) biosensors in pharmaceutical analysis. Critical reviews in analytical chemistry, 45(2), 97-105.
[25] Homola, J. (2003). Present and future of surface plasmon resonance biosensors. Analytical and bioanalytical chemistry, 377, 528-539.
[26] Wang, Q., Ren, Z. H., Zhao, W. M., Wang, L., Yan, X., Zhu, A. S., ... & Zhang, K. K. (2022). Research advances on surface plasmon resonance biosensors. Nanoscale, 14(3), 564-591.
[27] Ravindran, N., Kumar, S., CA, M., Thirunavookarasu S, N., & CK, S. (2023). Recent advances in Surface Plasmon Resonance (SPR) biosensors for food analysis: A review. Critical Reviews in Food Science and Nutrition, 63(8), 1055-1077.
[28] Fathi, F., Rashidi, M. R., & Omidi, Y. (2019). Ultra-sensitive detection by metal nanoparticles-mediated enhanced SPR biosensors. Talanta, 192, 118-127.
[29] Torun, Ö., Boyacı, İ. H., Temür, E., & Tamer, U. (2012). Comparison of sensing strategies in SPR biosensor for rapid and sensitive enumeration of bacteria. Biosensors and Bioelectronics, 37(1), 53-60.
[30] Piliarik, M., Vaisocherová, H., & Homola, J. (2009). Surface plasmon resonance biosensing. Biosensors and Biodetection, 65-88.
[31] Rizal, C., & Belotelov, V. (2019). Sensitivity comparison of surface plasmon resonance (SPR) and magneto-optic SPR biosensors. The European Physical Journal Plus, 134(9), 435.
[32] Boozer, C., Yu, Q., Chen, S., Lee, C. Y., Homola, J., Yee, S. S., & Jiang, S. (2003). Surface functionalization for self-referencing surface plasmon resonance (SPR) biosensors by multi-step self-assembly. Sensors and Actuators B: Chemical, 90(1-3), 22-30.
[33] Kabashin, A. V., & Nikitin, P. I. (1998). Surface plasmon resonance interferometer for bio-and chemical-sensors. Optics communications, 150(1-6), 5-8.
[34] Nikitin, P. I., Grigorenko, A. N., Beloglazov, A. A., Valeiko, M. V., Savchuk, A. I., Savchuk, O. A., ... & Salzer, R. (2000). Surface plasmon resonance interferometry for micro-array biosensing. Sensors and Actuators A: Physical, 85(1-3), 189-193.
[35] Singh, P. (2016). SPR biosensors: historical perspectives and current challenges. Sensors and actuators B: Chemical, 229, 110-130.

[36] Xinglong, Y., Dingxin, W., Xing, W., Xiang, D., Wei, L., & Xinsheng, Z. (2005). A surface plasmon resonance imaging interferometry for protein micro-array detection. Sensors and Actuators B: Chemical, 108(1-2), 765-771.
[37] Sheridan, A. K., Harris, R. D., Bartlett, P. N., & Wilkinson, J. S. (2004). Phase interrogation of an integrated optical SPR sensor. Sensors and Actuators B: Chemical, 97(1), 114-121.
[38] Berini, P. (2008). Bulk and surface sensitivities of surface plasmon waveguides. New Journal of Physics, 10(10), 105010.
[39] Fan, H., & Berini, P. (2016). Bulk sensing using a long-range surface-plasmon dual-output Mach–Zehnder interferometer. Journal of Lightwave Technology, 34(11), 2631-2638.
[40] Tencer, M., Nie, H.-Y., Berini, P., "Electrochemical differentiation and ToF-SIMS characterization of thiol-coated gold features for (bio)chemical sensor applications," Journal of the Electrochemical Society, Vol. 156, pp. J386-J392, 2009.
[41] Felix-Rendon, U., Berini, P., & De Leon, I. (2021). Ultrasensitive nanoplasmonic biosensor based on interferometric excitation of multipolar plasmonic modes. Optics Express, 29(11), 17365-17374.
[42] Mostafavi, F., Jafari, Z., Lollie, M. L., You, C., De Leon, I., & Magaña-Loaiza, O. S. (2022). Conditional quantum plasmonic sensing. Nanophotonics, 11(14), 3299-3306.
[43] Valero, M., De Leon, I., Ray, M., & Berini, P. (2024). Multiplexed biosensors based on interference of surface plasmons in multimode nanoslits. Applied Optics, 64(1), 50-63.
[44] Valero, M., Mayoral-Astorga, L. A., Northfield, H., Choi, H. W., De Leon, I., Ray, M., & Berini, P. (2025). Selective modal excitation in a multimode nanoslit by interference of surface plasmon waves. Nanoscale Advances.
[45] Asahi Glass Company, "Technical Information Cytop," distributed by Bellex International Corporation, http://www. bellexinternational.com/.
[46] Hale, G. M., & Querry, M. R. (1973). Optical constants of water in the 200-nm to 200-μm wavelength region. Applied optics, 12(3), 555-563.
[47] Maier, S. A. (2007). Plasmonics: fundamentals and applications (Vol. 1, p. 245). New York: springer.
[48] Johnson, P. B., & Christy, R. W. (1972). Optical constants of the noble metals. Physical review B, 6(12), 4370.
[49] Barnes, W. L., Preist, T. W., Kitson, S. C., & Sambles, J. R. (1996). Physical origin of photonic energy gaps in the propagation of surface plasmons on gratings. Physical Review B, 54(9), 6227.
[50] Khodami, M., & Berini, P. (2019). Grating couplers for (Bloch) long-range surface plasmons on metal stripe waveguides. JOSA B, 36(7), 1921-1930.
[51] Chen, C., & Berini, P. (2010). Grating couplers for broadside input and output coupling of long-range surface plasmons. Optics express, 18(8), 8006-8018.
[52] Palik, E. D. (Ed.). (1998). Handbook of optical constants of solids (Vol. 3). Academic press.
[53] Asif, M., Krupin, O., Wong, W. R., Hirbodvash, Z., Lisicka-Skrzek, E., Hahn, C., ... & Berini, P. (2020). Wafer-bonded surface plasmon waveguide sensors with in-plane microfluidic interfaces. Journal of Micromechanics and Microengineering, 30(9), 095004.
[54] Sekhar, D., Lisicka-Skrzek, E., & Berini, P. (2023). Wafer-bonded deep fluidics in BCB with in-plane coupling for lab-on-a-chip applications. Micro and Nano Engineering, 21, 100227.
[55] Heavens, O. S. (1965). Principles of Optics. By Born and Wolf. 1964.(Pergamon). The Mathematical Gazette, 49(370), 485-485.
[56] Mandel, L., & Wolf, E. (1995). Optical Coherence and Quantum Optics Cambridge Univ. Press, Cambridge
[57] Hariharan, P. (2010). Basics of interferometry. Elsevier.
[58] Malacara Hernández, D. (2015). Óptica básica.
[59] Saleh, B. E., & Teich, M. C. (2019). Fundamentals of photonics. john Wiley & sons.

[60] Mehra, R., & Tripathi, J. (2010). Mach zehnder Interferometer and it's Applications. International Journal of Computer Applications, 1(9), 110-118.
[61] Rarity, J. G., Tapster, P. R., Jakeman, E., Larchuk, T., Campos, R. A., Teich, M. C., & Saleh, B. E. A. (1990). Two-photon interference in a Mach-Zehnder interferometer. Physical review letters, 65(11), 1348.
[62] Saghaei, H., Elyasi, P., & Karimzadeh, R. (2019). Design, fabrication, and characterization of Mach–Zehnder interferometers. Photonics and Nanostructures-Fundamentals and Applications, 37, 100733.
[63] Dandridge, A. (2024). Fiber optic sensors based on the Mach–Zehnder and Michelson interferometers. Fiber optic sensors: an introduction for engineers and scientists, 213-248.
[64] Ouyang, B., Li, Y., Kruidhof, M., Horsten, R., van Dongen, K. W., & Caro, J. (2019). On-chip silicon Mach–Zehnder interferometer sensor for ultrasound detection. Optics Letters, 44(8), 1928-1931.
[65] Khan, A., Krupin, O., Lisicka-Skrzek, E., & Berini, P. (2013). Mach-Zehnder refractometric sensor using long-range surface plasmon waveguides. Applied Physics Letters, 103(11).

5.4 Supplementary file

The following section provides the supplementary file, which follows verbatim.

Supplementary Materials for:

Fabrication of Surface Plasmon Interferometric Sensors Exploiting Multimode Nanoslits

Marcos Valero,[1,2] Howard Northfield,[2] Hyung Choi,[2] Luis-Angel Mayoral-Astorga,[2] Graham Killaire,[3] Arnaud Weck,[3,4,6] Israel De Leon,[2,5] Mallar Ray,[1] and Pierre Berini[2,3,6,*]

[1]School of Engineering and Sciences, Tecnológico de Monterrey, Monterrey, Nuevo León 64849, Mexico
[2]School of Electrical Engineering and Computer Science, University of Ottawa, Ottawa, Ontario K1N 6N5, Canada
[3]Department of Physics, University of Ottawa, Ottawa, Ontario K1N 6N5, Canada
[4]Department of Mechanical Engineering, University of Ottawa, Ontario, Canada, K1N 6N5
[5]ASML Netherlands B.V., De Run 6501, 5504 DR Veldhoven, The Netherlands.
[6]Nexus for Quantum Technologies Institute, University of Ottawa, Ottawa, Ontario K1N 6N5, Canada

* pberini@uottawa.ca

Section A: E-beam lithography

The wafer bearing PMMA is placed into the e-beam lithography (EBL) tool. Once inside, and after the vacuum is engaged, the software is launched with the prepared layout design. The first step in the process involves global and local alignment to ensure precision. Global alignment is to define the location of the sample in the chamber. For global alignment, three points are selected to define the overall wafer area and establish the framework for the entire process. These points, measured in millimeters, are located at coordinates (0,25) at the top of the wafer, (-25,0) on the left side, and (0,-25) at the bottom. Local alignment is then performed to define the location of the patterning on the sample. Three "local" points are identified on the sample, in millimeters coordinates (0,10), (-8,-5), and (8,-5) were arbitrarily selected. These points allow the system to horizontally track the wafer's position closely and compensate for distance variations from the electron source to the sample surface due to sample orientation and thickness deviations. Together, the global and local alignments ensure the electron beam remains precisely focused and positioned during the patterning process.

Once the global and local alignment is completed, the next step is to configure the E-beam system parameters for the exposure process. These are: acceleration voltage (EHT, kV), which determines the depth of penetration and resolution of the electron beam, with higher voltages providing finer resolution; aperture diameter (AD, μm), which controls the beam's focus and precision, where smaller apertures result in more detailed patterning; working distance (WD, mm), defined as the space between the sample surface and the electron beam source, which influences beam focus and convergence; step size (SS, nm), which defines the distance between beam scans; starting area dose (AD, μC/cm²) which sets the number of electrons delivered to the resist per unit area. With these parameters (and some non-user definable parameters) the system refines the AD. This is the parameter that is altered, using a "dose factor", a percentage factor, when optimizing the exposure during process development, to avoid overexposure or underexposure.

The e-beam exposure process was divided into two exposure steps performed in a single loading session. The first exposure was for the large dimension alignment features and labeling, which require less precision. Here to save time, exposure settings were used that result in a faster exposure. Without unloading the sample, the second exposure of the grating couplers was performed. The grating couplers are small dimension features which require greater exposure precision. Here the exposure settings were changed for the best feature resolution. This two-step approach offers time optimization, and the best resolution of the critical features, the grating couplers. The two exposures were performed without sample unloading so the relative positioning between the alignment mark and gratings, required for subsequent wet lithography, is maintained. The specific exposure parameters for both steps are summarized in Table S3.

Section B: Bi-layer photolithography process

Once the edge bead was removed, we prepared the CYTOP surface for photolithography by exposing the wafer to an isotropic oxygen plasma under the following conditions: oxygen flow at 10 SCCM, pressure of 3 Pa, and a power of 25 W for 30 seconds. This process increases slightly the surface roughness to promote the adhesion of photoresist without compromising the thickness of the layer. The wafer was then subjected to an HDMS (Hexamethyldisilazane) treatment. HDMS is a silane coupling agent that reacts with hydroxyl groups on the substrate, forming a thin siloxane layer that creates a hydrophobic surface. This treatment enhances the adhesion of photoresists by improving their wetting properties and ensuring uniform coverage. The sample was placed in an HMDS oven at 100 °C for 18 min, allowing the chemical to vaporize and uniformly coat the substrate. Specifically, the process included three dehydration purge cycles and three exit purge cycles to remove residual water and prevent contamination. The chamber was maintained within a pressure range of 10–500 Torr, with a base pressure of 1 Torr, under a dry nitrogen atmosphere to ensure consistent and uniform coating.

Immediately after HDMS treatment, the sample is transferred to the spinner for the application of the lift-off resist LOR-1A. Once in the spinner, the sample is secured under vacuum, LOR-1A is carefully dispensed over the entire surface of the wafer using a pipette to ensure full coverage, and the spin-coating procedure detailed in Table S6 of the supplementary file is executed. Following this, the sample undergoes a post-spin bake at 185°C for 5 min to cure the LOR-1A layer. The (positive) photoresist SPR 955 is then applied using the same spinning parameters (Table S6), followed by a post-spin relaxation step, during which the vacuum is released, and the sample is left to rest for 60 s. The wafer is then baked at 90 °C for 5 min to cure the SPR 955 layer. At this stage, the wafer is ready for UV (365 nm, I-line filtered) exposure in the mask aligner (OAI 200-IR) to define the microfluidic channel patterns.

The I-line exposure dose specified by the SPR 955 manufacturer is 95 mJ/cm². This dose was achieved using an exposure time of ~10 s, calculated based on the I-line intensity produced by the mask aligner (measured using a UV radiometer). If the exposure time is too short, the photoresist will not be fully exposed resulting in incomplete development, and conversely, if the exposure time is too long, unintended exposure of areas outside the desired pattern occurs due to scattering effects reducing the resolution and sharpness of the features. The brightfield photolithography mask bears labelling, dicing marks, designs for the microfluidic channels and alignment marks that register to those defined during the e-beam lithography step to ensure that the microfluidic channels align precisely to grating couplers and nanoslits.

After exposure, the wafer is developed by immersion in MF-24A (aqueous TMAH developer) for 90 s, during which the exposed areas of the photoresist are dissolved. After 45 s, the sample is subjected to ultrasonic agitation at 30% power and 80 kHz for 10 s. The sample is then removed from the ultrasonic bath and manually agitated for the final 35 seconds. Once development is complete, the sample is rinsed thoroughly with deionized water to stop the development process and remove any residue. Finally, the sample is dried using nitrogen. A chip bearing developed lithography featuring devices J1 (Table 1, main text), can be seen in Fig. 5a of the main text.

After development, the next step was to deposit and lift-off an aluminum mask, which acts as a protective layer covering the areas where CYTOP should not be etched, when forming the microfluidic channels. The aluminum layer, 45 nm thick, was deposited on the wafer using e-beam evaporation. This thickness was chosen to balance durability during etch and ease of lift-off. The lift-off process also had to be precisely controlled, as excessive time or higher temperatures could lead to cracks in the aluminum mask, rendering it unusable. To lift off the aluminum, we used 1165 solvent in two stages: an initial dirty bath followed by a clean bath, both heated to 46 °C. The wafer was immersed for 1 min in each bath, enough to clear the wafer from unwanted aluminum (leaving the wafer in the solvent for too long risks cracking the aluminum mask). After the lift-off was completed, the sample was rinsed with deionized water to remove any residual chemicals, then dried thoroughly with a nitrogen gun to ensure a clean surface. The resulting aluminum

mask protects the areas of CYTOP that are to remain intact, whereas the open areas corresponded to the microfluidic channels to be etched in the next step. A chip featuring the aluminum mask is shown in Fig. 5b of the main text.

Section C: Laser cutting of gasket

The laser cut holes in the gasket material were generated using a Light Conversion Pharos laser outputting 1030 nm, 312 fs pulses. Holes were generated via repeatedly passing the laser in circles of diameters ranging from 300-600 μm via a trepanning technique. The circular toolpath was accomplished by keeping the samples fixed in place and moving the laser beam via a galvo scanner (Aerotech AGV-10HPO) equipped with a telecentric f-theta lens (Silloptics S4LFT4147/328) to focus the pulses to an in-focus spot size of ~20 μm. Holes were drilled using a repetition rate of 1 kHz as higher repetition rates were observed to cause increased physical and chemical degradation of the surrounding gasket material due to heat buildup. A variety of pulse energies were tested depending on the thickness of the gasket and the need to penetrate through protective layers used to cover the adhesive surfaces of the material. These protective covers lead to multiple material interfaces and although the gasket alone could be cut at low pulse energies down to 10 s of μJ, the total system of top protector, gasket and bottom protector was cut using a pulse energy as high as 100 μJ. Overall, 400 μm diameter circular tooling paths were observed to yield the optimal result for the microfluidic interfacing.

Section D: Optical test set-up

To characterize the plasmonic interferometer, an optical setup was used to illuminate the chip with two Gaussian beams and to capture the resulting radiated signal. The setup is detailed in Fig. S1 and includes several components to ensure precise illumination of the device and signal detection. A coherent Gaussian beam of wavelength $\lambda_0 = 850\,\mathrm{nm}$ was generated using a single-mode fiber-coupled laser diode (QPhotonics, QFLD-850-100S-PM, 100 mW). The fiber tip was mounted on an x-y-z positioner to align the output beam to the optical axis of the setup and positioned at the focal plane of a beam-expanding microscope objective (Newport N-20x, NA = 0.4). Adjusting the z-position of the objective enabled precise control of the beam size, achieving a collimated beam with a radius of approximately 1 mm at the output. The beam was TM-polarized relative to the grating couplers using a linear polarizer (Thorlabs LPVIS050-MP2) and a λ/2 waveplate (Thorlabs Achromatic, 690-1200 nm). Power adjustments were made using neutral density (ND) filters (Thorlabs NDUV04A).

The beam was then split into two equal parts by a non-polarizing 50:50 beam splitter (Thorlabs, BS013), beam splitter 1 (BS1). The two beams are directed along different paths, one of which includes mirrors (Thorlabs BB1-E02) mounted on a nanometric translation stage (Thorlabs Nanomax 300) to control the optical path length difference (ΔL). A path length change of $\Delta L = \lambda_0/2$ induces a phase difference of $\Delta\phi = \pi$ between the beams. It is important to note that in Fig. S1, $\Delta L/2$ is shown because each step of the nanometric stage effectively reduces or increases ΔL by twice the physical displacement of the stage due to the configuration of the mirrors. The radius of the beams was reduced to $w = 5\,\mu\mathrm{m}$ at the focal plane of the microscope objective (Nikon Plan 10×, NA = 0.25) using the beam expander. The Gaussian beams were aligned with the grating couplers on the plasmonic interferometer, exciting surface plasmon polaritons (SPPs). These SPPs converge at the nanoslit, where interference occurs.

To locate and align the Gaussian beams on the grating couplers, the setup incorporated broadband visible illumination from a fiber illuminator (Thorlabs OSL2IR). The light was introduced via a beam splitter (Thorlabs BS013) and focused onto the sample. The reflected light was directed back through the microscope objectives and captured by CCD2 (Thorlabs DCC1645C), allowing precise visualization of the device under test.

To study the interference modes, a 63× water-immersion objective (Nikon Plan Fluor, NA = 1.2, model MRH08620) was used to image the radiated intensity through the nanoslit. This objective minimizes

reflection and scattering effects, providing the spatial resolution required to distinguish dipolar and quadrupolar modes.

The images produced by the optical microscope at the output nanoslit plane were captured at 5 frames per second using CCD1 (Thorlabs DCC1645C). From these videos, a cutline transverse to the slit was extracted to compare with the calculated one-dimensional intensity distributions. Experimental values were then normalized to their maximum to mitigate variations caused by camera calibration and optical losses. This approach ensured comparability with theoretical predictions without requiring absolute transmission values.

For radiated power measurements, a 10× microscope objective (Nikon Plan, NA = 0.25, model MRH00020) was employed. This choice leveraged the consistency of integrated power changes regardless of the observation distance, simplifying data acquisition.

The overall schematic of the optical setup is shown in Figure S1a, while a conceptual zoom of the sensing region and nanoslit interrogation is presented in Figure S1b. A photograph of the actual experimental arrangement is shown in Figure S1c, highlighting key components such as the microchip holder, beam path, and optical detection elements.

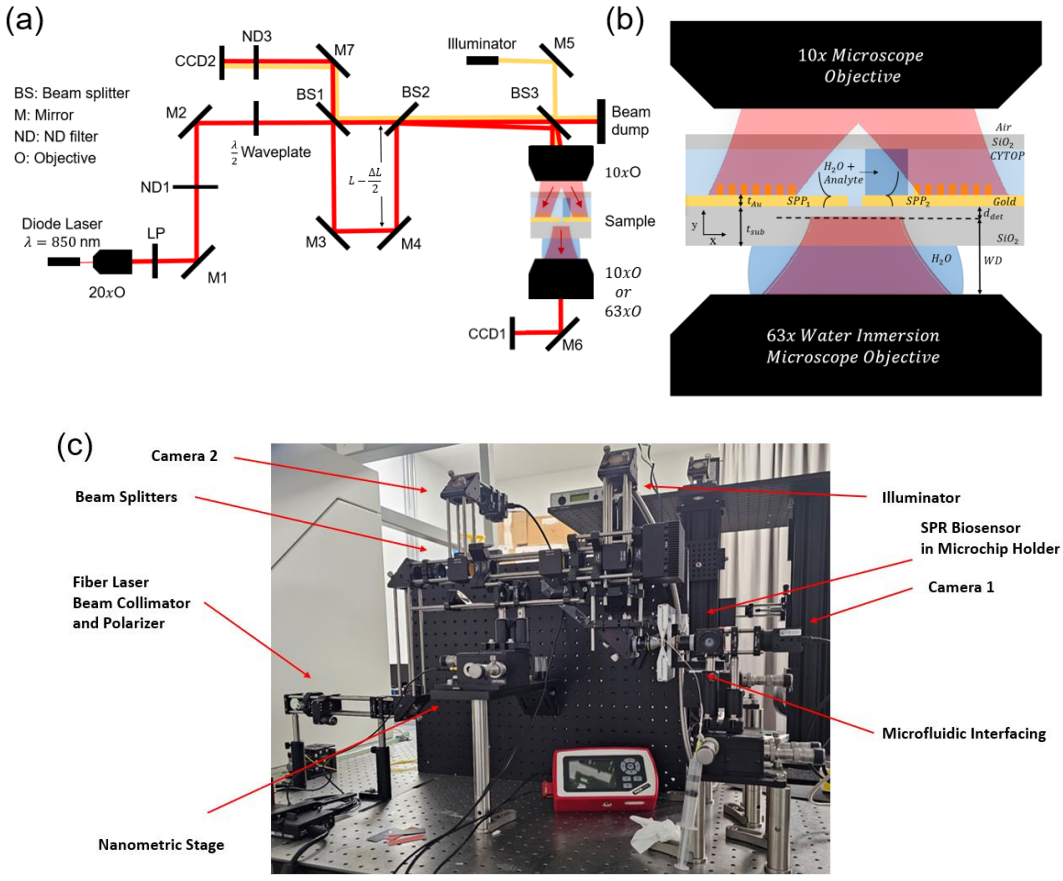

Figure S1. Optical setup for characterizing the plasmonic interferometer. (a) Schematic diagram of the interferometric test setup. Schematic of the optical setup for characterizing the plasmonic interferometer. Two Gaussian beams illuminate the device via grating couplers, exciting surface plasmon polaritons that

interfere at the nanoslit. Phase differences are controlled by a nanometric stage, and signals are captured using high-resolution microscope objectives and CCD cameras to analyze interference patterns and power distributions. (b) Zoomed-in conceptual diagram of the microchip under test, illustrating the dual-Gaussian beam interrogation of the biosensor via grating couplers. The resulting signal is collected through microscope objectives from both sides of the chip. This diagram highlights the main components of the interferometric sensor and the optical interrogation mechanism. (c) Photograph of the experimental setup used for characterization. Key components such as the SPR biosensor, microchip holder, CCD cameras, beam splitters, and fluidic connections are labeled.

Section E: Sensing solutions

To prepare the glycerol-water solutions necessary for refractometric sensing, we used the following linear equation for its refractive index ($n_{Solution}$) [1,2]:

$$n_{Solution} = n_{H_2O} + C \cdot (n_{Glycerol} - n_{H_2O}) \quad (1)$$

where C is the glycerol concentration in volume percentage (v/v), n_{H_2O} is the refractive index of water, and $n_{Glycerol}$ is the refractive index of pure glycerol. For our calculations, we used standard refractive index values at a wavelength of $\lambda = 589$ nm (sodium D-line): $n_{H_2O} = 1.333$ and $n_{Glycerol} = 1.472$ [3]. Using these values, we determined that a glycerol concentration of approximately 7% (v/v) would produce a refractive index change of $\Delta n = 10^{-2}$. Based on this, we prepared solutions with concentrations ranging from 0% to 10% (v/v) to systematically create different refractive index changes.

Δn is defined as the difference between the refractive index of a solution and that of pure water ($n_{Solution} - n_{H_2O}$), where $\Delta n = 0$ represents pure water. After preparing the solutions, we measured their refractive index using an Abbe refractometer (ATAGO, model NAR-3T, serial number 180474), which operates at the sodium D-line wavelength ($\lambda = 589$ nm). The results of the Δn calculations and measurements as a function of glycerol concentration are presented in Fig. S2. The experimental Δn values closely align with the theoretical predictions, validating our preparation. Specific points are highlighted at $C = 0\%$ ($\Delta n = 0$), $C = 3\%$ ($\Delta n = 0.0046$), and $C = 7\%$ ($\Delta n = 0.0101$). Thus, the change in refractive index from $C = 0\%$ to $C = 7\%$ will produce a phase shift of $\Delta\phi \sim \pi$ in the sensing SPP (neglecting dispersion).

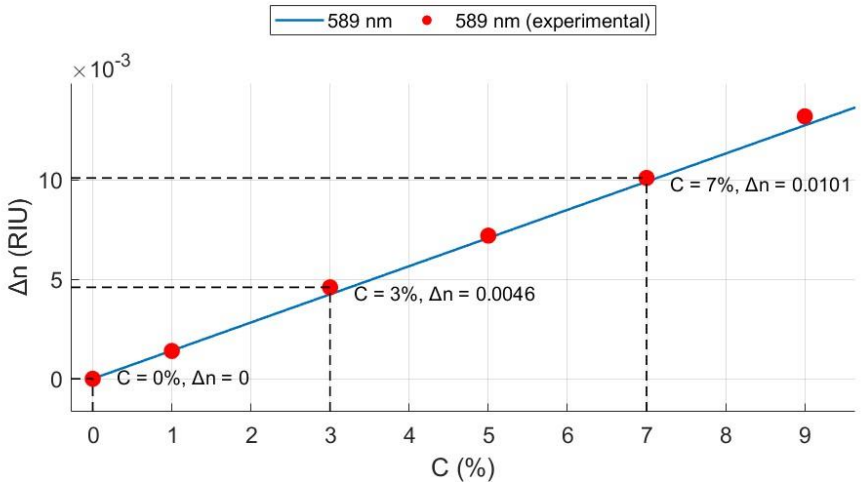

Figure S2. Computed (solid line) and measured (data points) refractive index change (Δn) in glycerol-water solutions as a function of glycerol concentration at a free-space wavelength of 589 nm.

Tables:

Table S1. Step-by-step cleaning process, detailing the chemicals used, time duration, and ultrasonic bath settings for each step, followed by nitrogen drying.

Step	Chemical	Time	Ultrasonic Settings	Action
1	Acetone	5 minutes	37 kHz, 100% power	Ultrasonic bath
2	Isopropyl alcohol (IPA)	5 minutes	37 kHz, 100% power	Ultrasonic bath
3	Deionized water	5 minutes	37 kHz, 100% power	Ultrasonic bath
4	N/A	N/A	N/A	Dried with nitrogen gun

Table S2. Spin-coating procedure for PMMA layer preparation.

Step	RPM	Acceleration (RPM/s)	Time (s)	Comments
1	---	100	10	Spread PMMA evenly across the wafer surface.
2	1000	---	5	Begin thinning the PMMA layer.
3	---	400	5	Allow the PMMA layer to settle uniformly.
4	3000	---	45	Achieve the final desired thickness.
5	0	-200	15	Gradually decelerate to ensure uniformity.

Table S3. Electron beam settings for the two exposure steps. The first step exposes alignment marks and labels, with higher aperture and current settings for faster processing. The second step, which patterns the grating couplers, uses higher voltage and a reduced aperture for finer precision. The dose factor is adjusted to ensure accurate exposure for the smaller grating features.

Parameter	First Step (alignment marks and labels)	Second Step (grating couplers)
EHT voltage (kV)	10.00	30.00
Aperture (µm)	30.00	10.00
Working distance (mm)	8.00	8.00
Dwell Time (µs)	2.60	2.90
Current (pA)	185.06	32.62
Step Size (nm)	16.00	6.00
Area Dose (µC/cm²)	187.95	262.75
Dose factor	1.00	0.82

Table S4. Optimized focused ion beam milling parameters for nanoslit fabrication.

Parameter	Optimal Setting
Acceleration voltage (kV)	30
Aperture (µm)	50
Current (pA)	100
Dwell time per spot (µs)	1
Spot spacing (nm)	2 (both vertical and horizontal)
Beam Travel Style	Double serpentine

Table S5. Spin-coating procedure for CYTOP deposition.

Step	RPM	Acceleration (RPM/s)	Time (s)	Comments
1	---	200	6	Spread CYTOP evenly across the wafer surface.
2	1000	---	10	Begin thinning the CYTOP layer.
3	---	200	3	Allow the CYTOP layer to settle uniformly.
4	1500	---	30	Achieve the final desired thickness.
5	0	-300	5	Gradually decelerate to ensure uniformity.

Table S6. Spin-coating procedure for LOR1A and SPR 955.

Step	RPM	Acceleration (RPM/s)	Time (s)	Comments
1	---	200	5	Spread SPR 955/LOR1A evenly across the wafer surface.
2	1000	---	5	Begin thinning the SPR 955/LOR1A layer.
3	---	500	4	Allow the SPR 955/LOR1A layer to settle uniformly.
4	3000	---	45	Achieve the final desired thickness.
5	0	-600	5	Gradually decelerate to ensure uniformity.

Table S7. Spin-coating procedure for AP3000 deposition.

Step	RPM	Acceleration (RPM/s)	Time (s)	Comments
1	---	300	10	Start spinning to spread AP3000 evenly.
2	3000	---	70	Maintain constant speed for uniform deposition.
3	---	-300	8	Gradual deceleration to avoid disruptions.

References:

[1] Weast, R. C. (1986). CRC handbook of chemistry and physics.

[2] Reis, J. C. R., Lampreia, I. M., Santos, Â. F., Moita, M. L. C., & Douhéret, G. (2010). Refractive index of liquid mixtures: theory and experiment. ChemPhysChem, 11(17), 3722-3733.

[3] Hoyt, L. F. (1934). New table of the refractive index of pure glycerol at 20 C. Industrial & Engineering Chemistry, 26(3), 329-332.

5.5 Figures of merit

From the sensogram shown in Figure 8b, we calculated various figures of merit to quantify the device's performance. The results are summarized in Table 5.1.

The noise level (δ) was determined from a stable interval in the sensogram, specifically between 12 and 25 seconds. This region displayed minimal signal variation, allowing for an accurate assessment of the baseline noise.

The signal change (ΔS) was calculated as the absolute difference in normalized power between consecutive transitions. Starting from 7% to 0%, the signal change represents the sensor's ability to distinguish between the highest and lowest refractive index steps. Similarly, the transitions from 0% to 3% and 3% to 7% reflect the sensor's response to intermediate refractive index changes. These signal changes indicate how effectively the sensor can respond to varying glycerol concentrations.

The signal-to-noise ratio (SNR) for each transition was given as:

$$\mathrm{SNR} = \frac{\Delta S}{\delta} \tag{5.1}$$

A higher SNR indicates a robust and distinguishable response, even in the presence of noise.

The bulk sensitivity (S_b), calculated as:

$$S_b = \frac{\Delta S}{\Delta n} \tag{5.2}$$

quantifies the device's ability to convert refractive index changes into measurable signal variations. This parameter is crucial for assessing the sensor's efficacy in detecting subtle changes in the analyte's refractive index.

Finally, the limit of detection (LOD) was calculated as:

$$\mathrm{LOD} = \frac{\delta}{S_b} \tag{5.3}$$

The LOD represents the smallest refractive index variation that the device can reliably detect, with smaller values indicating higher sensitivity.

These figures of merit were calculated for each transition observed in the sensogram, starting from 7% to 0%, then 0% to 3%, and finally 3% to 7%. The results in Table 5.1 highlight the sensor's figures of merit for bulk refractive index sensing. Each step exhibits varying sensitivity, as predicted in

previous studies [41-43], due to the sinusoidal relationship between sensitivity and the refractive index change. This sinusoidal behavior is reflected in all the calculated figures of merit. Notably, the highest sensitivity is observed for the transition from 3% to 7%, as expected, since this region corresponds to the steepest slope of the sinusoidal curve, where the signal changes most significantly with concentration.

While the figures of merit demonstrate the sensor's basic functionality, they are not yet competitive and fall below the expected values [43]. Specifically, the sensitivity is approximately 100 times lower than anticipated. Improving this sensitivity would require reducing the noise in the system, which is beyond the scope of this paper, as the primary focus is on the fabrication of the device and its preliminary testing.

Despite these limitations, the system shows a maximum SNR = 32.5, indicating that the signal is more than 30 times stronger than the noise. Additionally, the minimum calculated LOD = 2.47×10^{-4} RIU demonstrates the ability to detect very small refractive index variations. Overall, the system proves to be functional, and we successfully demonstrated the device's operation for bulk refractive index sensing in real time, as predicted.

Table 5.1: Figures of merit for bulk refractive index sensing transitions, including noise level (δ), signal change (ΔS), signal-to-noise ratio (SNR), bulk sensitivity (S_b), and limit of detection (LOD).

Metric	**7% → 0%**	**0% → 3%**	**3% → 7%**
δ	6.8×10^{-3}	6.8×10^{-3}	6.8×10^{-3}
ΔS	2.20×10^{-1}	6.09×10^{-2}	1.59×10^{-1}
SNR ($\Delta S/\delta$)	32.5	9.01	23.5
S_b ($\Delta S/\Delta n$) [1/RIU]	21.2	13.2	27.4
LOD (δ/S_b) [RIU]	3.20×10^{-4}	5.11×10^{-4}	2.47×10^{-4}

6

Conclusions

Summary and Conclusions

Sensors are fundamental tools that allow us to perceive, quantify, and understand the world around us. These tools operate either through natural biological mechanisms or through engineered devices that extend human observational capabilities far beyond our native senses. Over the years, technological progress has given rise to increasingly sophisticated sensors capable of detecting a wide array of physical, chemical, and biological phenomena. From the simplicity of early thermometers to the complexity of modern optical detection systems, sensors have become essential instruments in diverse fields such as environmental monitoring, industrial process control, and, most significantly in recent years, healthcare and biomedical diagnostics.

Within this broader technological evolution, biosensors have emerged as a specialized and highly impactful class of sensors. These devices are designed specifically to detect biological molecules or to monitor biochemical reactions. They typically integrate a biological recognition element—such as an enzyme, antibody, or nucleic acid—with a physical or chemical transducer that converts the biological interaction into a quantifiable signal. This combination enables biosensors to offer high specificity and sensitivity, making them indispensable for real-time medical diagnostics, disease monitoring, and detection of biomarkers associated with infections, chronic conditions, and metabolic disorders.

Among the wide range of biosensing techniques available today, Surface Plasmon Resonance (SPR) stands out for its label-free detection capability and exceptional sensitivity. SPR operates by exploiting the interaction between light and surface plasmons, which are collective oscillations of free electrons that occur at the interface between a metal and a dielectric material. When a biological binding event alters the local refractive index near the metal surface, this interaction shifts, and the change can be optically detected. This principle allows SPR-based sensors to detect molecular interactions in real time, with high precision and without the need for additional

chemical labels or fluorescent markers. Furthermore, the SPR platform can be miniaturized, making it amenable to the development of compact and potentially wearable biosensing devices, expanding its applicability beyond laboratory settings.

An emerging approach within this field is interferometric SPR, which combines the refractive index sensitivity of SPR with the phase sensitivity of optical interferometry. This combination enhances the detection resolution by measuring the phase difference between two surface plasmon waves, rather than relying solely on intensity variations. Despite its high potential, the application of interferometric SPR for multiplexed biosensing—where multiple analytes are detected simultaneously—remains underexplored.

To address this gap, we developed a novel interferometric SPR sensor with inherent multiplexing potential. The core of the device consists of a gold film deposited on a silica substrate, patterned with two grating couplers and a central nanoslit. This structure is encapsulated in a thin CYTOP layer, an amorphous fluoropolymer known for its optical transparency and chemical inertness. A microfluidic channel is etched above the slit to deliver analytes directly to the sensing region. When a laser beam illuminates the gratings, surface plasmons are excited and propagate along the gold-dielectric interface toward the nanoslit. One arm of the interferometer propagates through CYTOP, serving as the reference path, while the other passes through the analyte within the microfluidic channel, acting as the sensing path. The interference between these two plasmonic waves at the nanoslit results in a modulation of the transmitted optical signal, which depends sensitively on the refractive index difference between the two paths.

This architecture allows for precise control of the interference pattern, enabling selective excitation of different optical modes within the slit. In particular, we observed dipolar, quadrupolar, and hexapolar resonant modes, each corresponding to different spatial field distributions and interference conditions. By tuning the phase difference between the interfering plasmonic waves, it is possible to modulate the modal content of the transmitted light. This tunability was confirmed both numerically and experimentally and demonstrated strong agreement with theoretical predictions, showing how phase control can serve as a powerful tool to enhance sensitivity and selectivity in biosensing applications.

The interferometric nature of our design was validated through both bulk and surface sensitivity measurements. Using controlled water–glycerol mixtures to vary the refractive index, we observed periodic variations in the

transmitted signal as a function of the optical phase difference. Our results showed a bulk sensitivity of approximately $\pm\pi$ W/(m $\cdot$ RIU) and a surface sensitivity of around ± 0.002 W/(m $\cdot$ nm). These values correspond to an expected resolution of 6.3×10^{-6} RIU for bulk sensing and 10 pm for surface sensing, positioning our device among the most sensitive SPR platforms currently available.

To evaluate the scalability and potential for multiplexed detection, we proposed and simulated configurations consisting of periodic unit cells illuminated by a large Gaussian beam with a waist of 200 μm. By introducing shadowing elements to block direct illumination of the slits, we ensured that only surface plasmons generated at the gratings contribute to the interference. This configuration enables the parallel interrogation of multiple sensing units, allowing for high-throughput analysis within a compact footprint and laying the groundwork for future implementation of large two-dimensional biosensing arrays.

In parallel, we optimized the grating coupler design to maximize the efficiency of surface plasmon excitation. By systematically varying the pitch, duty cycle, and depth of the grating structures, we achieved coupling efficiencies as high as 55% for a Gaussian beam with a waist of 5 μm. This high efficiency is crucial for ensuring a strong signal-to-noise ratio, especially when dealing with multiplexed or low-concentration sensing scenarios.

Fabrication of the device was carried out through a six-step process, including gold film deposition, electron-beam lithography for grating patterning, focused ion beam (FIB) milling to create the nanoslit, spin-coating and etching of the CYTOP layer, wafer bonding, and final dicing into individual chips. To facilitate optical testing and microfluidic interfacing, we designed and fabricated a custom jig capable of simultaneously handling three microfluidic channels while allowing perpendicular optical access to the chip. This packaging approach supports parallel operation and stable measurement conditions, both of which are essential for practical biosensing applications.

Experimental validation confirmed the core operating principles of the device. By observing far-field intensity patterns, we verified the excitation of distinct resonant modes within the nanoslit and demonstrated consistency with our numerical simulations. Furthermore, the interferometric signal exhibited the expected periodicity in response to changes in analyte refractive index, substantiating the theoretical foundation of our sensing mechanism.

In summary, the interferometric SPR sensor we developed demonstrates high sensitivity, tunable modal behavior, and multiplexing capability, all

within a compact and integrable platform. These results establish a strong foundation for future development of portable and scalable biosensors capable of detecting multiple biomarkers with high resolution and specificity.

Future Work

The promising results achieved in this work lay the foundation for several exciting future research directions aimed at enhancing the performance, applicability, and integration of the proposed interferometric SPR biosensor.

One promising direction for improving both the stability and scalability of the sensor involves the integration of a spatial light modulator (SLM) into the optical setup. Unlike the current configuration, which requires optical beam splitters to generate and align two separate Gaussian beams for interferometric excitation, an SLM can be programmed to produce these beams holographically. This approach offers several key advantages. First, both beams—representing the two arms of the interferometer—can be generated from a single optical path and travel together as a mutual beam pair. This effectively transforms the system into a common-path interferometer, significantly reducing sensitivity to environmental noise and mechanical instabilities. Moreover, the holographic capabilities of the SLM enable the simultaneous generation of multiple pairs of Gaussian beams, each targeting a different sensing unit on the chip. This opens the door to true optical multiplexing, where several interferometric channels can be interrogated in parallel without increasing the optical complexity of the system.

Another key area of development is surface biomolecular sensing. By functionalizing the gold surface with selective biorecognition elements such as antibodies or aptamers, the device can be transformed from a general refractive index sensor into a true biosensor capable of detecting specific biomolecular interactions. This functionalization is essential for applications in clinical diagnostics, where specificity is paramount.

In parallel, the intersection of biosensing and quantum optics offers a compelling frontier. Replacing classical laser sources with quantum light sources, such as entangled photon pairs, and employing single-photon detectors could potentially push the sensitivity of the device beyond the classical shot-noise limit. This quantum-enhanced approach holds promise for achieving new benchmarks in detection resolution, particularly in low-signal regimes.

Another important direction involves revisiting the detection strategy itself. All measurements in this thesis focused on the total optical power trans-

mitted through the nanoslit, which greatly simplifies both the optical setup and data analysis. However, previous work showed that changes in the geometry of the nanoslit—such as its width—can alter the spatial distribution of the radiated field, potentially improving sensitivity. These far-field radiation patterns, which were not captured by power measurements alone, may contain valuable information for sensing. Future work could explore whether tracking these patterns—rather than just the total transmitted power—can lead to improved performance or new sensing modalities.

In addition, the use of structured light, such as beams carrying orbital angular momentum (OAM), represents another promising avenue. These beams interact differently with nanostructures and have the potential to enhance interactions with chiral molecules. Implementing such exotic beams would require the design of specialized grating couplers that align not only with the beam's polarization and angle but also with its helical phase front. In this sense, exotic beams may require exotic gratings. This line of work could open up opportunities in advanced biomolecular detection, particularly for targets with chiral or complex optical properties.

Finally, system miniaturization remains a critical goal. Transitioning from a laboratory-scale setup to a compact, robust, and portable system is essential for real-world deployment, especially in clinical or point-of-care settings where reliability and ease of use are crucial. Developing a self-contained, user-friendly version of the current sensor would significantly broaden its accessibility and impact.

Bibliography

1. Maier, S. A. (2007). *Plasmonics: Fundamentals and Applications*. Springer Science & Business Media.
2. Van Der Merwe, P. A. (2001). Surface plasmon resonance. *Protein-ligand interactions: hydrodynamics and calorimetry*, **1**, 137-170.
3. Schasfoort, R. B. M. (Ed.). (2017). *Handbook of Surface Plasmon Resonance*. The Royal Society of Chemistry.
4. Barnes, W. L., Dereux, A., & Ebbesen, T. W. (2003). Surface plasmon subwavelength optics. *Nature*, **424**(6950), 824–830.
5. Wang, J., Lin, W., Cao, E., Xu, X., Liang, W., & Zhang, X. (2017). Surface plasmon resonance sensors on Raman and fluorescence spectroscopy. *Sensors*, **17**(12), 2719.
6. Schasfoort, R. (2017). Introduction to surface plasmon resonance.
7. Johnson, P. B., & Christy, R. W. (1972). Optical constants of noble metals. *Physical Review B*, **6**(12), 4370–4379.
8. Raether, H. (2006). Surface plasmons on gratings. *Surface plasmons on smooth and rough surfaces and on gratings*, 91-116.
9. Homola, J. (2003). Surface plasmon resonance for biosensing: A mini review. *Sensors and Actuators B: Chemical*, **91**(1–3), 3–13.
10. Rich, R. L., & Myszka, D. G. (2000). Surface plasmon resonance: A versatile technique for biosensor applications. *Current Opinion in Biotechnology*, **11**(1), 54–61.
11. Freestone, I., Meeks, N., Sax, M., & Higgitt, C. (2007). The Lycurgus Cup—A Roman nanotechnology. *Gold Bulletin*, **40**(4), 270–277.
12. Wood, R. W. (1902). On a remarkable case of uneven distribution of light in a diffraction grating spectrum. *Philosophical Magazine*, **4**(21), 396–402.
13. Rayleigh, L. (1907). On the dynamical theory of gratings. *Proceedings of the Royal Society A: Mathematical, Physical and Engineering Sciences*, **79**(532), 399–416.
14. Kretschmann, E., & Raether, H. (1968). Radiative decay of non-radiative surface plasmons excited by light. *Zeitschrift für Naturforschung A*, **23**(12), 2135–2136.
15. Otto, A. (1968). Excitation of nonradiative surface plasma waves in silver by the method of frustrated total reflection. *Zeitschrift für Physik*, **216**(4), 398–410.
16. Kontio, J. (2013). Fabrication of Sub-Wavelength Photonic Structures by Nanoimprint Lithography.

17. Liedberg, B., Nylander, C., & Lundström, I. (1995). Biosensing with surface plasmon resonance—how it all started. *Biosensors and Bioelectronics*, **10**(8), 635–641.
18. Jonsson, U., et al. (1991). Real-time biospecific interaction analysis using surface plasmon resonance and biosensor technology. *BioTechniques*, **11**(5), 620–627.
19. Schuck, P. (1997). Use of surface plasmon resonance to probe the equilibrium and dynamic aspects of interactions between biological macromolecules. *Annual Review of Biophysics and Biomolecular Structure*, **26**, 541–566.
20. Myszka, D. G. (1997). Kinetic analysis of macromolecular interactions using surface plasmon resonance biosensors. *Current Opinion in Biotechnology*, **8**(1), 50–57.
21. Berini, P., & De Leon, I. (2012). Surface Plasmon–Polariton Amplifiers and Lasers.
22. Karimi, E., et al. (2014). Generating Optical Orbital Angular Momentum at Visible Wavelengths Using a Plasmonic Metasurface.
23. Lee, T., et al. (2018). Plasmonic- and Dielectric-Based Structural Coloring: From Fundamentals to Practical Applications.
24. Wu, X., et al. (2022). Light-Driven Microdrones.
25. Heeres, R. W., Kouwenhoven, L. P., & Zwiller, V. (2013). Quantum Interference in Plasmonic Circuits.
26. Asgarnezhad-Zorgabad, S. (2020). Coherent Amplification and Lasing of Weak Surface-Plasmon Polaritons in a Negative-Index Metamaterial with a Resonant Atomic Medium.
27. Burke, J. J., Stegeman, G. I., & Tamir, T. (1986). Surface-polariton-like waves guided by thin, lossy metal films. *Physical Review B*, **33**(8), 5186.
28. Berini, P. (2006). Figures of merit for surface plasmon waveguides. *Optics Express*, **14**(26), 13030-13042.
29. Krasavin, A. V., & Zayats, A. V. (2010). Silicon-based plasmonic waveguides. *Optics Express*, **18**(11), 11791-11799.
30. Edlén, B. (1966). The refractive index of air. *Metrologia*, **2**(2), 71.
31. Thormählen, I., Straub, J., & Grigull, U. (1985). Refractive index of water and its dependence on wavelength, temperature, and density. *Journal of Physical and Chemical Reference Data*, **14**(4), 933-945.
32. Thompson, R. C. (1990). *Optical waves in layered media*.
33. Safronov, K. R., Bessonov, V. O., Akhremenkov, D. V., Sirotin, M. A., Romodina, M. N., Lyubin, E. V., ... & Fedyanin, A. A. (2022). Miniature Otto prism coupler for integrated photonics. *Laser & Photonics Reviews*, **16**(4), 2100542.

34. Khodami, M., & Berini, P. (2019). Grating couplers for (Bloch) long-range surface plasmons on metal stripe waveguides. *JOSA B*, **36**(7), 1921-1930.
35. Turker, B., Guner, H., Ayas, S., Ekiz, O. O., Acar, H., Guler, M. O., & Dâna, A. (2011). Grating coupler integrated photodiodes for plasmon resonance-based sensing. *Lab on a Chip*, **11**(2), 282-287.
36. Cheng, L., Mao, S., Li, Z., Han, Y., & Fu, H. Y. (2020). Grating couplers on silicon photonics: Design principles, emerging trends and practical issues. *Micromachines*, **11**(7), 666.
37. Gupta, B. D., & Verma, R. K. (2009). Fiber-optic sensors based on surface plasmon resonance: A comprehensive review. *Sensors and Actuators B: Chemical*, **139**(1), 31-35.
38. Hassani, A., & Skorobogatiy, M. (2010). Plasmonic fiber optic refractometric sensors: From conventional architectures to recent design trends. *Sensors*, **17**(1), 12.
39. Jind, B., & Berini, P. (2024). Transverse magnetic supermodes in plasmonic optical fibers excited by radially polarized light. *Optics Express*, **32**(22), 38490-38503.
40. Abbas, H. K., & Mahdi, Z. F. (2023). Fabricate a highly sensitive surface plasmon resonance optical fiber sensor based on a D-shape fiber coated with gold (Au) nano-layer. *Results in Optics*, **12**, 100497.
41. Willets, K. A., & Van Duyne, R. P. (2007). Localized surface plasmon resonance spectroscopy and sensing. *Annual Review of Physical Chemistry*, **58**, 267–297.
42. Anker, J. N., Hall, W. P., Lyandres, O., Shah, N. C., Zhao, J., & Van Duyne, R. P. (2008). Biosensing with plasmonic nanosensors. *Nature Materials*, **7**(6), 442–453.
43. Schmidt, M. A., & Hill, R. T. (2016). Nanoparticle-based plasmonic sensors. *Chemical Reviews*, **116**(10), 4783–4822.
44. Zuñiga Gurrión, K. D. J., Díaz Flores, P. I., Sánchez Domínguez, M., & Navarro-Segura, M. E. (2023, October). Fabrication of bimetallic nanodendrites using the electrodeposition technique for the detection of molecules at trace level by SERS. In *X Workshop in R&D+ i & International Workshop on STEM of EPS* (pp. 191-198). Cham: Springer Nature Switzerland.
45. Freitas de Freitas, L., Varca, G. H. C., dos Santos Batista, J. G., & Benévolo Lugão, A. (2018). An overview of the synthesis of gold nanoparticles using radiation technologies. *Nanomaterials*, **8**(11), 939.
46. Raether, H. (1983). Excitation of surface polaritons by end-fire coupling. *Optics Letters*, **8**(7), 386–388.

47. Pors, A., Nielsen, M. G., & Willatzen, M. (2016). End-fire coupling efficiencies of surface plasmons for silver, gold, and aluminum. *Journal of the Optical Society of America B*, **33**(6), 1044–1051.
48. Son, G., Han, S., Park, J., Kwon, K., & Yu, K. (2018). High-efficiency broadband light coupling between optical fibers and photonic integrated circuits. *Nanophotonics*, **7**(12), 1845-1864.
49. Catchpole, K. R., Mokkapati, S., Beck, F., Wang, E. C., McKinley, A., Basch, A., & Lee, J. (2011). Plasmonics and nanophotonics for photovoltaics. *MRS Bulletin*, **36**(6), 461-467.
50. Kik, P. G., & Brongersma, M. L. (2007). Surface plasmon nanophotonics. In *Surface Plasmon Nanophotonics* (pp. 1-9). Dordrecht: Springer Netherlands.
51. Shalaev, V. M., & Kawata, S. (2006). *Nanophotonics with surface plasmons*. Elsevier.
52. Fang, Y., & Sun, M. (2015). Nanoplasmonic waveguides: Towards applications in integrated nanophotonic circuits. *Light: Science & Applications*, **4**(6), e294-e294.
53. Wassel, H. M., Dai, D., Tiwari, M., Valamehr, J. K., Theogarajan, L., Dionne, J., ... & Sherwood, T. (2012). Opportunities and challenges of using plasmonic components in nanophotonic architectures. *IEEE Journal on Emerging and Selected Topics in Circuits and Systems*, **2**(2), 154-168.
54. Wong, C. L., & Olivo, M. (2014). Surface plasmon resonance imaging sensors: A review. *Plasmonics*, **9**, 809-824.
55. Puiu, M., & Bala, C. (2016). SPR and SPR imaging: Recent trends in developing nanodevices for detection and real-time monitoring of biomolecular events. *Sensors*, **16**(6), 870.
56. Linman, M. J., Abbas, A., & Cheng, Q. (2010). Interface design and multiplexed analysis with surface plasmon resonance (SPR) spectroscopy and SPR imaging. *Analyst*, **135**(11), 2759-2767.
57. Steiner, G. (2004). Surface plasmon resonance imaging. *Analytical and Bioanalytical Chemistry*, **379**(3), 328-331.
58. Li, C., Le, V., Wang, X., Hao, X., Liu, X., & Kuang, C. (2021). Resolution enhancement and background suppression in optical super-resolution imaging for biological applications. *Laser & Photonics Reviews*, **15**(1), 1900084.
59. Chen, B., Wood, A., Pathak, A., Mathai, J., Bok, S., Zheng, H., ... & Gangopadhyay, S. (2016). Plasmonic gratings with nano-protrusions made by glancing angle deposition for single-molecule super-resolution imaging. *Nanoscale*, **8**(24), 12189-12201.

60. Meyer, S. A., Le Ru, E. C., & Etchegoin, P. G. (2011). Combining surface plasmon resonance (SPR) spectroscopy with surface-enhanced Raman scattering (SERS). *Analytical Chemistry*, **83**(6), 2337-2344.
61. Bousiakou, L. G., Gebavi, H., Mikac, L., Karapetis, S., & Ivanda, M. (2019). Surface enhanced Raman spectroscopy for molecular identification—A review on surface plasmon resonance (SPR) and localised surface plasmon resonance (LSPR) in optical nanobiosensing. *Croatica Chemica Acta*, **92**(4), 479-494.
62. Nurrohman, D. T., & Chiu, N. F. (2021). A review of graphene-based surface plasmon resonance and surface-enhanced Raman scattering biosensors: Current status and future prospects. *Nanomaterials*, **11**(1), 216.
63. Touahir, L., Jenkins, A. T. A., Boukherroub, R., Gouget-Laemmel, A. C., Chazalviel, J. N., Peretti, J., ... & Szunerits, S. (2010). Surface plasmon-enhanced fluorescence spectroscopy on silver-based SPR substrates. *The Journal of Physical Chemistry C*, **114**(51), 22582-22589.
64. Dostálek, J., & Knoll, W. (2008). Biosensors based on surface plasmon-enhanced fluorescence spectroscopy. *Biointerphases*, **3**(3), FD12-FD22.
65. Fan, W., Lawrie, B. J., & Pooser, R. C. (2015). Quantum plasmonic sensing. *Physical Review A*, **92**(5), 053812.
66. Saleviter, S., Fen, Y. W., Omar, N. A. S., Daniyal, W. M. E. M. M., Abdullah, J., & Zaid, M. H. M. (2018). Structural and optical studies of cadmium sulfide quantum dot-graphene oxide-chitosan nanocomposite thin film as a novel SPR spectroscopy active layer. *Journal of Nanomaterials*, **2018**(1), 4324072.
67. Lee, J. S., Huynh, T., Lee, S. Y., Lee, K. G., Lee, J., Tame, M., ... & Lee, C. (2017). Quantum noise reduction in intensity-sensitive surface-plasmon-resonance sensors. *Physical Review A*, **96**(3), 033833.
68. Nazri, N. A. A., Azeman, N. H., Luo, Y., & Bakar, A. A. A. (2021). Carbon quantum dots for optical sensor applications: A review. *Optics & Laser Technology*, **139**, 106928.
69. Lu, H., Dai, S., Yue, Z., Fan, Y., Cheng, H., Di, J., ... & Zhao, J. (2019). Sb_2Te_3 topological insulator: Surface plasmon resonance and application in refractive index monitoring. *Nanoscale*, **11**(11), 4759-4766.
70. Liu, N., Wang, S., Lv, J., Lu, Y., & Zhang, J. (2023). Refractive index biosensor based on topological ring resonator. *Optics Communications*, **541**, 129542.
71. Trzaskowski, M., Napiórkowska, A., Augustynowicz-Kopeć, E., & Ciach, T. (2018). Detection of tuberculosis in patients with the use of a portable SPR device. *Sensors and Actuators B: Chemical*, **260**, 786-792.

72. Huang, Y., Zhang, L., Zhang, H., Li, Y., Liu, L., Chen, Y., ... & Yu, D. (2020). Development of a portable SPR sensor for nucleic acid detection. *Micromachines*, **11**(5), 526.
73. Prabowo, B. A., Alom, A., Secario, M. K., Masim, F. C. P., Lai, H. C., Hatanaka, K., & Liu, K. C. (2016). Graphene-based portable SPR sensor for the detection of Mycobacterium tuberculosis DNA strain. *Procedia Engineering*, **168**, 541-545.
74. Fu, E., Chinowsky, T., Nelson, K., Johnston, K., Edwards, T., Helton, K., ... & Yager, P. (2007). SPR imaging-based salivary diagnostics system for the detection of small molecule analytes. *Annals of the New York Academy of Sciences*, **1098**(1), 335-344.
75. Zhang, X. L., Liu, Y., Fan, T., Hu, N., Yang, Z., Chen, X., ... & Yang, J. (2017). Design and performance of a portable and multichannel SPR device. *Sensors*, **17**(6), 1435.
76. Li, X., Jia, C., Ma, B., Wang, W., Fang, Z., Zhang, G., & Guo, X. (2015). Substrate-induced interfacial plasmonics for photovoltaic conversion. *Scientific Reports*, **5**(1), 14497.
77. Baba, A., Aoki, N., Shinbo, K., Kato, K., & Kaneko, F. (2011). Grating-coupled surface plasmon enhanced short-circuit current in organic thin-film photovoltaic cells. *ACS Applied Materials & Interfaces*, **3**(6), 2080-2084.
78. Chen, J. Y., Wu, H. C., Chiu, Y. C., & Chen, W. C. (2014). Plasmon-enhanced polymer photovoltaic device performance using different patterned Ag/PVP electrospun nanofibers. *Advanced Energy Materials*, **4**(8), 1301665.
79. Hsu, H. L., Juang, T. Y., Chen, C. P., Hsieh, C. M., Yang, C. C., Huang, C. L., & Jeng, R. J. (2015). Enhanced efficiency of organic and perovskite photovoltaics from shape-dependent broadband plasmonic effects of silver nanoplates. *Solar Energy Materials and Solar Cells*, **140**, 224-231.
80. Kasowaki, L., & Charles, E. (2023). Emerging trends in plasmonics for nanophotonics: From theory to applications.
81. Scheller, F., & Schubert, F. (1991). *Biosensors*. Elsevier.
82. Turner, A. P. (2013). Biosensors: Sense and sensibility. *Chemical Society Reviews*, **42**(8), 3184-3196.
83. Karunakaran, C., Rajkumar, R., & Bhargava, K. (2015). Introduction to biosensors. In *Biosensors and Bioelectronics* (pp. 1-68). Elsevier.
84. Turner, A., Karube, I., & Wilson, G. S. (1987). *Biosensors: Fundamentals and Applications*. Oxford University Press.
85. Ronkainen, N. J., Halsall, H. B., & Heineman, W. R. (2010). Electrochemical biosensors. *Chemical Society Reviews*, **39**(5), 1747-1763.

86. Dhull, V., Gahlaut, A., Dilbaghi, N., & Hooda, V. (2013). Acetylcholinesterase biosensors for electrochemical detection of organophosphorus compounds: A review. *Biochemistry Research International*, **2013**(1), 731501.
87. Skládal, P. (2024). Piezoelectric biosensors: Shedding light on principles and applications. *Microchimica Acta*, **191**(4), 184.
88. Pohanka, M. (2017). The piezoelectric biosensors: Principles and applications, a review. *International Journal of Electrochemical Science*, **12**(1), 496-506.
89. Ramanathan, K., & Danielsson, B. (2001). Principles and applications of thermal biosensors. *Biosensors and Bioelectronics*, **16**(6), 417-423.
90. Xie, B., & Danielsson, B. (2007). Thermal biosensor and microbiosensor techniques. *Handbook of Biosensors and Biochips*, **2**, 1-19.
91. Damborský, P., Švitel, J., & Katrlík, J. (2016). Optical biosensors. *Essays in Biochemistry*, **60**(1), 91-100.
92. Borisov, S. M., & Wolfbeis, O. S. (2008). Optical biosensors. *Chemical Reviews*, **108**(2), 423-461.
93. Chen, C., & Wang, J. (2020). Optical biosensors: An exhaustive and comprehensive review. *Analyst*, **145**(5), 1605-1628.
94. Ligler, F. S., & Taitt, C. R. (Eds.). (2002). *Optical biosensors: Present & future*. Gulf Professional Publishing.
95. Watts, H. J., Lowe, C. R., & Pollard-Knight, D. V. (1994). Optical biosensor for monitoring microbial cells. *Analytical Chemistry*, **66**(15), 2465-2470.
96. Dey, D., & Goswami, T. (2011). Optical biosensors: A revolution towards quantum nanoscale electronics device fabrication. *BioMed Research International*, **2011**(1), 348218.
97. Das, S., Mazumdar, H., Khondakar, K. R., Mishra, Y. K., & Kaushik, A. (2024). Quantum biosensors: Principles and applications in medical diagnostics. *ECS Sensors Plus*, **3**(2), 025001.
98. Mostafavi, F., Jafari, Z., Lollie, M. L., You, C., De Leon, I., & Magaña-Loaiza, O. S. (2022). Conditional quantum plasmonic sensing. *Nanophotonics*, **11**(14), 3299-3306.
99. Lee, C., Lawrie, B., Pooser, R., Lee, K. G., Rockstuhl, C., & Tame, M. (2021). Quantum plasmonic sensors. *Chemical Reviews*, **121**(8), 4743-4804.
100. Mpofu, K. T., Lee, C., Maguire, G. E. M., Kruger, H. G., & Tame, M. S. (2022). Measuring kinetic parameters using quantum plasmonic sensing. *Physical Review A*, **105**(3), 032619.
101. Ma, F., Li, Y., Tang, B., & Zhang, C. Y. (2016). Fluorescent biosensors based on single-molecule counting. *Accounts of Chemical Research*, **49**(9), 1722-1730.

102. Taitt, C. R., Anderson, G. P., & Ligler, F. S. (2005). Evanescent wave fluorescence biosensors. *Biosensors and Bioelectronics*, **20**(12), 2470-2487.
103. Bauch, M., Toma, K., Toma, M., Zhang, Q., & Dostalek, J. (2014). Plasmon-enhanced fluorescence biosensors: A review. *Plasmonics*, **9**, 781-799.
104. Ali, M. (2017). *Raman Biosensors* (Doctoral dissertation, Université d'Ottawa/University of Ottawa).
105. Nurrohman, D. T., & Chiu, N. F. (2021). A review of graphene-based surface plasmon resonance and surface-enhanced Raman scattering biosensors: Current status and future prospects. *Nanomaterials*, **11**(1), 216.
106. Pyrak, E., Krajczewski, J., Kowalik, A., Kudelski, A., & Jaworska, A. (2019). Surface enhanced Raman spectroscopy for DNA biosensors—How far are we? *Molecules*, **24**(24), 4423.
107. Serebrennikova, K. V., Berlina, A. N., Sotnikov, D. V., Zherdev, A. V., & Dzantiev, B. B. (2021). Raman scattering-based biosensing: New prospects and opportunities. *Biosensors*, **11**(12), 512.
108. Singh, P. (2016). SPR biosensors: Historical perspectives and current challenges. *Sensors and Actuators B: Chemical*, **229**, 110-130.
109. Olaru, A., Bala, C., Jaffrezic-Renault, N., & Aboul-Enein, H. Y. (2015). Surface plasmon resonance (SPR) biosensors in pharmaceutical analysis. *Critical Reviews in Analytical Chemistry*, **45**(2), 97-105.
110. Guo, X. (2012). Surface plasmon resonance based biosensor technique: A review. *Journal of Biophotonics*, **5**(7), 483-501.
111. Rich, R. L., & Myszka, D. G. (2000). Advances in surface plasmon resonance biosensor analysis. *Current Opinion in Biotechnology*, **11**(1), 54-61.
112. Torun, Ö., Boyacı, İ. H., Temür, E., & Tamer, U. (2012). Comparison of sensing strategies in SPR biosensor for rapid and sensitive enumeration of bacteria. *Biosensors and Bioelectronics*, **37**(1), 53-60.
113. Homola, J. (2003). Present and future of surface plasmon resonance biosensors. *Analytical and Bioanalytical Chemistry*, **377**, 528-539.
114. Ravindran, N., Kumar, S., CA, M., Thirunavookarasu, S. N., & CK, S. (2023). Recent advances in Surface Plasmon Resonance (SPR) biosensors for food analysis: A review. *Critical Reviews in Food Science and Nutrition*, **63**(8), 1055-1077.
115. Wang, Q., Ren, Z. H., Zhao, W. M., Wang, L., Yan, X., Zhu, A. S., ... & Zhang, K. K. (2022). Research advances on surface plasmon resonance biosensors. *Nanoscale*, **14**(3), 564-591.
116. Kashif, M., Bakar, A. A. A., & Hashim, F. H. (2016). Analysing surface plasmon resonance phase sensor based on Mach-Zehnder interferometer technique using glycerin. *Optics Communications*, **380**, 419-424.

117. Gao, Y., Gan, Q., Xin, Z., Cheng, X., & Bartoli, F. J. (2011). Plasmonic Mach–Zehnder interferometer for ultrasensitive on-chip biosensing. *ACS Nano*, **5**(12), 9836-9844.
118. Liu, Q., Tu, X., Kim, K. W., Kee, J. S., Shin, Y., Han, K., ... & Park, M. K. (2013). Highly sensitive Mach–Zehnder interferometer biosensor based on silicon nitride slot waveguide. *Sensors and Actuators B: Chemical*, **188**, 681-688.
119. Meng, X., Li, S., Li, J., Guo, Y., Han, Y., Wang, Y., ... & Shen, J. (2022). Refractive index sensing of twin-core fiber based on Mach-Zehnder interference and SPR effect. *Journal of Physics D: Applied Physics*, **55**(18), 185103.
120. Patel, P. B., & Hamde, S. T. (2017). Analysis of the Mach–Zehnder interferometer waveguide structure for refractive index measurement. *Journal of Optics*, **46**(4), 398-402.
121. Berini, P. (2009). Long-range surface plasmon polaritons. *Advances in Optics and Photonics*, **1**(3), 484-588.
122. Guzman C, R., Martinez A, C. G., & Guzman S, J. R. (2019). LRSPP-based interferometric structures for bio sensing.
123. Qian, G., Fu, X. C., Zhang, L. J., Tang, J., Liu, Y. R., Zhang, X. Y., & Zhang, T. (2017). Hybrid fiber resonator employing LRSPP waveguide coupler for gyroscope. *Scientific Reports*, **7**(1), 41146.
124. Fuentes-Fuentes, M. A., May-Arrioja, D. A., Guzman-Sepulveda, J. R., Arteaga-Sierra, F., Torres-Cisneros, M., Likamwa, P. L., & Sánchez-Mondragón, J. J. (2019). Suspended LRSPP for the development of highly integrated active plasmonic devices. *Optics Express*, **27**(6), 8858-8870.
125. Homola, J., Dostalek, J., Chen, S., Rasooly, A., Jiang, S., & Yee, S. S. (2002). Spectral surface plasmon resonance biosensor for detection of staphylococcal enterotoxin B in milk. *International Journal of Food Microbiology*, **75**(1-2), 61-69.
126. Dostálek, J., Vaisocherová, H., & Homola, J. (2005). Multichannel surface plasmon resonance biosensor with wavelength division multiplexing. *Sensors and Actuators B: Chemical*, **108**(1-2), 758-764.
127. Kushwaha, A. S., Kumar, A., Kumar, R., & Srivastava, S. K. (2018). A study of surface plasmon resonance (SPR) based biosensor with improved sensitivity. *Photonics and Nanostructures-Fundamentals and Applications*, **31**, 99-106.
128. Guo, X. (2012). Surface plasmon resonance based biosensor technique: A review. *Journal of Biophotonics*, **5**(7), 483-501.
129. Chang, Y. F., Wang, Y. C., Huang, T. Y., Li, M. C., Chen, S. Y., Lin, Y. X., ... & Lin, K. J. (2025). AI integration into wavelength-based SPR

biosensing: Advancements in spectroscopic analysis and detection. *Analytica Chimica Acta*, 343640.

130. Mahmudin, L., Suharyadi, E., Utomo, A. B. S., & Abraha, K. (2015). Optical properties of silver nanoparticles for surface plasmon resonance (SPR)-based biosensor applications. *Journal of Modern Physics*, **6**(08), 1071.
131. Li, J. (2020). A review: Development of novel fiber-optic platforms for bulk and surface refractive index sensing applications. *Sensors and Actuators Reports*, **2**(1), 100018.
132. Grassi, J. H., & Georgiadis, R. M. (1999). Temperature-dependent refractive index determination from critical angle measurements: Implications for quantitative SPR sensing. *Analytical Chemistry*, **71**(19), 4392-4396.
133. Berini, P. (2008). Bulk and surface sensitivities of surface plasmon waveguides. *New Journal of Physics*, **10**(10), 105010.
134. Topor, C. V., Puiu, M., & Bala, C. (2023). Strategies for surface design in surface plasmon resonance (SPR) sensing. *Biosensors*, **13**(4), 465.
135. Das, S., Devireddy, R., & Gartia, M. R. (2023). Surface plasmon resonance (SPR) sensor for cancer biomarker detection. *Biosensors*, **13**(3), 396.
136. Sarıkaya, A. G., Osman, B., Çam, T., & Denizli, A. (2017). Molecularly imprinted surface plasmon resonance (SPR) sensor for uric acid determination. *Sensors and Actuators B: Chemical*, **251**, 763-772.
137. Naimushin, A. N., Soelberg, S. D., Nguyen, D. K., Dunlap, L., Bartholomew, D., Elkind, J., ... & Furlong, C. E. (2002). Detection of Staphylococcus aureus enterotoxin B at femtomolar levels with a miniature integrated two-channel surface plasmon resonance (SPR) sensor. *Biosensors and Bioelectronics*, **17**(6-7), 573-584.
138. Cooper, M. A. (Ed.). (2009). *Label-free biosensors: Techniques and applications*. Cambridge University Press.
139. Olaru, A., Bala, C., Jaffrezic-Renault, N., & Aboul-Enein, H. Y. (2015). Surface plasmon resonance (SPR) biosensors in pharmaceutical analysis. *Critical Reviews in Analytical Chemistry*, **45**(2), 97-105.
140. Das, S., Singh, S., Chawla, V., Chawla, P. A., & Bhatia, R. (2024). Surface plasmon resonance as a fascinating approach in target-based drug discovery and development. *TrAC Trends in Analytical Chemistry*, **171**, 117501.
141. Myszka, D. G., & Rich, R. L. (2000). Implementing surface plasmon resonance biosensors in drug discovery. *Pharmaceutical Science Technology Today*, **3**(9), 310-317.
142. Navratilova, I., & Hopkins, A. L. (2011). Emerging role of surface plasmon resonance in fragment-based drug discovery. *Future Medicinal Chemistry*, **3**(14), 1809-1820.

143. Yanase, Y., Hiragun, T., Yanase, T., Kawaguchi, T., Ishii, K., & Hide, M. (2013). Application of SPR imaging sensor for detection of individual living cell reactions and clinical diagnosis of type I allergy. *Allergology International*, **62**(2), 163-169.
144. Yanase, Y., Hiragun, T., Ishii, K., Kawaguchi, T., Yanase, T., Kawai, M., ... & Hide, M. (2014). Surface plasmon resonance for cell-based clinical diagnosis. *Sensors*, **14**(3), 4948-4959.
145. Masson, J. F. (2017). Surface plasmon resonance clinical biosensors for medical diagnostics. *ACS Sensors*, **2**(1), 16-30.
146. Pandey, P. S., Raghuwanshi, S. K., Shadab, A., Ansari, M. T. I., Tiwari, U. K., & Kumar, S. (2022). SPR based biosensing chip for COVID-19 diagnosis—A review. *IEEE Sensors Journal*, **22**(14), 13800-13810.
147. Aljbar, N. A., Mahdi, B. R., Khalid, A. H., Attallah, A. H., Abdulwahid, F. S., & Haider, A. J. (2024). Enhanced surface plasmon resonance (SPR) fiber optic sensor for environmental monitoring: A coreless fiber–based design. *Plasmonics*, 1-10.
148. Dostálek, J., & Homola, J. (2006). SPR biosensors for environmental monitoring. *Surface Plasmon Resonance Based Sensors*, 191-206.
149. Daniyal, W. M. E. M. M., Fen, Y. W., Fauzi, N. I. M., Hashim, H. S., Ramdzan, N. S. M., & Omar, N. A. S. (2020). Recent advances in surface plasmon resonance optical sensors for potential application in environmental monitoring. *Sens. Mater*, **32**(12), 4191-4200.
150. Piliarik, M., Párová, L., & Homola, J. (2009). High-throughput SPR sensor for food safety. *Biosensors and Bioelectronics*, **24**(5), 1399-1404.
151. Situ, C., Mooney, M. H., Elliott, C. T., & Buijs, J. (2010). Advances in surface plasmon resonance biosensor technology towards high-throughput, food-safety analysis. *TrAC Trends in Analytical Chemistry*, **29**(11), 1305-1315.
152. Ladd, J., Taylor, A., & Jiang, S. (2006). SPR biosensors for food safety. *Surface Plasmon Resonance Based Sensors*, 207-227.
153. Desmet, C., Vindas, K., Alvarado Meza, R., Garrigue, P., Voci, S., Sojic, N., ... & Engel, E. (2020). Multiplexed remote SPR detection of biological interactions through optical fiber bundles. *Sensors*, **20**(2), 511.
154. McGrath, T. F., Buijs, J., Huet, A. C., Delahaut, P., Elliott, C. T., & Mooney, M. H. (2013). Assessment of a multiplexing high throughput immunochemical SPR biosensor in measuring multiple proteins on a single biosensor chip. *Sensors and Actuators B: Chemical*, **186**, 423-430.
155. Taylor, A. D., Ladd, J., Yu, Q., Chen, S., Homola, J., & Jiang, S. (2006). Quantitative and simultaneous detection of four foodborne bacterial pathogens

with a multi-channel SPR sensor. *Biosensors and Bioelectronics*, **22**(5), 752-758.

156. Dostálek, J., Vaisocherová, H., & Homola, J. (2005). Multichannel surface plasmon resonance biosensor with wavelength division multiplexing. *Sensors and Actuators B: Chemical*, **108**(1-2), 758-764.
157. Usachev, E. V., Agranovski, E., Usacheva, O. V., & Agranovski, I. E. (2015). Multiplexed Surface Plasmon Resonance based real-time viral aerosol detection. *Journal of Aerosol Science*, **90**, 136-143.
158. Homola, J., Koudela, I., & Yee, S. S. (1999). Surface plasmon resonance sensors based on diffraction gratings and prism couplers: sensitivity comparison. *Sensors and Actuators B: Chemical*, **54**(1-2), 16-24.
159. Murugan, D., Tintelott, M., Narayanan, M. S., Vu, X. T., Kurkina, T., Rodriguez-Emmenegger, C., ... & Pachauri, V. (2024). Recent advances in grating-coupled surface plasmon resonance technology. *Advanced Optical Materials*, **12**(34), 2401862.
160. Yoon, J., Kim, J. Y., Kim, J., Yoon, H., Neşeli, B., Park, H. H., & Kurt, H. (2023). Inverse design of a Si-based high-performance vertical-emitting meta-grating coupler. *Photonics Research*, **11**(6), 897-905.
161. Rahman, F., De La Rue, R. M., & De La Rue, S. A. (2011). Constructing and enhancing the superior LED: photonic crystal and photonic band-gap structures for light extraction and emission control. *Proceedings of [Conference/Journal]*, **Volume**(Issue), 209-224.
162. Turker, B., Guner, H., Ayas, S., Ekiz, O. O., Acar, H., Guler, M. O., & Dâna, A. (2011). Grating coupler integrated photodiodes for plasmon resonance-based sensing. *Lab on a Chip*, **11**(2), 282-287.
163. Caucheteur, C., Voisin, V., & Albert, J. (2015). Near-infrared grating-assisted SPR optical fiber sensors: design rules for ultimate refractometric sensitivity. *Optics Express*, **23**(3), 2918-2932.
164. Kravets, V. G., Jalil, R., Kim, Y. J., Ansell, D., Aznakayeva, D. E., Thackray, B., ... & Grigorenko, A. N. (2014). Graphene-protected copper and silver plasmonics. *Scientific Reports*, **4**(1), 5517.
165. Rifat, A. A., Ahmed, R., Yetisen, A. K., Butt, H., Sabouri, A., Mahdiraji, G. A., ... & Adikan, F. M. (2017). Photonic crystal fiber-based plasmonic sensors. *Sensors and Actuators B: Chemical*, **243**, 311-325.
166. Kneale, C., & Booksh, K. S. (2017). Numerical Optimization of Material Configurations for the Development of Surface Plasmon Resonance Devices. *arXiv preprint arXiv:1702.06883*.
167. Tene, T., Bellucci, S., Arias Arias, F., Carrera Almendariz, L. S., Flores Huilcapi, A. G., & Vacacela Gomez, C. (2024). Role of graphene in surface plasmon resonance-based biosensors. *Sensors*, **24**(14), 4670.

168. Cheng, L., Mao, S., Li, Z., Han, Y., & Fu, H. Y. (2020). Grating couplers on silicon photonics: Design principles, emerging trends and practical issues. *Micromachines*, **11**(7), 666.

169. Dalgoutte, D. G., & Wilkinson, C. D. W. (1975). Thin grating couplers for integrated optics: an experimental and theoretical study. *Applied Optics*, **14**(12), 2983-2998.

170. Shi, W., Veerasubramanian, V., Plant, D. V., Jaeger, N. A., & Chrostowski, L. (2014, February). Silicon photonic Bragg-grating couplers for optical communications. In *Next-Generation Optical Networks for Data Centers and Short-Reach Links* (Vol. 9010, pp. 63-74). SPIE.

171. Xiao, Z., Luan, F., Liow, T. Y., Zhang, J., & Shum, P. (2012). Design for broadband high-efficiency grating couplers. *Optics Letters*, **37**(4), 530-532.

172. Vörös, J., Ramsden, J. J., Csucs, G., Szendrő, I., De Paul, S. M., Textor, M., & Spencer, N. D. (2002). Optical grating coupler biosensors. *Biomaterials*, **23**(17), 3699-3710.

173. Wendler, L., & Kraft, T. (1999). Theory of grating-coupler-assisted infrared spectroscopy of lower-dimensional electron systems: Local optics of anisotropic multilayer systems with grating. *Physica B: Condensed Matter*, **271**(1-4), 33-98.

174. Lim, Y. D., Li, H. Y., Zhao, P., Tao, J., Guidoni, L., & Tan, C. S. (2021). Design and fabrication of grating couplers for the optical addressing of trapped ions. *IEEE Photonics Journal*, **13**(4), 1-6.

175. Schmidt, C., Ma, C., Benthin, F., Yang, J., Rugeramigabo, E. P., Zopf, M., & Ding, F. (2024). High efficiency grating couplers for strain tunable GaAs quantum dot based entangled photon sources. *AIP Advances*, **14**(1).

176. Sapra, N. V., Vercruysse, D., Su, L., Yang, K. Y., Skarda, J., Piggott, A. Y., & Vučković, J. (2019). Inverse design and demonstration of broadband grating couplers. *IEEE Journal of Selected Topics in Quantum Electronics*, **25**(3), 1-7.

177. Scheerlinck, S., Schrauwen, J., Laere, F. V., Taillaert, D., Thourhout, D. V., & Baets, R. (2007). Efficient, broadband and compact metal grating couplers for silicon-on-insulator waveguides. *Optics Express*, **15**(15), 9625-9630.

178. Taillaert, D., Baets, R., Dumon, P., Bogaerts, W. W., Van Thourhout, D., Luyssaert, B., ... & Wouters, J. (2005, June). Silicon-on-insulator platform for integrated wavelength-selective components. In *Proceedings of 2005 IEEE/LEOS Workshop on Fibres and Optical Passive Components, 2005* (pp. 115-120). IEEE.

179. Van Laere, F., Roelkens, G., Ayre, M., Schrauwen, J., Taillaert, D., Van Thourhout, D., ... & Baets, R. (2007). Compact and highly efficient grating couplers between optical fiber and nanophotonic waveguides. *Journal of Lightwave Technology*, **25**(1), 151-156.
180. Pockrand, I. (1978). Surface plasma oscillations at silver surfaces with thin transparent and absorbing coatings. *Surface Science*, **72**(3), 577-588.
181. Raether, H. (2006). Surface plasmons on gratings. In *Surface plasmons on smooth and rough surfaces and on gratings* (pp. 91-116).
182. Wang, J., Glesk, I., & Chen, L. R. (2014). Subwavelength grating filtering devices. *Optics Express*, **22**(13), 15335-15345.
183. Ulrich, R. (1973). Efficiency of optical-grating couplers. *Journal of the Optical Society of America*, **63**(11), 1419-1431.
184. Ho, C. P., Zhao, Z., Li, Q., Takagi, S., & Takenaka, M. (2018). Tunable grating coupler by thermal actuation and thermo-optic effect. *IEEE Photonics Technology Letters*, **30**(17), 1503-1506.
185. Tame, M. S., McEnery, K. R., Özdemir, Ş. K., Lee, J., Maier, S. A., & Kim, M. S. (2013). Quantum plasmonics. *Nature Physics*, **9**(6), 329-340.
186. Fitzgerald, J. M., Narang, P., Craster, R. V., Maier, S. A., & Giannini, V. (2016). Quantum plasmonics. *Proceedings of the IEEE*, **104**(12), 2307-2322.
187. Lee, C., Lawrie, B., Pooser, R., Lee, K. G., Rockstuhl, C., & Tame, M. (2021). Quantum plasmonic sensors. *Chemical Reviews*, **121**(8), 4743-4804.
188. Liu, Y., Ouyang, C., Xu, Q., Su, X., Yang, Q., Ma, J., ... & Zhang, W. (2022). Moiré-driven electromagnetic responses and magic angles in a sandwiched hyperbolic metasurface. *Photonics Research*, **10**(9), 2056-2065.
189. Yang, Y., Qin, P., Lin, X., Li, E., Wang, Z., Zhang, B., & Chen, H. (2019). Type-I hyperbolic metasurfaces for highly-squeezed designer polaritons with negative group velocity. *Nature Communications*, **10**(1), 2002.
190. Garcia-Vidal, F. J., Martin-Moreno, L., Ebbesen, T. W., & Kuipers, L. (2010). Light passing through subwavelength apertures. *Reviews of Modern Physics*, **82**(1), 729-787.
191. Weiner, J. (2009). The physics of light transmission through subwavelength apertures and aperture arrays. *Reports on Progress in Physics*, **72**(6), 064401.
192. Genet, C., & Ebbesen, T. W. (2007). Light in tiny holes. *Nature*, **445**(7123), 39-46.
193. Bethe, H. A. (1944). Theory of diffraction by small holes. *Physical Review*, **66**(7-8), 163.

194. Ebbesen, T. W., Lezec, H. J., Ghaemi, H. F., Thio, T., & Wolff, P. A. (1998). Extraordinary optical transmission through sub-wavelength hole arrays. *Nature*, **391**(6668), 667-669.
195. Kinoshita, S., Yoshioka, S., & Miyazaki, J. (2008). Physics of structural colors. *Reports on Progress in Physics*, **71**(7), 076401.
196. Kinoshita, S., & Yoshioka, S. (2005). Structural colors in nature: the role of regularity and irregularity in the structure. *ChemPhysChem*, **6**(8), 1442-1459.
197. Xie, Y., Liu, H., Jia, H., & Zhong, Y. (2015). Surface-mode model of the extraordinary optical transmission without plasmons. *Optics Express*, **23**(5), 5749-5762.
198. Rodrigo, S. G., de Leon-Perez, F., & Martin-Moreno, L. (2016). Extraordinary optical transmission: fundamentals and applications. *Proceedings of the IEEE*, **104**(12), 2288-2306.
199. Gordon, R., Sinton, D., Kavanagh, K. L., & Brolo, A. G. (2008). A new generation of sensors based on extraordinary optical transmission. *Accounts of Chemical Research*, **41**(8), 1049-1057.
200. Yue, W., Wang, Z., Yang, Y., Li, J., Wu, Y., Chen, L., ... & Zhang, X. X. (2014). Enhanced extraordinary optical transmission (EOT) through arrays of bridged nanohole pairs and their sensing applications. *Nanoscale*, **6**(14), 7917-7923.
201. Neumann, L., Pang, Y., Houyou, A., Juan, M. L., Gordon, R., & Van Hulst, N. F. (2011). Extraordinary optical transmission brightens near-field fiber probe. *Nano Letters*, **11**(2), 355-360.
202. Du, G., Yu, F., Lu, Y., Kai, L., Chen, C., Yang, Q., ... & Chen, F. (2023). Ultrafast Dynamics of Extraordinary Optical Transmission through Two-Slit Plasmonic Antenna. *Nanomaterials*, **13**(16), 2284.
203. Lee, K. L., Chen, P. W., Wu, S. H., Huang, J. B., Yang, S. Y., & Wei, P. K. (2012). Enhancing surface plasmon detection using template-stripped gold nanoslit arrays on plastic films. *ACS Nano*, **6**(4), 2931-2939.
204. Wei, J., Singhal, S., Kofke, M., & Waldeck, D. H. (2010, June). Transmission SPR of gold nanoslit array and ultrasensitive detection of a retinol binding protein. In *2010 4th International Conference on Bioinformatics and Biomedical Engineering* (pp. 1-4). IEEE.
205. Chung, P. Y., Lee, K. L., Schultz, G., Wei, P. K., & Batich, C. (2010). Multispectral Refractive Index Sensing Using Surface Plasmon Resonance on Gold Nanoslits. *MRS Online Proceedings Library (OPL)*, **1253**, 1253-K10.

206. Sieben-Xu, L., Offermans, P., Brom-Verheyden, G., Brongersma, S. H., & Calama, M. C. (2011). High performance surface plasmon resonance sensor based on two dimensional ultra-thin metal nanoslit arrays. In *IEEE* (pp. 1374-1377).
207. Liu, H., & Lalanne, P. (2010). Comprehensive microscopic model of the extraordinary optical transmission. *Journal of the Optical Society of America A*, **27**(12), 2542-2550.
208. Beermann, J., Søndergaard, T., Novikov, S. M., Bozhevolnyi, S. I., Devaux, E., & Ebbesen, T. W. (2011). Field enhancement and extraordinary optical transmission by tapered periodic slits in gold films. *New Journal of Physics*, **13**(6), 063029.
209. Peer, A., & Biswas, R. (2016). Extraordinary optical transmission in nanopatterned ultrathin metal films without holes. *Nanoscale*, **8**(8), 4657-4666.
210. Whitesides, G. M. (2006). The origins and the future of microfluidics. *Nature*, **442**(7101), 368-373.
211. Stone, H. A., & Kim, S. (2001). Microfluidics: basic issues, applications, and challenges. *AIChE Journal*, **47**(6), 1250.
212. Tabeling, P. (2023). *Introduction to Microfluidics*. Oxford University Press.
213. Nguyen, N. T., Wereley, S. T., & Shaegh, S. A. M. (2019). *Fundamentals and Applications of Microfluidics*. Artech House.
214. Gravesen, P., Branebjerg, J., & Jensen, O. S. (1993). Microfluidics-a review. *Journal of Micromechanics and Microengineering*, **3**(4), 168.
215. Battat, S., Weitz, D. A., & Whitesides, G. M. (2022). An outlook on microfluidics: the promise and the challenge. *Lab on a Chip*, **22**(3), 530-536.
216. Wang, D. S., & Fan, S. K. (2016). Microfluidic surface plasmon resonance sensors: From principles to point-of-care applications. *Sensors*, **16**(8), 1175.
217. Lee, H. J., Goodrich, T. T., & Corn, R. M. (2001). SPR imaging measurements of 1-D and 2-D DNA microarrays created from microfluidic channels on gold thin films. *Analytical Chemistry*, **73**(22), 5525-5531.
218. Singh, P. (2016). SPR biosensors: historical perspectives and current challenges. *Sensors and Actuators B: Chemical*, **229**, 110-130.
219. Wang, Z., Wilkop, T., Xu, D., Dong, Y., Ma, G., & Cheng, Q. (2007). Surface plasmon resonance imaging for affinity analysis of aptamer–protein interactions with PDMS microfluidic chips. *Analytical and Bioanalytical Chemistry*, **389**, 819-825.
220. Beni, G., & Hackwood, S. (1981). Electro-wetting displays. *Applied Physics Letters*, **38**(4), 207-209.

221. Manz, A., Graber, N., & Widmer, H. Á. (1990). Miniaturized total chemical analysis systems: a novel concept for chemical sensing. *Sensors and Actuators B: Chemical*, **1**(1-6), 244-248.
222. Zimmerman, W. B. (Ed.). (2006). *Microfluidics: History, Theory and Applications* (Vol. 466). Springer Science & Business Media.
223. Xia, Y., & Whitesides, G. M. (1998). Soft lithography. *Angewandte Chemie International Edition*, **37**(5), 550-575.
224. Kopp, M. U., Mello, A. J. D., & Manz, A. (1998). Chemical amplification: continuous-flow PCR on a chip. *Science*, **280**(5366), 1046-1048.
225. Harrison, D. J., Fluri, K., Seiler, K., Fan, Z., Effenhauser, C. S., & Manz, A. (1993). Micromachining a miniaturized capillary electrophoresis-based chemical analysis system on a chip. *Science*, **261**(5123), 895-897.
226. Andersson, H., & Van Den Berg, A. (2004). Microfabrication and microfluidics for tissue engineering: state of the art and future opportunities. *Lab on a Chip*, **4**(2), 98-103.
227. Andersson, H., & Van den Berg, A. (2003). Microfluidic devices for cellomics: a review. *Sensors and Actuators B: Chemical*, **92**(3), 315-325.
228. Van den Berg, A., & Segerink, L. (Eds.). (2014). *Microfluidics for Medical Applications*.
229. Mark, D., Haeberle, S., Roth, G., Von Stetten, F., & Zengerle, R. (2010). Microfluidic lab-on-a-chip platforms: requirements, characteristics and applications. In *Microfluidics Based Microsystems: Fundamentals and Applications* (pp. 305-376).
230. Haeberle, S., & Zengerle, R. (2007). Microfluidic platforms for lab-on-a-chip applications. *Lab on a Chip*, **7**(9), 1094-1110.
231. Dittrich, P. S., & Manz, A. (2006). Lab-on-a-chip: microfluidics in drug discovery. *Nature Reviews Drug Discovery*, **5**(3), 210-218.
232. Srinivasan, V., Pamula, V. K., & Fair, R. B. (2004). An integrated digital microfluidic lab-on-a-chip for clinical diagnostics on human physiological fluids. *Lab on a Chip*, **4**(4), 310-315.
233. Nge, P. N., Rogers, C. I., & Woolley, A. T. (2013). Advances in microfluidic materials, functions, integration, and applications. *Chemical Reviews*, **113**(4), 2550-2583.
234. Mou, L., & Jiang, X. (2017). Materials for microfluidic immunoassays: a review. *Advanced Healthcare Materials*, **6**(15), 1601403.
235. Roy, E., Pallandre, A., Zribi, B., Horny, M. C., Delapierre, F. D., Cattoni, A., ... & Haghiri-Gosnet, A. M. (2016). Overview of materials for microfluidic applications. In *Advances in Microfluidics—New Applications in Biology, Energy, and Materials Sciences* (p. 335).

236. Wang, B., Prinsen, P., Wang, H., Bai, Z., Wang, H., Luque, R., & Xuan, J. (2017). Macroporous materials: microfluidic fabrication, functionalization and applications. *Chemical Society Reviews*, **46**(3), 855-914.
237. Carvell, T., Burgoyne, P., Fraser, A. R., & Bridle, H. (2024). Categorising hybrid material microfluidic devices. *Frontiers in Lab on a Chip Technologies*, **3**, 1412290.
238. Copperwhite, R., O'Sullivan, M., Boothman, C., Gorin, A., McDonagh, C., & Oubaha, M. (2011). Development and characterisation of integrated microfluidics on waveguide-based photonic platforms fabricated from hybrid materials. *Microfluidics and Nanofluidics*, **11**, 283-296.
239. Torres-Alvarez, D., Bosques-Palomo, B., Martínez-Dibildox, A., Marcos-Abdala, A., Jiménez-Nuñéz, R., Morones-Ramírez, J. R., ... & Aguirre-Soto, A. (2024). Introduction of the lowest printable (channel) characteristic length (LPCL) as a geometrical metric for the SLA 3D printing of embedded negative micro-structures. *Progress in Additive Manufacturing*, 1-13.
240. Qian, J. Y., Hou, C. W., Li, X. J., & Jin, Z. J. (2020). Actuation mechanism of microvalves: A review. *Micromachines*, **11**(2), 172.
241. Lau, A. T., Yip, H. M., Ng, K. C., Cui, X., & Lam, R. H. (2014). Dynamics of microvalve operations in integrated microfluidics. *Micromachines*, **5**(1), 50-65.
242. Kim, J., Stockton, A. M., Jensen, E. C., & Mathies, R. A. (2016). Pneumatically actuated microvalve circuits for programmable automation of chemical and biochemical analysis. *Lab on a Chip*, **16**(5), 812-819.
243. Ferretti, P., Pagliari, C., Montalti, A., & Liverani, A. (2023). Design and development of a peristaltic pump for constant flow applications. *Frontiers in Mechanical Engineering*, **9**, 1207464.
244. Ebrahimi, S., et al. (2023). Optimizing the design of a serpentine microchannel based on particles focusing and separation: A numerical study with experimental validation. *Sensors and Actuators A: Physical*, **358**, 114432.
245. Safavieh, R., Tamayol, A., & Juncker, D. (2015). Serpentine and leading-edge capillary pumps for microfluidic capillary systems. *Microfluidics and Nanofluidics*, **18**, 357-366.
246. Altay, R. (2020). Fluid mixing efficiency enhancement in microchannels having spiral elliptic and curved structures with various baffle geometries. *Doctoral Dissertation*.
247. Raza, W., Islam, N., & Samad, A. (2023). Design and analysis of a novel Bi-layer curved serpentine chaotic micromixer for efficient mixing. *Chemical Engineering and Processing-Process Intensification*, **183**, 109246.

248. Araz, M. K., Tentori, A. M., & Herr, A. E. (2013). Microfluidic multiplexing in bioanalyses. *Journal of Laboratory Automation*, **18**(5), 350-366.
249. Liao, Z., et al. (2018). Recent advances in microfluidic chip integrated electronic biosensors for multiplexed detection. *Biosensors and Bioelectronics*, **121**, 272-280.
250. He, S., et al. (2015). Multiplexed microfluidic blotting of proteins and nucleic acids by parallel, serpentine microchannels. *Lab on a Chip*, **15**(1), 105-112.
251. Dishinger, J. F., & Kennedy, R. T. (2008). Multiplexed detection and applications for separations on parallel microchips. *Electrophoresis*, **29**(16), 3296-3305.
252. Ghodbane, M., et al. (2015). Development and validation of a microfluidic immunoassay capable of multiplexing parallel samples in microliter volumes. *Lab on a Chip*, **15**(15), 3211-3221.
253. Ren, H., et al. (2021). Multiplexed serpentine microchannels for high-throughput sorting of disseminated tumor cells from malignant pleural effusion. *Sensors and Actuators B: Chemical*, **337**, 129758.
254. Gallagher, R. H., et al. (1975). *Finite Element Analysis: Fundamentals*. Prentice Hall, Englewood Cliffs.
255. Szabó, B., & Babuška, I. (2021). *Finite Element Analysis: Method, Verification and Validation*.
256. Bhavikatti, S. S. (2005). *Finite Element Analysis*. New Age International.
257. Zienkiewicz, O. C., et al. (1977). *The Finite Element Method* (Vol. 3). London: McGraw-Hill.
258. Jagota, V., Sethi, A. P. S., & Kumar, K. (2013). Finite element method: an overview. *Walailak Journal of Science and Technology (WJST)*, **10**(1), 1-8.
259. Courant, R. (1994). Variational methods for the solution of problems of equilibrium and vibrations. *Lecture Notes in Pure and Applied Mathematics*, 1-1.
260. Hrennikoff, A. (1941). Solution of problems of elasticity by the framework method.
261. McHenry, D. (1943). A lattice analogy for the solution of stress problems. *Journal of the Institution of Civil Engineers*, **21**(2), 59-82.
262. Argyris, J. H., & Kelsey, S. (1960). *Energy Theorems and Structural Analysis* (Vol. 60). London: Butterworths.
263. Turner, M. J., Clough, R. W., Martin, H. C., & Topp, L. J. (1956). *Journal of Aeronautical Science*.
264. Clough, R. W. (1990). Original formulation of the finite element method. *Finite Elements in Analysis and Design*, **7**(2), 89-101.

265. Silvester, P. P., & Ferrari, R. L. (1996). *Finite Elements for Electrical Engineers*. Cambridge University Press.
266. Jin, J. M. (2015). *The Finite Element Method in Electromagnetics*. John Wiley & Sons.
267. Yan, M., & Qiu, M. (2007). Analysis of surface plasmon polariton using anisotropic finite elements. *IEEE Photonics Technology Letters*, **19**(22), 1804-1806.
268. Smajic, J., Hafner, C., Raguin, L., Tavzarashvili, K., & Mishrikey, M. (2009). Comparison of numerical methods for the analysis of plasmonic structures. *Journal of Computational and Theoretical Nanoscience*, **6**(3), 763-774.
269. Leelawattananon, T., Lorchalearnrat, K., & Chittayasothorn, S. (2017, July). Simulation of copper thin film thickness optimization for surface plasmon using the finite element method. In *SIMULTECH* (pp. 188-195).
270. Tariq, S. M., Fakhri, M. A., Salim, E. T., Hashim, U., & Alsultany, F. H. (2022). Design of an unclad single-mode fiber-optic biosensor based on localized surface plasmon resonance by using COMSOL Multiphysics 5.1 finite element method. *Applied Optics*, **61**(21), 6257-6267.
271. Mondal, T. P., Mahmud, R. R., Rafi, S. A., Islam, M. S., & Barua, B. (2025). Design and optimization of a highly sensitive surface plasmon resonance biosensor for accurate detection of Mycobacterium tuberculosis. *IEEE Sensors Journal*.
272. *Wave Optics Module User's Guide*, COMSOL Multiphysics v. 5.4 (COMSOL AB, 2018).
273. DesignWorks. (n.d.). *DW200 PDA Layout*. DesignWorks. Retrieved from https://www.designw.com/PDA-Layout.php
274. KLayout. (n.d.). Galleries. *KLayout: Layout Viewer & Editor*. Retrieved from https://www.klayout.de/galleries.html
275. Chrostowski, L., Shoman, H., Hammood, M., Yun, H., Jhoja, J., Luan, E., & Knights, A. P. (2019). Silicon photonic circuit design using rapid prototyping foundry process design kits. *IEEE Journal of Selected Topics in Quantum Electronics*, **25**(5), 1-26.
276. Rizvi, S. (Ed.). (2018). *Handbook of Photomask Manufacturing Technology*. CRC Press.
277. Luttge, R. (2009). Massively parallel fabrication of repetitive nanostructures: nanolithography for nanoarrays. *Journal of Physics D: Applied Physics*, **42**(12), 123001.
278. Useller, J. W. (1969). *Clean Room Technology* (Vol. 5074). Technology Utilization Division, National Aeronautics and Space Administration.

279. Xu, T. (2007). Characterization of minienvironments in a clean room: design characteristics and environmental performance. *Building and Environment*, **42**(8), 2993-3000.
280. Naughton, P. (2019). History of cleanrooms. *ASHRAE Journal*, **61**(11), 38-54.
281. Whyte, W. (2010). *Cleanroom Technology: Fundamentals of Design, Testing and Operation*. John Wiley & Sons.
282. Holbrook, D. (2009). Controlling contamination: the origins of clean room technology. *History and Technology*, **25**(3), 173-191.
283. Murugan, D., Tintelott, M., Narayanan, M. S., Vu, X. T., Kurkina, T., Rodriguez-Emmenegger, C., ... & Pachauri, V. (2024). Recent advances in grating coupled surface plasmon resonance technology. *Advanced Optical Materials*, **12**(34), 2401862.
284. Chen, Y., Shu, Z., Zhang, S., Zeng, P., Liang, H., Zheng, M., & Duan, H. (2021). Sub-10 nm fabrication: methods and applications. *International Journal of Extreme Manufacturing*, **3**(3), 032002.
285. Chou, S. Y., Krauss, P. R., Zhang, W., Guo, L., & Zhuang, L. (1997). Sub-10 nm imprint lithography and applications. *Journal of Vacuum Science & Technology B: Microelectronics and Nanometer Structures Processing, Measurement, and Phenomena*, **15**(6), 2897-2904.
286. Schroth, T. (1996). New HEPA/ULPA filters for clean-room technology. *Filtration & Separation*, **33**(3), 245-244.
287. Sadir, R. A., Villarmosa, A., & Figueiredo, L. (2016). Clean room technology: An overview of clean room classification standards. In *Clean Room Technology in ART Clinics* (pp. 39-52).
288. Madou, M. J. (2018). *Fundamentals of Microfabrication: The Science of Miniaturization*. CRC Press.
289. Thompson, L. F. (1983). An introduction to lithography.
290. Sharma, E., Rathi, R., Misharwal, J., Sinhmar, B., Kumari, S., Dalal, J., & Kumar, A. (2022). Evolution in lithography techniques: microlithography to nanolithography. *Nanomaterials*, **12**(16), 2754.
291. Chen, J., Zhou, Y., Wang, D., He, F., Rotello, V. M., Carter, K. R., ... & Nugen, S. R. (2015). UV-nanoimprint lithography as a tool to develop flexible microfluidic devices for electrochemical detection. *Lab on a Chip*, **15**(14), 3086-3094.
292. Chen, Y. (2015). Nanofabrication by electron beam lithography and its applications: A review. *Microelectronic Engineering*, **135**, 57-72.

293. Vieu, C., Carcenac, F., Pepin, A., Chen, Y., Mejias, M., Lebib, A., ... & Launois, H. (2000). Electron beam lithography: resolution limits and applications. *Applied Surface Science*, **164**(1-4), 111-117.
294. Pimpin, A., & Srituravanich, W. (2012). Review on micro-and nanolithography techniques and their applications. *Engineering Journal*, **16**(1), 37-56.
295. Melngailis, J. (1987). Focused ion beam technology and applications. *Journal of Vacuum Science & Technology B: Microelectronics Processing and Phenomena*, **5**(2), 469-495.
296. Córdoba, R. (2024). Additive nanofabrication using focused ion and electron beams.
297. Watkins, R. E. J., Rockett, P., Thoms, S., Clampitt, R., & Syms, R. (1986). Focused ion beam milling. *Vacuum*, **36**(11-12), 961-967.
298. Ramotowski, R. S. (2012). Metal deposition methods. In *Lee and Gaensslen's Advances in Fingerprint Technology* (pp. 55-81).
299. Fuentes, G. G. (2015). Surface engineering and micro-manufacturing. In *Micromanufacturing Engineering and Technology* (Vol. 2, pp. 459-486).
300. Martín-Palma, R. J., & Lakhtakia, A. (2013). Vapor-deposition techniques. In *Engineered Biomimicry* (pp. 383-398). Elsevier.
301. Norrman, K., Ghanbari-Siahkali, A., & Larsen, N. B. (2005). Studies of spin-coated polymer films. *Annual Reports Section C (Physical Chemistry)*, **101**, 174-201.
302. Larson, R. G., & Rehg, T. J. (1997). Spin coating. In *Liquid Film Coating: Scientific Principles and Their Technological Implications* (pp. 709-734). Springer.
303. Donnelly, V. M., & Kornblit, A. (2013). Plasma etching: Yesterday, today, and tomorrow. *Journal of Vacuum Science & Technology A*, **31**(5).
304. Cardinaud, C., Peignon, M. C., & Tessier, P. Y. (2000). Plasma etching: principles, mechanisms, application to micro-and nano-technologies. *Applied Surface Science*, **164**(1-4), 72-83.
305. Sugawara, M. (1998). *Plasma Etching: Fundamentals and Applications* (Vol. 7). OUP Oxford.
306. Alexe, M., & Gösele, U. (Eds.). (2013). *Wafer Bonding: Applications and Technology* (Vol. 75). Springer.
307. Ramm, P., Lu, J. J. Q., & Taklo, M. M. (Eds.). (2012). *Handbook of Wafer Bonding*. John Wiley & Sons.
308. Efrat, U. (1993, October). Optimizing the wafer dicing process. In *Proceedings of 15th IEEE/CHMT International Electronic Manufacturing Technology Symposium* (pp. 245-253). IEEE.
309. Franssila, S. (2010). *Introduction to Microfabrication*. John Wiley & Sons.

310. Brandner, J. J., Gietzelt, T., Henning, T., Kraut, M., Moritz, H., & Pfleging, W. (2008). Microfabrication in metals and polymers. *Advanced Micro- and Nanosystems*, **5**, 267-320.
311. Qin, Y., Brockett, A., Ma, Y., Razali, A., Zhao, J., Harrison, C., ... & Loziak, D. (2010). Micro-manufacturing: research, technology outcomes and development issues. *The International Journal of Advanced Manufacturing Technology*, **47**, 821-837.
312. Kakani, S. L. (2004). *Material Science*. New Age International.
313. Shackelford, J. F. (2000). *Materials Science for Engineers*. Upper Saddle River, New Jersey.
314. Guo, Q., Reddy, K. M., Liu, J., & Jiao, S. (2010). *Fundamentals of Materials Science*.
315. Bever, M. B. (1985). *Encyclopedia of Materials Science and Engineering*.
316. Li, H. Y., Zhou, S. M., Li, J., Chen, Y. L., Wang, S. Y., Shen, Z. C., ... & Zhang, X. X. (2001). Analysis of the Drude model in metallic films. *Applied Optics*, **40**(34), 6307-6311.

Annex 1: Simulation Workflow Using COMSOL Multiphysics

The Finite Element Method (FEM) in COMSOL Multiphysics is highly effective for designing and optimizing Surface Plasmon Resonance (SPR) devices, thanks to its intuitive interface, multi-physics capabilities, and advanced meshing tools. COMSOL's Wave Optics Module excels at modeling electromagnetic interactions, accurately simulating how electromagnetic waves engage with nanostructures and propagate at metal-dielectric interfaces where surface plasmon polaritons (SPPs) are excited. This module's capacity to integrate simulations, including those combining electromagnetic waves with other physical phenomena, makes it essential for developing complex SPR systems.

The steps for successfully simulating mode analysis and scattering simulations in COMSOL are as follows:

1. Open the Model Wizard: Launch COMSOL and open the Model Wizard. Choose the "Wave Optics Module" and decide on either a 2D or 3D geometry, depending on the complexity of your Surface Plasmon Resonance (SPR) device.

2. Select Physics: Choose "Electromagnetic Waves, Frequency Domain (ewfd)" as the physics interface.

3. Set Up Study Types:

    - For Mode Analysis, select this study type to examine the natural propagation modes of electromagnetic structures.
    - For Scattering Simulations, select a study that models how an external source, like a TM-polarized Gaussian beam, interacts with the SPR system.

4. Define Parameters: Specify key variables like operating wavelength, beam waist, grating period, slit dimensions, and power.

5. Create Geometry: Construct the geometry of the SPR device, incorporating essential components such as nanoslits, gratings, and waveguides.

6. Add Perfectly Matched Layers (PMLs): Place PMLs at the boundaries of your geometry to simulate an open system environment.

7. Define Materials: Assign the appropriate material properties to each component of the SPR device.

8. Set Up Meshing: Divide the geometry into finite elements for numerical computation.

9. Configure Electromagnetic Ports and Sources: Define electromagnetic ports to introduce the excitation source.

10. Set Up Parametric Sweeps: Explore a range of design variables, such as grating period and slit width.

11. Run Simulations: Execute the simulations for both mode analysis and scattering scenarios.

12. Post-Processing and Analysis: Analyze results using COMSOL's advanced post-processing tools.

13. Iterate and Refine: Adjust design parameters and rerun simulations to fine-tune the device.

Ultimately, this workflow not only aims to maximize grating coupling efficiency and optimize nanoslits for desired SPR modes but also allows for the simulation of various factors that critically impact the performance of SPR devices. For instance, COMSOL can simulate the effects of changes in the analyte's refractive index, especially within integrated microfluidic environments, on the SPR signal.

In addition to optical simulations, COMSOL's multi-physics capabilities enable the integration of thermal effects, fluid-structure interactions, and mechanical deformations. This holistic approach helps predict how external factors, like temperature changes or structural stress, may impact the performance and reliability of the SPR sensor in real-world conditions. By accounting for these interconnected effects, researchers can develop more reliable and efficient SPR devices tailored for applications in biomedical diagnostics, environmental sensing, and integrated photonic platforms.